THE UNIVERSITY *of* EDINBURGH

Exploring coherence and disorder: an analysis of spatial patterning within the neuromesodermal progenitor niche.

Matthew French

A thesis submitted for the degree of Doctor of Philosophy

MRC Centre for Regenerative Medicine

The University of Edinburgh

2023

Declaration

I declare that the work presented here in this thesis is my own, unless otherwise stated. The work described in this thesis has not been submitted for any other degree or professional qualification.

Matthew French
February 2023

“There should be no such thing as boring mathematics.”

Edsger Dijkstra

Acknowledgments

I would first like to thank my PI Prof Sally Lowell for giving me the opportunity to study in her lab, as well as my other supervisors Prof Valerie Wilson and Prof Kim Dale for the project's creation and their help during it. I would like to thank Sally further for her continued support throughout my studies, patiently giving me the time and space to find my feet as I slowly got to grips with the terrifyingly complex and vast field of development. But also for culturing an uncommonly healthy and supportive lab environment that promoted fun and a genuine interest in science, which reflects in the work we do.

I would like to thank Dr Matt Malaguti for always sharing his encyclopaedic knowledge of development and providing PhD saving feedback. Many thanks go to Rosa for teaching me dissection techniques, then being kind enough to do them for me anyway and preserving my sanity while making my experiments much better. I would like to thank Dr Guillaume Blin for his support over the years and always helping me trouble shoot all things Pickcells, and creating the software in the first place. It has been so central to my project I couldn't have got anywhere without it. I have spent a lot of time on Pickcells learning its ins and outs, it really has a lot of character and I have become quite attached to it, so I would also like to extend my thanks to Pickcells itself. We have had our ups and downs over the years, but I have come to appreciate your numerous idiosyncrasies and the feeling of mutual understanding is second to none. Truly, there is no other software like you. Thanks go to all past and present members of the Wilson, Blin, and Lowell lab, it has been a pleasure working with you all.

Thanks go to the Eastbio programme for accepting me and introducing me to the friends in the cohort I endured this with, somehow we go through it together. Thanks go to Señor Aaron for accompanying me on the journey to discover the wild world of NMPs, which really helped us while trapped together during lockdown. Thanks go to the Imperial gang, exploring Edinburgh with you all has been a blast. And thanks you to my family for the love, support and encouragement.

Finally, I would like to thank my partner Dr Emily Clark for her steadfast support throughout my studies, whether it be consoling me after a horrific lab mistake or showing an interest when I get excited about a new type of graph, you really helped bear the weight over the years and I will do all I can to return your kindness.

Abstract

How regulatory frameworks control cellular identity and organisation via cell-cell communication is a poorly understood yet fundamental process in development. Different signalling pathway regulatory mechanisms can create a variety of spatial patterns of transcription factor (TF) expression and differentiation, however quantitatively assessing multicellular organisation in 3D has only recently been made possible due to advances in imaging and image analysis tools. Downstream analysis methods are still in their infancy and require further development to utilise the newly available information.

Neuromesodermal progenitors (NMPs) are a bipotent population of cells in the post gastrulation epiblast that self-renew while allocating cells to neural and mesodermal tissues of the trunk. Gradients of Retinoic acid, Wnt, and FGF signalling direct the neural vs mesoderm cell fate decision and regionalise the axial progenitor niches, but the spatial patterning of TF expression has not been quantified. Further, previous work shows that the Notch signalling pathway also regulates the cell fate decision in NMPs, but this is not well characterised and it’s unknown if Notch contributes to any TF patterning.

I aimed to use systems biology inspired analysis methods to investigate the role of Notch signalling in NMP fate and patterning. First, I investigated the pro-neural effect of Notch inhibition in NMPs and identified which Notch components are expressed. Then, I developed quantitative analysis methods that show differential spatial patterning of key TF fate markers in NMP niches in vitro and in vivo. Finally, I explored how Notch influences this patterning, overall providing a framework for future work to analyse spatial gene expression data.

Lay Summary

Regenerative medicine aims to produce therapies to treat currently uncurable diseases by either exploiting our own natural regeneration or looking to embryo development to make tissues from scratch. Researching embryo development often involves trying to understand what we call stem cells. Stem cells are cells in the embryo that replicate themselves and have the potential to be many other cell types, such as muscle cells or nerve cells. These are termed “stem” cells since groups of different adult cell types originate or “stem” from a single parent cell type in the embryo. But stem cells will only stop replicating and turn into specialised adult cells, what we call differentiation, with the right signals.

We know that groups of stem cells talk to each other and collectively decide what to do, whether it be to keep replicating or stop and differentiate. Inconveniently, there isn’t a dictatorial master cell issuing out orders throughout development that we can target. Even more inconveniently, stem cells don’t just have one communication channel, they use many simultaneously in a complex web of short and long range conversations between their neighbours and far away cells (far being relative to cells, a few hair widths can count as “long range”). The stem cell environment is a noisy one.

The focus of this thesis is an understudied short range communication channel which works in conjunction with longer range channels to organise a particularly interesting group of stem cells called neuromesodermal progenitors (NMPs). These are stem cells that can make many tissues in the body’s trunk (from the neck down) including spinal cord, peripheral nerves, and skeletal muscles. If we can control these, we can make tissues from scratch to replace when damaged or to test drugs on, instead of people or animals.

Not only must NMPs decide on the right time to differentiate, but they must also decide on the right place. Replication or differentiation is spatially organised to make sure that the many tissues they make have the right size and shape. They do this

very reproducibly, almost all humans are nearly symmetrical with similar body proportions, the same number of vertebrae etc. But we don’t come close to this level of reproducibility when we culture NMPs ourselves and try to make tissues from them. The problem is that these communication pathways and decision-making processes are incomprehensibly complex.

As it turns out, the underlying control logic in the decision-making processes of stem cells are quite like the ones used in machines made by engineers. For instance, similar feedback mechanisms found in central heating systems to maintain constant room temperatures can also be found in stem cells. As such, many of the techniques and theory behind engineering can be directly applied to understand biology. The key thing engineers have to offer, is they have figured out ways to describe very complex machines so everyone is on the same page. They do this with consistent mathematical languages that simply describes modules within a larger system and can do so without getting unnecessarily bogged down in the detail, capturing the essential “role” of each component within the broader picture.

In this thesis I develop and explore engineering inspired methods to understand how short-range communication controls the spatial organisation of NMP stem cell differentiation. Specifically, I quantify how ordered the differentiated and undifferentiated stem cells are in their niche. This is important so when I disrupt their communication channels and NMPs can’t talk to their neighbours, we can tell how their organisation changes. This information will give us clues as to how and why they use these signals to organise so we can replicate that and better control NMP differentiation.

Contents:

List of Figures

Chapter 1:

Introduction

1.1 Systems and synthetic biology in development.

1.1.1 Engineering and Biology, what's the difference?

Over the last half century, fundamental links between biology and engineering have rapidly come into focus. As our knowledge of biological systems have advanced, cross-disciplinary collaborations between these fields have flourished. While inter-disciplinary researchers often find it hard to reconcile the differences in scientific process and problem solving, fundamental similarities in the materials at hand have proven that the two disciplines have a lot to offer each other. Like machines designed by engineers, we now understand that biological systems have innate logic and modularity. For instance, DNA stores and confers information to produce protein actuators that compute logic to generate a programmed response of cell function. The structure of DNA and proteins are highly modular, with the all-illusive "design" of these modular systems being shaped by evolutionary pressure. As such, many of the hugely successful ideas and methodologies developed from engineering can be directly applied to biological research.

The nascent field of systems and synthetic biology takes advantage of the similarities between biology and engineering, applying principles from engineering, such as control theory (Del Vecchio et al., 2016), to rationally design and control biological components (Cameron et al., 2014, Lienert et al., 2014). Scientists in this field have undertaken the herculean effort to characterise, design and create biological tools and products because biological systems are in effect masterpieces of engineering. For instance, the evolutionary laws that guide the "design" of

biological components eliminate wasted energy through natural selection, producing exceptionally efficient molecular machinery. While this can cause many headaches for researchers when their beloved genetic constructs are promptly disposed of by cells for being too energy intensive, evolution has produced enviously efficient and robust biological systems that carry out a wide variety of specialised functions. Harnessing this would be greatly beneficial for society and solve crucial problems which cannot be fixed with current engineering materials.

1.1.2 An engineer's approach to biology.

While remarkable progress has been made in the design of biological tools and products, a common blockade in our efforts is that we fundamentally do not understand biological systems enough to harness them. Mostly we are mere guides for existing biological systems rather than true masters of them, harking back to the infamous phrase endemic to synthetic biology literature, "What I cannot create, I do not understand" - Richard Feynman. This is the foundational idea of the bottom-up approach, which looks to build systems from the ground up.

A counter to this approach is that we do not have to understand everything about a system to control it. To paraphrase my Masters degree project PI Dr Guy-Bart Stan, "to this day we are still learning new things about wind and turbulence, but planes have been successfully flying the skies for decades". A good example of this is directed evolution technology, such as the 2018 Nobel prize winning phage display method, where we do not fully understand the mechanisms of evolution nor how to rationally design proteins, so an expedited analogue of evolution was created to design proteins for us. While it is true we do not understand the true design principles of proteins enough to produce them directly, we can understand it enough to guide the biological mechanisms to meet our needs.

These two opposing methodologies, the bottom up and top-down approach, are central to systems and synthetic biology. Both have their merits and can be used to create novel products or understand natural laws, or even creating products to understand natural laws.

Research scientists mostly operate with a reverse engineering approach. Here, scientists are presented with unfathomably complex and dynamic “products” to first characterise the design, then understand the design goals and purpose of each component. In contrast, engineering frequently operates in a three stage forward engineering process, where (i) one starts with design goals, then (ii) using scientific knowledge produces a design to meet those goals, and ultimately (iii) produces a physical product from the design.

Differences in approaches to reverse engineering by biologists and engineers were explored by Lazebnik (2002) in an entertaining thought experiment, how would a biologist go about fixing a radio? The author posits that a traditional approach from biology would first characterise all the individual radio components and observe how breaking them this affects the system. But too often this is destined to hit a wall and fall short of true understanding as biologists, and pharmaceutical interests, focus on individual targets to find a panacea drug target. To understand complex systems, mathematical languages are required to describe the system as a whole to break the deadlock and enable true understanding.

1.1.3 Systems biology in development: Stem cell populations and cell fate decisions.

Some researchers in developmental biology are adopting systems biology inspired approaches to understand key processes that are too complex to be investigated with traditional techniques (Kitano, 2002, Hu and Zeng, 2012). We wish to understand the control mechanisms in early embryo development enough to exploit them for our needs, including therapies for regenerative medicine or non-clinical applications such as in vitro cultured meat to meet global food supply demands. While we know much about development, failure in attempts to design and implement therapies or technologies from our knowledge highlights crucial gaps in our understanding.

The underpinning issue is that focussing on single components with one or two degrees of separation (the components that closely interact with the component of

the study) does not accurately represent the system that is controlling the behaviour we are interested in. The complexity is too great to overcome this way, and so mathematical languages are required describe the system as a whole and build a more complete picture of the biological system in question. There is no doubt we have learned much with a traditional approach and has produced vital information used in medicine and industry, but due to the sheer complexity of some biological systems, a top-down mathematical approach is required to truly comprehend the supposed design and goals of the biology we want to exploit.

Embryonic stem (ES) cells have largely been the focus of regenerative medicine as these are cells with two defining characteristics; (i) the potential to make any adult cell, termed pluripotency, and (ii) self-renewal with no known division limit. Although, pluripotency exists only for a short window; many other stem cell populations with multipotency and self-renewal exist throughout development that serve similar purposes. The key principles of maintaining stem cell pool's potency, population size, and how cell fate decisions are organised are critical to understand for stem cell technologies.

Embryonic cells communicate to each other to coordinate gene expression and establish tissue structures (Lander, 2011). No single master cell population exists in the developing embryo which coordinates all other cell fates, rather cells collectively organise and regulate developmental processes. Stem cell proliferation, differentiation, and cell movement (among other processes) occur in coordination to establish tissue structures and maintain progenitor pools. Embryo development is also resistant to perturbations e.g. development can proceed normally after reduction or addition of cells through grafting studies. Cell fate decisions, movement, and proliferation are controlled to consistently produce similar tissue structures, although these structures are not ultimately precisely identical since separate embryos' development are not the same in terms of cell number, position, and timing. Correction for perturbations implies feedback mechanisms regulate variations back to a "steady state" or a functional target.

A principle in control theory dictates a trade-off in feedback performance when tuning perturbation control (Garpinger et al., 2014), and this also applies to biological systems (Lander, 2011, Del Vecchio et al., 2016). The more robustness to uncertainty designed into a system, the potential performance is reduced and an acceptable balance between these is the goal for engineering such systems. For example, developmental control via long range diffusible chemical gradient signalling is central to models for embryo development and organisation (Wolpert, 1969). The longer a morphogen gradient covers, the higher functional potential can be achieved. But with increasing distance, the gradients need to be steeper as shallow gradients are more susceptible to stochasticity. To achieve steep gradients, the diffusion speed of the signal can be decreased, but then the increased time diffusing molecules take to cover the gradient range results in a trade-off for responsiveness.

The regulatory frameworks for achieving such robustness observed *in vivo* despite extensive stochastic influence generally in development are not fully understood, appreciating the presence of trade-offs in design of regulatory frameworks developed from engineering is beneficial when tyring reverse engineering biological frameworks.

However, problems such as these are inherently complex and challenging to address with traditional experimental techniques. Incorporating novel experimental and mathematical system's biology inspired approaches allows the interrogation of the biological systems governing stem cell populations as a whole system.

1.2 Early mouse development.

The major events leading up to the establishment of neuro-mesodermal progenitors are outlined in brief (extensively reviewed elsewhere [(Tam and Behringer, 1997, Tam and Loebel, 2007, Bardot and Hadjantonakis, 2020, Chazaud and Yamanaka, 2016)]).

1.2.1 Pre-implantation

Mouse development begins at fertilisation where the sperm and ovum fuse to form a fertilised egg or zygote. This singe cell is totipotent, meaning it has the potential to form all tissues of the embryo and extra-embryonic tissue. This totipotency is maintained as the large zygote undergoes symmetric divisions, without expansion (Rossant and Tam, 2009, Wennekamp et al., 2013, Nichols and Smith, 2012), to create progressively smaller nearly identical cells termed blastomeres (Tarkowski and Wróblewska, 1967). Soon after the 8-16 stage cell stage, the blastomere undergo compaction to form the morula and first lineage segregation occurs (Rossant and Tam, 2009, Wennekamp et al., 2013). Polarised cells around the outer edge of the morula will eventually contribute cells to the trophectoderm (TE), whereas the non-polarised cells at the core of the developing embryo remain totipotent and give rise to the inner cell mass (ICM). At embryonic day 3.5 (E3.5) post fertilisation, the morula undergoes cavitation to form the blastocyst (Smith and McLaren, 1977) where totipotent cells in the inner cell mass (ICM) segregates to two populations, the pluripotent epiblast and hypoblast (or primitive endoderm [PE]) (Chazaud et al., 2006). Pluripotency in the pre-implantation epiblast is maintained by the expression of a core network of transcription factors (TFs) genes *octamer-binding transcription factor 4* (Oct4), Nanog, and *SRY-box2* (Sox2) [reviewed by Chambers and Tomlinson (2009)].

1.2.2 Post implantation – establishing the posterior/anterior axis.

At approximately E4.5 the embryo implants into the uterine wall via the trophoblast. At this stage the epiblast and PE populations rearrange to form the egg cylinder. At this point, the PE cells surrounding the epiblast are termed the visceral endoderm (VE). From approximately E5.5, the pluripotent epiblast forms an epithelial layer wherein a symmetry breaking event creates the anterior/posterior (AP) axis before lineage specification from pluripotency [reviewed by Arnold and Robertson (2009)]. To summarise, the AP axis in the epiblast is established in the egg cylinder by

secreted signals originating from the epiblast, the VE, and the ectoplacental ectoderm (ExE), including bone morphogenic protein (BMP), Wnts, and Nodal. This establishes the distal VE (DVE) signalling centre arises which expresses antagonists to TGF-beta (*left-right determination factor 1* [Lefty1], *Cerberus* [Cer1])) and Wnt (*Dikkopf 1* [Dkk1]) which diffuse into the epiblast to first create a Proximal-distal gradient of expression. The location of factors expressed the DVE migrate anteriorly and cells in the anterior VE (AVE) are established as a signalling centre, creating the AP gradient of TGF-beta and Wnt expression in the epiblast [reviewed by (Stower and Srinivas, 2014, Arkell and Tam, 2012)].

1.2.3 Gastrulation

At E6.5, the process of gastrulation, the segregation of the pluripotent epiblast to the three germ layers (Ectoderm, Mesoderm, and Endoderm) begins with the formation of the node and the primitive streak (PS) (Arnold and Robertson, 2009). The PS arises on the posterior epiblast opposite to the AVE [reviewed by (Beddington and Robertson, 1999, Arnold and Robertson, 2009)].

In the PS, epithelial cells undergo an epithelial to mesenchymal transition (EMT) and ingress between the epiblast and the VE and migrate anteriorly to form the nascent mesoderm and definitive endoderm (DE) [reviewed by (Nakaya and Sheng, 2008)]. PS formation is driven by signalling molecules in a cascade of Nodal, BMP, and Wnt3 which localise the expression of T- Brachyury (T) to the PS (Ben-Haim et al., 2006) and then to maintain BMP signalling from the extraembryonic ectoderm (Brennan et al., 2001, Ben-Haim et al., 2006). Mutants for Wnt3, Nodal, or BMP4 cause sever defects in PS formation (Conlon et al., 1994, Liu et al., 1999, Winnier et al., 1995). Proper EMT and mesoderm migration within the PS is dependent on *Fibroblast growth factor receptor* (Fgfr1) (Yamaguchi et al., 1994, Deng et al., 1994, Ciruna and Rossant, 2001) and *Fibroblast growth factor 8* (Fgf8)(Minowada et al., 1999) which is expressed in the PS (Crossley and Martin, 1995).

Between E6.5 to E7.5, the PS extends distally to the posterior pole to link with a signalling centre termed the node. The timing and location of cells that enter the PS

determines fate, which has been explored by extensive fate mapping of cells in the epiblast (Beddington, 1994, Wilson and Beddington, 1996, Kinder et al., 1999, Tam and Behringer, 1997, Lawson et al., 1991, Lu et al., 2001). The first nascent mesoderm to ingress in the posterior most PS, in close proximity to BMP4 signals from the ExE, form extraembryonic tissues (Winnier et al., 1995). Cells that enter later and at the intermediate or anterior streak are fated to lateral plate, paraxial and cardiac mesoderm. Cells that ingress the anterior-most tip of the PS are fated to midline axial mesendoderm tissues such as the notochord, prechordal plate, and DE.

The gradients of Fgf, Wnt, and Nodal signalling molecules, established during the AP axis formation, upstream of TFs determine the position of mesoderm subtype fates. TF genes can demark fate, such as the mesoderm marker and Wnt/β-catenin target T which is expressed broadly in the PS, node, notochord throughout gastrulation and later in axial elongation. Other genes are expressed along the signalling gradients of the PS such as *MIX1 homeobox-like 1* (Mixl1) expression located in the intermediate PS, *Mesoderm posterior 1* (Mesp1) is expressed in streak and more anterior tissues which marks cardiac progenitors, and *Forkhead box protein A2* (Foxa2) in the anterior streak labelling mesendoderm tissues. *Orthodenticle homeobox 2* (Otx2) expression marks the anterior neuroectoderm (Arnold and Robertson, 2009).

While fate is highly regionalised in the gastrulating epiblast, potency is not predetermined. Anterior and posterior pieces of the E7.5 epiblast are pluripotent, as defined by tumorgenicity after grafting to the testis capsule (Beddington, 1983). Further, the core network of Nanog, Oct4, and Sox2 is expressed in the E7.5 epiblast (Brons et al., 2007, Tesar et al., 2007).

1.3 Axial elongation and Neuromesodermal progenitors (NMPs).

1.3.1 Axial elongation

Pluripotency persists until E8.0-E8.25 at the onset of somitogenesis (Osorno et al., 2012, Damjanov et al., 1971). The loss of pluripotency in the epiblast is marked by

the extinction of Nanog and the reduction of Oct4 at the 2-4 SP stage, teratoma assays for equivalent embryo tissues of the presomitic or 2-5 SP epiblasts showed the 2-5 somite epiblast no longer forms endoderm (Osorno et al., 2012).

This event signals the end of gastrulation and the onset of axial elongation and organogenesis, where the now established anterior posterior axis elongates to produce precursory organ tissues. Axial progenitors in the post-gastrulation epiblast are the source of cells that make the neural and mesodermal tissues until E10.5 when the neuropore encloses the primitive streak and the tailbud forms. From E10.5 to E13.5, the tail bud is the source of cells for neural tube and mesodermal tissues until axial elongation cessation at E13.5 [reviewed by (Wymeersch et al., 2021, Henrique et al., 2015, Wilson et al., 2009)]. To explore the differentiation routes of tissues to understand their origin, axial progenitor pools that provide the cells driving axial elongation has been the subject of extensive research.

1.3.2 Evidence for *in vivo* bipotent progenitors

Like the epiblast during gastrulation, the post gastrulation epiblast contains regions of fate with gradients of TF and signalling gene expression. Fate mapping and retrospective clonal analysis experiments identified bi-fated stem-cell like populations which contribute to neural and mesodermal tissues which are retained throughout axial elongation [reviewed Wymeersch et al. (2021)].

Evidence for cells post gastrulation that are bipotent to neural and mesoderm germ layers with stem cell like properties first came from lineage tracing single cells within Hensen’s Node of the chick embryo, which contributed to notochord and ventral neural tube (Selleck and Stern, 1991). Similarly in mouse embryos, labelling single cells of the node/streak in early head fold stage embryos showed descendants in neural and mesodermal tissues (Lawson et al., 1991, Forlani et al., 2003).

Retrospective clonal analysis, utilising spontaneously repairing non-functional lacZ gene to label clones specifically in the myotome (Nicolas et al., 1996) or neural tube (Mathis and Nicolas, 2000) indicated individual clones that persisted for a long anterior posterior timeframe, suggesting the presence of long term stem-cell like

populations. Using this technique in the entire embryo reconfirmed the presence of single cells that are retained for long anterior posterior distances during axial elongation, but crucially that also simultaneously contribute to both neural and mesodermal tissues (Tzouanacou et al., 2009).

1.3.3 E8.5 Epiblast fate regionalisation.

In a similar way to the epiblast at gastrulation, fate mapping of cells in the E8.5 epiblast identifies high regionalisation of fate and the locations of bipotent progenitors. Dye injection or homotopic grafting of cells in different locations around the E8.5 epiblast shows the dorsal part of the node-streak border (NSB) and anterior caudal lateral epiblast (CLE) as the location of bipotent NMPs (Figure 1.1a), contributing to neural tube and somitic tissues (Cambray and Wilson, 2007, Wymeersch et al., 2016, Mugele et al., 2018 preprint). Interestingly, these experiments showed the NSB and CLE do not contribute to the same sections of the neural tube and somitic tissues, where the NSB progeny is located in the ventral neural tube and medial somites, but the CLE progeny are located in lateral somitic tissues and lateral neuroectoderm. Further, the balance of neural vs mesoderm contribution is equal in NSB cells, but cells in the CLE progressively anterior and lateral contribute more to neural tissues, and posterior and medial contribute more to mesoderm (Wymeersch et al., 2016). The fate of cells located progressively posterior in the CLE and PS results in cells contributing to only paraxial mesoderm and eventually lateral plate paraxial mesoderm, termed lateral and paraxial mesoderm progenitors (LPMPs), and similarly cells located anterior of the node only contributes to neuroectoderm (Cambray and Wilson, 2007, Wymeersch et al., 2016, Mugele et al., 2018 preprint, Kinder et al., 1999, Wilson and Beddington, 1996). Live imaging of individual epiblast cells with dual fates in chick embryos reveal they are located between neural and mesoderm only fated stem zones (Wood et al., 2019 preprint, Guillot et al., 2021).

While there is a high level of fate regionalisation, heterotopic grafting within the epiblast and germ layer potency assays of different epiblast regions indicates that while specific regions (the NSB and CLE) contribute cells to neural or mesoderm

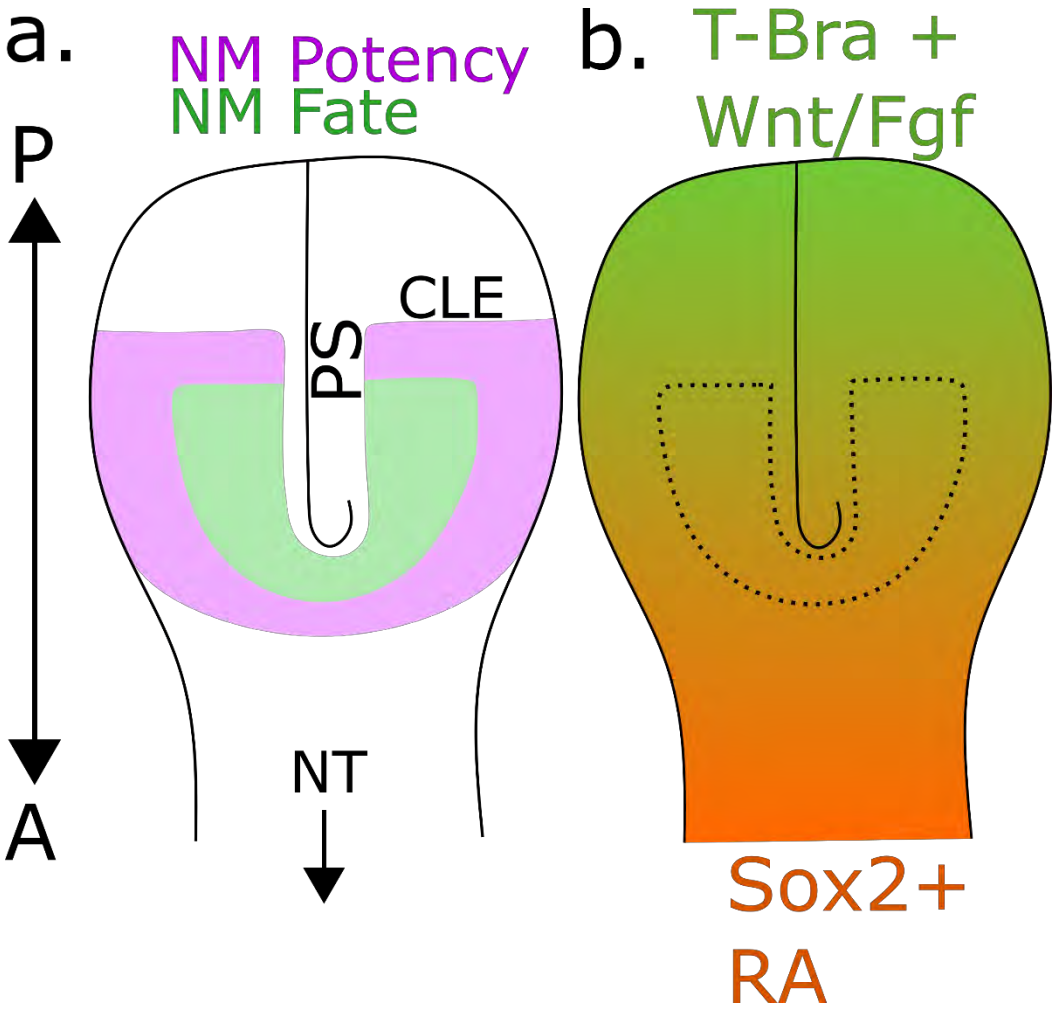

Figure 1.1 E8.5 embryo fate map and Sox2 T gradient, adapted from Wymeersch et al. (2016).

a. Epiblast with primitive streak (PS) and caudal lateral epiblast (CLE) showing bi potent regions (magenta) which are not lineage restricted to neural or mesoderm fate, and the bi-fated (green) region where during normal development cells contribute to both the neural tube and paraxial mesoderm. b. Current opinion on the opposing anterior posterior gradient of T and Sox2 driven by Wnt/Fgf and opposed by RA (Gouti et al., 2017) that form overlap to create the u-shaped CLE.

tissue and contain individual dual-fated cells, a broader region are bipotent (Figure 1.1a)(Wymeersch et al., 2016, Cambray and Wilson, 2007). The bipotency region extends more lateral and posterior from the CLE than previously defined from bi-fated CLE (Figure 1.1a), indicating a level of positional plasticity of fate.

1.3.4 Neural vs mesoderm cell fate decision.

A complex intracellular gene regulatory network (GRN) and signalling pathways controls the neural vs mesoderm fate (Table 1.1), as well as hox gene expression and other processes like proliferation, motility, and morphology. Knockout studies have shown that many of these genes have distinct morphologies and are essential for proper axial elongation (Wymeersch et al., 2021), implicating a high degree of complexity in controlling axial elongation. The key genes and signalling pathways involved in NMP maintenance, mesoderm differentiation and neural differentiation will be outlined as describe in Table S1.

NMPs are identified generally identified by the coexpression the pluripotency TF marker Sox2 and the mesoderm TF marker T, among other caudal epiblast markers nonspecific to NMPs such as NK1 Homeobox 2 (Nkx1.2) and *Caudal-type homeobox 2* (Cdx2) (Cambray and Wilson, 2007, Delfino-Machín et al., 2005, Garriock et al., 2015, Martin and Kimelman, 2012, Wymeersch et al., 2021, Amin et al., 2016, Tsakiridis et al., 2014). In the epiblast and tailbud, Sox2 and T each form opposing gradients and the regions of coexpression coincides with the CLE and NSB (Figure 1.1b)(Wymeersch et al., 2016, Guillot et al., 2021, Cambray and Wilson, 2007), providing a link to bi-potency and TF expression.

T is an essential and conserved regulator of the primitive streak and notochord throughout development, persisting in the tailbud in the CNH and tailbud (Wilkinson et al., 1990). In the context of NMPs, T is a target of and controls Wnt and FGF signalling pathways (Yamaguchi et al., 1999) while upregulating the nascent mesoderm markers Tbx6 and *Mesogenin 1* (Msgn1) (Wittler et al., 2007, Koch et al., 2017, Nowotschin et al., 2012).

Tbx6 expression emerges first in the epiblast with T (Takemoto et al., 2011, Javali et al., 2017) which then upregulates Msgn1 in the PS and into the pre-somitic mesoderm (PSM) (Nowotschin et al., 2012, Wittler et al., 2007). As Tbx6 and Msgn1 are upregulated, they first repress Sox2 while maintaining T and self-upregulating to confirm the cell fate choice to mesoderm (Javali et al., 2017, Nowotschin et al., 2012, Takemoto et al., 2011, Bouldin et al., 2015, Ruvinsky et al., 1998, Koch et al., 2017). As the nascent mesodermal cells enter the PSM, T is downregulated by Msgn1 (Wilkinson et al., 1990, Yoon and Wold, 2000) while Tbx6 is maintained and the wavefront/clock genes for somitogenesis initiate [reviewed by (Pourquié, 2001)]. The Wnt/FGF/T mesoderm driver has been described as a positive feedback loop facilitating a bistable switch dynamic between NMP and mesoderm identity (Gouti et al., 2017, Koch et al., 2017), created by Sox2 and Tbx6/Msgn1 mutual inhibition and subsequently T inhibition by Tbx6/Msgn1.

Sox2 is essential to balance the positive feedback for NMP maintenance and neural differentiation. Sox2 is primarily expressed in pluripotent and neural tissues (Feng and Wen, 2015), but in the caudal epiblast Sox2 is a target of Retinoic acid (RA) and Wnt/FGF signalling through the N1 enhancer (Takemoto et al., 2006), as opposed to the N2 enhancer predominantly active in pluripotent cells. Sox2 represses T and nascent mesoderm markers Tbx6 and Msgn1 (Blassberg et al., 2022, Koch et al., 2017, Takemoto et al., 2011), and is upregulated when neural fated cells in the epiblast transition through the pre-neural tube.

Neural commitment is regulated by RA signalling emanating from the somites (Vermot et al., 2005), which upregulates Sox2, with neural markers, and inhibits FGF (Cunningham et al., 2016, Olivera-Martinez and Storey, 2007). RA is necessary for NMP establishment (Gouti et al., 2017), but NMPs are not thought to be receiving RA signals post E8.5 due to the high expression of the RA metabolising enzyme *Cytochrome P450 Family 26 Subfamily A Member 1* (Cyp26a1) which is upregulated by RA itself and T/Cdx2 (Loudig et al., 2000, Abu-Abed et al., 2001, Koch et al., 2017, Savory et al., 2009, Vidigal et al., 2010).

Mesoderm differentiation displays more dynamic processes than neural differentiation. During mesoderm differentiation, NMP identity is actively repressed by mature mesoderm identity, but both identities are driven by local Wnt/FGF. Also, the nascent mesoderm in the epiblast actively migrates to the PS away from the NMP region. In contrast, neural differentiation occurs passively, where cells enter the pre-neural tube passively with decreased motility (Romanos et al., 2021) and gain a neural identity as they move away from the Wnt/FGF signalling centre and closer to RA secreting somites (Olivera-Martinez and Storey, 2007), ultimately upregulating neural genes (Gouti et al., 2017). The passive neural movement relative to the primitive streak occurs due to increased proliferation found in the NMP niche (Guillot et al., 2021), driven by Wnt/FGF signalling.

Maintaining NMPs identity has been theorized to occur from balanced by signals from pro-mesodermal Wnt/FGF and pro-neural RA (Gouti et al., 2017, Sambasivan and Steventon, 2021), mathematical modelling of a minimal gene regulatory network controlled by RA and Wnt/FGF signals can recapitulate changes in proportions of TF expression found from in vitro manipulations. Further, Wnt/FGF and RA does not exclusively control mesoderm and neural differentiation, Wnt/FGF also drives progressively posterior Hox gene expression via Cdx2 (Subramanian et al., 1995, van den Akker et al., 2002), and the NMP marker Nkx1.2 (Sasai et al., 2014) which was found to be required for Wnt related T expression in P19 carcinoma cells (Tamashiro et al., 2012). During axial elongation, the NMP populations change and have distinct transcriptional profiles (Wymeersch et al., 2019).

There is an interesting dynamic where RA, Wnt, and FGF all upregulate negative regulators of their own expression. Such as Cyp26A1 being upregulated RA (Loudig et al., 2000, Loudig et al., 2005), or Wnt/FGF targets Sox2 (Takemoto et al., 2006), which inhibits T, Cdx2, and Tbx6 TF expression which upregulated Wnt/FGF genes. This indicates a level of self-regulation in the form of closed loop negative feedback, which is a feature of biological systems to achieve perfect adaptation to perturbations (Ferrell, 2016, Khammash, 2021).

While it can be said that neural and mesoderm signals are balanced to maintain NMPs with appropriate differentiation, the mechanisms of neural vs mesoderm differentiation have entirely distinct dynamics. The regulatory landscape determining the regionalisation of NMP potency and fate in the epiblast is not likely to be a simple case of equal opposing neural vs mesoderm signals. While extensive characterisation has been carried out to understand the key regulators of NMP maintenance and differentiation, the underlying regulatory principles that confer robustness and reproducibility are yet to be determined.

1.4 *In vitro* culture of NMP-like cells (NMP-LC).

Various methods of culturing NMPs *in vitro* have been developed where 2D and 3D cultures of pluripotent embryonic stem cells are guided through gastrulation and into axial elongation with exogenous morphogens (Wymeersch et al., 2021, Van den Brink et al., 2014, Beccari et al., 2018).

1.4.1 Mouse ESC differentiation to NMP-LC.

1.4.1.1 Naive preimplantation 2iLIF.

ESCs can be derived from the ICM preimplantation E4.5 mouse embryos (Evans and Kaufman, 1981, Martin, 1981). These ESCs were cultured with foetal calf serum (FCS) grown on a bed of mouse embryonic fibroblasts (MEFs), termed feeder cells since the MEFS provided Leukaemia Inhibitory Factor (LIF) which promotes self-renewal (Smith et al., 1988). Instead of feeders, ESCs can be cultured with recombinant LIF and FCS (LIF/FCS) on gelatinised culture plates. ESCs cultured this way and have been shown to exhibit all attributes of the preimplantation epiblast in terms of potency and identity [reviewed by Nichols and Smith (2009)].

However, this ESC population has shown to be heterogeneous and a minority of spontaneous differentiation can be observed (Morgani et al., 2017, Ying and Smith, 2003). This is due to Oct4/Sox2 driven FGF4 activation of the ERK pathway which drives differentiation to hypoblast identity [reviewed by Silva and Smith (2008)]. Spontaneous differentiation is normally inhibited by factors in FCS such as BMPs

(Ying et al., 2003), but FCS varies between batches and produces inconsistent cultures.

To prevent spontaneous differentiation, ESCs can be cultured in chemically defined media including two inhibitors PD0325901 (PD03) (MEK/Erk pathway inhibitor) and CHIR (GSK3β inhibitor and Wnt/β-catenin agonist) termed 2i/LIF (Silva and Smith, 2008). This produces a homogenous population of ESCs and is considered the "ground" or "naive" state (Marks et al., 2012, Morgani et al., 2017, Nichols and Smith, 2009, Silva and Smith, 2008).

1.4.1.2 Post implantation – Primed EpiSCs and EpiLCs.

Pluripotent stem cells have been derived from post implantation epiblast cells, termed epiblast stem cells (EpiSCs) (Osorno et al., 2012, Brons et al., 2007, Tesar et al., 2007). Instead of 2i/LIF, EpiSCs are cultured in chemically defined serum-free media (N2B27) supplemented with Fgf and Activin (N2B27/FGF/Activin) on fibronectin coated plates to support pluripotent TF Oct4, Sox2, Nanog expression (Tesar et al., 2007, Brons et al., 2007). Pluripotent EpiSCs cannot be cultured in Fgf/Activin from epiblasts in embryos beyond 2-4 SPs (Osorno et al., 2012), these cells do not form stable Oct4+Nanog+ cell lines and rapidly differentiate after passaging.

EpiSCs are heterogenous and unlike 2i/LIF ground state, EpiSCs do not directly recapitulate *in vivo* epiblast-like transcriptional profile (Kojima et al., 2014a) and sub populations express mesoderm and mesoderm markers (Kojima et al., 2014b). While up to 30% of EpiSC of are biased to neural or mesoderm fate, representing PS or neural like cells, they retain pluripotency and Oct4 expression (Tsakiridis et al., 2014).

1.4.1.3 ESC to NMP-LC differentiation models.

NMP-LCs can be differentiated from ESCs or EpiSCs with the addition of Fgf and CHIR, attaining T/Sox2 coexpression and bi-potency, as shown by *in vivo* grafting with contribution to both paraxial mesoderm and neural tube (Gouti et al., 2014).

ESCs from LIF/Ser are cultured in N2B27 for two days in Fgf to recapitulate the ESC to EpiSC transition, then for 24 hours in Fgf and CHIR to stimulate Wnt and caudal NMP marker genes. EpiSCs are cultured in N2B27 for 48 hours in Fgf and CHIR.

While the NMP transcriptome changes dramatically from E8.5 to E13 (Wymeersch et al., 2019), comparative transcriptome analysis suggests that NMP-LCs from ESCs and EpiSCs cells are most similar to the E8.5 embryo, with EpiSCs having the closest transcriptome to the in vivo NMP signature (Edri et al., 2019). But in the culture NMP-LCs tend to include more mature mesoderm and neural cell types (Edri et al., 2019, Gouti et al., 2017).

Recently, a 3D culture model of gastrulation and axis elongation termed gastruloids has presented an attractive culture method to study spatial organisation of NMP-LCs and their derivatives (Van den Brink et al., 2014, Beccari et al., 2018). In this method, aggregates of ~250-300 2i/LIF cells are deposited in u-well culture plates in N2B27. These are left for 48 hours, then given a CHIR pulse to initiate a symmetry breaking event and stimulate Wnt/T and posteriorising. After 24 hours the CHIR is withdrawn and the aggregates are cultured for a further 48 hours, where extensive T expression coalesces to a single pole and extension along this axis occurs. Transcriptional profiling shows cells at the tip of the extending pole are NMP-LCs expressing T,Sox2, Tbx6, Cdx2, Wnt3a, FGF8 among other NMP and caudal epiblast markers (Beccari et al., 2018). Also, these gastruloids produce gradients of T and Sox2 expression with mesoderm derivative, even exhibit characteristics of somitogenesis and neural tube formation when cultured in ~10% Matrigel (van den Brink et al., 2020, Veenvliet et al., 2020).

1.4.2 Human hESC to NMP.

1.4.2.1 Human ESC culture.

Human ESCs (hESCs) can be derived from the ICM of preimplantation blastocysts (Bongso et al., 1994, Thomson et al., 1998). However, like EpiSCs, hESCs require culturing in Fgf and Activin to maintain self-renewal. hESCs cultured this way

resemble primed pluripotency rather than the naïve state in mouse (Rossant, 2015). Recently, a naïve like state in hESC culture has been achieved by culturing the ICM of expanded blastocysts in N2B27 supplemented with inhibitors for MAPK/Erk (PD03), GSK3 (CHIR), and protein kinase C (PKC) (Gö6983) as well as LIF (Guo et al., 2016).

1.4.2.2 hESC to human NMP-LC (hNMP-LC) culture.

hNMP-LCs can be differentiated from primed hESCs, starting from a Fgf and Activin pluripotency maintenance media, by culturing hESCs in Fgf and CHIR for 72 hours, similar to EpiSC culture (Gouti et al., 2014). As previously described, NMPs are usually defined as T/Sox2 copositive, reduced or extinct Nanog, and the expression of trunk Hox genes (Wymeersch et al., 2021, Osorno et al., 2012). hNMP-LC differentiation has been reported to be highly efficient, with near 100% Sox2/T co-expression in hNMP-LC (Lippmann et al., 2015, Denham et al., 2015) compared to 40-80% for mouse EpiSC or ESC derived NMP-LCs (Tsakiridis et al., 2014, Gouti et al., 2014, Gouti et al., 2017). Extended culture of hNMPs in CHIR/Fgf/Gdf11 has been reported acquire up to lumbar Hox10 and Hox11 paralog group expression (Lippmann et al., 2015). After hNMP-LCs differentiation, these can be differentiated further to mesoderm by maintaining in CHIR, or to spinal cord identities by switching from Wnt/Fgf to RA exogenous signals (Lippmann et al., 2015, Verrier et al., 2018, Gouti et al., 2014). Modulating sonic hedge-hog (Shh) and transforming growth factor beta (TGF-β) signalling can produce hNMP-LC derived spinal cord subtypes which can incorporate into in vivo embryonic spinal cord (Wind et al., 2021) and even proliferate in a rat cervical hemi-contusion model (Olmsted et al., 2022). More recently, the culture of hESCs in 3D has been shown to produce human gastruloids that resemble the mouse gastruloids, with elongating caudal tissue growth and hNMP-LCs at the “posterior” tip (Moris et al., 2020).

1.5 Notch signalling in the NMP niche

Wnt/FGF signalling are crucial for the formation of axial patterning and NMPs and somitogenesis, Notch signalling is also a pathway required for somitogenesis that

interacts with the Wnt/FGF in PSM and somitic tissues (Wahl et al., 2007, Carrieri and Dale, 2017, Pourquié, 2001), but it's activity in NMPs is largely understudied.

1.5.1 Canonical Notch signalling.

Notch signalling is an evolutionarily conserved signalling pathway which regulates a multitude of cell fate decisions throughout embryonic development and adult tissue homeostasis in all metazoans (Ehebauer et al., 2006, Siebel and Lendahl, 2017, Chiba, 2006). Canonical Notch signalling is a juxtracrine signalling pathway where surface ligands presented on a cell surface membrane activate receptors on adjacent cells to regulate downstream genes. In vertebrates, surface ligands *delta like canonical Notch ligand 1/3/4* (Dll1/3/4) and *Jagged 1/2*(Jag1/2) bind to *notch receptor 1/2/3/4* (Notch1/2/3/4)(Kopan and Ilagan, 2009). Receptors comprise of three domains that cross the membrane; an extracellular domain comprising of EGF repeats (which the ligand binds to) and a negative regulatory region, a regulatory domain which consists of two cleavage sites (S2 and S3), and the nuclear intracellular domain (NICD)(Kovall et al., 2017). Although multiple non-canonical mechanisms of notch receptor activation have been demonstrated(LaFoya et al., 2016), canonical Notch signalling initiates with torsion of the ligand-receptor complex (Kopan and Ilagan, 2009, Kovall et al., 2017). This torsion exposes the S2 cleavage domain for α-secretase ADAM metalloproteases to cleave this site and releasing the ligand bound extracellular domain. Subsequently, cleavage of the second domain S3, via a γ-secretase, releases the NICD to translocate to the nucleus. Here the NICD recruits coactivators CSL, MAML and p300 to remodel chromatin and upregulate the expression of various downstream genes, with Hes/Hey repressors the most common downstream targets of canonical Notch signalling. The γ-secretase inhibitors DAPT and LY4115243 are common in pharmacological manipulations of Notch, which block the s3 cleavage of the NICD to translocate to the nucleus, thereby blocking CSL dependant signalling.

Fringe genes are a set of homologs (Lunatic, Manic, and Radical Fringe) which modify the notch receptor on specific EGF repeats to facilitate a O-linked glycosylation and fucosylation before translocation to the membrane (Rampal et al.,

2005). In vitro studies have shown that this can enhance the interaction of Dll1-Notch1 interaction (LeBon et al., 2014). Lunatic fringe (Lfng) associated with somitogenesis in the PSM (Williams et al., 2016, Hicks et al., 2000), but in PSM it has been suggested to inhibit Dll1-Notch1 signalling (Okubo et al., 2012).

Notch is involved as a regulator of many differentiation processes throughout development and somatic homeostasis. Although in principle Notch is a simple signalling pathway, potential regulatory roles notch for Notch in a novel system can be difficult to predict; its signalling components are known to interact with many other signalling pathways and regulate multiple processes through various non-canonical mechanisms (LaFoya et al., 2016). Ultimately, Notch signalling is contextually dependant and often unpredictable. Further, its expression dynamics are often oscillatory (Kageyama et al., 2018), which makes it hard to study as time is not always possible to include as a controlled parameter in genetic assays.

Notch components are usually associated with the nascent PSM and are essential for the presomitic mesoderm and somitogenesis (Bessho et al., 2001a, Hofmann et al., 2004, Wahl et al., 2007). Notch signalling knockout via deletion of the Pofut1 gene, encoding the O-fucosyltransferase required for Notch receptor maturation in the endoplasmic reticulum, have no observable phenotypic consequence throughout implantation and gastrulation until E8.5 in mouse, where severe defects in organogenesis occur and embryos do not survive beyond E9 (Shi et al., 2005, Shi and Stanley, 2003). Specifically, embryos past E9 in Pofut1 mutants are much smaller with “kinked” neural tube and defective somites. Further, ectopic overexpression of Notch in the epiblast during gastrulation disrupts germ layer specification by disrupting nodal signalling and promotes neuroectoderm specification over mesoderm lineages (Souilhol et al., 2015), which had been previously reported with in vitro Notch manipulation of ESCs (Lowell et al., 2006).

1.5.2 Notch component spatial expression *in vivo* and interaction with NMP related genes.

Notch deletion studies have shown that Notch signalling is essential for development and somitogenesis (Swiatek et al., 1994, Conlon et al., 1995, Bessho et al., 2001b, Krebs et al., 2003, Barsi et al., 2005), but the focus has not been on axial progenitors in the epiblast and to date thorough exploration of Notch in NMPs has not been carried out. Transcriptional and genomic data from the literature suggests that numerous Notch genes are expressed in the NMP niche and directly interact with NMP genes, providing a preliminary model of regulation for experimental testing. Although the oscillatory nature of Notch limits the certainty to whether Notch is present in fixed tissue samples. The presence of Notch components and their relationship to NMP related genes are summarised below:

1.5.2.1Notch Ligands.

Dll1 is a putative target of Wnt3a in synergy with T and Tbx6 (Hofmann et al., 2004, Koch et al., 2017, White and Chapman, 2005). From E7.5 (late streak) through to E12.5, Dll1 expression via ISH is positive in caudal embryo, most prominently PS, PSM, and tail bud (Bettenhausen et al., 1995). The signal is strongest in the PSM and PS E8.5-E9.5 and in the TBM and PSM from E10.5-E12.5. Due to the angle of images, it is unclear if Dll1 is expressed in the epiblast, but it is clear expression is found at the midline and in the PSM (Grainger et al., 2012, Bettenhausen et al., 1995). Cross sections of Chick epiblasts at HH8 stage show Dll1 is widely expressed at HH8 stage in the NMP region (Akai et al., 2005). Microarray hybridisation assay (Wymeersch et al., 2019) and single cell RNAseq (Gouti et al., 2017) of micro-dissected CLE regions both identify the Dll1, along with Tbx6, to be upregulated in nascent mesoderm progenitors in E9 embryo compared to E8. Tbx6 is an essential nascent mesoderm marker which both upregulates Dll1 expression, and is also downstream target of Notch signalling via a RBP-Jk binding site in the PSM (Hofmann et al., 2004, White and Chapman, 2005). Dll1 is required for presomitic mesoderm TBx6 expression (Bettenhausen et al., 1995). Of note, knockdown of T expression in the caudal end of an E8.5 embryo results in a down regulation Dll1,

along with Tbx6 and Cyp26a1, and an upregulation of Dll3 ligand (Vidigal et al., 2010). Curiously, deletion of Fgf receptor 1 causes an expansion of Dll1 expression in the caudal E9.5 embryo (Wahl et al., 2007), indicating a negative regulatory mechanism.

Dll3 is a target of T (Vidigal et al., 2010) and is widely expressed in the primitive streak and paraxial mesoderm from E7.-E8.5 and in the tailbud at E9.5 (Dunwoodie et al., 1997, Przemeck et al., 2003). Again, it is unclear if Dll3 is expressed in the epiblast without cross sections. It has been demonstrated that Dll1 and Dll3 are not functionally equivalent in the developing mouse embryo, where Dll3 is located primarily in the golgi apparatus rather than at the membrane, and do antagonise each other's expression (Geffers et al., 2007). Dll3 cannot activated Notch1 in trans and has been implicated as a sole inhibitor through cis inhibition of Notch1 receptor while attenuating Dll1 expression (Ladi et al., 2005, Chapman et al., 2011).

Jag1 is a putative target of canonical Notch (Manderfield et al., 2012, Castel et al., 2013) and contains conserved TCF/LEF sites in its promoter (Katoh and Katoh, 2006), Jag1 is also expressed in the primitive streak and PSM at E7.5 (Przemeck et al., 2003), E8.5 (del Barco Barrantes et al., 1999) and in at low levels in the PS E9.5 (Barsi et al., 2005). Interestingly, Jag1 is increased broadly in the posterior following Lfng mutation in E9.5 (Zhang and Gridley, 1998), suggesting a regulatory relationship. It is not clear if Jag1 is expressed more broadly in the epiblast or just the PS.

1.5.2.2 Notch Receptors.

The Notch receptors are putative targets of canonical Notch signalling and required for Notch signalling. Notch receptors Notch1,2, and 3 have differential expression levels and patterns from E7.5 to E9.5 (Williams et al., 1995, Barsi et al., 2005, Hamada et al., 1999). Notch1 is absent at E7.5 but present in the PS and posterior portions at E9.5. Notch2 is found in the PS at E7.5 and E8.5 but appears absent at E9.5. Notch3 is widely expressed in the PSM and PS at E7.5 and E8.5.

Notch1 (Swiatek et al., 1994, Conlon et al., 1995), and Notch2 (Hamada et al., 1999, McCright et al., 2006) mouse mutants are embryo lethal. Notch3 mutants do not result in embryo lethality but did show defects (Krebs et al., 2003). Notch1 is thought to be the primary mediator of trans Notch signalling via Dll1 expression. Deletion of Notch1 results in accelerated differentiation towards mesoderm fates in human ESC (hESC) cultures (Jang et al., 2008) and upregulation in mouse ESCs results in enhanced neural differentiation (Lowell et al., 2006). Overexpression of the cleaved intra-cellular compartment form of Notch3, Notch3-ICD, in HEK293 cells showed increased LEF and N-Cadherin expression, promoted cell survival via pAKT upregulation (Wang et al., 2007).

T binds to Notch1 and Notch4 receptor promoters and is downregulated in T mutants (Koch et al., 2017) in E8.5 caudal cells, and also bind to the Notch3 promoter in mice embryoid bodies (EB) (Lolas et al., 2014) and the PS of Zebrafish (Gentsch et al., 2013).

1.5.2.3 Hes/Hey.

Hes1,5,7 and Hey1/2 genes are downstream targets of Notch signalling (Nishimura et al., 1998, Katoh and Katoh, 2007, Maier and Gessler, 2000, Castel et al., 2013). At E8.5, Hes1 is expressed in a stripe at the pre-neural tube boundary over the node (Lobe, 1997) and posterior portions at E9.5 (Hamada et al., 1999). In chick embryos, Hey2 is identified in the caudal PSM and tailbud in the E11.5 mouse embryo, but hey1 was absent (Leimeister et al., 2000). At, E9 Hes5 is expressed in the primitive streak (Shi and Stanley, 2003). Hes5, along with Dll1, expression is extensive in chick HH8 epiblast NMP region and in neural tube (Akai et al., 2005). Suggesting Notch may be more active in Chick than mouse. Notch independent Hes1 inhibits Notch signalling and promotes neural differentiation in ES cells (Kobayashi and Kageyama, 2010, Lowell et al., 2006) and neural progenitors. Hes7 is strongly expressed in the PS region at E8.5 (Ferjentsik et al., 2009) and is expressed in NMP by SC-RNAseq of gastruloids (Veenvliet et al., 2020), and Tbx6 upregulates Hes7 in the PSM (Gonzalez et al., 2013).

Hes6 and Hes3 are not thought to be under the control of Notch signalling. But Hes6 is a repressor of Hes1 mediated inhibition and promotes neural fates in neurons of the ventricular zone (Bae et al., 2000). Hes6 is not present at E8.5 but can be identified in posterior portions of E9.5 embryo (Bae et al., 2000). Similar to Hes1, Hes3 can be found in a stripe across the left to right axis in the E8.5 epiblast just anterior of the primitive streak(Lobe, 1997). Hes3 is upregulated after T knockdown in the E8.5 embryo (Vidigal et al., 2010).

1.5.2.4 Fringe genes.

Lfng is a target of Notch signalling and is present in the E8.5 PS and CLE (Dias et al., 2020), and has been shown to oscillate through the PSM to the posterior tail bud at E10.5 (Fujimuro et al., 2014). However, Hes7 repressed Lfng expression (Chen et al., 2005) which shows stronger expression in the PS. No other fringe genes were identified.

1.5.2.5 Non canonical Wnt/Notch signalling

The Wnt/Notch pathways are closely related in many contexts in controlling stem cell populations and somitogenesis (Chalamalasetty et al., 2011, Galceran et al., 2004, Hayward et al., 2008, Hofmann et al., 2004, Wahl et al., 2007), the pathways overlap often across species and has been termed “Wntch” signalling [reviewed by (Descalzo and Arias, 2012)].

Wntch signalling generally refers to a subset of non-canonical notch signalling, where Notch components, such as the NICD or Notch1, can interact with Wnt via β-catenin at the membrane, in the cytoplasm, or in the nucleus to regulate gene expression with RBP-j (Acar et al., 2021, Hayward et al., 2005, Hayward et al., 2008, Wang et al., 2007, Shimizu et al., 2008). Highlighting the close relationship between Notch and Wnt outside canonical Notch signalling. It is not clear if such interactions are involved in the NMP context.

1.5.3 Evidence for Notch signalling in the NMP niche.

Direct evidence of Notch's involvement in NMP cell fate decisions comes from unpublished work from Haston (2018) in the Dale lab. The author treated GFP expressing and non-GFP Hamilton hamburger stage 4 (HH4) embryos with the γ-secretase inhibitors DAPT and LY4115243, and a DMSO control. At HH7-9, the NSB (an NMP containing region) in GFP expressing chick was grafted to the NSB of a non- GFP expressing host embryo and cultured for 27-29 hours. The embryos were fixed and four transverse sections along the A-P axis were used to quantity the GFP expressing graft contribution to different lineages. As expected, contribution to both somitic mesoderm and neural tube is observed in the DMSO control. Notch inhibition resulted in no mesoderm contribution and increased neural lineage commitment from the NSB. No change in total contribution to either lineage was observed, suggesting a switch in NMP cell fate decision by restricting NMPs to neural fates.

An investigation into c-Myc in NMPs revealed a crucial role in maintaining NMP identity by upregulating Sox2 and FGF (Mastromina et al., 2018). In this study, the authors showed c-Myc was regulated by Notch signalling, when inhibiting Notch abolished c-Myc in posterior explants in mouse embryos, providing indirect evidence for a route of Notch to regulate NMP identity.

1.5.4 Notch signalling gene expression spatial patterning.

Juxtacrine Notch signalling can create two characteristic spatial gene expression patterns, commonly depending on whether signalling is primarily mediated via Delta or Jagged. First, the classic model of lateral inhibition regulation via Dll1 mediated signalling creates checkerboard spatial gene expression and acts via "sender" and "receiver" cells (Collier et al., 1996), where the sender cells express surface ligands and receiver cells express receptors (Figure 1.2a). Whether a cell becomes a receiver or sender cell is thought to depend on the relative levels of receptors and ligands, which both regulate via cis (same cell) inhibition as well in trans (adjacent cells) activation(Chiba, 2006, Saravanamuthu et al., 2009, Feng et al., 2010)

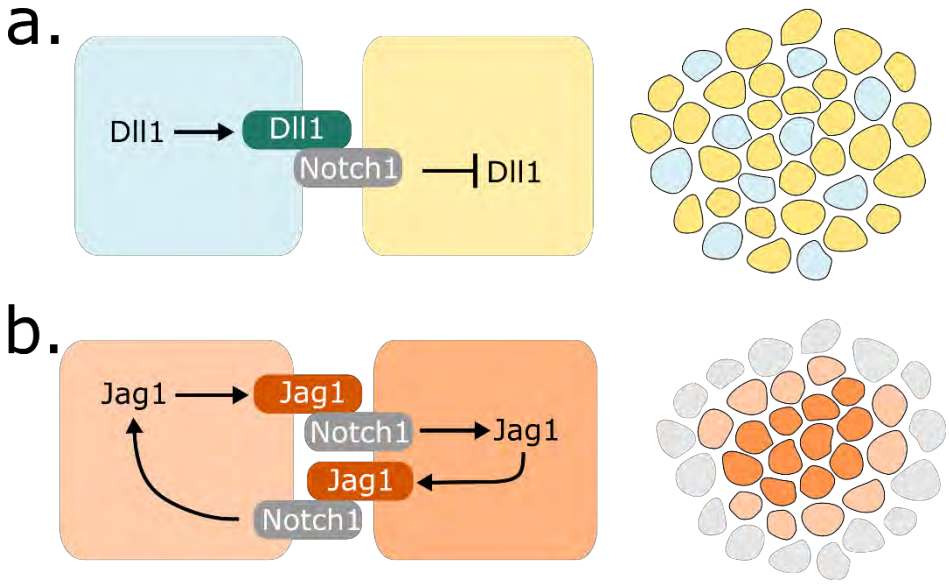

Figure 1.2 Classical model of lateral inhibition and lateral induction

a. Dll1 mediated lateral inhibition Notch signalling represses neighbouring cell expression of Dll1, creating a uni-directional signal that manifests as a heterogenous "salt and pepper" pattern. b. Jag1 mediated lateral induction Notch signalling that upregulated Jag1 in neighbouring cells, creating a feedback loop to homogenise the population.

In the case of lateral inhibition, trans activation results in the NICD downregulating Notch ligands. Taken together, a negative feedback loop is created between receptors and ligands to create binary identities of notch components which are often result in different cell fate/types. Lateral induction contrasts lateral inhibition, where trans activation upregulates ligands expression to create large homogenous populations (Figure 1.2b.) Jagged mediated signalling has been shown to create a positive feedback loop for lateral induction in multiple contexts (Saravanamuthu et al., 2009, Feng et al., 2010) . However, lateral induction and inhibition are not mutually exclusive and can occur simultaneously, mathematical modelling suggests a balance between Delta/Jagged signalling can exist to create hybrid sender/receiver

identities and regulate allocation to multiple cell fates from initial asymmetries of Delta/Jagged content (Boareto et al., 2015, Boareto et al., 2016).

As well as trans regulation, Notch can regulate in cis. Although the mechanisms for cis inhibition remain unclear, multiple Notch ligands have shown to inhibit receptor activity in cis and mathematical modelling suggests strong cis inhibition of ligands and receptors presented on the same membrane promote a “winner take all” scenario (Sprinzak et al., 2010). Similarly, cis induction of Notch has been demonstrated with the Notch1 receptor and Dll1 ligand, and Notch receptor affinity modulation by fringe genes can accentuate this cis induction (Nandagopal et al., 2019). As such, cis regulation can theoretically create heterogeneous spatial patterns as they are not dependant on neighbour signalling.

Overall, the necessary components for trans lateral induction and inhibition (Dll1, Jag1, Notch1, Notch2, Notch3, Hes1, Hes5, Hes7, Lfng), and cis regulation, are present in the PS, and potentially the CLE, of the E8.5 embryo. There is evidence Notch may play a pro-NMP and pro-mesodermal role in NMPs, but whether this organises NMP TF expression into spatial patterns characteristic of Notch signalling is unknown. For instance, it is possible Jag1 or Dll1 associated Notch signalling in NMPs in the epiblast promote NMP identity and survival through c-Myc. But as required for the classical model of Dll1 mediated lateral inhibition, a Notch mediated negative regulatory mechanism has not been demonstrated in the NMP context.

1.6 Spatial patterning quantification methods.

Taken together, the literature suggests that gradients of mesoderm and neural potency, fate, and TF expression exists in the epiblast which are controlled by cell-cell signalling pathways and intracellular gene networks. This raises the question of how to define NMPs, as either bi-fated or bi-potent, as discussed by Binagui-Casas et al. (2021), and more importantly how are fate and potency regulated and controlled in the NMP niche. Further, with the number of TF or signalling genes interacting and the 3D organisation of tissues, a quantitative systems biology is suited to solve problems surrounding the definition of axial progenitors, their location

relative to developmental axis, and finally quantify neighbour-based patterning of TF expression in the epiblast. Recently, advances in image analysis and transcriptomics has greatly improved the detail in which gene expression and spatial protein localisation data can be collected, increasing the capacity for 3D quantification of spatial patterning.

With the recent technology of spatial transcriptomics, pipelines have been developed to quantify RNA expression, identify niches, and infer cell-cell communication between cell types (Schapiro et al., 2017). However, these are 2D and do not capture the full 3D niche required to assess patterning. To get around this, researches have used techniques that stack multiple slices of tissues, all processed with spatial transcriptomics, and draw inference between planes and render the 3D organisation of the tissue (Qiu et al., 2022 preprint, Lozachmeur et al., 2023 preprint, Kaur et al., 2023 preprint, Wang et al., 2022). However, the resolution in Z is not yet sufficient to track individual nuclei across planes and assess 3D patterning.

Images of immunofluorescent stains and nuclei can be analysed with a variety of tools to segment and quantify individual cells in 3D. These tools provide quantitative and spatial information on protein content at the single cell level. This approach is hugely beneficial to capture spatial organisation and patterning *in vivo* and has been used to reveal fine grain details, which cannot accurately be observed by eye. Quantification of is essential for a systems biology approach.

One such tool is Pickcells (Blin, 2018), which utilises the segmentation algorithm NesSys (Blin et al., 2019) to segment in 3D z-stack images of nuclei, collected via confocal or light sheet images, and quantify the TF intensity of each nuclei and their relative position in space(Blin et al., 2018, Malaguti et al., 2019). Pickcells utilises Delaunay triangulation to identify the neighbours of each cell and create a network of cells in 3D, which can then be analysed to potentially quantify protein content patterning in 3D.

Like Pickcells and HistoCat, CytoMap (Stoltzfus et al., 2020) is a spatial image analysis environment which can analyse segmented samples in 3D, quantify TF or RNA expression, identify niches, and infer cell-cell communication. But this pipeline

primarily relies on binary definitions of cell state, which may not be applicable optimal when describing TF expression along a differentiation gradient, such as gradients of T, Sox2, and Tbx6 in the epiblast.

3D quantification of expression of T and Sox2 has been quantified in NMPs in mouse (Wymeersch et al., 2016), chick (Guillot et al., 2021), and zebrafish (Fulton et al., 2021, Toh et al., 2022). Gradients of TF expression in zebrafish have been quantified and the processes regulating these patterns were explored using mathematical modelling (Fulton et al., 2021 preprint, Spiess et al., 2022 preprint). While these provide an fantastic template for analysis of TF along a gradient, the gradients were analysed along a single axis (anterior posterior), while NMPs exist in an epithelial epiblast with at least two axis to consider (Anterior-posterior, distance to the midline) which are fundamental to fate and positional identity. Methods to accommodate this will be required.

Methods to quantifying neighbour-based pattering in 3D to infer local cell-cell communication regulatory principles, rather than cell-cell communication pathways, are still in their infancy. The quantification of lateral inhibition or induction is possible with the use of spatial autocorrelation methods such as Ripley's K (Ripley, 1976). This can discern whether in a point cloud whether points are evenly distributed in space, or if they cluster together (lateral induction), or if they are regularly interspaced (lateral inhibition). It has been used to quantify Notch enforced lateral inhibition within neurons (Jafari Mamaghani et al., 2010). However, these rely on binary definitions, it may be the case that this is not applicable when quantifying TF expression in a system as dynamic as NMPs and continuous measurements are required.

None of the aforementioned analysis pipelines are immediately applicable to analyse neighbour based spatial patterning in the E8.5 epiblast, current techniques either require adapting or novel metrics need developing.

1.7 Scope of the thesis.

Following the review showing extensive Notch component expression *in vivo* within NMP contexts, coupled with the unpublished data from Haston (2018) showing a switch in NMP fate following Notch inhibition, suggests Notch may play a crucial role in regulating NMP cell fate decisions. Further, a wealth of information regarding Wnt, FGF, and Retinoic acid signalling pathways has been collected characterising the relationship between fate markers and signalling genes in NMPs. To further understand Notch contributes to the local cell-cell communication regulatory mechanisms may control NMP cell fate decisions, methods to quantify the spatial patterning of TFs within the epiblast are required. The current state of available 3D analysis pipelines suggests novel quantification methods capable of assessing patterning within the E8.5 epiblast require developing.

In this thesis I aim to address these problems and test the hypothesis that (i) Notch signalling influences NMP cell fate decisions and fate marker TF expression and (ii) in the NMP niche, the nascent mesoderm is surrounded by non-mesoderm cells indicative of Notch mediated lateral inhibition. I also aim to provide mathematical systems biology inspired approaches to create consistent and unbiased definitions and analysis pipelines, overall increasing transferability of the data I collect.

In Chapter 3 I investigate the effect of Notch inhibition on NMP cell identity and differentiation in a variety of *in vitro* NMP models. Also, I further explore the extent of Notch component expression by datamining public RNAseq datasets. In Chapter 4, I develop neighbour based mathematical methods to quantify the spatial patterning of T, Sox2, Tbx6 in the E8.5 epiblast, evaluating heterogeneity and similarity to lateral inhibition enforced lateral inhibition. Finally, in chapter 5 I apply this analysis pipeline to explore the effect of Notch inhibition on spatial TF patterning in NMP culture models.

Table 1.1 Wnt/FGF/RA/Notch signalling and NMP TF gene interactions.

Gene	Target	Regulation type	Species/Context	Reference
T	Tbx6	DNA promoter binding + downregulation in T mutant mouse in vivo NMPs.	Mouse	(Koch et al., 2017)
	Wnt3a	Ntl (T analogue) induces Wnt.	Zebrafish	(Martin and Kimelman, 2008)
		DNA promoter binding ChIP-chip ES cell. Downregulation T mutant E7.5-8.5 embryo.	Mouse ES cell differentiation and embryo mutant.	(Evans et al., 2012)
	Fgf8	DNA promoter binding ChIP-chip ES cell. Downregulation T mutant E8.0 embryo.	Mouse ES cell differentiation and embryo mutant.	(Evans et al., 2012)
	Nkx1.2	DNA promoter binding + upregulation in T mutant mouse in vivo NMPs.	Mouse E8.5 Embryo	(Koch et al., 2017)
	Wnt3a	DNA promoter binding + downregulation in T mutant mouse in vivo NMPs.	Mouse E8.5 Embryo	(Koch et al., 2017)
	Fgf8	DNA promoter binding + downregulation in T mutant mouse in vivo NMPs.	Mouse E8.5 Embryo	(Koch et al., 2017)
	Dll1	DNA promoter binding + downregulation in T mutant mouse in vivo NMPs; In synergy with	Mouse E8.5 Embryo	(Koch et al., 2017, Hofmann et al., 2004,

		T/Tbx6 upregulates via DNA promoter binding; Mouse in vivo. T knockdown RNAi reduces Dll1 expression in caudal end E8,5 mouse embryo.		Vidigal et al., 2010)
	Dll3	T knockdown RNAi reduces Dll3 expression.	caudal end E8,5 mouse embryo.	(Vidigal et al., 2010)
	Dll4	DNA binding ChIP-seq.	Mouse E7 primitive streak	(Lolas et al., 2014)
	Msgn1	DNA promoter binding + downregulation in T mutant mouse in vivo NMPs.	Mouse E8.5 Embryo	(Koch et al., 2017)
		ChIP-seq promoter binding.	Mouse ES cell differentiation.	(Evans et al., 2012)
	T	DNA promoter binding + downregulation in T mutant mouse in vivo mouse in vivo NMPs.	Mouse E8.5 Embryo	(Koch et al., 2017)
	Notch1	DNA promoter binding + downregulation in T mutant mouse in vivo NMPs.	Mouse E8.5 Embryo	(Koch et al., 2017)
	Notch3	Chip-Seq in in vitro Mouse ES to EB formation. Zebrafish in vivo primitive streak ChIP-Seq.	Mouse in vitro and Zebrafish.	(Lolas et al., 2014, Gentsch et al., 2013)
	Notch4	DNA promoter binding + downregulation in T mutant.	Mouse E8.5 Embryo.	(Koch et al., 2017)
	Cyp26a1	DNA promoter binding + downregulation in T mutant mouse in vivo NMPs.		(Koch et al., 2017, Vidigal et al., 2010)

		T knockdown RNAi reduces Cyp26a1 expression in caudal end E8,5 mouse embryo.		
	Hes3	T knockdown RNAi reduces Hes3 expression in caudal end E8,5 mouse embryo.	Mouse E8.5 Embryo	(Vidigal et al., 2010)
Sox2	T	Sox2 redirects Wnt upregulation of T.	Mouse ES cell differentiation.	(Blassberg et al., 2022)
	Cdx2	DNA promoter binding + upregulation in Sox2 mutant mouse in vivo NMPs.	Mouse E8.5 Embryo	(Koch et al., 2017)
	Dll1			
	Dll3			
	Notch1			
	Cyp26a1			
	Lfng			
	Tbx6	DNA promoter binding + upregulation in Sox2 mutant mouse in vivo NMPs.		(Takemoto et al., 2011, Koch et al., 2017)
	Hes3	ES promoter binding site analysis.	Mouse.	(Katoh and Katoh, 2007)
	Hes6			
	Tbx6	Promoter occupancy.	Mouse ES cells	(Blassberg et al., 2022)
	Msgn1	Promoter occupancy.	Mouse ES cells	(Blassberg et al., 2022)
	Nkx1-2	Promoter occupancy.	Mouse ES cells	(Blassberg et al., 2022)
Cdx2	Dll1	DNA promoter binding.	Mouse in vivo and in vitro.	(Grainger et al., 2012)
	Wnt5a	Upregulation by ChIP-seq and RNAseq.	EpiSC derived NMPs.	(Amin et al., 2016)
	Fgf8			(Amin et al., 2016)
	Cyp26a1	DNA promoter binding.	E8.5 embryos.	(Savory et al., 2009)
	Wnt3a			

	T			
cMyc	FGF8 Sox2	Downregulation after Inhibition.	ES cells and explants of posterior embryos.	(Mastromina et al., 2018)
Cyp26a1	RA	Metabolises RA – required for posterior identity.		(Abu-Abed et al., 2001)
Tbx6	Sox2	Negative, direct promoter binding.		(Takemoto et al., 2011, Koch et al., 2017, Javali et al., 2017)
	Msgn1	DNA promoter binding + downregulation in Tbx6 mutant NMPs.		(Koch et al., 2017, Wittler et al., 2007)
	Hes7	Positive regulation PSM.	Mouse.	(Gonzalez et al., 2013)
		Binding sites for T box in Hes 7 promoter.	Mouse PSM	
	Dll1	Positive regulation in synergy with T/Tbx6, upregulates via DNA promoter binding.	Mouse in vivo.	(Hofmann et al., 2004, White and Chapman, 2005)
Msgn1	Tbx6	Positive, Msgn1 mutant downregulates Tbx6.	E8.5 embryo	(Nowotschin et al., 2012)
		Chip seq and microarray, upregulates Tbx6 and binds to promoter.	E8.5 embryo.	(Chalamalasetty et al., 2014)
	T	Inhibitory, Msgn1 mutant has expanded T domain.	E9.5 mouse embryo.	(Yoon and Wold, 2000)
	Lfng Notch1/2 Dll1/3	ChIP-seq promoter binding.	ESC and in vivo for segmentation clock.	(Chalamalasetty et al., 2011)
Hes1	Hes1	Negative regulation of .	Mouse fibroblasts NIH-3T3 cells.	(Sasai et al., 1992)

Hes6	Hes1	Antagonises Hes1 expression and Hes1 inhibitory effect.	NIH3T3 fibroblasts.	(Bae et al., 2000)
Hes7	Hes7	Represses own promoter.	Mouse.	(Bessho et al., 2003, Bessho et al., 2001a, Chen et al., 2005, Hayashi et al., 2018)
	Lfng	Repress promoter – N-box.	Mouse.	(Chen et al., 2005)
FGF8	Dll1	Negative regulation inferred by increase in Dll1 following FgfR1 mutant.	E9.0 embryos.	Wahl et al. (2007)
	Lfng	Positive regulation.	Mouse E8.5 Fgf8 overexpression and mutant.	(Naiche et al., 2011)
	T	Positive regulation and requirement from Fgf8 inhibition.	Mouse embryos.	(Olivera-Martinez et al., 2012)
	Sox2	N1 enhancer binding sites.	Chicken embryos.	(Takemoto et al., 2006)
	Nkx1.2	Upregulation after treatment with Fgf.	Chick embryo explants.	(Sasai et al., 2014)
	RARβ	Fgf treatment strongly down regulated RARβ	Chicken embryos HH4, neural tube explants.	(Olivera-Martinez and Storey, 2007)
Wnt3a/β-Catenin	Dll1	In synergy with T/Tbx6 upregulates via DNA promoter binding. Mouse in vivo.		(Hofmann et al., 2004)
	T	Direct promoter binding upregulation.		(Yamaguchi et al., 1999, Yoshikawa et al., 1997)
	Tbx6	Direct promoter binding upregulation.		(Yamaguchi et al., 1999, Dunty Jr et al., 2008)

	Msgn1	Direct promoter binding upregulation.		(Nowotschin et al., 2012, Wittler et al., 2007)
Wnt3/β-Catenin	Sox2	TCF/LEF site in N1 enhancer – chicken embryos.		(Takemoto et al., 2006)
β-Catenin TCF/LEF	Hes7	Overexpressing Active beta-Catenin and Lef1 activates Hes7 promoter.		(Gonzalez et al., 2013)
	Jag1	Bioinformatic searches for TCF/LEF sites in Jag1 promoter across human, mouse, chimpanzee.		(Katoh and Katoh, 2006)
	Dll1	TCF/LEF site in promoter.	Mouse.	(Galceran et al., 2004)
RA	Nkx1.2	RAR deletion reduces Nkx1.2 expression. Upregulated in mouse NMPs with RA treatment, no Rare site mentioned.	Mouse in vitro NMPs.	(Cunningham et al., 2016)
	FGF	Inhibitory.	Mouse CNH in vivo.	(Olivera-Martinez et al., 2012)
	Cyp26a1	Contains RAR in promoter and is upregulated upon treatment with RA.	Mouse.	(Loudig et al., 2000, Loudig et al., 2005)
	Sox2	Rar site found upstream and upregulated with RA treatment.	Mouse.	(Cunningham et al., 2016)
NICD	Hes1	Upregulation. Single CSL binding site in mouse.	Mouse.	(Nishimura et al., 1998, Katoh and Katoh, 2007, Castel et al., 2013)
	Hes5	Upregulation. Double CSL binding site in mouse.	Mouse	(Nishimura et al., 1998, Katoh and Katoh, 2007)

	Hes7	Upregulation.	Mouse.	(Bessho et al., 2001a)
	β-Catenin	RBP-jK NICD Inhibition within nucleus, Notch1 inhibition at membrane..	HEK293T cells.	(Acar et al., 2021)
	Tbx6	Notch controlled enhancer critical for Tbx6 expression found in paraxial mesoderm, but not PS.	E9.5 mouse embryo.	(White et al., 2005)
	Myc	Upregulation in mouse NMPs.		(Mastromina et al., 2018, Palomero et al., 2006)
	Hey1	Single CSL binding site, upregulation.	Mouse.	(Maier and Gessler, 2000, Katoh and Katoh, 2007, Castel et al., 2013)
	Hey2			
	Jag1	RBP-jK binding site and upregulation.	Mouse myoblasts.	(Castel et al., 2013)

Chapter 2:

Materials and Methods

2.1 Materials.

Table 2.1. Reagents.

Product	Manufacturer	Catalogue number
2-Mercaptoethanol, 50mM (1000x).	Life Technologies	31350010
Accutase® solution	Sigma-Aldrich	A6964
Activin-A (Human/murine/rat raised in E. coli)	Peprotech	120-14E
B-27® Supplement	Gibco	17504-044
Benzyl alcohol	Sigma-Aldrich	8421
Benzyl benzoate	Sigma-Aldrich	B6630
Bovine serum albumin (solid)	Sigma-Aldrich	A3059
Chiron / CHIR 99021	Axon	1386
Corning® Matrigel® Growth Factor Reduced (GFR) Basement Membrane Matrix, LDEV-free, 10 mL	Corning	354230
DAPI	Sigma	D9542
DAPT	Abcam	ab120633
Dimethyl sulphoxide, dehydrated	VWR	23500.26
DMEM/F-12	Gibco	21331-020
dNTP Mix (10mM)	Invitrogen	18427-013
Donkey serum	Sigma	D9663
Dulbecco's Phosphate Buffered Saline (PBS)	Sigma-Aldrich	D8537
EDTA (for tissue culture)	VWR	20301.186
Ethanol absolute 100%	VWR Chemicals	20821.33
Foetal calf serum	Life technologies	10270106
Formaldehyde solution, 37-41%	Fisher Chemical	F/1501/PB08
Geltrex™ LDEV-Free Reduced Growth Factor Basement Membrane Matrix	Gibco™	A1413201
Gelatin, powder	Gelatin, powder	G1890
Glasgow minimum essential medium	Sigma	G5154

Glycerol	CalBiochem	356350
HyCloneTM Water, molecular biology grade	Fisher Scientific	SH3053802
IWP2	Biotechne	3533/10
KnockOutTMSerum Replacement	Gibco	10828028
Leica™ Immersion Oil type F	Leica™ Microsystems	11513859
LightCycler® 480 Probes Master(2X)	Roche	4887301001
LightCycler® 480 SYBR Green I Master	Roche	4707516001
L-glutamine, 200mM	Invitrogen	25030-024
LY411575	Carbosynth	FL104120
M2 Medium	Sigma	M7167-100mL
MEM non-essential amino acids, 100x	Invitrogen	11140-036
Methanol AnalaR Normapur®	VWR	20847.24
mTeSR™ Plus	Stem Cell technologies	100-0276
N-2® Supplement	Gibco	17502-048
Neurobasal® Medium	Gibco	21103049
PD 0325901	Axon	1408
Penicillin (10,000 U/mL) / streptomycin (10,000 µg/mL)	Invitrogen	15140-122
Phosphate buffered saline tablets	Sigma-Aldrich	P4417-100TAB
Random Primers	Invitrogen	48190-011
RNAseOUTTM Recombinant Ribonuclease Inhibitor (40 U/µL)	Invitrogen	10777019
RNAseZap® RNAse decontamination solution	Ambion	AM9780
Sodium pyruvate, 100mM	Invitrogen	11360-039
Sodium Azide	G-Biosciences	786-299
TritonTMX-100	Sigma	X100-100ML
Trypsin 2.5%, 100x	Invitrogen	15090-046
Universal Probe Library probes	Roche	-
Y 27632 dihydrochloride Rock inhibitor	Axon	1683

Table 2.2. Plasticware and culture ware.

Product	Manufacturer	Catalogue number
CentriStar™ Centrifuge tubes, 15mL clear polypropylene	Corning	430790
CentriStar™ Centrifuge tubes, 50mL clear polypropylene	Corning	430828
Costar® Clear TC-treated multiple well plates, 6well	Corning	3516
Costar® Clear TC-treated multiple well plates, 12well	Corning	3513
Costar® Clear TC-treated multiple well plates, 24well	Corning	3524

ibidi Polymer coverslip	ibidi	10814
CryoTubeTM Vials, 1.0mL	Thermo Fisher Scientific	377224
Microscope slides	VWR	ECN 631-1553
Micro tubes with screw cap, 1.5mL	Sarstedt	72692005
Multiply® µStrip Pro PCR tubes	Sarstedt	72.991.002
NunclonTM Delta sturface 4-well plate.	Thermo Fisher Scientific	176740
Reagent reservoir 25mL	Thermo Fisher Scientific	8093-11
Round bottom polypropylene test tube with snap cap, 14mL	Falcon	352059
Syringe filter unit, 0.22µm, Millex-GP	Millipore	SLGP033RS
µ-Slide 8 Well high - ibiTreat	Ibidi	80806
µ-Slide 18 Well	Ibidi	81816
sticky-Slide 8 Well high	ibidi	80808
Sterilin™ Clear Microtiter™ Plates, 96 well U-bottom non-TC treated	Thermo Scientific™	612U96
Sterilin™ Clear Microtiter™ Plates, 96 well V-bottom non-TC treated	Thermo Scientific™	612V96
Sterilin™ Clear Microtiter™ Plates, lid for 96 well plates	Thermo Scientific™	642000
Sterilin™ Polystyrene 30mL Universal Containers	Thermo Fisher Scientific	128A/FS
TC-treatedculture dish, 100mm	Corning	430167
ViewPlate-96 Black, Optically Clear Bottom, Tissue Culture Treated, Sterile, 96-Well with Lid	PerkinElmer	6005182

Table 2.3. Manufacturer kits.

Product	Manufacturer	Catalogue number
Absolutely RNA Miniprep Kit	Agilent	400800
M-MLV Reverse Transcriptase Kit	Invitrogen	28025
Alexa Fluor™ 647 Antibody Labelling Kit	Invitrogen™	A20186
D-Tube™ Dialyzer Mini, MWCO 12-14 kDa	Millipore	71505
ViewRNA™ Cell Plus Assay Kit	Invitrogen™	88-19000-99

Table 2.4. Standard solution compositions.

Solution	Composition
Activin A stock solution, 20µg/mL	100µg/mL Activin A (Peprotech) dissolved in sterile-filtered 0.1% BSA (Sigma) in PBS to achieve final 20µg/mL concentration.

BABB	1:2 mix of benzyl alcohol: benzyl benzoate
Blocking solution (for ICC)	5% Donkey serum (Sigma), 0.1% TritonTMX-100 (Sigma), 0.03% Sodium azide in PBS
Formaldehyde fixative solution, 4% & 8%	1:10 or 1:5 dilution of 40% Formaldehyde solution (Fisherchemical, as supplied) in PBST for 0.4% and 0.8% respectively.
Gelatin, 0.1%	1% gelatin (Sigma) in water and autoclaved, then diluted to 0.1% in PBS (Sigma)
Glutamine/Pyruvate	100mM L-glutamine (Invitrogen), 50mM sodium pyruvate (Invitrogen)
90% Glycerol	1:10 dilution of PBST in 100% Glycerol for imaging mounting media.
Leukaemia inhibitory factor, human, 100,000 units/mL	Made in-house by tissue culture staff. Briefly, Cos7 cells are transfected with plasmid to produce LIF. The concentration is assayed using indicator cells, and diluted in PBS to final concentration.
PBS, non-sterilised.	One PBS tablet (Sigma-Aldrich) dissolved in 200mL deionised water yields 0.01M phosphate buffer, 0.0027M KCl and 0.137M NaCl, pH7.4 at 25°C
PBST	Non sterilised PBS (Sigma-Aldrich) with 0.1% (or 0.5% for permeabilisation) Triton X-100 (Sigma)
Trypsin (1:5)	Prepared by tissue culture staff. 0.186g of EDTA (VWR) added to 500mL PBS (Sigma) and filter-sterilised. 5mL chick serum (Sigma) and 20mL 100x Trypsin (Invitrogen) added. . This solution was diluted 1:5 in PBS prior to use.

Table 2.5. Primary antibodies.

Target Antigen	Clone	Host	Dilution	Vendor	Cat #
Oct-04	C-10	Mouse	1:200	Santa Cruz	Sc-5279
Id1	37-2	Rabbit	1:200	Biocheck	BCH-1/37-2
HoxC9	HOXCA6E6	Mouse	1:200	Abcam	ab50839
Hoxb4	Monoclonal	rat	1:50	DSHB	I12 anti-Hoxb4
Id1	37-2	Rabbit	1:200	Biocheck	BCH-1/37-2
LaminB1	Polyclonal	Rabbit	1:1000	Abcam	Ab16048
LaminBR	E398L Recombinant	Rabbit	1:200-400	Abcam	ab201349

Nanog	eBIOMLC-51	Rat	1:200	eBiosciences	14-5761-80
Nuclear pore complex (NPC)	Mab414	Mouse	1:1000	Abcam	ab24609
Sox2	EPR3131	Rabbit	1:100-1:200	Abcam	ab92494
T-Brachyury NL557	Polyclonal Goat	Goat	1:200-300	R&D Systems	NL2085R
T-Brachyury	Polyclonal	Goat	1:200-400	R&D	AF2085
Tbx6	Polyclonal	Goat	1:100-200	R&D Systems	AF4744

Table 2.6. Secondary antibodies.

Host species	Species recognised	Excitation wavelength (nm)	Manufacturer	Catalogue number
Donkey	Goat	488	Invitrogen	A11055
		568	Invitrogen	A11057
		594	Abcam	AB150132
		647	Invitrogen	A21447
	Mouse	405	Invitrogen	A48257
		488	Invitrogen	A21202
		568	Invitrogen	A10037
		647	Invitrogen	A31571
	Rabbit	405	Invitrogen	A48258
		488	Invitrogen	A21206
		555	Invitrogen	A31572
		647	Invitrogen	A31573
	Rat	488	Invitrogen	A21208
		568	Abcam	AB175475

Table 2.7. qPCR primer sequences with UPL probe number.

Gene	Species	Forward sequence	Reverse Sequence	UPL probe
SDHA	Mouse	CAGTTCCACCCCACAGGTA	TCTCCACGACACCCTTCTGT	71
T (Brachyury)	Mouse	ACTGGTCTAGCCTCGGAGTG	TTGCTCACAGACCAGAGACTG	27
TBP	Mouse	GGGGAGCTGTGATGTGAAGT	CCAGGAAATAATTCTGGCTCA	97
Ywhaz	Mouse	TTACTTGGCCGAGGTTGCT	TGCTGTGACTGGTCCACAAT	9

Sox2	Mouse	GTGTTTGCAAAAAGGGAAAAG T	TCTTTCTCCCAGCCCTAGTCT	34
Tbx6	Mouse	ccgagaaaatggcagaaact	gtgtatccccactcccacag	21
Dll1	Mouse	gggcttctctggcttcaac	taagagttgccgaggtccac	103
Sox2	Human	TGGACAGTTACGCGCACAT	CGAGTAGGACATGCTGTAGGT	-
Tbx6	Human	agctctgtgggaacagaaatg	accggaatcacatccagaag	9
Jag1	Human	gaatggcaacaaaacttgcat	agccttgtcggcaaatagc	42
Hes1	Human	ttacggcggactccatgt	agaggtgggttggggagt	63
TBP	Human	gaacatcatggatcagaacaaca	atagggattccgggagtcat	87

2.2 Methods.

2.2.1 Immunofluorescence

2.2.1.1 2D Fixation:

Human and mouse cells cultured on 2D surfaces were fixed by removing half the culture media, then gently adding an equal volume to remaining media of PBS + 8% PFA (Sigma) + 0.1% Triton X-100 (Sigma) for 10-15 minutes at room temperature. Achieving a final concentration of 0.4% PFA. The cells were then washed three times in PBS + 0.1% Triton X-100 (Sigma) (PBST) with an incubation period of 5 minutes each.

2.2.1.2 Replating and fixing for high throughput imaging.

When fixing hNMP-LCs for high throughput imaging and single cell analysis, a new TC-treated 96 well imaging plate (PerkinElmer) is coated with Geltrex™ for 1 hour at 37°C. The following processes were carried out with a 12-channel pipette and separate reagent reservoirs. The hNMP-LC culture media was aspirated, and cells were gently washed in 100uL of PBS and again aspirated. Then 20uL of Accutase is added to each well and incubated for 2 minutes at 37°C, after which 120uL of un-supplemented N2B27 is added to quench the Accutase. The cells are then firmly pipetted up and down to dissociate the colonies and create a single cell suspension. 60uL of this solution is then transferred to the new plate coated with Geltrex and left to adhere without disturbing the plate for 15-20 minutes. To fix, 60uL of PBST+0.8%

PFA (Sigma) was gently added for 10-15 minutes. After which three PBST washes for 5 minutes each after performed.

2.2.1.3 Embryo, gastruloid, and 3D human NMP aggregate fixation.

Free floating tissues were fixed in PBS + 4% PFA (Sigma) + 0.1% Triton X-100 (Sigma) for 1 hour at room temperature with gentle agitation. All further steps were performed on a shaker with gentle agitation at room temperature. The tissues were then washed three times in PBST for 15 minutes, then permeabilised in a PBS + 0.5% Triton X-100 (Sigma) for 30 minutes. Then the tissues were washed with three times for 5 minutes in PBST before neutralising the PFA in 50mM NH4Cl in PBST for 30 minutes. Finally, the tissues were washed three times for 15 minutes in PBST.

2.2.1.4 LaminB1 primary antibody conjugation to Alexa647 Fluorophore

Conjugation of Rabbit anti LaminB1 (Abcam) to a fluorophore was carried out by the Alexa Fluor™ 647 Antibody Labelling Kit (Invitrogen) as by the manufacturer's instructions. Before conjugation, the sodium azide preservative in the antibody solution (as shipped) is removed by dialysis using from the D-Tube™ Dialyzer Mini (MWCO 12-14 kDa [Millipore]). The tube and floating ring were assembled and then placed onto 1,000,000x volumes of PBS, relative to the antibody solution (in this case 100mL of PBS to 100uL antibody solution), at 4°C in a glass beaker for 5 minutes to pre-wet the dialysis membrane. Next, the antibody solution was added to the dialysis chamber and placed onto the PBS to dialyse for one hour with a magnetic stirrer to gently agitate the PBS. The PBS was replaced and dialysed for a further two hours, the PBS was changed a further two times with 2 hour dialysis periods. The temperature of the PBS was maintained at 4°C throughout dialysis. After the antibody solution was dialysed, it was removed from the chamber and could then be conjugated using the Alexa Fluor™ 647 Antibody Labelling Kit (Invitrogen).

2.2.1.5 Antibody staining of 2D cells.

Fixed cells were incubated with blocking solution (PBST + 0.5% Donkey Serum + 0.03% [Sigma] Sodium Azide [G-Biosciences]) for one hour at room temperature. Primary antibodies were diluted in blocking solution to the desired concentration and centrifuged at 738g for 5 minutes. After this, the BLOCK + primary antibody solution was carefully added to cells for 4 hours at room temperature or overnight at 4°C. All incubations and washes were performed on a shaker with gentle agitation. After primary stain cells were washed three times with PBST for 5 minutes each.

Secondary antibodies were diluted in blocking solution and centrifuged at 300g for 5 minutes. This was then added to the cells with a 1 hour incubation period at room temperature or 4 °C overnight. If DAPI is required, DAPI is diluted 1:10,000 in blocking solution and added to cells for 5 minutes. The cells were then washed with PBST three times for 5 minutes each.

For sequential stains with conjugated primary antibodies of the same host as non-conjugated primary antibodies, primary and secondary stained cells were incubated with blocking solution containing 5% donkey serum + 5% serum(s) of the primary antibody host for 1 hour at room temperature. Conjugated primaries were diluted in the 5% Donkey serum + 5% host serum(s) blocking solution and added to the cells for 4 hours at room temperature or 4 °C overnight. After this staining cells were washed three times in PBST for 5 minutes each.

2.2.1.6 Embryo, gastruloid, and 3D human NMP aggregate staining:

All incubations and washes were performed on a rotating platform with gentle agitation. Fixed tissues in suspension were incubated in blocking solution overnight at 4°C. Primary antibodies were diluted in blocking solution to the desired concentration, centrifuged at 300g for 5 minutes, and then added to a 4-well plate. The tissues were transferred into this solution for 24 hours at room temperature on a rotating platform with gentle agitation. After primary stain cells were washed three times with PBST for 15 minutes each.

Secondary antibodies were diluted in blocking solution, centrifuged at 300g for 5 minutes, and then added to a 4-well plate. The tissues were transferred to the secondary solution with a 24 hour incubation period at room temperature. The cells were then washed with PBST three times for 5 minutes each.

For sequential stains with conjugated primary antibodies of the same host as non-conjugated primary antibodies, primary and secondary stained cells were incubated with blocking solution containing 5% donkey serum + 5% serum(s) of the primary antibody host overnight at 4°C hour at room temperature. Conjugated primaries were diluted in the 5% Donkey serum + 5% host serum(s) blocking solution and added to the cells for 4 hours at room temperature or 4 °C overnight. After this staining cells were washed three times in PBST for 5 minutes each.

2.2.1.7 Mounting of stained samples for imaging

2D cells were mounted in PBST or 90% glycerol (CalBiochem) in PBST, depending on the desired objective's immersion refractive index. Non-adhered samples were progressively dehydrated in methanol (VWR) + PBST at 10%, 25%, 50%, 75%, 90%, and x2 100% methanol concentration steps, with 5 minutes per step. Tissues were kept in 100% ethanol for 5 minutes, then transferred directly to imaging chamber housing BABB mounting solution. The tissues were left in BABB for a minimum of 10 minutes prior to imaging.

For embryos, using a pipette tip the posterior portions were manipulated to lie with the epiblast facing down closest to the objective lens (Fig 2.1.b).

2.2.1.8 Imaging of stained samples

2D Cells were imaged using a Leica SP8 inverted confocal microscope, the Opera Phenix Plus high-content screening system, or Zeiss brightfield microscope. Tissues in suspension mounted in BABB were imaged using a Leica SP8 inverted confocal microscope and x40 oil immersion objective.

Optimal signal gain and laser intensity and settings were determined ad hoc for each experiment, settings were maintained across replicates where possible. Positive controls were used to bring the signal just below saturation, to provide maximum signal to noise but prevent saturated pixels. Images were collected in 16 bit grayscale.

Z stacks were spaced <0.35um and <0.5um XY pixel size were used as minimum pixel density for nuclear segmentation.

2.2.2 Cell culture

2.2.2.1 Mouse cell lines

In this study, the E14Ju09 cell line was used as wild-type mouse embryonic stem cells. E14Ju09 is a clonal stem cell line derived from E14TG2a ES cells by the Transgenics Unit staff. The E14tg2a were derived from129/Ola chimeric embryos and are hypoxanthine phosphoribosyltransferase deficient (Hooper et al. 1987).

2.2.2.2 Naïve mouse ES culture

Naïve ES cells were cultured on gelatine coated cell culture dishes at 37°C and 5% CO2. The composition of the medium was either LIF/FCS or 2i/FCS/LIF as described in tables X. Cells were passaged at 70-80% confluency at a ratio of 1:10, typically every three days. To passage ES cells, culture dishes were coated with 0.1% gelatine in PBS for 15 minutes before plating. The medium was aspirated and cells washed in sterile PBS (sigma) once before adding 0.05% Trypsin EDTA solution. The plate was gently tapped to ensure cell detachment, then 5-10 volumes of fresh medium was added to the cells to quench the trypsin EDTA. The cells and medium were transferred to a universal tube and pelleted at 300g for three minutes. The media was aspirated and the pellet resuspended in fresh media, which is then plated onto the gelatinised culture wells.

In the transition from FCS/LIF to 2i/FCS/LIF media, FCS/LIF cells were plated at 5,000/cm2 in FCS/LIF on gelatinised plates, then the next day the media was replaced with 2i/FCS/LIF. Cells were passaged using 2i/LIF/FCS media as described

above 1:5 for at least 10 days (approximately). After this period, routine passaging was as described above with 2i/FCS/LIF media and a 1:10 ratio split every three days.

Table 2.8. LIF/Serum media composition.

Component	Volume	Final conc.
Glasgow Minimum Essential Medium (GMEM, Sigma)	500ml	-
Foetal Calf Serum (FCS, Gibco)	51ml	10%
L-Glutamine/Sodium pyruvate solution.	11ml	L-Glutamine 2mM Sodium pyruvate 1mM
Non-Essential Amino Acids (NEAA, Gibco)	5.5ml	1X
0.1M 2-mercaptoethanol	567.5µl	100nM
LIF	567.5µl	100U/ml

Table 2.9. 2i/FCS/LIF media composition.

Component	Volume	Final conc.
Glasgow Minimum Essential Medium (GMEM, Sigma)	500ml	-
Foetal Calf Serum (FCS, Gibco)	51ml	10%
L-Glutamine/Sodium pyruvate solution	11ml	L-Glutamine 2mM Sodium pyruvate 1mM
Non-Essential Amino Acids (NEAA, Gibco)	5.5ml	1X
0.1M 2-mercaptoethanol	570µl	100nM
LIF	570µl	100U/ml
CHIR 99021	15µl	3µM
PD 0325901	5µl	1µM

2.2.2.3 Gastruloid culture

Gastruloid culture was carried out as described (van den Brink et al., 2020). 2i/LIF/FCS cells are washed in PBS before adding 0.05% Trypsin EDTA solution. After ES colony detachment, 5-10 volumes of fresh 2i/LIF/FCS were added to quench the Trypsin EDTA solution. The cells and media were transferred to a universal tube and pelleted by centrifugation at 300g for 3 minutes. The media was aspirated, and the pellet was resuspended in cold PBS, making sure to create a

single cell suspension. This PBS wash was repeated once more, then the cell pellet was resuspended in prewarmed N2B27 to create a single cell solution. The cells were then counted and then a solution of N2B27 medium with 8,250 cells/mL was made. 40uL of this medium, containing ~330 cells, was plated into untreated u-bottom 96 wells and incubated for 48 hours at 36 °C and 5% CO2. At 48 hours, 150uL of N2B27 and 3uM CHIR99021 (Axon) were added into the well, the last half of the media was expelled forcefully to dislodge the aggregate but without spilling the medium. The aggregates were cultured for a further 24 hours to Day 3, after which 150uL of media was removed and replaced with 150uL fresh N2B27. After a further 24 hour incubation to Day 4, another media change was performed as before. For experiments inhibiting Notch or Wnt, this media change from Day 4 to Day 5 was supplemented with DAPT, IWP2, or an equal amount of DMSO for the 24 hour period. At Day 5, the gastruloids in each condition were transferred to a six-well plate and washed in 1-2 volumes of PBS before being fixed as described.

Table 2.10. N2B27 media composition.

Component	Volume	Final conc.
DMEM/F12 (Gibco)	50ml	
Neurobasal (Gibco)	50ml	
L-Glutamine 1ml 2mM	1ml	2mM
50mM 2-Mercaptoethanol	200µl	100nM
N2 (Gibco)	0.5mL	0.5X
B27 (Gibco)	1ml	0.5X

2.2.2.4 EpiSC culture

EpiSCs were cultured in media composing of N2B27, recipe as described above, + 20ng/mL Activin (Peprotech) + 10ng/mL recombinant human FGF Basic (R&D Systems).

EpiSCs were passaged when 70-80% confluency was reached. To passage EpiSCs, culture plates were coated with 7.5ug/mL bovine fibronectin (Sigma) for at least 15

minutes at RT. EpiSCs were then washed with sterile PBS and treated with Accutase for 3-5 minutes at 37°C. After this period the plate was tapped to detach the cells and 4-5 volumes of fresh N2B27 media added to quench the accutase. The cells were then pelleted at 300g for 3 minutes and carefully resuspended in fresh N2B27/Activin/FGF media, maintaining clumps of cells and preventing single cell suspension. Routinely, cells were cultured in a 6 well plate and split in a 1:8 ratio split to passage cells every 2 days.

2.2.2.5 EpiSC to NMP-LC differentiation

EpiSC to NMP-LC differentiation was performed as described in Gouti et al 2014, EpiSCs were cultured in N2B27 supplemented with 20ng/mL recombinant human FGF Basic (R&D Systems) and 3uM CHIR99021 (Axon) for 48 hours. Culture wells were coated with either with 7.5ug/mL bovine Fibronectin (Sigma) dissolved in PBS for at least 15 minutes at RT or 100ug/mL Matrigel dissolved in PBS for 1 hour at 37°C. Tor prepare the Matrigel, aliquots from -20°C were thawed by placing on ice at 4°C overnight, after which the appropriate amount of Matrigel was transferred to ice cold PBS using chilled pipette tips. EpiSCs the cells were detached the same as during passaging, resuspended in NB27/FGF/CHIR media, then plated at 6000 cells/cm2. After the 48 hour period, cells were fixed or RNA collected as described in X and Y respectively.

2.2.2.6 Human ES cell line

For wild type human ES cells, the clinical grade hESC cell line MasterShef7 was used. MasterShef7 is a male ES cell line generated by the Centre of Stem Cell Biology at the University of Sheffield (Vitillo et al., 2020).

2.2.2.7 Human ES culture

MasterShef7 hESCs were cultured on Geltrex™ (Gibco) coated wells in mTeSR Plus™ media. To passage hESCs, the Geltrex™ aliquot stored at -20°C was thawed on ice at 4°C overnight, then using ice cold tips the Geltrex™ was transferred to ice cold DMEM to 100ug/mL. Culture wells were coated in DMEM + 100ug/mL Geltrex™

for 1 hour at 37°C to induce gelation. Once 70-80% hESC confluency was reached, hESCs were passaged at a 1:10 ratio every 4-5 days. To passage, the hESCs were washed in PBS before adding Accutase (typically 200uL in a 6 well plate). After treating the cells with Accutase for 5 minutes at 37°C, the dishes were gently tapped and cells detached. 3-4 volumes of fresh mTeSR Plus™ media was added to quench the Accutase. The hESCs were pelleted at 300g for 3 minutes then resuspended in fresh mTeSR Plus with 10uM Y-27632 dihydrochloride (Axon) and plated onto Geltrex coated wells. After 24 hours, the media was replaced with a double feed (4mL for a 6 well plate) of fresh mTeSR Plus media. With a double feed, mTeSR Plus™ media was changed after 2-3 days.

2.2.2.8 Human ES to hNMP-LC differentiation

hESCs were differentiated to hNMP-LCs as described in (Gouti et al 2014, Wind et al 2021). hESCs were detached and pelleted as with routine passaging (as previously described). Also, a culture well was coated with Geltrex as previously described. hESC pellet was resuspended in N2B27 (recipe below) supplemented with 10uM Y-27632 (Axon) with the desired concentration of recombinant FGF basic (R&D systems) and CHIR99021 (Axon). Typically, 20ng/mL FGF and 2uM or 3uM CHIR99021 was used. hESCs were plated at 10,000 cells/cm2. After 24 hours, the media was aspirated and fresh prewarmed N2B27/FGF/CHIR media without Y-27632 was added. hESCs were cultured for a further 48 hours and then fixed or RNA collected as described. For signal pathway manipulation from Day3 to Day 4 after hNMP-LC differentiation, N2B27/FGF/CHIR was supplemented with the gamma-secretase inhibitor LY 411575 (CarboSynth) at 150nM, or the porcupine inhibitor IWP2 (Biotechne) at 2.5uM, or an equal amount of DMSO. After the 24-hour period to Day 4, cells were either fixed, RNA collected as previously described, or replated for fixing and high throughput imaging as described.

2.2.3 Cryopreservation

2.2.3.1 Cell freezing

To cryopreserve mouse cells, they were subject to trypsinisation/accutase treatment and pelleting following standard passaging routines described above. Cells were re-suspended in knockout serum replacement (KSR)(Gibco) +10% DMSO. 1ml of FCS/KSR +DMSO solution was used per aliquot equating to approximately half a 70-80% confluent 6 well plate. The cells in KSR/DMSO solution were then aliquoted to a cryovial and snap frozen in dry ice, which were then transferred to -80°C for short-term storage (under three months) or to liquid nitrogen tanks for long-term storage.

For hESCs, the cells were subject to accutase treatment, as described above, and gently resuspended in knockout serum replacement (KSR)(Gibco) +10% DMSO to prevent single cell dissociation. These were then placed into a Corning™ CoolCell™ LX cell freezing vial container. Which were then placed into -80°C overnight to achieve 1°C per minute cooling. The aliquots were then placed into liquid nitrogen tanks for storage.

2.2.3.2 Cell thawing

To defrost all cell types, 4mL of the appropriate culture medium was prewarmed in a universal tube. The frozen aliquot of cells was thawed in a water bath at 37°C and immediately added to the warmed media. Cells were then pelleted and re-suspended in fresh prewarmed culture medium and then plated onto pre-coated plates.

2.2.4 Q RT-PCR methods

2.2.4.1Quantitative real-time PCR

Quantitative real-time PCR was performed using a LightCycler® 480 Real-Time PCR system and white Roche LightCycler® 480 384 well plates, with a total 10uL reaction volume. Two qPCR systems were used, the first of which is the Taq DNA polymerase and Roche Universal Probe library (UPL). The UPL utilises 165 8-9 base pair oligonucleotide probes to quantitatively measure target sequences with a high specificity. This is measured using a fluorescein (FAM) on the 5’ end and a dark

quencher dye at the 3' end. Following the DNA polymerase extension step, the 3' quencher is hydrolysed and separated from the FAM allowing signal detection.

The primers used in this assay system were designed using the online UPL Assay Design Centre provided by Roche.

Table 2.11. Roche Probemaster reaction components.

Reagent	Volume per reaction (µl)	Final concentration
LightCycler® 480 Probes Master	5	1X
Nuclease free water	1.5	-
Forward primer	0.45	450nM
Reverse primer	0.45	450nM
UPL probe	0.1	100nM
Sample cDNA	2.5	-

Table 2.12. Roche Probemaster cycling conditions.

Step	Temperature (°C)	Duration (min:s)	Ramp rate (°C/s)	Number of cycles
Pre-incubation	95	05:00	4.8	1
Denaturation	95	00:05	4.8	
Annealing	60	00:10	2.5	45
Extension	72	00:01	4.8	
Cooling	40	02:00	2.5	1

Alternatively, I use the SYBR® Green I system. In this system, the SYBR® Green I dye binds to the major groove of DNA, where this complex fluoresces to provide a read out for total DNA content in the reaction. Melting curves were used with this system to verify a single amplicon.

Table 2.13. SYBR® Green I reaction components.

Reagent	Volume per 10µl reaction (µl)	Final concentration
SYBR® Green I Master	4	1X
Forward primer	0.8	1µM
Reverse primer	0.8	1µM
Sample cDNA	2.4	-

Table 2.14. SYBR® Green I cycling conditions.

Step	Temperature (°C)	Duration (min:s)	Ramp rate (°C/s)	Number of cycles
Pre-incubation	95	05:00	4.8	1
Denaturation	95	00:05	4.8	
Annealing	58	00:10	2.5	45
Extension	72	00:20	4.8	
Acquisition	81	00:01	2.5	

Table 2.15. SYBR® Green I cycling conditions.

Temperature (°C)	Duration (min:s)	Ramp rate (°C/s)	Acquisition
95	00:01	4.8	None
65	00:10	2.5	None
95		0.11	Continuous (5 acquisitions per °C)

cDNA samples were loaded into the wells of a 384 plate, already containing the other reagents, in triplicates for technical replicates. Serial dilutions of target PCR amplicon or pGem®-T Easy plasmid containing the target amplicon sequence were plated at known concentrations to produce a standard curve and determine primer efficiencies, which was calculated by the Roche LightCycler® 480 software.

For each gene, the mean concentration and standard deviation was calculated from the technical triplicates. Outliers +/- 0.5 cycles from the other replicates were removed, but no less than two technical replicates were used in downstream analysis. Mean concentrations were normalised to house-keeping genes, which was TBP in human tissues, or the geometric mean of TBP and SDHA in mouse tissues. Values displayed in graphs are raw relative values.

2.2.5 RNA methods

2.2.5.1 Total RNA isolation

Total RNA was extracted from cultured cells using the Absolutely RNA Miniprep Kit (Agilent Technologies), following the manufacturer's instructions. The concentration of the isolated RNA was measured using a NanoDrop™ Lite spectrophotometer (Thermo Fisher). RNA samples were stored at -80°C. For all RNA work in non-TC work areas, surfaces and equipment were cleaned with RNAse-Zap (Ambion).

2.2.5.2 cDNA synthesis from RNA

cDNA was synthesised from RNA by using Moloney-Murine Leukaemia Virus Reverse Transcriptase (M-MLV RT [Invitrogen]) according to manufacturer's instructions. 300ng of RNA isolated from cultured cells, 50ng of random primers (Invitrogen), and 1uL of 10mM dNTP mix (Invitrogen) were mixed in a nuclease-free PCR tube (Sarstedt) and made up to 12uL using nuclease-free water (Fisher 72 scientific). Using a thermocycler (Biometra), the mixture was heated to 65°C for 5 minutes, then cooled at 4°C for 5 minutes. After this, 1uL RNaseOUT recombinant ribonuclease inhibitor, 4uL First-strand buffer (5x), 2uL DTT (0.1M) (all Invitrogen) were added to each reaction. Next, an incubation period of 37°C for 2 minutes was

carried out before adding 1uL (200U) if M-MLV RT. The reaction was then incubated for 25°C for 10 minutes, 37°C for 50 minutes, and finally a 15-minute incubation of 70°C. To prepare for qPCR, 180uL if nuclease free water (Fisher 72 Scientific) was added to the reaction and stored at -20°C.

2.2.5.3 Hybridisation chain reaction.

Hybridisation chain reaction was carried out using the ViewRNA™ Cell Plus Assay Kit (Thermofisher) as per the manufacturers instructions. Incubation periods were extended to four hours when used in whole mount gastruloids. During wash steps, 0.1% Triton (Sigma) was supplemented to the PBS + RNAase inhibitor washing buffer.

2.2.6 Embryology

2.2.6.1 Mice maintenance

Mice were bred and housed in the Animal Unit of the Centre for Regenerative Medicine in accordance with the provisions of the Animals Act 1986 (Scientific procedures). All work with live mice was carried out by staff of the Animal Unit.

2.2.6.2 Embryo dissections

Pregnant female mice were culled by cervical dislocation by the Animal Unit staff. The uterus was dissected from the mice and placed into M2 media at RT, whereafter the decidua and Reicherts membrane were removed using forceps. These dissections were performed with a StereoZoom SMZ-U dissection microscope (Nikon) and carried out by Rosa Migueles and myself.

For immediate fixation and imaging, the posterior epiblast portions, from the initial curvature of the trunk to the allantois region, were cut apart using type 12-D scalpels – as described in Figure 2.2a.

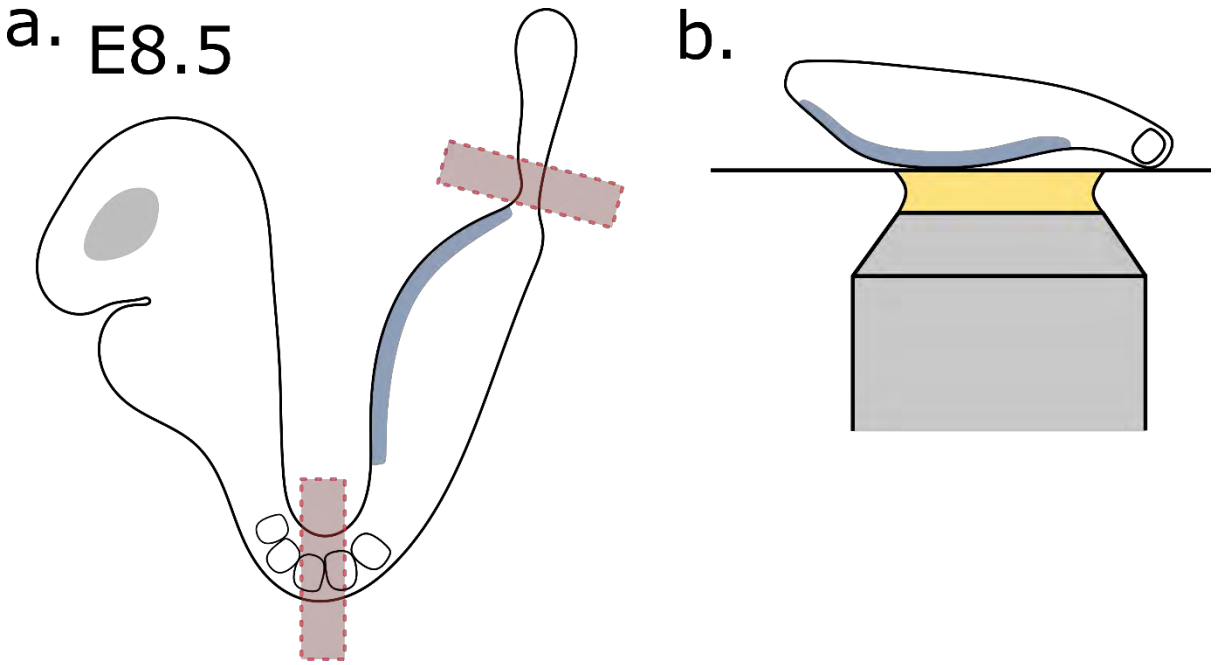

Figure 2.1 E8.5 Mouse embryo dissection and mounting strategy.

a. E8.5 4-6SP embryo indicating cutting zones in red. Blue shaded area indicates dorsal side. b. Illustration of mounting orientation for imaging, such that the epiblast is closest to the microscope objective (in grey with immersion fluid indicated in yellow) and lies as flat as possible perpendicular to the imaging plane.

2.2.6.3 Embryo culture

For embryo culture, the anterior portion up to the beginning of the somites was removed while in M2 media. These were immediately transferred to N2B27 media supplemented with Pen/Strep antibiotics and either 150nM LY411575 or an equal amount of DMSO. These were cultured statically in an incubator at 37°C and 5% CO2 for 12 hours. This process was carried out by Rosa Migueles. After this time the embryos were further dissected (carried out by me), isolating the posterior epiblast as a flat tissue structure (as described Figure 2.2b). The samples were then fixed as described in section x.

2.2.7 Image analysis

2.2.7.1 Nuclear segmentation using Pickcells and NesSys

3D single nuclei segmentation was performed using the Nuclear envelope segmentation system (NesSys) (Blin et al 2019). NesSys segments nuclei based upon nuclear envelope marker and employs a tree-structured ridge-tracing method with a shape ranking training classifier to generate shapes, which are then linked in 3D. LaminB1 or LaminBR were routinely used as the nuclear envelope marker.

Confocal Z-stacks were imported to .tif if image files was under 4GB, or as .ics files if over 4GB. The steps in Pickcells for nuclear ridge segmentation were followed as per the software's pipeline. A new shape classifier was trained and saved per experiment, and segmentation parameters were optimised per experiment based upon the image signal intensity and pixel density. Embryos were segmented and manually edited in separate experiments within the Pickcells software. Gastruloids were segmented using the high throughput pipeline provided in the Pickcells software, the resulting segmentations were visually assessed for accuracy but not manually edited. Before segmentation, the nuclear envelope signal in Gastruloids were manually normalised per experiment in ImageJ using the brightness/contrast function.

2.2.7.2 Calculating Neighbour interactions

Embryo epiblasts were manually isolated within the Pickcells software before neighbour identification. Neighbour identification was carried out by an inbuilt feature of Pickcells, which identifies neighbouring nuclei to each individual nuclei by Delaunay Triangulation.

The edge list for each nuclei and its neighbour was exported to R for analysis.

2.2.7.3 Immunofluorescence normalisation.

Raw values of Mean Signal Intensity per nuclei were exported from Pickcells and manually normalised to each other in R for analysis. Positive control samples or sub-regions of tissues (such as the PSM in embryos or ES cells in vitro) were used to manually align the TF signal.

In Gastruloids and some Embryos that were quantified in BABB, the TF signal was corrected for in Z assuming a loss of 30% signal per 150uM Z depth.

2.2.7.4 Patterning quantification.

Two primary metrics were used in this study to determine heterogeneity. First is the coefficient of variation of TF signal intensity for a nuclei and its neighbours defined as the cell niche ($X = \{x_1, x_2, x_3 \dots x_n\}$), defined as the standard deviation (σ_X) normalised by the mean ($\bar{X}$) as below:

$$CV_X = \frac{\sigma_X}{\bar{X}}$$

Second, the neighbour ratio (NR) was a metric used to describe the ratio of a nuclei's (C) TF expression compared to the average of its neighbouring nuclei (N) defined as below:

$$NR_{(C,N)} = \ln\left(\frac{C}{\bar{N}}\right)$$

2.2.7.5 Epiblast Normalisation

The process for epiblast normalisation is outlined below:

1. The raw XYZ coordinates of an individual embryo epiblast are manually oriented such that the Anterior Posterior axis aligns with the Y axis, such that the epiblast is as close to symmetric and the Z axis is as flat as possible, creating new XYZ coordinates.
2. Each cells position along a principle curve (as measured 0->*n* in uM) in the new YZ plane is using found the slingshot package (Street et al., 2018). This metric is used herein as the anterior-posterior (AP) axis position.
3. Starting from 0, cells +/- 20-30uM (a parameter which can be optimised) along from this AP position are isolated. This is the start of the loop, the AP position will increase in steps of ~5uM (a parameter which can be optimised) and run through to the terminal nuclei of the epiblast.
4. In the XZ plane, each cell's position along the epiblast curve is found using the slingshot package (as measured 0->*n* in uM). This is termed the left/right (LR) position value. The direction of position 0->n along the curve is ensured to orient from left to right.
5. The cells expressing the top 10% levels of T are identified, and the average LR value of these cells is determined as the midline, not any individual cell.
6. The LR midline value is subtracted from all other cell's LR value, in doing so normalising the position of each cell to the midline. Cells to the left of the midline have negative LR values, and to the right positive LR values.
7. After this normalisation, the distance from the midline as a percentage from the epiblast edge is calculated. First, the LR values for cells to the left of the midline are divided by the LR value furthest cell on the left side (identified by containing a negative LR value), and similarly for the right side (identified by containing a positive LR value).
8. This information is stored and loops back to step 3, where the next AP position is +~5uM (a parameter for optimisation) from the previous subset position. The small increase in AP position results in each cell's LR position being calculated multiple times.
9. After the entire AP axis has been run through, the multiple values of LR position and relative LR position for each cell has been calculated, among other metrics. The average of these values from every loop is carried forward.

Next, the process to align multiple epiblasts and normalise the relative LR position is outlined below:

1. First, the AP position of the start of the notochord is manually identified in each epiblast, and the AP position of this is subtracted from each cell's AP value. Such that position ~0 is the start of the notochord.

2. To normalise the length of the primitive streak, each cells new notochord normalised AP value is divided by the posterior most value, creating a relative position along the primitive streak from the Notochord. This relative AP value is carried forward.
3. Next, the LR position is either maintained as L/R or negative values are converted to positive values (indicating left positions), effectively digitally folding at the midline to combine LR sides of the epiblast.
4. Starting from 0, cells from all epiblasts +/- 0.05 relative AP values (a parameter for optimisation) from the starting position (S) are isolated.
5. The relative AP value is normalised to the percentage of cells isolated($C_i = \{AP|\ AP > (S - 0.05)\ OR\ AP < (S + 0.05)\}$ relative to the total number of cells (C_t), calculated by $NAP = AP \cdot (\frac{n(C_i)}{n(C_t)})$
6. Then, the process loops back to step 4, where the AP position is increased by a step of 0.015 (a parameter for optimisation). Again, calculating multiple values of renormalised LR values for each cell. The loop finishes at the posterior most cell's AP position.
7. After the process has run through, the average of the renormalised LR values for each cell are used as the final normalised LR position.

2.2.7.6 Neighbour Smoothing and Neural-NMP-Mesoderm pseudospace

For the Wt E8.5 embryos image analysis, the TF signal for each nuclei was iteratively smoothed by taking the average TF signal of the nuclei and its neighbours. This new average (AvTF+1) was then used in another round, where the average AvTF signal of a nuclei was calculated (AvTF+2). This was repeated 10 times (AvTF+10) for each TF measured to spatially smooth the TF signal. After which, the log(AvTF+10) signal was used as an input for PCA dimension reduction and maintain the Euclidean structure of the TF signal. The pseudospace route from Neural to NMP to Mesoderm was identified using the Slingshot package in this PCA space, along with all cells that are neighbouring a cell in the pseudospace.

The NMP ROI was manually identified, defined as >1.5 and <3.6 pseudospace units (a.u.) and <0.6 normalised X (distance to midline) units (as calculated during the epiblast normalisation process).

2.2.7.7 TF simulation

The TF values in the Wt E8.5 dataset were simulated in R using the rnorm function in the compositions package in R. This function generates random numbers that follows a normal distribution, defined by a standard deviation and mean provided. In this case, the input was calculated by using the standard deviation and mean of a nuclei's TF expression and the TF expression of its neighbours.

2.2.7.8 Colour schemes.

Graphical representation was carried out in the R software (Team, 2021) and base ggplot2 package. The viridis package (Garnier et al., 2021) or scientific colour maps (Crameri, 2018) were used to visualise colour in R. MATLAB was used to display violin SuperPlots (Kenny and Schoen, 2021).

Chapter 3:

Notch gene expression and a pro-mesodermal effect in NMPs.

3.1 Introduction and aims.

In this chapter I set out to explore how Notch is influences NMP cell fate decisions. Unpublished data from the Haston (2018) has shown that inhibiting Notch restricts the fate of NMPs in vivo in chick embryos, and c-Myc has been shown to be controlled by Notch and upregulates Sox2/Fgf signalling in NMPs (Mastromina et al., 2018), but little is known about the role of Notch in mammalian NMPs.

To address this, the aims of this chapter are as follows.

i. Reanalyse published SC-RNAseq datasets to identify notch genes that are expressed in mouse NMPs and the nascent mesoderm within mouse NMP niches. This will indicate which cells might be sending and receiving Notch signals, and which Notch ligands and receptors might be mediating this communication, providing candidate targets for experimentally manipulating Notch in this system.
ii. Determine whether Notch components expressed in vivo are also expressed in cultured mouse and human NMPs and their derivatives, and whether Notch inhibition influences cell fate decisions in these culture systems.
iii. Collect quantitative gene expression data that can be cross-compared between experimental replicates, experimental methodologies, and animal models. The aim is to create a data resource that can, in future work, inform mathematical models that describe neural v mesoderm fate decisions in space and time.

3.2 Results.

3.2.1 SC-RNAseq of mouse in vivo NMPs reveals Notch gene expression is active within NMP niches.

Three published SC- RNAseq datasets of mouse embryos, ranging from E7.5 to E9.5 stages, were re-analysed to identify the presence of Notch component gene expression in NMPs and the nascent mesoderm. The first dataset comes from Gouti et al. (2017),where the authors micro dissected the CLE of a E8.5 and E9.5 embryo before performing SC-RNAseq. This dataset was combined with a second data set containing SC-RNAseq of the micro dissected E8.0 CLE (Dias et al., 2020). The third comes from Pijuan-Sala et al. (2019) who performed SC-RNAseq on entire embryos throughout gastrulation, including E7.5 to E8.5 which were used in this analysis.

A panel of the expression of key NMP markers, such as T, Sox2, Nxk1.2, and Cdx2 expression, from the CLE datasets reconfirms their assessment that these represent putative NMPs (Figure 3.1. a.). Numerous Notch component genes are also expressed, including the Notch receptors Notch1/3, ligands Dll1/3 and Jag1; downstream Hes genes Hes1/7, and Hey1, and limited expression of Fringe genes Lfng, Rfng, and Mfng. All notch components, except Dll1/3 and Rfng, are increasingly expressed as development progresses from E8.0 to E9.5, with most absent at E8.0 (Figure 3.1. a.). Notch2 appears to be widely expressed in all cell types at all stages.

Spearman’s linear correlation and hierarchical clustering for Notch and NMP genes for the E8.5 and E9.5 datasets analysis identifies three main clusters of association (i) Tbx6 associated nascent mesoderm with PSM genes such as Dll1,Dll3, Hes7,

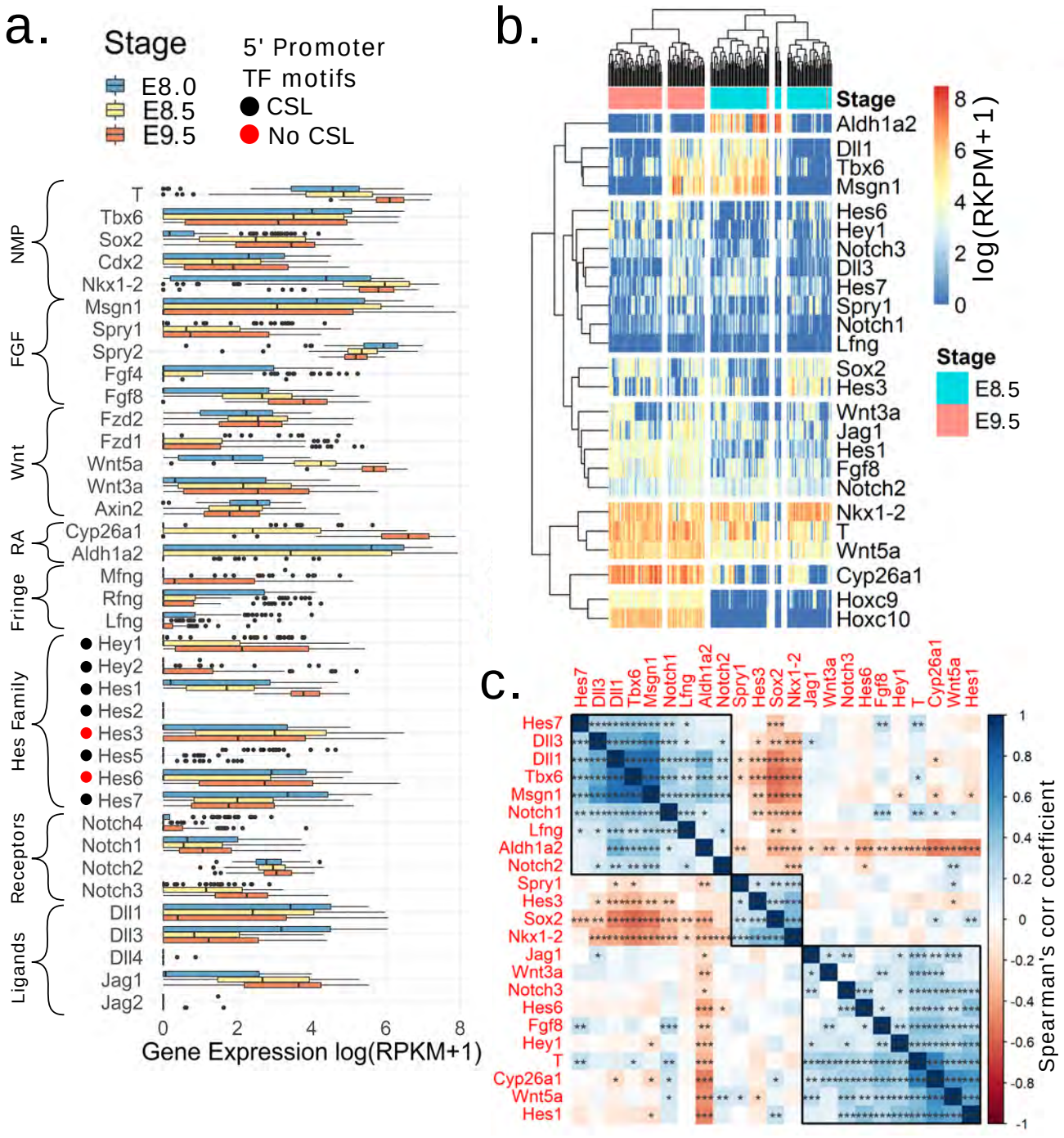
a.
Stage
E8.0
E8.5
E9.5
5' Promoter
TF motifs
CSL
No CSL
NMP
FGF
Wnt
RA
Fringe
Hes Family
Receptors
Ligands
T
Tbx6
Sox2
Cdx2
Nkx1-2
Msgn1
Spry1
Spry2
Fgf4
Fgf8
Fzd2
Fzd1
Wnt5a
Wnt3a
Axin2
Cyp26a1
Aldh1a2
Mfng
Rfng
Lfng
Hey1
Hey2
Hes1
Hes2
Hes3
Hes5
Hes6
Hes7
Notch4
Notch1
Notch2
Notch3
Dll1
Dll3
Dll4
Jag1
Jag2
0
2
4
6
8
Gene Expression log(RKPM+1)
b.
Stage
Aldh1a2
Dll1
Tbx6
Msgn1
Hes6
Hey1
Notch3
Dll3
Hes7
Spry1
Notch1
Lfng
Sox2
Hes3
Wnt3a
Jag1
Hes1
Fgf8
Notch2
Nkx1-2
T
Wnt5a
Cyp26a1
Hoxc9
Hoxc10
8
6
4
2
0
log(RKPM+1)
Stage
E8.5
E9.5
c.
Hes7
Dll3
Dll1
Tbx6
Msgn1
Notch1
Lfng
Aldh1a2
Notch2
Spry1
Hes3
Sox2
Nkx1-2
Jag1
Wnt3a
Notch3
Hes6
Fgf8
Hey1
T
Cyp26a1
Wnt5a
Hes1
1
0.8
0.6
0.4
0.2
0
-0.2
-0.4
-0.6
-0.8
-1
Spearman's corr coefficient

Figure 3.1 SC-RNAseq identifies many Notch component and downstream Hes genes expressed in the E8.0, E8.5, and E9.5 CLE.

Dataset for this figure from Gouti et al. (2017) and Dias et al. (2020), normalisation to RPKM performed by authors of Dias et al. (2020). a. Boxplots of log(RPKM+1) for NMP markers and Notch genes. Black dots represent outliers, defined as values >[75th percentile + 1.5*(interquartile range)] or <[25th percentile - 1.5*(interquartile range)]. After combining the E8.5 and E9.5 dataset only, (b.) gene expression hierarchical clustering and (c.) correlation analysis by linear Spearman's rank correlation coefficient and hierarchical clustering identifies a Tbx6+ PSM-like profile, a Sox2+ Neural profile, and a novel T+ Wnt/Notch/FGF profile within the NMP population.

Notch1, Rfng Lfng (ii) Sox2 associated cluster with Nkx1.2, Mfng and unexpectedly (iii) a T associated Wnt and Notch cluster, associated with Jag1, Wnt3a, Hes1 and Hey1 (Fig1.1. b,c). Cluster (i) and (ii) anticorrelate, but (iii) does not correlate or anticorrelate with either cluster (Figure 3.1. c). Components of the two other smaller clusters of (iv) Notch3, Fzd2, Hes6 and (v) Fgf8, Axin2, and Cyp26a1 partially positively correlate with the T associated cluster (iii), namely Fgf8, Notch3, and Cyp26a1. Overall suggesting extensive Notch expression within NMPs, not just the PS.

For the whole embryo dataset, due to the entire embryos being sequenced and the loss of spatial context, NMPs and the nascent mesoderm require sub-setting based on *a priori* knowledge of TF identity. Based on the gene expression profile from the Gouti Diaz data set, NMPs were defined as T+/Sox2+/Nkx1.2+/Tbx6-, and the nascent mesoderm within the NMP niche found defined as T+/Tbx6+/Nkx1.2+ (Figure 3.2.a.). The nascent mesoderm was included in this dataset for analysis as some cells in the CLE expressed Tbx6 (Figure 3.1. a.)(Javali et al., 2017). This whole embryo dataset provides many more cells (1642 NMPs and 2321 nascent mesoderm total) compared to the CLE datasets (248 total), with at least three embryos per stage.

In the NMPs and Nascent-mesoderm subsets, most notch components and Hes genes directly controlled by Notch are not as highly expressed compared to the CLE dataset (Figure 3.2.a.). Hes7 is highly expressed in NMPs and the nascent mesoderm, but Hes5 and Hey1 are not as highly expressed compared to the CLE dataset. Only small subsets of cells express the Notch receptors and ligands previously identified. Although the expression is lower here than in the CLE dataset, again Notch components are increasingly expressed from E7.5 to E8.5, with only Hes7 expressed before E8.5 (Figure 3.2.a.). Hes5 is expressed in a subset of cells in the E8.5 stage, but was absent in the CLE dataset (Figure 3.1.a.). Spearman's correlation analysis of the E8.5 stage embryos recapitulates the anticorrelating Tbx6/Dll1/Dll3/Notch1/Hes7 nascent mesoderm and Sox2/Nkx1.2 cluster from the Gouti Diaz dataset, but the T/Jag1 cluster is absent and T correlates with the nascent mesoderm cluster.

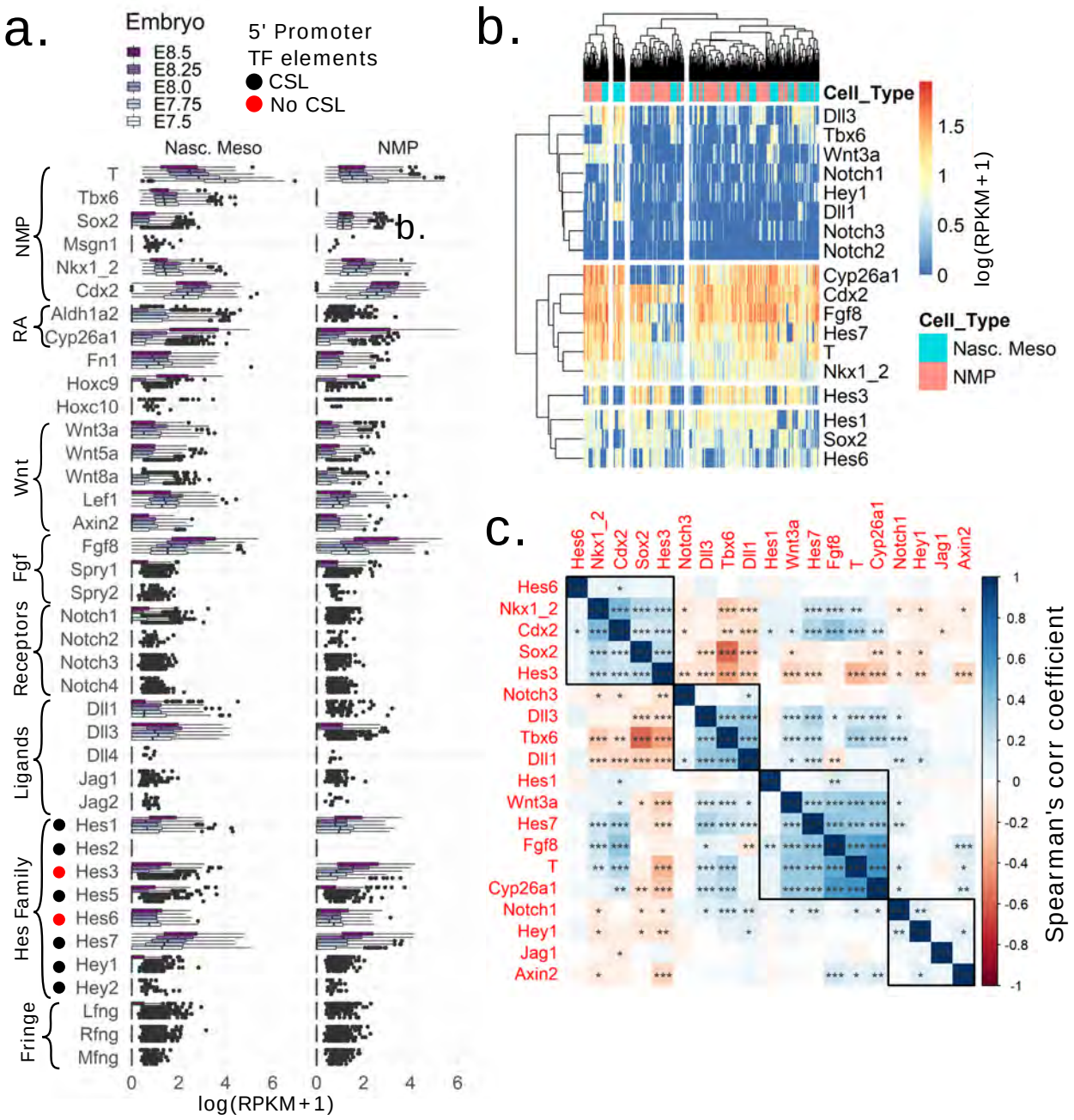

Figure 3.2 SC-RNAseq of E7.5 to E8.5 NMPs and nascent mesoderm identifies Notch component and downstream Hes genes.

Dataset for this figure from (Pijuan-Sala et al., 2019), normalisation to RPKM performed by the authors. a. Boxplots of NMP markers and Notch genes in NMPs and Nascent mesoderm subsets. Black dots represent outliers, defined as values >[75th percentile + 1.5*(interquartile range)] or <[25th percentile - 1.5*(interquartile range)]. b. E8.0 to E8.5 embryo hierarchical clustering of gene expression. c. Spearman's rank correlation coefficient correlation analysis by and hierarchical clustering identifies a Tbx6+ PSM-like profile, a Sox2+ Neural profile, but no novel T+ Wnt/Notch/FGF profile for the E8.5 embryo set.

Overall, many Notch component and downstream target genes are expressed in NMPs. This includes a PSM like expression profile in Tbx6+ cells that are present in NMPs niches from E7.5 to E9.5, but from E8.5 to E9.5 a novel set of Wnt/Notch/FGF correlated genes emerges, namely the T/Wnt3a/Jag1 identified in the CLE dataset. Further, Hes genes Hes3 and Hes6 that interact with Notch components but are not directly controlled via NICD RBP-J are also expressed. Taken together, this suggesting that NMPs and nascent mesoderm cells are receiving Notch signals and can signal to each other via Notch. Supporting the hypothesis that Notch signalling is involved in the NMP to mesoderm cell fate decision, but the exact mechanism remains unclear.

3.2.2 Notch inhibition reduces T/Tbx6 and increases Sox2 expression *in vivo*.

Having shown that Notch components are expressed in mouse embryos and associated with NMP markers, I next asked whether Notch inhibition influences differentiation of NMPs in vivo.

To answer this question, embryos were dissected at the 4-6 somite pair (SP) E8.5 stage and statically cultured for 12 hours in serum-free media (N2B27) with the gamma-secretase inhibitor LY (an inhibitor of Notch activation) or DMSO control with three embryos per condition (embryo dissection and transfer to culture media was carried out by Rosa Migueles). The time frame of 12h was selected because this was sufficient to allow gene expression changes (explored by live imaging of T/Sox2 during Notch or Wnt inhibition in gastruloids – data not shown), but without the dramatic tissue morphology changes expected during embryo turning and tailbud formation at E9-10. To minimise the total tissue amount and prevent diluting of the inhibitor, the head portion of the embryo at the first somite was removed, leaving the rest of the somites present (Figure 3.3.a). The embryos were fixed and immunohistochemistry was performed to label the NMP fate markers Sox2, T, Tbx6, and LaminB1 (Figure 3.3.c.). Embryos were imaged and then segmented in 3D, using Pickcells and the nuclear envelope marker LaminB1, where the TF expression for each nuclei was quantified and nuclei in the epiblast were manually labelled.

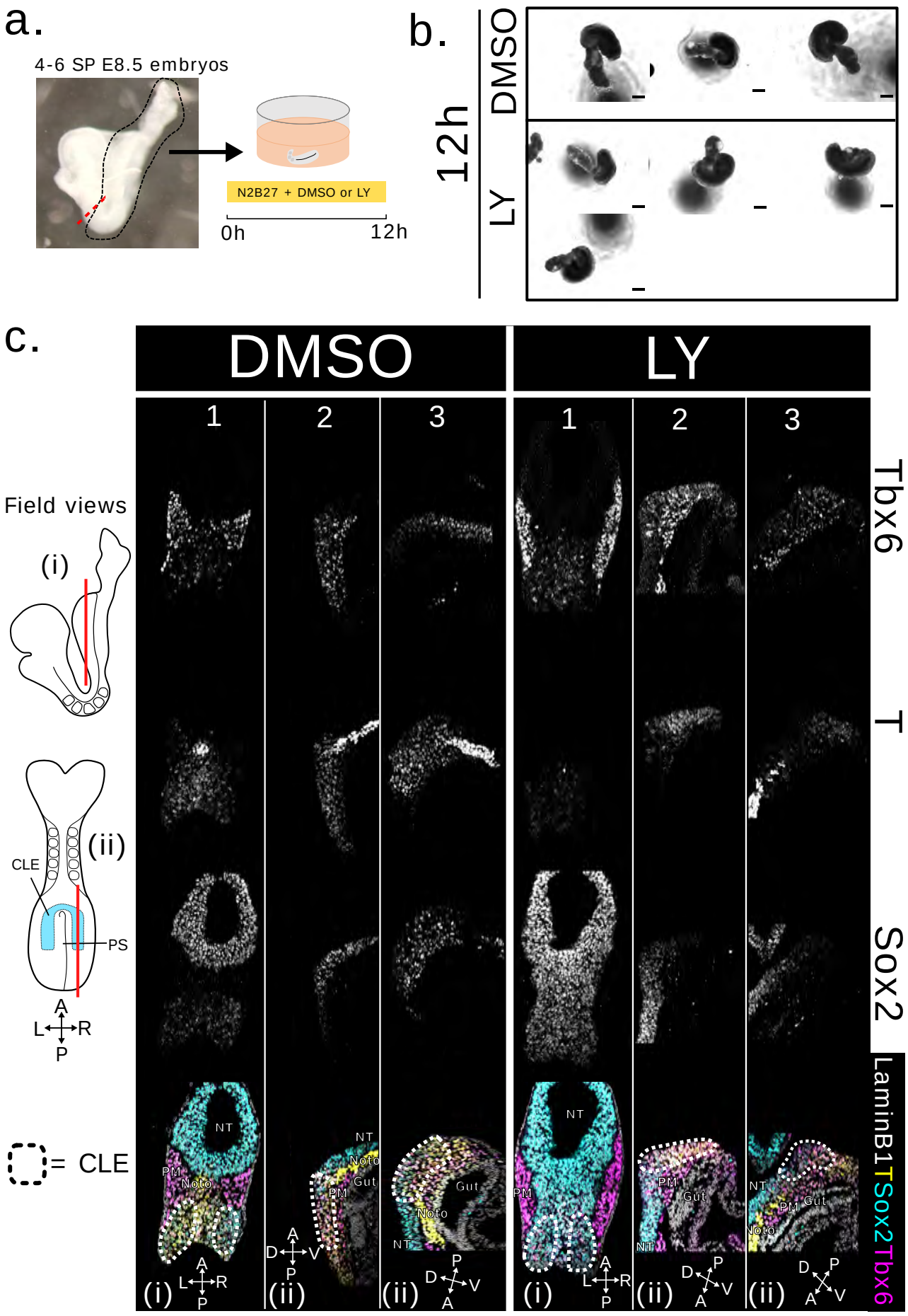
a.
4-6 SP E8.5 embryos
N2B27 + DMSO or LY
0h
12h
b.
12h
DMSO
LY
c.
DMSO
LY
1
2
3
Field views
(i)
(ii)
CLE
PS
A
L
R
P
= CLE
Tbx6
T
Sox2
LaminB1TSox2Tbx6
NT
PM
Noto
Gut
D
V

Figure 3.3 Notch inhibition affects NMP gene regulatory network with a pro-neural effect.

a. Graphic demonstrating the isolation of posterior portions of 4-6 somite pair (SP) embryos and the culture conditions DMSO or LY 150nM in N2B27. b. Bright field images of the dissected posterior embryos portions after 12-hour culture showing similar gross morphologies. c. Graphic showing views of IF panel of confocal microscopy in cultured embryos, red line indicates the optical slice through the tissue axis, where (i) the field is showing a the left (L) to right (R) in X and anterior (A) to posterior (P) in Y. In (ii) the field is a dorsal (D) to ventral (D) slice through the caudal lateral epiblast. The caudal lateral epiblast is outlined by the dashed white lines. Tissue structures Notochord (Noto), the neural tube (NT), the paraxial mesoderm (PM), and hind gut (gut) are marked. The confocal images of the NMP niche stained for T, Sox2 and Tbx6 in three embryos per condition DMSO or LY. Scale bars indicate 100um.

All embryos, whether treated with LY or with DMSO control, appeared to develop broadly normally as the structures expected in a ~E9.0 embryo, such as the epiblast, primitive streak, hind gut, notochord, closing neural tube folds, and presomitic mesoderm are present with a normal morphology and TF expression (Figure 3.3.b). The caudal ends of the embryos appear to begin folding (Figure 3.3.b,c.) as expected of an embryo at ~E9.0. During the 12-hour period, 6 more somites would be expected. Although it was not clear how many extra somites were formed during the culture period in this experiment.

To evaluate changes in TF expression following Notch inhibition, first a visual comparison of one z slice for each raw image showing the epiblast, including CLE, indicates that the LY-treated embryos exhibit a decrease in T and Tbx6 with an increase in Sox2 within NMP associated regions after Notch inhibition, compared with DMSO-treated controls (Figure 3.3.c.). As identified by Javali et al. (2017) and the RNA-seq datasets, Tbx6 expression exists in the CLE with low Sox2 and low Tbx6 expression (see previous section).

Next, I sought to quantitatively assess this question. NMPs are generally defined as T+/Sox2+, to isolate NMPs in this analysis +/- gates for TF expression were manually set using values from nuclei in the entire image, including regions used as TF-ve controls such as the PSM and gut endoderm. However, doing so with this dataset shows very few nuclei in the epiblast are Sox2- (Figure 3.4.a). As such, it is likely using T+/Sox2+ gating in this dataset des not isolate the NMP niche and includes cells outside the bipotent CLE. How to isolate the NMP and surrounding niche for analysis will be addressed in later chapters, for this analysis T+/Sox2+ gates are used define posterior epiblast/NMPs and a T+/Sox2+/Tbx6+ or Tbx6+ only TF gate for the nascent mesoderm.

Using T+/Sox2+ gates, a significant increase in Sox2 expression and a decrease in T expression was measured for T+/Sox2+ cells in the LY treated epiblast compared to the DMSO control (Figure 3.4.b). A significant reduction in Tbx6 expression was measured for Tbx6+ cells in the epiblast, but not in T+/Sox2+/Tbx6+ cells (Figure 3.4.b). Indicating Notch signalling has a pro-NMP and pro-mesodermal effect.

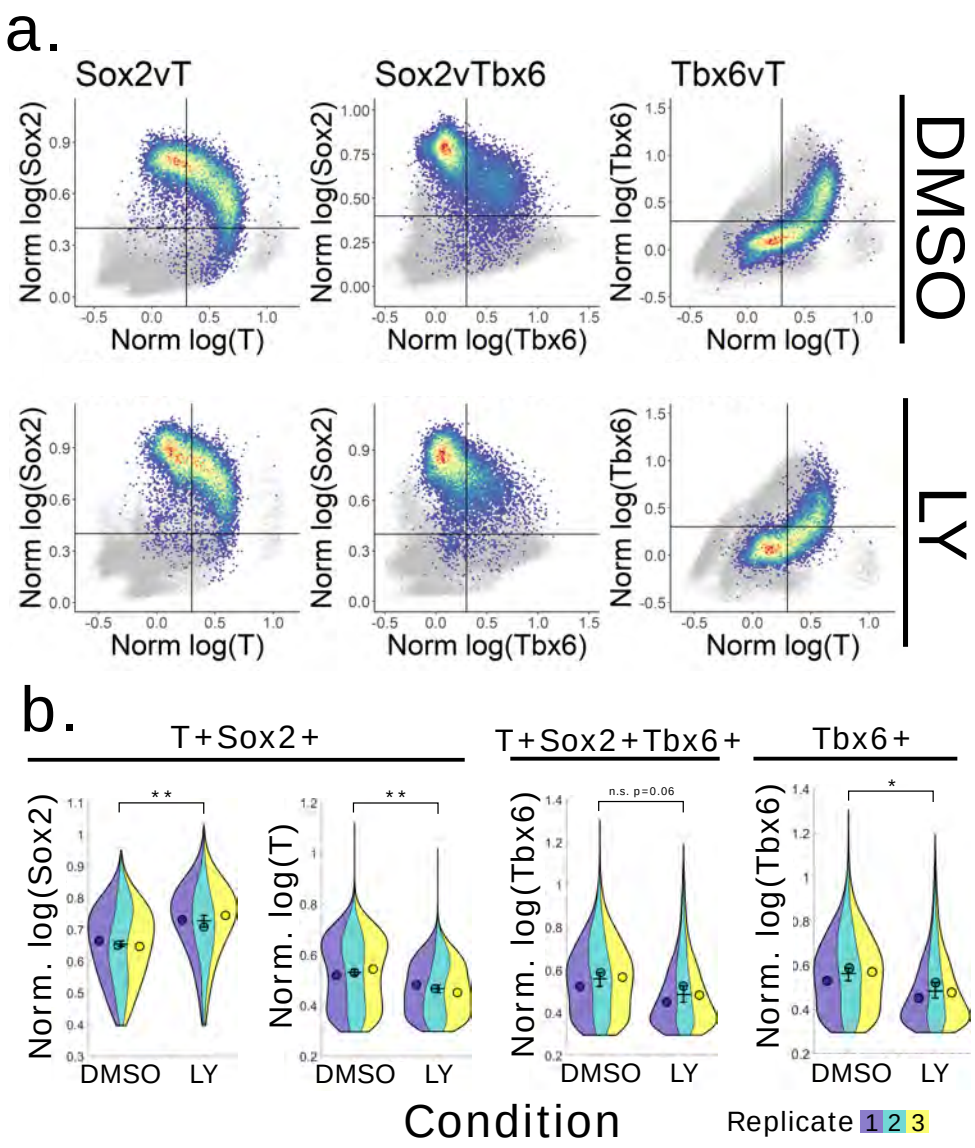

Figure 3.4 Quantification of Notch inhibition in cultured embryos.

Quantification of single cell TF signal intensities via Pickcells. a. Displayed as pairwise density plots of normalised TF intensity between DMSO and LY conditions, also showing defined differentiation paths in state space. Density plots show the subset of epiblast cells over the non-epiblast cells (grey). b. Comparison of DMSO vs LY treatments with Violin SuperPlots (Kenny and Schoen, 2021) shows a significant reduction in T expression, a significant increase in Sox2 in T+Sox2+ cells, a Tbx6 in Tbx6+ cells ($p<0.01$), but no significant decrease in Tbx6 in Sox2+T+Tbx6+ cells. Tests were performed on log(Raw TF) and statistical test completed by one way ANOVA. ***=$p<0.001$, ** = $p<0.01$, *=$p<0.05$. Error bars show standard error. N=3.

Interestingly, clear paths in TF expression state space between neural, NMP, and mesoderm cell states can be observed in the Sox2, T, Tbx6 density plots (Figure 3.4.a). Much of the state space is underoccupied compared to these regions. Indicating a high degree of regulation for TF identity in the epiblast.

Overall, this indicates that Notch signalling supports T and Tbx6 expression and inhibits Sox2 expression in the epiblast, and that cell identity by TF expression in the embryo is highly controlled and guided along a narrow path from neural to NMP and mesoderm.

3.2.3 EpiSC to NMP differentiation is highly heterogeneous.

To further investigate the role of Notch regulation in the NM decision in mouse NMPs, *in vitro* models were explored.

Mouse NMP-like cell (NMP-LC) can be differentiated from EpiSCs. I performed the differentiation protocol, as reported by Gouti et al. (2014), by culturing EpiSC in N2B27 supplemented with bFGF and CHIR on Fibronectin coated plates for 48 hours (Figure 3.5a). Despite considerable attempts at optimisation, I consistently observed a significant number of cells and colonies lifted during the washing steps after PFA fixation (data not shown). It was not clear whether this was a particular subset of cells that did not bind efficiently to Fibronectin, or if it was a sporadic detachment of all cell types in the culture. Because of this, I used Matrigel for subsequent experiments to increase cell adhesion. This successfully prevented cell lifting.

After differentiating EpiSCs to NMP-LCs and performing immunohistochemistry to label T and Sox2, considerable heterogeneity in colony morphology, size, and Sox2/T expression can be observed (Figure 3.5.b.). Many colonies contained Sox2/T double positive cells, however many colonies, and portions of colonies, are single positive for either Sox2 or T. Further, a substantial proportion of the population appear to be negative for Sox2 and T, and these were located both in the 3D aggregates and less dense flat sheets of cells. It was common for some biological replicates to fail to produce NMPs and produce single positive cells only (Figure

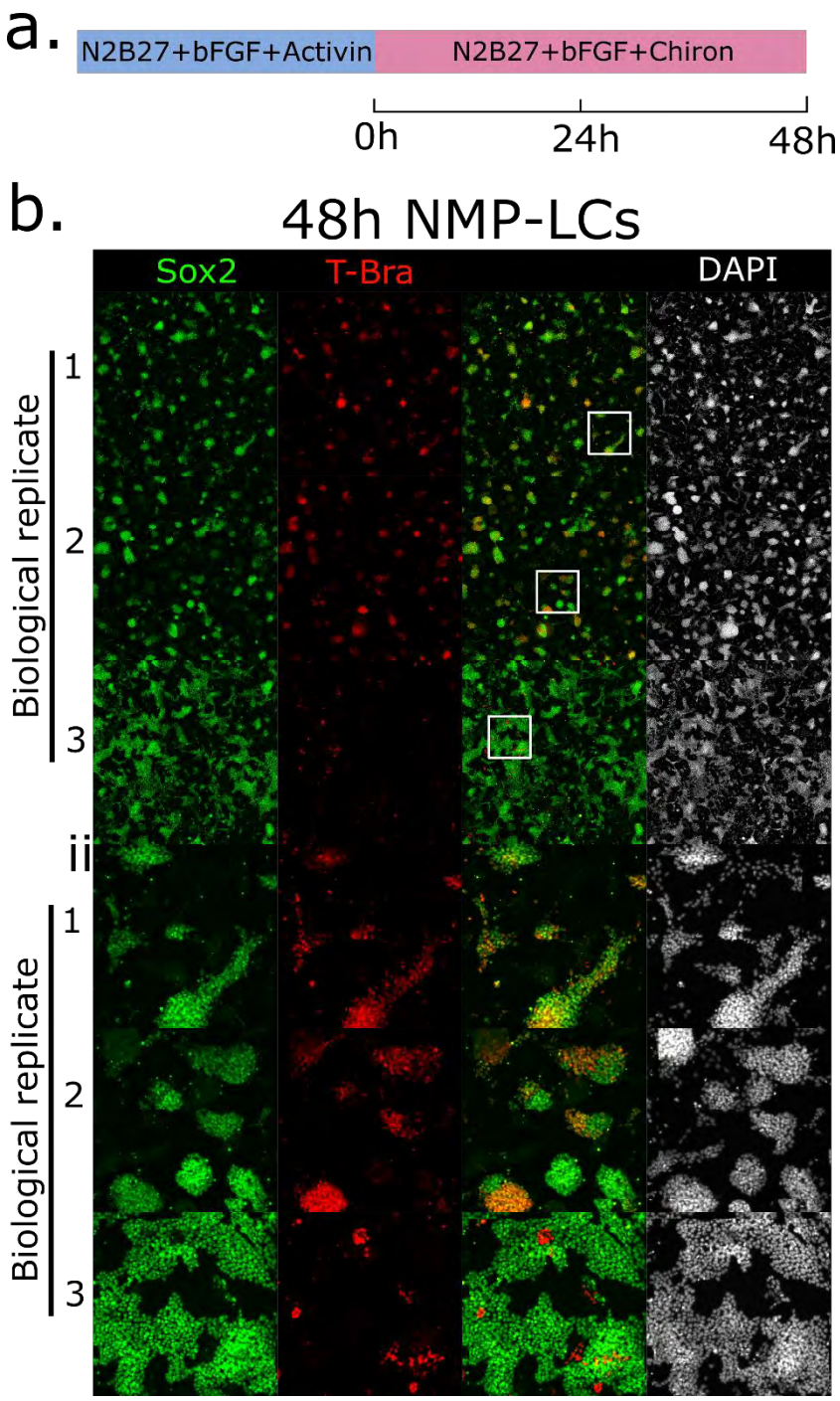

Figure 3.5 High variability in T, Sox2, and colony size and morphology in EpiSC to NMP-LC differentiation.

a. Graphic of culture conditions as described in Gouti et al. (2014). b. Brightfield IF of Sox2 and T in NMP-LCs with DAPI for three biological replicates, showing presence of T+Sox2+ cells, but significant heterogeneity in colony size and morphology (ii) was observed with (i) many cells and colonies of T-Sox2-. (ii) are magnified views corresponding to the white rectangle inset in (i).

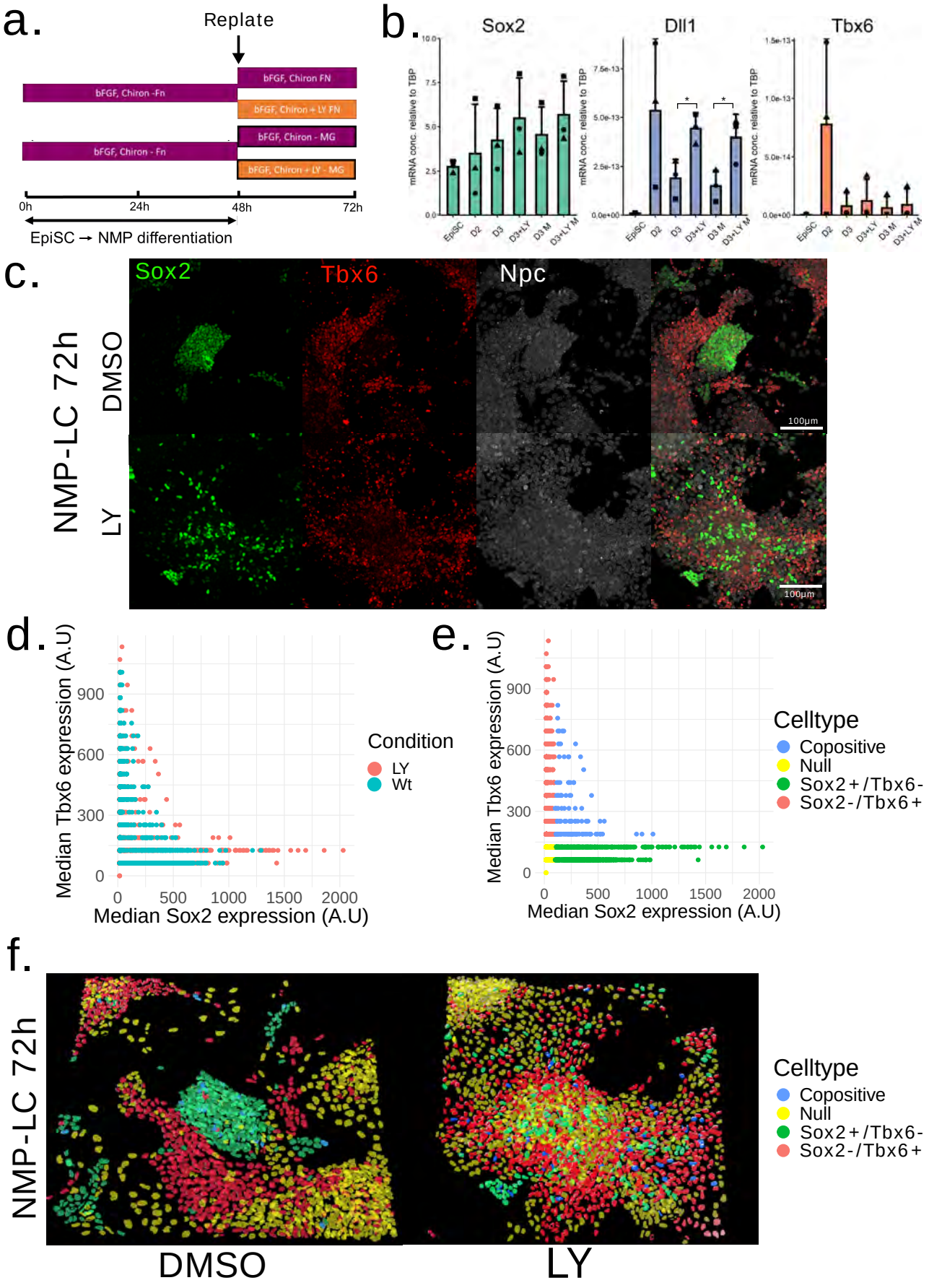
a.
Replate
bFGF, Chiron -Fn
bFGF, Chiron FN
bFGF, Chiron + LY FN
bFGF, Chiron - Fn
bFGF, Chiron - MG
bFGF, Chiron + LY - MG
0h
24h
48h
72h
EpiSC → NMP differentiation
b.
Sox2
Dll1
Tbx6
mRNA conc. relative to TBP
EpiSC
D2
D3
D3+LY
D3 M
D3+LY M
c.
Sox2
Tbx6
Npc
NMP-LC 72h
DMSO
LY
100µm
d.
Median Tbx6 expression (A.U)
Median Sox2 expression (A.U)
Condition
LY
Wt
e.
Median Tbx6 expression (A.U)
Median Sox2 expression (A.U)
Celltype
Copositive
Null
Sox2+/Tbx6-
Sox2-/Tbx6+
f.
NMP-LC 72h
DMSO
LY
Celltype
Copositive
Null
Sox2+/Tbx6-
Sox2-/Tbx6+

Figure 3.6 Notch inhibition in NMP-LCs increases Dll1 expression but many non-epiblast Tbx6-Sox2- cells exist.

a. Graphic showing culture conditions of mEpiSCs to mNMP-LCs and replating at 48 hours into DMSO or LY supplemented media for 24 hours. Cells were also plated onto Fibronectin or Matrigel. b. qRT-PCR analysis of Sox2, Tbx6 and Dll1 after notch inhibition with a significant increase in Dll1 in the Notch inhibited condition ($p<0.05$) in Matrigel and Fibronectin coated wells, there was no significant difference in Sox2, Tbx6 in DMSO or LY. No significant difference in any genes was found between Matrigel and Fibronectin. c. Confocal IF of Sox2 and Tbx6 in mNMP-LCs at after 24 hours of LY Notch inhibited and a DMSO control. The spatial patterning is variable with many Sox2-Tbx6- cells appear visible. This is confirmed after quantification (d.) and +/- gating (e.) in Pickcells, where many Tbx6-Sox2- (null-yellow) cells can be seen in a 3D render of the image. Render was performed in Pickcells. Error bars show standard deviation. ***=$p<0.001$** = $p<0.01$, *=$p<0.05$.

3.5.b.ii). When double positive Sox2/T cells did appear, they tended to locate primarily in 3D colonies, which limits the extent of single cell resolution to address the balance of cell fate decisions. Confocal image acquisition quality high enough to resolve single cells in dense cultures limits the speed of acquisition, which results in fewer fields that can be acquired in an acceptable timeframe.

3.2.4 Notch inhibition of EpiSC derived NMP-LCs has limited effect on NM fate decision.

Despite the heterogeneity in EpiSC to NMP-LC differentiation, I attempted to use this culture system investigate how Notch regulates the neural vs mesoderm fate and other Notch components. If Notch negatively regulates Notch components in NMPs this may indicate lateral inhibition.

NMP-LCs were cultured on Fibronectin and after the 48 hour differentiation, then to facilitate NMP-LC adhesion for fixing as previously described, the cells were re-plated onto Matrigel. As a control, NMP-LCs were also plated onto fibronectin in line with established protocols (Gouti et al., 2014, Tsakiridis and Wilson, 2015). After replating, the NMP-LCs were treated with LY or a DMSO control for a further 24 hours (Figure 3.6.a). After this period, total RNA was collected and qPCR was performed to quantify the changes in gene expression of fate markers and Notch components. No significant effect in any gene studied occurred between the Fibronectin and Matrigel cultures.

No significant effect was observed on fate markers Sox2 or Tbx6 gene expression after Notch inhibition (Figure 3.6.b). I next examined expression of the Notch ligand Dll1, which is a marker or early mesoderm that associates with Tbx6 and is commonly negatively regulated in lateral inhibition. Dll1 is expressed in NMP-LCs and is significantly upregulated during from EpiSC to NMP-LC differentiation at D3, in both Fibronectin and Matrigel coated wells, after Notch inhibition (Figure 3.6.b). Although the levels of gene expression are very low compared to other genes. This indicates that Notch signalling has a negative regulatory effect on Dll1 but is upregulated by other signalling pathways.

High variation in gene expression was observed for all genes and conditions in NMP-LCs compared to EpiSCs, reflecting the earlier observation of heterogeneity between replicates ((Figure 3.6.b). These results do not support a clear effect of the Notch inhibitor on NMP differentiation markers but indicate Notch signalling negatively regulates Dll1 expression in the nascent mesoderm. High variation was observed between replicates, which could mask the effects of Notch inhibition, making these data difficult to interpret.

To obtain higher resolution data, I developed a pipeline to quantify protein content of marker transcription factors at the single cell level. Again, NMP-LCs were differentiated from EpiSC and replated at 48 hours into media supplemented with LY or DMSO (Figure 3.6.a). After a 24 hour period, immunochemistry labelling and imaging of Sox2 and Tbx6 was performed to establish neural vs mesoderm identity, with Nuclear pore complex (NPC) labelling for nuclear segmentation (Figure 3.6.c). Single cell segmentation and nuclear TF content quantification was carried out in Pickcells.

After quantifying gene expression and gating into +/- bins (Figure 3.6.d,e), a large proportion of the fields shown are Tbx6-Sox2- (Figure 3.6.e,f.), it is not clear what cell type these double negative cell types are. This observation suggest that large numbers of fields would need to be examined to characterise the relatively rare Tbx6+ and Sox2+ cells. Furthermore, visual comparison raw images of DMSO and LY conditions indicates that there is considerable heterogeneity in the numbers of Sox2+ and Tbx6+ cells between different regions of the culture(Figure 3.6.f), again indicating that large numbers of images would need to be analysed in order to extract any true differences between experimental conditions . These observations, taken together with the time-consuming nature of imaging, segmentation and quantification, let me to the conclusion that this experimental system is not tractable for obtaining interpretable quantitative data.

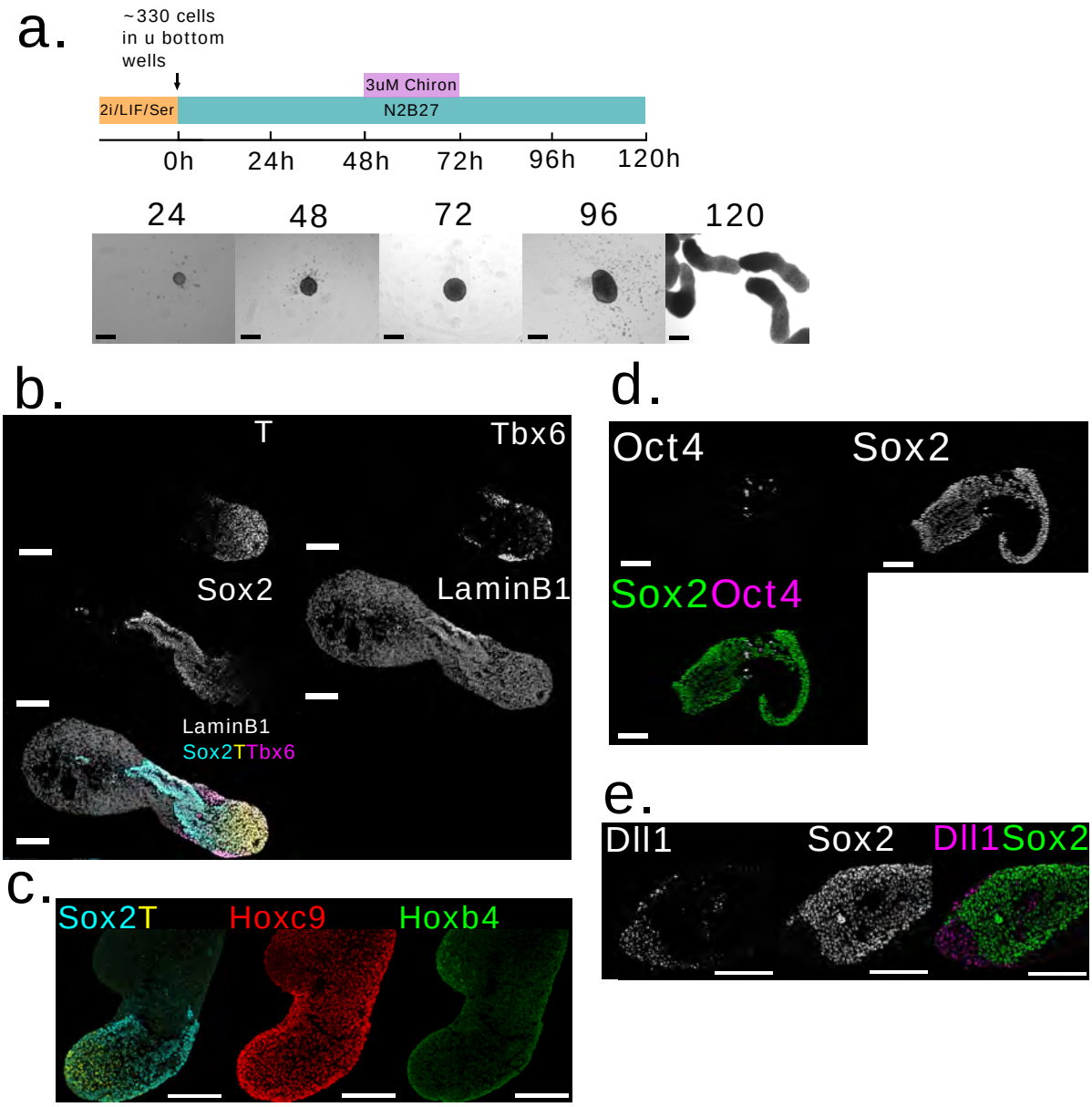

Figure 3.7 Characterisation of mouse gastruloids.

a. Protocol of mouse gastruloid culture (van den Brink et al., 2020) and representative brightfield images of gastruloids during culture stages. Confocal imaging of gastruloids with a panel of NMP markers. IF shows the “posterior” tips coexpress T and Sox2 with intermittent Tbx6 (b,c,e). Also, by IF the posterior tips are Hoxc9+ve (c.) and Oct4-ve (d.). Hybridisation chain reaction of mRNA transcripts show Dll1 is expressed in the posterior tips adjacent to Sox2+ cells (e). All scale bars indicate 100um.

3.2.5 Notch inhibition reduces mesoderm differentiation and NMP maintenance in mouse gastruloids.

Having established that monolayer cultures are not a suitable model system to test the effects of Notch inhibition, I sought an alternative in-vitro system that would overcome this problem. Gastruloids are 3D cultures of pluripotent cells differentiating to posterior cells including NMPs and their derivatives, which self-organise and extend along an “anterior” to “posterior” axis. Gastruloids have been reported to reproducibly acquire NMP-LC states capable of self-maintenance and expansion (Van den Brink et al., 2014, van den Brink et al., 2020), and are amenable to pharmacological manipulation. They therefore seemed a promising experimental system to test the effects of Notch inhibition on NMP TF expression.

I first set out to characterise NMP populations within gastruloids. Gastruloid culture was performed as previously described (van den Brink et al., 2020), outlined in (Figure 3.7.a), where ~300-330 cells from a 2i/LIF/serum culture were deposited into a u-bottomed well and left to aggregate. After 48 hours, the clusters were treated with a 24-hour CHIR pulse, after which CHIR was withdrawn, and the clusters spontaneously polarise and extend along an axis from the established pole.

To confirm the presence of putative NMPs, gastruloids were immunolabelled with select markers (Figure 3.7b,c,d,e). Gastruloids were confirmed to contain a large region of Sox2+/T+ cells with intermittent Tbx6+ cells on the ‘caudal’ extending end (Figure 3.7.b.). The gastruloids were Oct4-ve, aside from a small population of cells within the ‘anterior’ domain (Figure 3.7.d.). The Sox2/T positive cells, with the majority of the gastruloid axis, were confirmed to be Hoxb4 negative and Hoxc9 positive and so have acquired a trunk identity (Figure 3.7.c).

I next examined the expression of Notch components within gastruloids. The expression of Dll1 was observed by hybridisation chain reaction, identifying domains of Dll1 expression within and adjacent to Sox2- regions (Figure 3.7.e). Indicating Notch ligands are not limited to and are adjacent to the NMP niche (Figure 3.8).

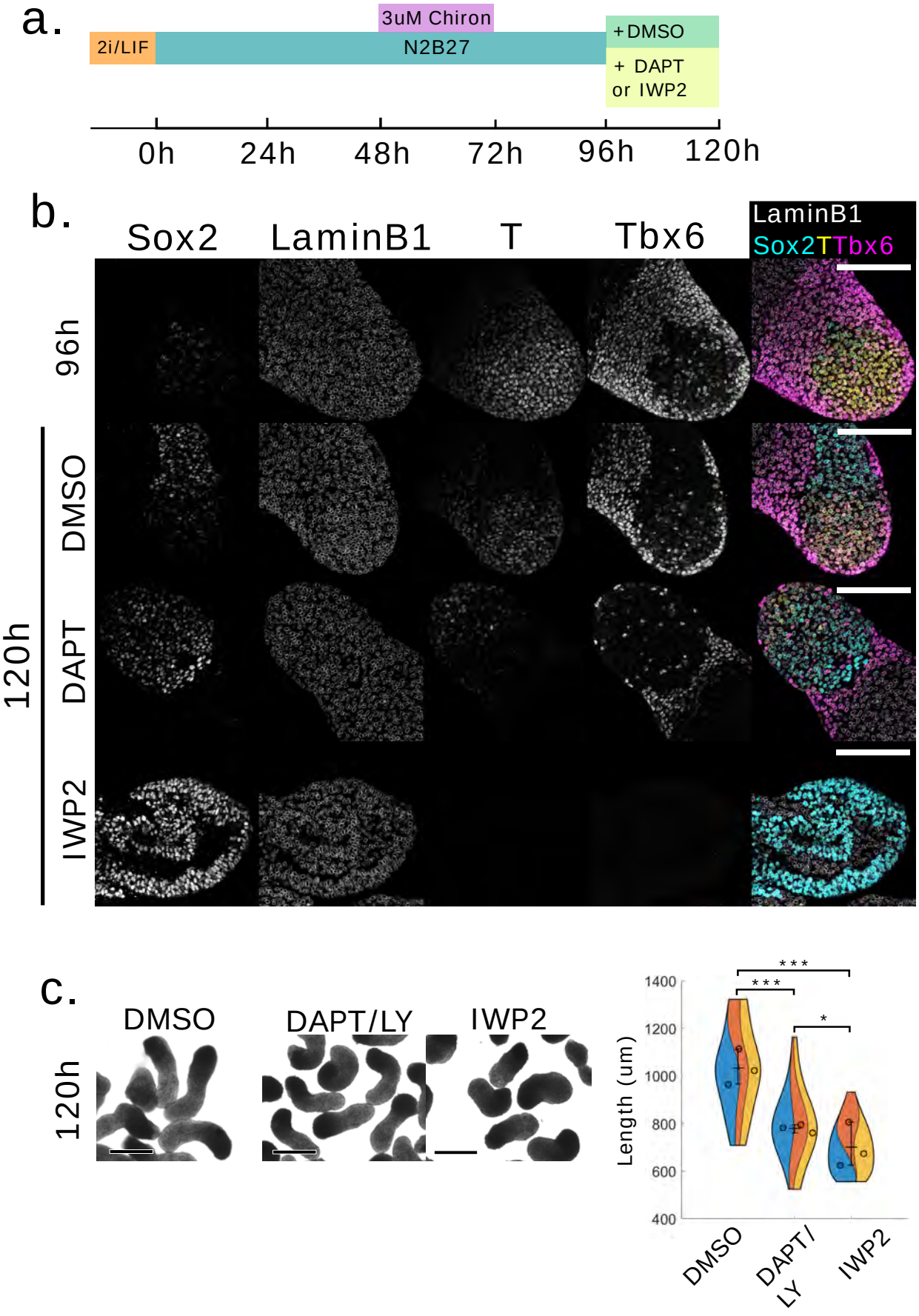
a.
3uM Chiron
2i/LIF
N2B27
+DMSO
+ DAPT
or IWP2
0h
24h
48h
72h
96h
120h
b.
Sox2
LaminB1
T
Tbx6
LaminB1
Sox2TTbx6
96h
120h
DMSO
DAPT
IWP2
c.
120h
DMSO
DAPT/LY
IWP2
Length (um)
1400
1200
1000
800
600
400
***
***
*
DMSO
DAPT/
LY
IWP2

Figure 3.8 Notch inhibition of gastruloids has a pro-neural effect and inhibits elongation.

a. Gastruloid culture protocol of Notch and Wnt inhibition. LY, IWP2 or DMSO is added at 96 hours, when NMPs emerge, for 24 hours. b. Representative confocal images showing the “posterior” end of gastruloids from each condition, IF stained Sox2, T, Tbx6 and a nuclear marker LaminB1 used for 3D segmentation in PickCells. Scale bars indicate 100um. c. Representative brightfield images of 120h gastruloids in each condition, and quantification of gastruloid length shown by Violin SuperPlots (Kenny and Schoen, 2021) displaying distributions of separate biological replicates (represented by colour) and mean per replicate. n=3, technical replicates ~10 gastruloids per biological replicate. A significant decrease in the mean length per replicate after Notch or Wnt inhibition, and Wnt inhibition resulted in shorter gastruloids than Notch inhibited was measured. Statistical significance performed using multiple comparison Tukey HSD test. Error bars show standard error. Tests were performed on normalised TF values and statistical test completed by one way ANOVA. ***=$p<0.001$, ** = $p<0.01$, *=$p<0.05$. Scale bars indicate 500um.

I next investigated how Notch signalling regulates NM cell fate decision in mouse gastruloids, using the gamma secretase inhibitor DAPT to inhibit the Notch pathway. To confirm that gastruloids are a suitable experimental model for testing the effects of signalling-pathway-manipulation on NMP differentiation, I performed parallel experiments using the Wnt inhibitor IWP2. Wnt is known to contribute to the maintenance of NMP self-renewal and to promote differentiation into mesodermal fates at the expense of neural fates (Tsakiridis et al., 2014), inhibiting Wnt presents an ideal positive control for mesoderm and NMP identity inhibition. Gastruloids were allowed to develop for 96 hours, to the point at which NMPs are established (van den Brink et al., 2020), and then treated with DAPT, IWP2, or an equal amount of DMSO for 24 hours (Figure 3.8.a.). Notch or Wnt inhibition both result in a significant reduction in gastruloid length, with Wnt inhibition producing a more severe phenotype (Figure 3.8.c). Indicating Wnt or Notch inhibition reduces elongation perhaps via reduced proliferation or altered tissue architecture.

As expected, immunofluorescence labelling of Sox2, T, Tbx6 shows inhibiting Wnt via IWP2 abolished NMP and mesoderm identity with little or no Tbx6 or T expression observed after the 24-hour period (Figure 3.8.b), and the remaining cells are either Sox2+ or Tbx6-T-Sox2-. This which is confirmed by single cell segmentation and quantification (Figure 3.9.c).

Recapitulating the *ex vivo* experiment, Notch inhibition reduces T and Tbx6 expression and increases Sox2 expression compared to the DMSO control (Figure 3.8.b). This is confirmed by 3D single cell segmentation and quantification, showing a significant decrease in T and Tbx6, and a significant increase in Sox2 after Notch inhibition (Figure 3.9a,b). When compared to Wnt inhibition, Notch inhibition does not have as strong an effect as some residual Tbx6, and T expression is found after Notch inhibition (Figure 3.9.a). This indicates Notch supports T and Tbx6 expression, but Wnt may have a more central role than Notch in mesoderm differentiation and NMP maintenance.

Whether Notch regulates early, or late mesoderm differentiation is not clear. With further evaluation on the effect of Notch inhibition on Tbx6 and T expression, it

appears T high and Tbx6 medium expressing cells are underrepresented compared to the DMSO condition, (Figure 3.9.a) yet Tbx6+ high cells remain. This indicates Notch inhibition may abolish the T high and Tbx6 medium cell state first and Tbx6 high cells are less affected. The limited effect on Tbx6 high cells suggests a potential threshold in the capacity of Notch to regulate Tbx6 expression beyond which Notch is not required. But this will require further investigation, as this effect may arise from Notch signalling being partially inhibited.

Interestingly, cells expressing very high T expression levels usually associate with Notochord cells (Wilkinson et al., 1990) and were often observed after Notch inhibition, appearing to be overrepresented compared to the DMSO control (Figure 3.9a.). But a method that can quantitatively assess relative changes in cell populations and control for highly heterogenous gastruloids was not immediately obvious.

Overall, again Notch inhibition reduces T and Tbx6 expression in NMPs and derivatives. But when compared to Wnt, Notch signalling seems to not be as important to maintain NMP identity and mesoderm differentiation. Some other observations of interest following Notch inhibition were identified which may warrant future investigations.

3.2.6 hNMP differentiation optimisation via high throughput analysis identifies distinct hNMP-LC cell states.

I next set out to establish a system for testing how Notch signalling influences differentiation of human cells. Multiple publications have reported the differentiation of hNMPs from hESCs at a high efficiency (Gouti et al., 2014, Lippmann et al., 2015, Wymeersch et al., 2021, Frith and Tsakiridis, 2019), defined by the percentage of T+/Sox2+ cells, by culturing hESCs in N2B27 with FGF and CHIR for 72 hours, similar to EpiSC to NMP-LC differentiation (Figure 3.10a.).

To optimise the culture of hNMP-LCs from hESCs for Notch manipulation, first a seeding density and CHIR concentration scan was performed at 10,000, and 20,000

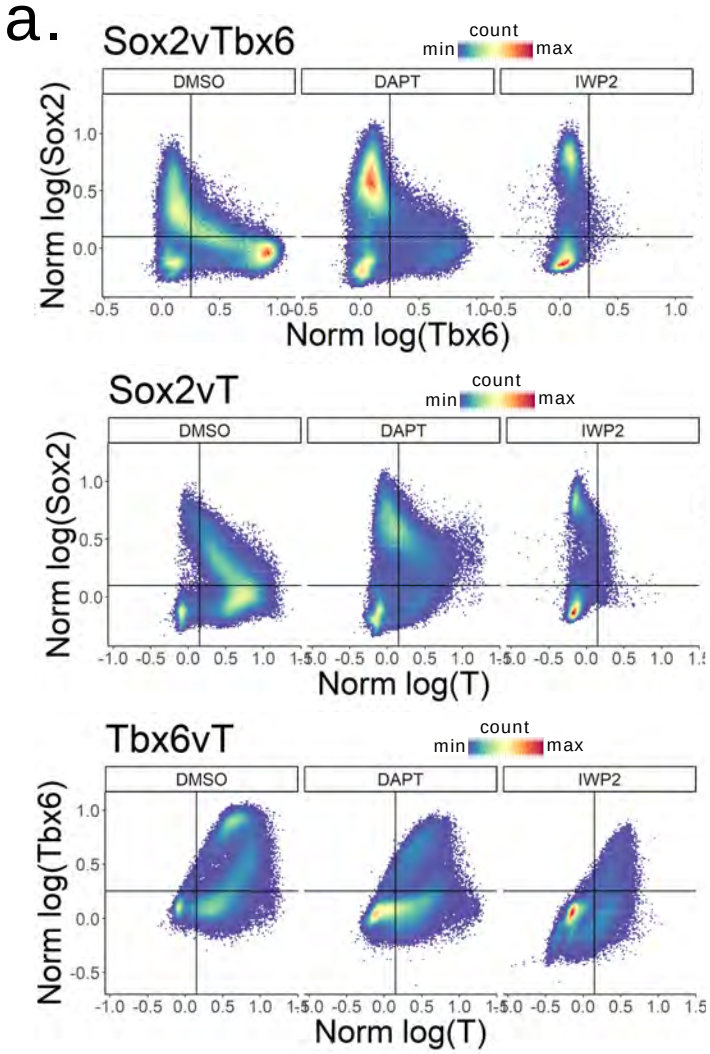
a.
Sox2vTbx6
count
min
max
DMSO
DAPT
IWP2
Norm log(Sox2)
Norm log(Tbx6)
Sox2vT
Norm log(T)
Tbx6vT

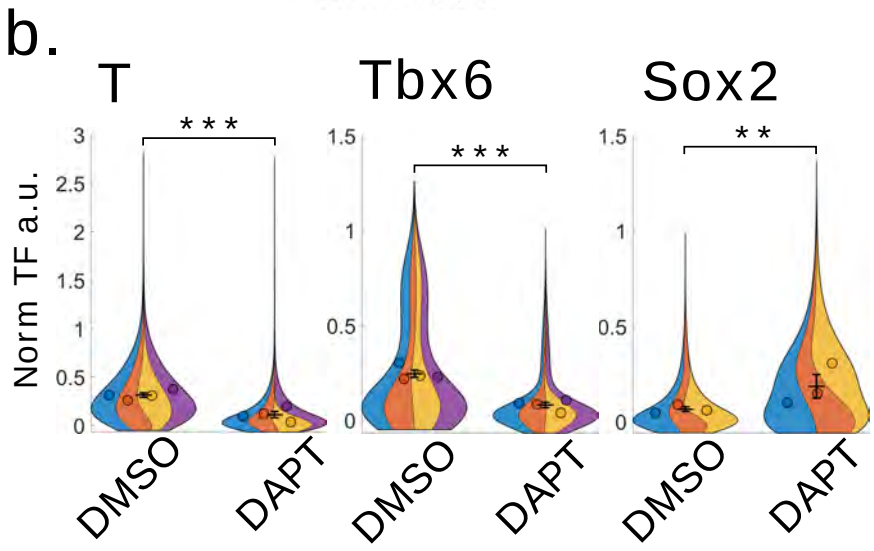
b.
T
Tbx6
Sox2
Norm TF a.u.
* * *
* * *
* *
DMSO
DAPT

Figure 3.9 Notch inhibition of gastruloids significantly affects NMP marker TF with a pro-neural effect.

a. Density plot of pairwise TF expression identifies the high T and high Tbx6 cell state lost after Notch inhibition and increased effect of Wnt inhibition. Lines indicate +/- gates. b. 3D segmentation and quantification of Sox2, Tbx6, and T in three gastruloids per condition across four replicates shows a significant decrease in Tbx6 and T after Notch inhibition, and a significant increase in Sox2. Error bars show standard error. n=4 for T/Tbx6, n=3 Sox2, ***=p<0.001** = p<0.01, *=p<0.05. Three gastruloids used for each replicate.

and 40,000 cells per cm2 at 2 and 3 uM CHIR (Figure 3.10.c.). 10,000 cells per cm2 resulted in colonies with an epithelial morphology in 2uM and 3uM CHIR (Figure 3.10.c.). Sox2 expression was maintained at 10,000 and 20,000 cells/cm2 in 2uM, but at 20,000 cells with 3uM CHIR little Sox2 was observed.

As such, the 10,000/cm2 seeding density was utilised to scan an optimal CHIR/FGF condition to achieve high T/Sox2 coexpression. CHIR and FGF were titrated at 1,2,3 and 4uM and 20, 50, and 100ng/mL concentrations respectively. Representative images from this experiment show FGF and CHIR in hNMP-LC differentiation appear to have opposing effects, where increased FGF prevents mesoderm induction, as reflected by low T expression in high FGF media (Figure 3.10a), and increasing CHIR induces mesoderm differentiation, observed by the increasing T and Tbx6 expression (Figure 3.10.b).

However, the technical challenges identified from analysing 2D cultures of mouse NMPs apply in this context also. Primarily the loss of high throughput from balancing image quality vs image acquisition speed to ensure accurate single cell

segmentation, among others. To solve this, a methodology akin to cytospinning was developed where cells are resuspended as single cells and left to adhere to coated imaging wells (Figure 3.10.d). After 15-20 minutes, cells were fixed and then immunohistochemistry can be performed. This allows unbiased and representative image acquisition in culture formats which can then be imaged in high content microscopes, also presenting a simple challenge for single cell segmentation software. Further, this method quantification allows bespoke complexing of signals and more representative protein content compared to reporter cell lines and FACS, with the added benefit of providing high signal to noise ratios.

This method was used to quantify T, Sox2, and Tbx6 expression in the FGF vs Chiron state space previously explored to suggest optimal culture conditions to achieve a hNMP-LC state similar to that found in embryos. This analysis recapitulated the previous observation that FGF and CHIR show opposing effects in mesoderm induction during hESC to hNMP-LC differentiation (Figure 3.10.e).

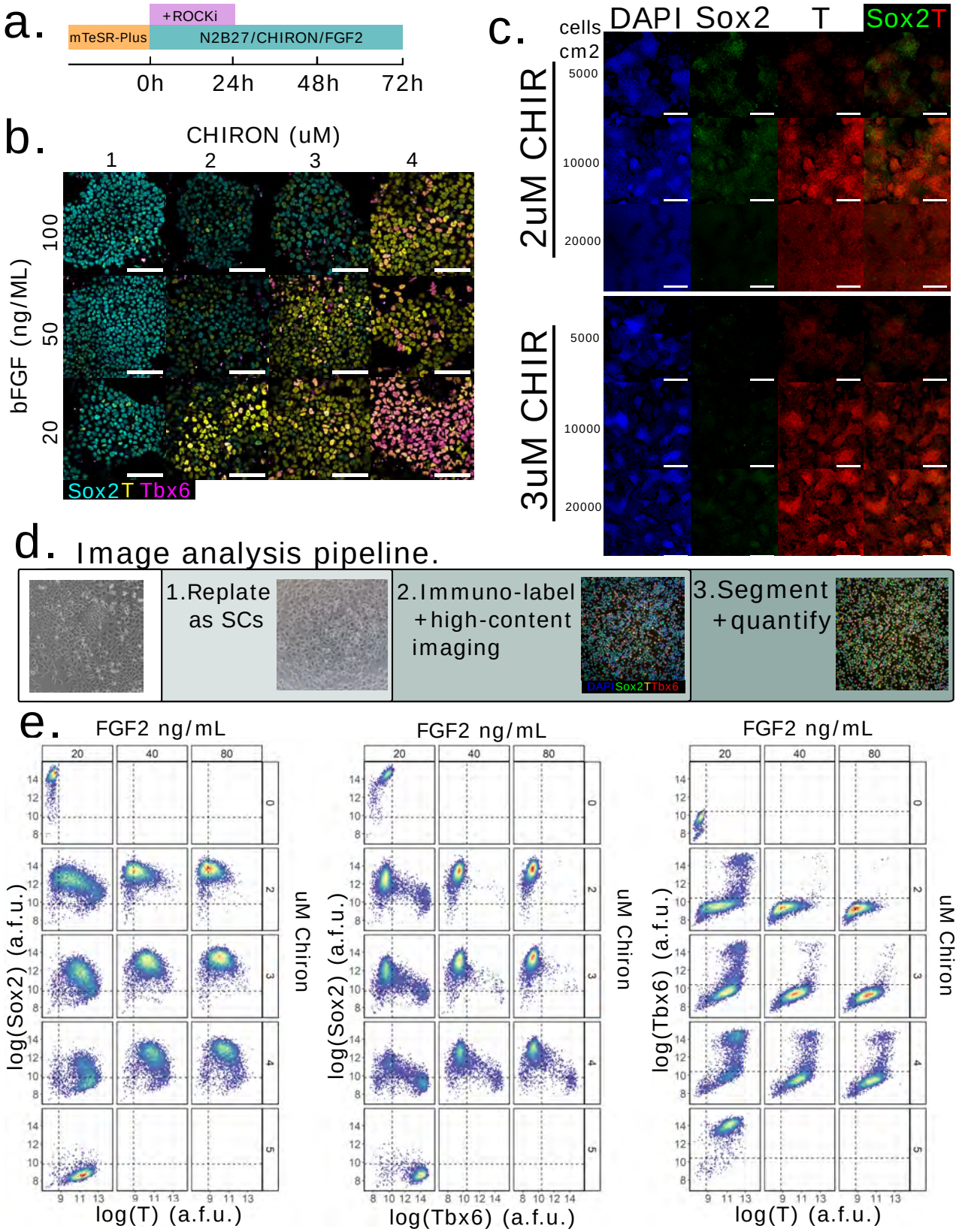
a.
+ROCKi
mTeSR-Plus
N2B27/CHIRON/FGF2
0h
24h
48h
72h
b.
CHIRON (uM)
1
2
3
4
bFGF (ng/ML)
100
50
20
Sox2T Tbx6
c.
cells
cm2
DAPI Sox2 T
Sox2T
2uM CHIR
5000
10000
20000
3uM CHIR
5000
10000
20000
d. Image analysis pipeline.
1.Replate as SCs
2.Immuno-label +high-content imaging
DAPI Sox2T Tbx6
3.Segment +quantify
e.
FGF2 ng/mL
20
40
80
uM Chiron
0
2
3
4
5
log(Sox2) (a.f.u.)
log(T) (a.f.u.)
log(Tbx6) (a.f.u.)

Figure 3.10 FGF, Chiron, and plating density optimisation for hESC to hNMP-LC differentiation and high-throughput single cell imaging and quantification methodology.

a. Culture protocol as described in (Gouti et al., 2014, Frith and Tsakiridis, 2019). b. Confocal IF of Sox2, T and Tbx6 across a FGF and CHIR concentration scan. Scale bar 50um c. Plating density of hESCs (in cells per cm2) scan in 2uM and 3uM CHIR with IF of T and Sox2. Scale bar 500uM. d. Graphic showing process of the high throughput single cell imaging method. e. Pairwise density plots for Sox2, T, Tbx6 in a FGF and Chiron scan, using quantification methodology described with +/- gates (d.), which reveals TF profiles that match in vivo mouse NMPs are closest in 2uM and 3uM with 20ng/mL FGF.

Interestingly, high concentrations of FGF and CHIRON (80ng/mL bFGF and 4uM CHIR) can achieve a high Sox2+/T+ purity as indicated by +/- gates (Figure 3.10.e). Visual comparisons of T/Sox2 expression distributions in mouse embryos and gastruloids compared to hNMP-LCs show a less defined neural-NMP-mesoderm TF path in hNMP-LCs, and a much broader distribution of T/Sox2 expression (Figure 3.10.e, 3.9.a, 3.4.a). This indicates T/Sox2 expression *in vivo* is more effectively controlled and maintained to certain cell states than *in vitro* using exogenous CHIR and Wnt.

Of note, the distribution of Tbx6 appears to be more bimodal than T or Sox2, where “medium” levels of Tbx6 are rare (Figure3.10.e). This was not observed in mouse embryos or gastruloids (Figure 3.9.a, 3.4.a), which tend to show a continuum of Tbx6 levels (Figure 3.9.a, 3.4.a). This may be due to the use of potent exogenous chemical inhibitors in the human cultures, which push cells more quickly towards differentiation and don’t allow intermediate states to persist. Using TF states not common *in vivo* when studying the GRN that balances cell fate decisions may have unknown consequences and produce artefacts. However, these observations may simply be a difference between mouse and human NMP-LCs.

With this in consideration, I aimed to identify the condition that produces the most similar cell state to *in vivo* NMPs, with T/Sox2+ with some Tbx6 expression. 3uM and 20ng/mL produces high T with many Tbx6+ cells, 2uM and 20ng/mL FGF produces low Sox2 and T with some Tbx6+ cells, but more T-ve cells (Figure 3.10.e.). At 3uM and 40ng/mL FGF, the expression of Tbx6 is low with a high T/Sox2+ population, however as mentioned this creates a TF state that does not resemble mouse *in vivo* NMPs. Since T and Sox2 form continuous expression gradients *in vivo,* and different concentrations of CHIR achieve different T+/Sox2+ identities along this gradient, using multiple conditions that produce different T+/Sox2+ states will increase the confidence that the effect of TF expression can be attributed to NMPs. Taken together, 20ng/mL of FGF and 2uM or 3uM CHIR were utilised to match the TF states found in mice and study hNMP-LCs.

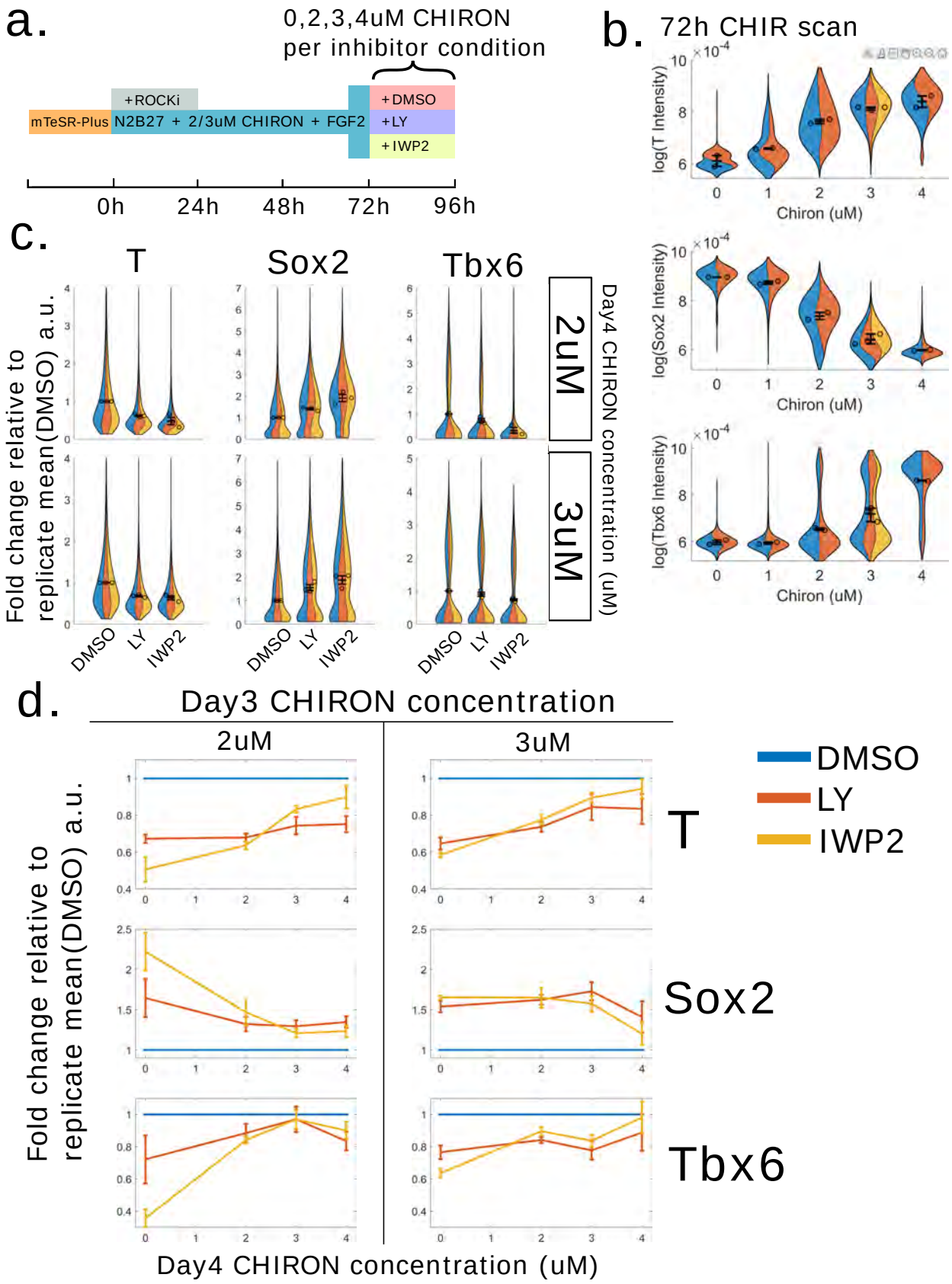
a.
0,2,3,4uM CHIRON
per inhibitor condition
+ROCKi
mTeSR-Plus
N2B27 + 2/3uM CHIRON + FGF2
+DMSO
+LY
+IWP2
0h
24h
48h
72h
96h
b.
72h CHIR scan
log(T Intensity)
log(Sox2 Intensity)
log(Tbx6 Intensity)
Chiron (uM)
c.
T
Sox2
Tbx6
2uM
3uM
Day4 CHIRON concentration (uM)
Fold change relative to replicate mean(DMSO) a.u.
DMSO
LY
IWP2
d.
Day3 CHIRON concentration
2uM
3uM
T
Sox2
Tbx6
DMSO
LY
IWP2
Fold change relative to replicate mean(DMSO) a.u.
Day4 CHIRON concentration (uM)

Figure 3.11 Notch inhibition in hNMP-LCs has pro neural effect.

a. Culture protocol where hNMP-LCs are differentiated with 2 and 3uM CHIR, then LY IWP2, or DMSO added for 24 hours. During inhibition, hNMP-LCs were cultured with varying amounts of Chiron. b. Quantification of T, Sox2 and Tbx6 at day 3 (72 hours) hNMP-LCs across a CHIR titration, using high throughput single cell quantification method. c. Violin SuperPlots displaying relative fold changes in T, Tbx6, and Sox2 relative to the mean of the replicate at Day 4. Inhibiting Notch or Wnt reduces T and Tbx6, while increasing Sox2. Colours represent biological replicates in b. and c. n=3. d. Line-graphs normalised to the mean of the replicate DMSO condition showing the effect on T, Tbx6, and Sox2 after increasing Chiron in Notch or Wnt inhibited conditions. At 0uM CHIR, Wnt has a stronger pro-neural effect. All error bars show standard error.

3.2.7 Notch inhibition reduces mesoderm differentiation and NMP maintenance in human NMPs.

The experiments described in the previous section optimised conditions for differentiating human NMPs. I next used this optimised hNMP-LC culture to test the effects of Notch inhibition on fate TF and Notch component expression. In order test that hNMPs in these context respond as expected to pharmacological manipulations and provide a positive control for NMP and mesoderm inhibition, I used IWP2 to inhibit the Wnt pathway. Unlike Notch, the role of Wnt signalling in NMPs is well established: it supports maintenance of NMPs and promotes their differentiation into mesoderm.

To investigate if Notch regulates differentiation in hNMP-LCs, hNMP-LCs were derived in 2uM and 3uM CHIR in a standard 72, or three day, culture (D3-2uM and D3-3uM henceforth) and then treated with LY, IWP2, or DMSO for a further 24 hours (Figure 3.11.a). For the 24-hour inhibition, the CHIR concentration from 0 to 72 hours was maintained. The expression of T/Sox2/Tbx6 at 72 hours, and after Wnt or Notch inhibition was quantified using the high throughput imaging method previously described.

Quantification of T/Sox2/Tbx6 in hNMP-LCs collected at 72 hours confirms the acquisition of the two hNMP-LC states previously identified to resemble mouse NMPs, namely a T-medium/Tbx6-low/Sox2+ and T-high/Tbx6-high/Sox2+ profile with D3-2uM and D3-3uM Chiron respectively (Figure 3.11.b). As seen before, a bi-modal distribution of Tbx6 is observed.

As expected, Wnt inhibition downregulates T/Tbx6 and increases Sox2 expression relative to the DMSO control in both D3-2uM and D3-3uM conditions (Figure 3.11.c.). Notch inhibition downregulates T, Sox2, and Tbx6 in both D3-2uM and D3-3uM conditions (Figure 3.11.c.).This results shows Notch has a similar effect in hNMP-LCs compared to mouse NMPs with a pro-mesodermal effect. But also, Wnt inhibition appears to have a stronger pro-neural effect (Figure 3.11.c.), this indicates Wnt has may have a more prominent role in NMP maintenance.

3.2.8 Notch displays a role distinct to Wnt in controlling T expression.

My experiments with mouse and human cells suggest that Notch promotes mesoderm differentiation of NMPs similarly to Wnt (Figure 3.4, 3.8, 3.9). However, Notch is not thought to directly upregulate Tbx6 in the epiblast (White et al., 2005) and Notch inhibition affects T, therefore a mechanism to indirectly upregulate Tbx6 via T seemed possible. Since Notch signalling appears to be upstream of T, and T is a known target of Wnt signalling (Yamaguchi et al., 1999), Notch regulating T with Wnt seemed possible. Understanding this is relevant to studying Notch inhibition while culturing hNMP-LCs with exogenous CHIR and Fgf, which is not the case for the *ex vivo* and gastruloid culture as they are self-sustaining systems. The interaction of Wnt and Notch in NMPs and how Notch regulates T/Sox2/Tbx6, whether it does so indirectly or directly, in NMPs is unknow. The addition of exogenous CHIR may confound a conclusion on the effect of Notch inhibition.

With this information and the known close signalling relationship of Notch and Wnt (Descalzo and Arias, 2012), this raised the possibility that Notch may act in upstream, downstream, or in conjunction with Wnt in this differentiation pathway to regulate T or Tbx6. For instance, I reasoned that if Wnt is downstream of Notch, then addition of high doses of CHIR might override the requirement for Notch in this system for T/Tbx6 expression. Also, the optimal choice in whether to add or remove CHIR/Fgf to each condition while studying Notch inhibition was not clear.

To account for this with a quantitative system biology approach, in the same experiment as the previous section (Figure 3.11.c.), I treated the two D3-2uM and D3uM hNMP-Cs to a series of CHIR concentrations with Notch or Wnt inhibition for 24 hours, in doing so challenging the dynamics of the GRN and explore how these pathways contribute to control NMP cell identity. The expression of T/Sox2/Tbx6 was quantified using the high throughput imaging method previously described.

Scaling the y-axis relative to the DMSO control highlights details in the relationship between CHIR concentrations and Wnt/Notch in D3-2uM and D3-3uM conditions

(Figure 3.11.d.). As expected, increasing CHIR can rescue the effect on T/Sox2/Tbx6 from Wnt inhibition, with 4uM CHIR and IWP2 or DMSO having little difference in T, Sox2, and Tbx6 expression for both the 2uM and 3uM derived hNMP-LCs. Increasing CHIR linearly increases T expression with IWP2 relative to the DMSO control.

Conversely, increasing CHIR with Notch inhibition does not increase T expression relative to the DMSO control in the D3-2uM condition and maintains a 20-30% reduction in fold change (Figure 3.11.d.). However, a slight increase in relative fold change T expression with increasing CHIR concentration during Notch inhibition for the D3-3uM condition was observed, but this was not as strong a rescue effect as when inhibiting Wnt. The effect on Sox2 and Tbx6 modulating CHIR during Notch inhibition is less clear but resembles Wnt inhibition. This suggests that Notch and Wnt independently regulate T expression.

Finally, since it us unknown whether Notch can directly regulate T or Wnt/FGF. A plausible indirect mechanism would include Notch inhibition upregulating Sox2 to then inhibit T. Evaluating this dataset can suggest if this is the case. The changes in TF expression for T and Sox2/Tbx6 following Notch inhibition and increasing CHIR do not directly correlate with each other (Figure 3.11.d.). In the D3-2uM condition, T is consistently downregulated at a 20-30% reduction in relative fold change across CHIR concentrations, but the reduction in fold change fluctuates for Sox2 and Tbx6 across CHIR concentrations. This indicates a degree of independence in the effect of Notch inhibition between each TF, for instance where the strength of T downregulation following manipulation is not reflected by a similarly strong upregulation for Sox2, suggesting that T inhibition is not controlled solely by Sox2.

Overall, this result indicates that Notch signalling can regulate T expression either downstream or independently of Wnt, as increasing CHIR during Notch inhibition or during Wnt inhibition had different effects on T/Sox2/Tbx6 expression. Further, this mechanism is not necessarily directly via Sox2. The data reinforces the observation in mouse NMPs that Wnt inhibition has a stronger pro-neural effect than Notch

inhibition, and potentially a more important role in maintaining NMPs and mesoderm differentiation.

3.2.9 NMP differentiation time course suggests the location of thresholds in TF expression for commitment to mesoderm identity.

I have demonstrated that Notch regulates T/Sox2/Tbx6 expression and many Notch components are expressed in NMPs within the CLE, this poses the question as to what mechanism Notch operates in. So far, the results indicate a positive feedback role for Notch, but for Dll1 mediated lateral inhibition a negative regulatory element must be present. In a hypothetical lateral inhibition regime with Tbx6/Dll1/Notch1 expressing nascent mesoderm cells, neighbouring Tbx6/Dll1/Notch1 expressing cells will activate Hes genes and repress Dll1 expression (Collier et al., 1996, Boareto et al., 2016), and potentially regulate mesoderm fate markers also. For Tbx6/Dll1 cells to repress Tbx6/Dll1 expression in neighbouring cells, the capacity of Tbx6 expression to be negatively regulated requires elucidating. Tbx6 so far has demonstrated a bimodal expression pattern, recapitulating the previous descriptions in the literature of a bistable switch for mesoderm commitment (Bouldin et al., 2015, Koch et al., 2017). A bistable switch is self-reinforcing and often contains a threshold by which the positive feedback prevents reverting back to the original cell state. Also, lineage tracing of cells labelled by Tbx6 expression revealed that some previously Tbx6 expressing cells were found in neural tissues (Concepcion et al., 2017). Together, this suggests a threshold exists for mesoderm commitment along the Tbx6 expression profile.

The location of this threshold will impact the dynamic range of a lateral inhibition regulatory mechanism. For instance, if little Tbx6 expression is required to initiate the commitment to mesoderm, this will cast doubt on the presence of lateral inhibition controlling neighbouring mesoderm differentiation via Tbx6. To date this has not been explored quantitatively.

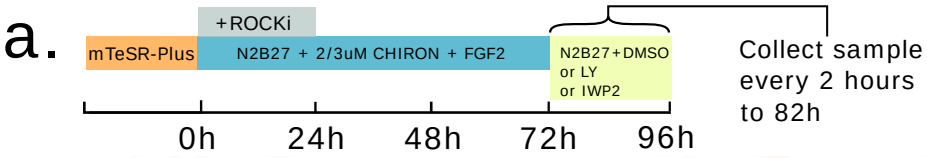
a.
+ROCKi
mTeSR-Plus
N2B27 + 2/3uM CHIRON + FGF2
N2B27+DMSO
or LY
or IWP2
Collect sample
every 2 hours
to 82h
0h
24h
48h
72h
96h

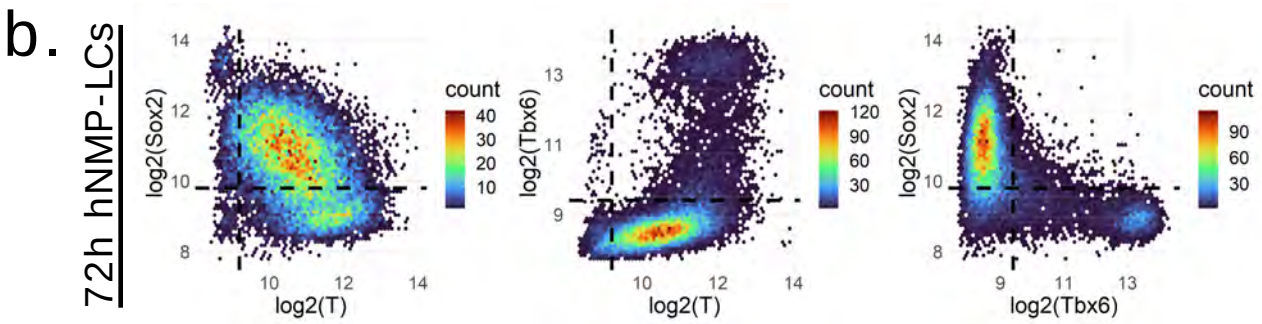
b.
72h hNMP-LCs
log2(Sox2)
log2(T)
count
log2(Tbx6)
log2(Tbx6)

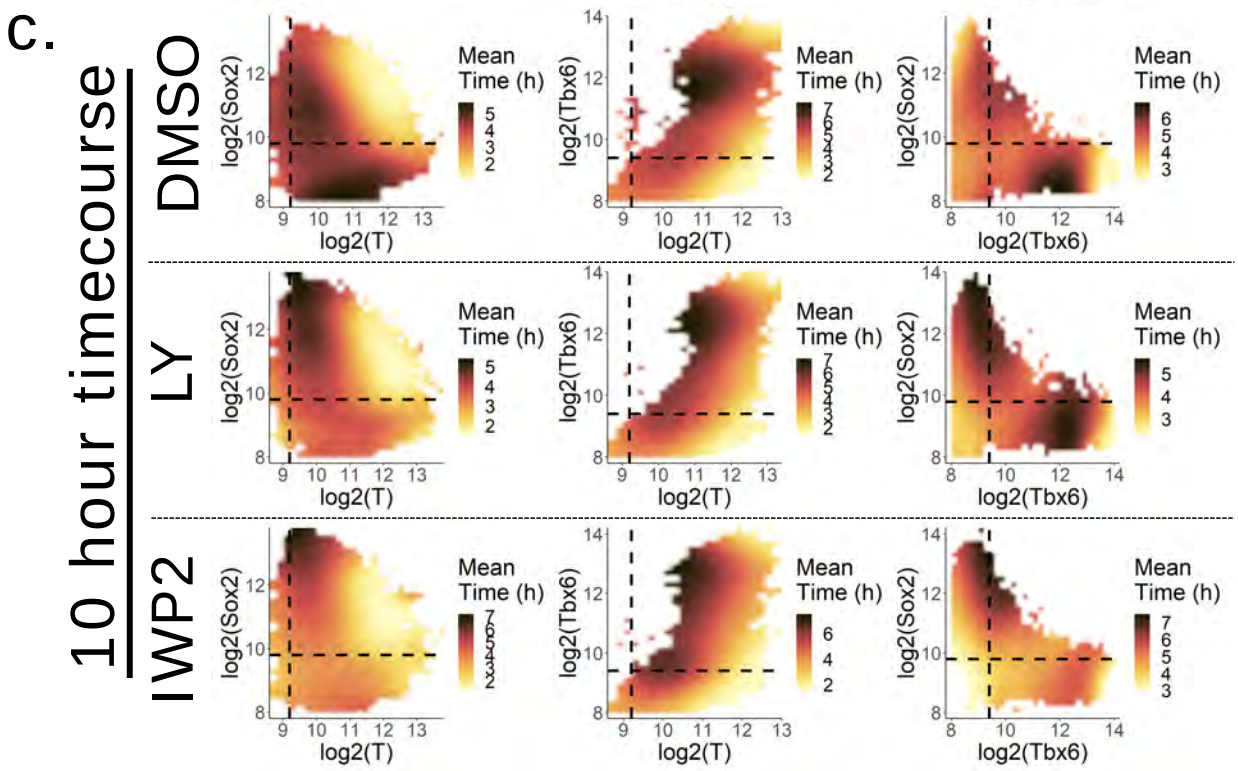
c.
10 hour timecourse
DMSO
LY
IWP2
log2(Sox2)
log2(T)
Mean
Time (h)
log2(Tbx6)
log2(Tbx6)

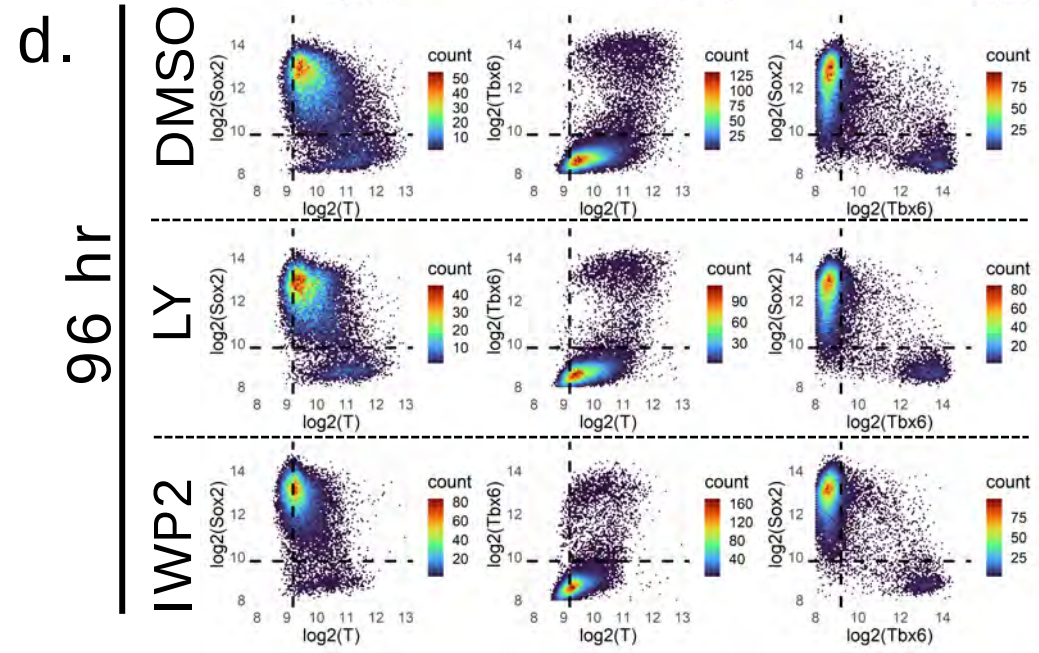
d.
96 hr
DMSO
LY
IWP2
log2(Sox2)
log2(T)
count
log2(Tbx6)
log2(Tbx6)

Figure 3.12 Time course of spontaneous differentiation in hNMPs.

a. Graphic for culture conditions where hNMP-LCs were differentiated from hESCs with 2uM and 3uM Chiron in multiple wells, then at 72 hours IWP2 or LY was added to inhibited Wnt and Notch respectively with a DSMO control. Every two hours, a well for each condition was replated and fixed, then IF performed to stain T, Sox2, and Tbx6 for high throughput imaging. b. Density plots of pairwise TF comparison in 2uM and 3uM hNMPs at 72 hours before treatment, with a 0uM Chiron and 4uM control included to +/- gate each TF. Clear differentiation paths between cell states can be observed. c. Pairwise plots showing the average time post treatment of cells in bins. Bins were smoothed by a spatially averaging bins and linear interpolation. Gradients of indicate movement of cells through Euclidian TF space towards attractor cell states, indicating points of divergence and limits of commitment. d. Day 4 (96h) timepoint for the DMSO, LY, and IWP2 condition showing pairwise density plots, showing the neural and mesoderm attractor states previously identified. N=1. Lines indicate +/- gate.

To observe if a defined TF threshold for mesoderm commitment for any TF exists, and how Notch or Wnt signalling shapes any potential threshold, I showcase how the high throughput method (see section 3.2.6) can be used to explore the time dimension. As before, hNMP-LCs were differentiated in 2uM and 3uM CHIR to produce the a spectrum of Sox2+T+ identities found in NMP-LCs (Figure 3.12.a, b.). The NMP-LCs were then cultured in the absence of Fgf or CHIR in basal N2B27 to promote spontaneous differentiation to mesoderm or neural states. Samples were collected and fixed in an imaging plate every two hours for a 10-hour period to track the changes in TF expression over time, whereafter immunohistochemistry and high content imaging was performed. A final timepoint at 96 hours (24 hours post media change) was collected to further identify the cell states after spontaneous differentiation.

The final timepoint in the DMSO control condition at 24 hours explicitly shows the expected neural Sox2-high T/Tbx6-low and mesoderm T/Tbx6-high Sox2-low attractor states after spontaneous differentiation, with less overall T/Tbx6 expression (Figure 3.12.d.). Averaging the time points of cells located within TF expression space bins reveals the inferred movement of cells in time to attractor states overrepresented by later timepoints (Figure 3.12.c.). By identifying areas in TF space underrepresented by later timepoints and diverging splits in time gradients, one can infer the threshold of differentiation commitment to attractor states where cells states move towards during differentiation. As expected, when comparing Tbx6 and Sox2 in the DMSO condition two attractor states of neural Sox2+Tbx6- and mesoderm Sox2-Tbx6+ are present (Figure 3.12.c.), the divergence in commitment appears to reside in the Tbx6 low and Sox2 low domain. The gradient suggests that cells expressing low levels of Tbx6 do not travel into the Tbx6 high domain but revert to the neural Sox2+Tbx6- domain.

This analysis can also be extended to look at the attractor states and splits in identity commitment for NMP maintenance. When comparing the time gradients for the T/Sox2 graph in the DMSO condition, a split in commitment is in a Sox2 low domain, where Sox2-low, but not Sox2 negative, is committed to mesoderm and do not revert to Sox2+ neural states (Figure 3.12.c.). This split in gradient is much closer to the

background signal level than compared to Tbx6, indicating very low levels of Sox2 allow cells to revert to NMP or neural identity.

Interestingly, in the DMSO condition the T high and Sox2 domain is rapidly lost and is greatly underrepresented at later time points (Figure 3.12.c.). An attractor state at T-low and Sox2 low with a high representation of later time points is present, which better reflects the TF identities found in mouse cells cultured without exogenous Wnt stimulation via CHIR. This indicates this Sox2 high T high TF profile is unstable and potentially attained by potent exogenous signal stimulation.

To test if Notch signalling affects this threshold, I inhibited Notch by adding LY to the basal N2B27 media during the 10 hour period (Figure 3.12.a.). When compared to the Sox2/Tbx6 of the DMSO condition, Notch inhibition did not appear to change the split in gradient for Sox2/Tbx6 expression (Figure 3.12.c.). However, the balance of cells to either neural or mesoderm attractor states was altered where in the DMSO condition, most identities resided in the mesoderm Sox2-Tbx6+ domain, but with Notch inhibition this was more even (Figure 3.12.c.). Similarly, Wnt inhibition via IWP2 results in a similar split in the time gradients but an even greater shift in the balance to the neural attractor state.

Overall, this experiment indicates the presence of a threshold to mesoderm commitment in the Tbx6 medium range, suggesting Tbx6 low cells can revert to a NMP or neural identity. This threshold was unaffected with Notch or Wnt inhibition, but as before a pro-neural effect was recapitulated by showing a bias towards neural attractor states.

3.3 Discussion

The lineage tracing data from (Haston, 2018) showed that in chick embryos Notch permits ingression into the primitive streak from NMP regions, but precisely which Notch genes are expressed in NMPs and how they may regulate NMP related TF and signalling genes, nor the broader regulatory strategy is unknown. The aims of this chapter were to (i) further characterise the expression of Notch genes in mouse

and human NMPs and (ii) identify how Notch influences the NMP core gene regulatory network, and (iii) do so in quantitative systems biology inspired methods.

3.3.1 Notch gene expression *in vivo* indicates role in NMP maintenance in addition to mesoderm identity.

The expression of Dll1 has been commonly identified as a gene of interest in NMP niches (Wymeersch et al., 2019, Gouti et al., 2017, Guibentif et al., 2021), but other Notch genes have not been described in NMPs. Data mining published SC-RNAseq datasets of in vivo NMPs showed that many more Notch genes than just Dll1 are expressed in NMPs and the nascent mesoderm. From the CLE SC-RNAseq, which micro-dissected out the NMP region from E8.0, E8.5, and E9.5 embryo (Gouti et al., 2017, Dias et al., 2020), ligands (Dll1, Dll3, Jag1), Notch receptors (Notch1, Notch 2, Notch3), and Hes genes (Hes1, Hes7, Hey1) were expressed. However, there is considerable difference in the expression of Notch genes between the CLE and whole embryo datasets at E8.5 (Figure 3.1, 3.2), in particular Notch receptors and ligands. Only small subsets of cells express Notch1, Notch2, Notch3, and Jag1 in the NMP subset at E8.5, whereas this was higher in the CLE data. Without Notch receptor expression, Notch signalling cannot occur.

Notch2 appears to be invariantly expressed in both NMPs and the nascent mesoderm (Figure 3.1.a.), indicating all cells are responsive to Notch signals to a certain degree. Conversely, Notch1 correlates with the PSM like profile and Notch3 correlates with the T/Jag1/Wnt3a/Fgf8 module, suggesting differential regulatory mechanisms. But Noch1 and Notch3 are relatively lowly expressed, whether this is sufficient for extensive induction of Notch targets is unclear. Notch target genes Hes1, Hey1, and Hes7 are expressed in the T/Jag1/Wnt3a/Fgf8 profile (Figure 3.1c.), suggesting NMPs are receiving Notch signals as well as the nascent mesoderm.

However, the Hes genes Hes7 and Hes5 is still present in NMPs for the whole embryo dataset. SC-RNAseq of gastruloids indicated that Hes7 is expressed in NMPs (Veenvliet et al., 2020). While Hes7 is directly upregulated by Notch signalling

(Bessho et al., 2001a), Hes7 is upregulated by FGF4 in the PSM (Anderson et al., 2020). Fgf4 is active in the PS (Boulet and Capecchi, 2012) so this may be driving Hes7 expression. However, FGF4 was absent from the CLE data (Figure 3.1.a), so the Fgf4 signal may originate in from the PS only. Overall, from this we cannot be certain to what extent how active Notch signalling is and how much it contributes to from this dataset.

It is not clear why this difference in expression may be the case, but it is possible that non-CLE cells are included in the “NMP” subset used here due to manual +/- gating of genes to isolate NMPs. Due to the fact that bi-potency extends outside of the CLE (Wymeersch et al., 2016), cells are also likely to express Sox2, T and Nkx1.2 outside the CLE. This notion is supported by the median T and Sox2 being relatively similar in the whole embryo dataset (Figure 3.2.a.), whereas T is expressed at orders of magnitude greater than Sox2 in all the CLE data stages (Figure 3.1.a.), suggesting the manual NMP gating from the whole embryo contains cells across the full gradient of T and Sox2 expression. The CLE dataset is directly dissected from NMP niches *in vivo* which removes this variable and is likely to be the most representative, despite having fewer cell numbers.

To discuss why Notch genes may have been overlooked and the implications of assessing gene activity from RNA counts, SC-RNAseq studies rely on the identification of genes of interest by selecting the highest differential gene expression between cell types or differential gene expression after manipulation, or by manual examination on an individual case by case basis. It is possible Notch genes, and other many other genes, may have been overlooked in these analysis. Despite being expressed, not statistically significant between other cell types or between conditions would result in being lost among the vast RNA landscape. Individual evaluation of signalling pathways as I have performed is more tedious, but likely to be worthwhile in addition to unbiased genes of interest searching.

Regardless, this analysis showed the expression Notch gene in NMPs for the CLE dataset is extensive with ligands, receptors, and downstream Hes genes expressed in NMPs, not just the nascent mesoderm. In addition, Notch genes are increasingly

expressed from E7.5 to E9.5, where Notch gene expression is mostly limited to PSM-like in E7.5 to E8.5. This suggests the Notch regulatory role may change during axial elongation. It would be interesting to study RNAseq data from beyond E9.5 to ascertain how this trend changes after tailbud formation.

It is curious that Jag1/Notch3 is upregulated in NMPs from E8.5 to E9.5 (Figure 3.1a.), as Jag1 has been associated with lateral induction and can act as a ligand for Notch3 (Saravanamuthu et al., 2009, Manderfield et al., 2012, Boareto et al., 2016, Chen et al., 2010, Shimizu et al., 2000). This, included with the pro-mesodermal or pro-NMP identity effect of Notch signalling demonstrated, indicates Notch may contribute to the Wnt/FGF/T feedback. The timing of this is also curious, as the E8.5 to E9.5 period coincides with an expansion of the NMP population (Wymeersch et al., 2016, Guillot et al., 2021, Wymeersch et al., 2021) indicating the emergence of a Jag1 positive feedback may play a role in this expansion phase. Notch inhibition of gastruloids showed a decrease in length, suggesting lower proliferation (Figure 3.8.c). Myc was shown to maintain proliferation in NMPs and was controlled by Notch signalling (Mastromina et al., 2018, Palomero et al., 2006), perhaps providing a route of action for this contribution to NMP expansion. The effect of Notch inhibition on cell proliferation in NMPs could be investigated by studying the doubling time in vitro, or *in vitro* and *ex vivo* using proliferation markers such as Ki67 (Miller et al., 2018) or BrdU staining for newly synthesised DNA. Increased apoptosis should also be considered and staining for apoptotic makers such as Caspase3 (Eskandari and Eaves, 2022) could indicate if Notch inhibition reduces cell survival.

While transcriptome data is a powerful tool to investigate GRNs, the difference between protein level and transcript level is not guaranteed to directly correlate. Most data produced in this thesis is at the protein level for the NMP fate markers Sox2,T and Tbx6. Therefore, further investigation into the verifying the correlation between protein level and transcript level would benefit the interpretations when drawing comparisons between the two data sets.

3.3.2 Notch inhibition reduces Tbx6 expression, but also affects T and Sox2 expression in mouse and human NMPs.

Notch inhibition reduced Tbx6 expression in all contexts investigated, namely mouse embryos (Figure 3.4.b), in vitro gastruloids (Figure 3.9.b), and in vitro derived human NMPs (Figure 3.11.c). Critically, Tbx6 is not thought to be directly positively upregulated by Notch in the PS or epiblast, only in the PSM (White et al., 2005). Suggesting that the Tbx6 downregulation following Notch inhibition may occur indirectly. Interestingly, T was similarly downregulated along with an upregulation in Sox2 in these experiments. This suggests Notch signalling is upstream of T and/or Sox2 and has a role in NMP maintenance and is not limited to regulating the nascent mesoderm.

T is closely controlled by Wnt (Yamaguchi et al., 1999) and Notch closely regulates TF expression with Wnt in many systems (Descalzo and Arias, 2012, Wahl et al., 2007, LaFoya et al., 2016). This led to the experiment in hNMPs that explores if T/Tbx6 expression downregulation via Notch inhibition could be rescued from increased β-Catenin stabilisation via CHIR (Figure 3.11). However, increasing CHIR did not rescue T expression to the DMSO control level in the Notch inhibited condition but increasing CHIR did rescue T expression to the DMSO control level in the Wnt inhibited condition, suggesting Wnt and Notch independently regulate T.

In addition to this, increasing CHIR decreased the average expression of Sox2 relative to the DMSO control, whereas T remained at a stable 20-30% reduction suggesting there is a degree of independence in regulation between T and Sox2 (Figure 3.11.d). From this we can conclude that the Notch inhibitory effect is upstream of T/Tbx6 and not a consequence of upregulated Sox2. A similar experiment but instead modulating Fgf to elucidate whether Notch interacts with Fgf to control T/Tbx6 would be interesting, as there was an inferred negative regulatory relationship of Fgf on Dll1 (Wahl et al., 2007).

While the use of gamma secretase inhibitors to abolish Notch signalling is well documented, further explicit evidence to demonstrate the efficacy of Notch inhibition

in these experiments would benefit this analysis. Although, as I have explored many of the Notch components, including Jag1, Dll1, Notch1, Notch3, Hes7, and Hes1 seem to have T-box or Sox2 binding sites in their promoters and differentially express in T, Tbx6, and Sox2 mutants (Table 1.1), and thus may not be solely under the control of Notch. Therefore, in addition to Notch component differential expression analysis, reporters for Notch activity and NICD content are best suited to specifically assess Notch signalling inhibition.

Overall, this provides evidence that Notch has a positive regulatory role in T/Tbx6 expression and prevents upregulation of Sox2.

3.3.3 Wnt inhibition has a stronger pro-neural effect than Notch inhibition.

In hNMPs and mouse gastruloids, Wnt signalling inhibition via IWP2 resulted in a rapid depletion of T and Tbx6 with a similarly rapid increase in Sox2 (Figure 3.11, 3.8, 3.9). This effect was stronger than Notch inhibition, suggesting a more central role in NMP identity and maintenance. In none of the experiments did Notch inhibition result in complete abolishment of T, suggesting that Notch may in fact play a cooperative role in NMP maintenance. However, timeframes beyond 24 hours were not studied, so it is possible Notch inhibition does eventually result in a breakdown of the NMP maintenance circuit which was not captured. But it can be concluded that while Notch inhibition prevents mesoderm differentiation, in the short-term Notch is not as important for NMP maintenance than Wnt. This is consistent with the observation that Notch is downstream of FGF/Wnt (Wahl et al., 2007).

3.3.4 Possible direct regulatory mechanisms of Notch on NMPs.

With this information and the SC-RNAseq gene expression data, it is tempting to speculate on the role of Notch signalling based on known interactions of the Notch components and the core NMP GRN. It is well documented that Wnt and FGF are central to NMP maintenance (Wymeersch et al., 2021), much of the functional

information of Notch gene's interaction with Wnt/FGF comes from PSM in the wavefront/clock model (Conlon et al., 1995, del Barco Barrantes et al., 1999, Bessho et al., 2003, Anderson et al., 2020, Hofmann et al., 2004, Wahl et al., 2007, Hayward et al., 2008), which is spatially not far removed from the NMP context. Since many of the genes associated with the PSM are found in the epiblast and in NMPs, the question remains do they interact with any of the core NMP gene regulatory network to regulate the early mesoderm decision?

Considering a total theoretical gene regulatory network based on the interactions described in the literature for axial progenitors and the PSM, it is clear there are no known direct interactions of canonical Notch signalling upstream of Sox2, T, Wnt, or Fgf. But in the PSM some mechanisms have been proposed where Notch can indirectly modulate Wnt and Fgf. Hes7 is central to the periodicity in the PSM (Bessho et al., 2003) and has been suggested to interact with Wnt and Fgf in the PSM. There is indirect evidence that Hes7 upregulates Fgf signalling via inhibiting Dusp4, a negative regulator of Fgf/MAPK signalling (Niwa et al., 2007, Chu et al., 1996). Further, Hes7 is also thought to be upregulated by FGF4 signalling (Boulet and Capecchi, 2012, Anderson et al., 2020) in somites and Tbx6 in the PSM (Gonzalez et al., 2013). Hes7 is thought to create oscillations by inhibiting itself and Lfng for somitogenesis controlled by FGF and Notch (Bessho et al., 2001a, Bessho et al., 2003, Hirata et al., 2004, Chen et al., 2005), but whether this is occurring in the PS and NMPs is not clear. Also, Hes7 has been proposed to positively regulate Nkd1 to inhibit Wnt activity in the PSM (Ishikawa et al., 2004). It is not clear if Hes7 does directly regulate Fgf or Nkd1, but mathematical modelling has suggested such an interaction in a regulatory network is sufficient for oscillations in the PSM (Wang et al., 2013).

Hes7 is expressed both in NMPs and the Nascent mesoderm (Gouti et al., 2017, Veenvliet et al., 2020, Pijuan-Sala et al., 2019), where it positively correlates with the PSM profile genes such as Tbx6, Msgn1 and Dll1 (Figure 3.1.a,c), opening the possibility that Hes7 is upregulated by FGF/Notch in NMPs and increasingly so into the Nascent mesoderm where Wnt, FGF and Notch signals are increased. Nkd1 and Dusp4 are also expressed in the CLE dataset (data not shown), potentially allowing

for both upstream regulation of Wnt and Fgf via Hes7. Notch could act as a positive and/or negative regulator of NMP identity through these interactions, since a positive feedback role has been demonstrated so far for Notch on NMP and mesoderm, the Hes7 interaction to positively upregulate Fgf is more likely.

Also, Hes7 it thought to negatively regulate Dll1 and create oscillations in the PSM (Kageyama et al., 2018, Kageyama et al., 2023, Chen et al., 2005, Shimojo et al., 2016), which may present a route to explain the increase in Dll1 following Notch inhibition in EpiSC derived NMPs (Figure 3.6.b). Inhibiting Notch signalling may downregulate Hes7 and allow residual Wnt3a/T/Tbx6 to upregulate Dll1 (Hofmann et al., 2004, White and Chapman, 2005, Koch et al., 2017).

It is curious what the role of Notch independent Hes genes Hes3 and Hes6 are in NMPs (Figure 3.1.a.), since these are structurally similar to the other Hes proteins (Iso et al., 2003, Takebayashi et al., 1994) and are known to interact with Notch in other contexts. For instance, Hes6 has been shown to cooperatively bind to Hes1 and preventing its inhibitory effect (Bae et al., 2000), suggesting it is mechanistically possible that Hes6 expression protects NMPs from the inhibitory effects of Hes1. Hes3 has also been implicated in inhibiting Wnt signalling in the formation of the neural plate in xenopus (Hong and Saint-Jeannet, 2018) and acts in concert with Hes1 and Hes5 to regulate neural stem cell populations. Also, Hes3 is upregulated in NMPs after T knockdown (Vidigal et al., 2010). However, a potentially regulatory mechanism for these genes is not clear.

The Fringe genes are not highly expressed in any of the datasets, Hes7 binds to the promoter of Lfng and prepress its activity (Chen et al., 2005), so with widespread Hes7 expression this may prevent Lfng expression. Limited Fringe suggests no modulation Notch receptor/ligand binding in the context of NMPs. Although, since Notch3 and Notch1 differentially correlate with the NMP T/Jag1/Wnt3a/Fgf8 and the Tbx6/Dll1/Hes7 nascent mesoderm profiles (Figure 3.1,3.2), this could imply an underlying regulatory role.

The gene expression associations identified suggest a complex underlying regulatory landscape, it is theoretically possible that Notch may simultaneously

operate with lateral inhibition and lateral induction as described in another systems (Boareto et al., 2016). As described, the NMP Wnt/FGF/Notch profile, including Wnt3a/FGF8/Jag1/Cyp26a1/ Notch3/T expression, could form a positive feedback loop that would balance the inhibitory effects of the neural Sox2 profile induced by RA (Koch et al., 2017, Gouti et al., 2017). This Wnt/FGF/Notch loop would maintain T expression but also initiate Tbx6 expression with the PSM like expression profile, where the known Tbx6/Msgn1 identity represses the bipotent T/Sox2 regimes to reinforce the cell fate decision (Koch et al., 2017, Gouti et al., 2017, Takemoto et al., 2011). In addition to repressing Sox2 and NMP identity intracellularly, the Tbx6/Msgn1 with the Notch Dll1/Dll3/Notch1 profile may downregulate Dll1, in addition to other TFs, in neighbouring cells via Hes7. Since Notch is generally considered downstream of Fgf/Wnt (Hofmann et al., 2004, Wahl et al., 2007), the lateral inhibition of Tbx6 regulation may manifest as Notch controlled spatial patterns of Tbx6 and not T. The positive regulation of Notch on T/Tbx6 I have shown may be the more prominent result of total Notch inhibition, and lateral inhibition may require more specific downregulation of Notch targets to elucidate.

However, for this model to operate, Notch must be able to directly negatively regulate Tbx6 expression. Tbx6 has an Notch responsive element with a RBP-j binding site in its promoter (White et al., 2005). However, this is only active in the PSM, indicating that direct signals of Notch do not directly upregulate Tbx6 in the PS or epiblast. As opposed to Notch directly regulating Tbx6, it is possible that upregulation of Myc via Notch could upregulate Sox2 (Palomero et al., 2006, Mastromina et al., 2018) and thus inhibit Tbx6. But this might not act on quick enough time scale, conventionally Notch signalling operates over short time scales with short half-lives of notch component quick response times (Williams et al., 2016, Fior and Henrique, 2009, Hirata et al., 2004). As such, a novel negative regulatory mechanism between Notch signalling and Tbx6 would need to be present.

For a dynamic lateral inhibition model where Notch controls Tbx6 expression, it was important to understand if all Tbx6+ cells are committed to mesoderm. Lineage tracing of cells labelled by Tbx6 promoter activity identified a cell expressing Tbx6 was found in the hindbrain (Concepcion et al., 2017), suggesting Tbx6+ cells are not

all committed to mesoderm but this may be rare. The time course experiment with Notch and Wnt inhibition supported this by suggesting the commitment threshold for mesoderm in the Tbx6 spectrum lies somewhere in the Tbx6 medium expression range, not at the +ve line (Figure 3.12). This opens the possibility of a dynamic lateral inhibition/induction model where Tbx6+ cells emerge but then can be negatively regulated by Dll1 mediated lateral inhibition.

However, the interpretation of the attractor state analysis is limited by using the average time for each state space as cells would reach the theoretical attractor states at different times. The early cells would artificially reduce the average time and potentially mask attractor states occupied by early cells. A method which incorporates the changes in state space between timesteps could complement this analysis.

To speculate on the utility of lateral inhibition in the NMPs, Dll1 mediated lateral inhibition of neighbouring mesodermal cells may enforce a certain proportion of cells in the NMP progenitor pool to be allocated to mesoderm, as is the case in other lateral inhibition contexts (Collier et al., 1996, Chrysostomou et al., 2012, Kageyama et al., 2008). Further, since Notch appears to contribute to the Wnt/Fgf positive feedback loop to maintain T expression, lateral inhibition may act as negative regulation with Sox2 and RA to sharpen the boundary of mesoderm commitment while simultaneously being required for mesoderm differentiation by maintaining T expression.

Taken together, the complexity of the possible gene regulatory network from the extent of Notch, Wnt, and FGF gene expression and known interactions means there are many feasible regulatory mechanisms that could control mesoderm differentiation, raising many avenues for investigation.

3.3.5 Summary.

Overall, this chapter provides evidence that Notch has a pro-mesodermal effect upstream of T and Tbx6 in NMPs, but Notch inhibition did not completely abolish T in

any of the experimental systems. Also, it is unknown whether Notch inhibition prevents mesoderm differentiation by directly regulating via T or Tbx6.

Datamining SC-RNAseq of *in vivo* NMPs indicates Notch signalling is active in NMPs and the nascent mesoderm with the extensive expression of Notch receptors and downstream Hes genes. Different profiles of Notch/Wnt/FGF expression suggest many regulatory interactions are theoretically possible, but in conjunction with indirect regulation of T/Sox2 via Myc, it is possible that Notch interacts with FGF via Hes7 to positively regulate NMP differentiation. If this isn't the case, a novel positive regulatory element between the NICD or Hes genes and Wnt and/or T will require investigation. Complete investigations into the Notch genes identified in the SC-RNAseq analysis and how they may regulate signalling pathways in the NMP GRN are required to uncover the true mechanism.

However, a top-down approach to explore underlying regulatory principles can be carried out without knowing the full mechanism. I showed that Notch signalling negatively regulates Dll1 in NMPs yet positively regulates T, Jag1 is expressed with several Notch receptors, which may indicate a classical lateral inhibition and lateral induction model. If we can quantify the spatial patterning of NMP TFs, we can suggest whether these align with the tell-tale spatial patterning of Notch signalling. Further, this would allow a quantifiable change in patterning following Notch manipulation. Methods to accomplish this are addressed in the following chapter.

Chapter 4:

Exploring 3D neighbour-based TF spatial patterning analysis methods within the *in vivo* NMP niche.

4.1 Introduction

Notch signalling is known to create spatial patterns of TF expression and differentiation in progenitor populations via lateral inhibition and lateral induction (Collier et al., 1996, Saravanamuthu et al., 2009, Manderfield et al., 2012, Boareto et al., 2016). Although the exact mechanism is unknown, we do know that Notch regulates mesoderm differentiation and NMPs express the necessary components for both lateral induction and inhibition (see section 3.2.1.). This raises the question of which, if any, of these two spatial patterning mechanisms are involved and their overall purpose in maintaining NMPs and regulating mesoderm differentiation.

Characteristic lateral inhibition creates heterogeneity as the receiver cell acquires a state different to the sender cell, where notch signals from a sender cell inhibit Notch ligands in a receiver cells. Conversely, lateral induction homogenises the population where Notch signals from the sender cell upregulate Notch ligands and other genes, acquiring the same state as in a spatial positive feedback loop.

Each mechanism therefore generates different spatial patterns which are usually assessed by eye, but lateral inhibition-type or clustering patterns have been

quantified in 3D groups of cells or nuclei (Jafari Mamaghani et al., 2010, Weston et al., 2012). Similarly, various methods for computational analysis of spatial patterning have been published, but these are mostly designed for 2D spatial transcriptomics (Stoltzfus et al., 2020, Qiu et al., 2022, Lozachmeur et al., 2023, Kaur et al., 2023, Schapiro et al., 2017) or for quantifying the spatial distribution of select cell specific markers (Waites et al., 2018). These also focus on identifying discrete cell type identities rather than continuous cell states. In the case of NMPs in the CLE, the epiblast contains differentiating progenitor populations identified by a limited number cell-specific markers. The markers used here, namely Sox2, T, and Tbx6, form spatial gradients and so, as previously described (Chapter 3.2.2), +/- binning based on these markers does not capture the full repertoire of cell states in this system. None of the previously published methods for analysing spatial patterning are suited to address such a dynamic system as the NMP niche, necessitating the development of novel analysis methods.

This chapter aims to explore methods to quantify spatial patterning. This will set the groundwork for using these methods for assessing the effects of manipulating candidate signalling pathways that are hypothesised to regulate spatial patterning. The specific aims are:

1. Develop imaging and quantification pipelines capable of producing high enough quantities of accurately segmented images for statistical analysis.
2. Develop methodologies to graphically visualise the epiblast and mathematically define regions of interest (ROI) within the epiblast, such as the CLE. This methodology must also be consistent, with minimal human input, and capable of directly comparing separate embryos.
3. Develop or repurpose datasets that quantify heterogeneity and patterning of cell states. These measurements must be sensitive enough to pick up fine details in patterning that may suggest the presence or lack of specific patterns that may indicate lateral inhibition or induction.
4. Use randomised simulations to test the hypothesis that patterning of cell states is not random and is instead consistent with ordered spatial patterning mechanisms.

4.2 Results

First, the staining, confocal imaging, segmentation, TF quantification, and data normalisation was extensively optimised for E8.5 embryos. In this chapter, three embryos at E8.5 with ~6 somite pairs (SPs) were dissected (Carried out by Rosa Migueles), cut to isolate the posterior portion (carried out by myself), stained for NMP fate markers Sox2, T, an Tbx6 and imaged with a confocal microscope for analysis (Figure 4.1). Pickcells (refer to Materials and Methods section here) was used to segment the full embryo, quantify the TF intensity, manually label the epiblast (Figure 4.2.a), and perform Delaunay triangulation to identify neighbouring nuclei (between epiblast cells only), after which the TF intensities were manually normalised to each other for some downstream analysis (Figure 4.2.a.).

Pairwise density plots against each TF show each embryos TF profiles closely matched each other and resembles the cultured embryo and gastruloid data (Figure 4.2.b, 3.4a, 3.9a). Clear paths in TF expression between cell states can be observed and many TF profiles in TF space are underoccupied. Like the cultured embryos, using +/- gates from the whole embryo results in very few cells in the epiblast being Sox2-ve (Figure 4.2.b). This may complicate the NMP ROI definition process. Although only three embryos are used in this chapter where the segmentation was manually edited in Pickcells, this pipeline is now capable of accurately analysing many embryos in a semi-high throughput manner.

4.2.1 Different spatial patterning of T, Sox2, and Tbx6 observed in the epiblast.

To first preliminarily ask if any spatial patterning exists in the NMP niche, a raw confocal image of Sox2, T, and Tbx6 in the epiblast was first visually analysed. Anterior posterior gradients of T and Sox2 are apparent in the epiblast (Figure 4.1), and Tbx6 expression appears to arise in the Sox2+/T+ and T+ region and into the primitive streak, consistent with previous reports (Wymeersch et al., 2016, Guillot et al., 2021). When comparing a cell’s expression to neighbouring cells,

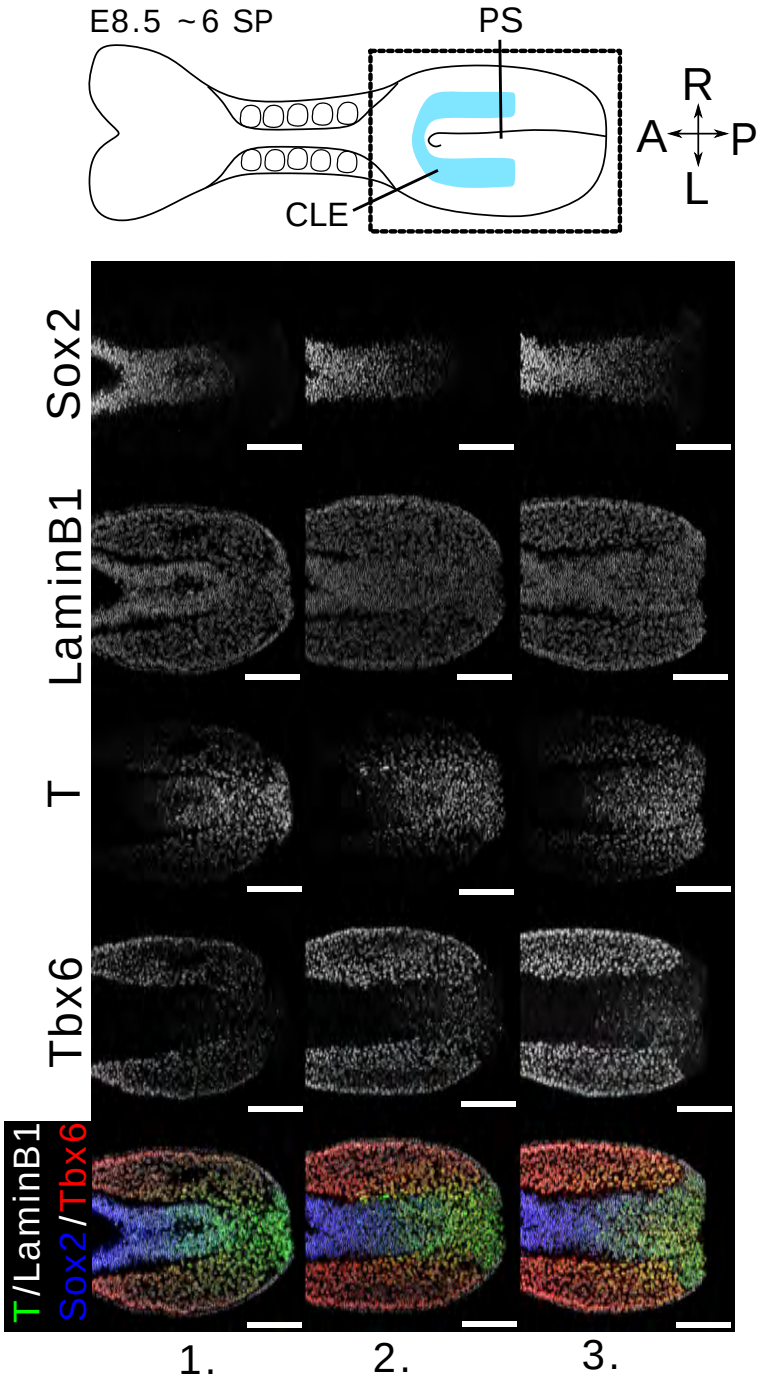

Figure 4.1 E.8.5 raw confocal IF images visual analysis.

Graphic showing view of view and location of NMP location in the caudal lateral epiblast (CLE, blue) and the primitive streak (PS) in the E8.6 ~6 somite pair (SP) embryo. Left/Right and Anterior/posterior axis shown. Three embryos make this dataset. Individual Z slice per image from confocal imaging of IF for Sox2, T, Tbx6 and LaminB1, showing different spatial patterns of TF expression in the CLE by eye, where Tbx6 seems more heterogenous than Sox2 or T. Graphic above showing the epiblast field of view and orientation in relation to the embryo. Scale bars indicate 100um.

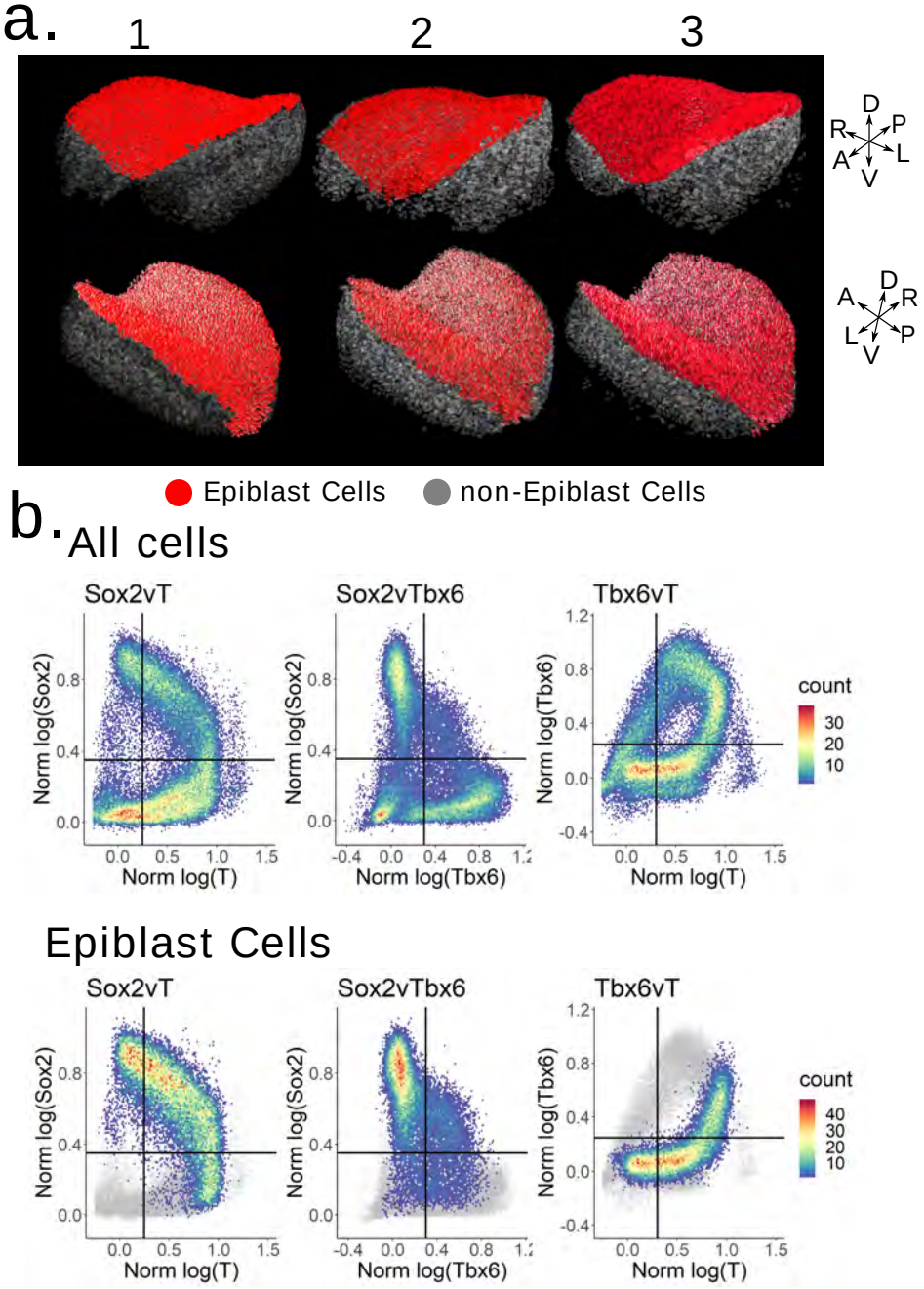

Figure 4.2 TF quantification and normalisation .

a. 3D renders of epiblast cells in red and non-epiblast cells in grey. Epiblast isolation and 3D render carried out in Pickcells. Dorval/Ventral, Left/Right and Anterior/posterior axis shown. b. Pairwise expression of normalised TF in the whole embryo and epiblast cells show clear differentiation paths and low embryo to embryo variability. Positive negative gates (black lines) for each TF found using whole embryo dataset.

neighbouring cells have similar Sox2 content (Figure 4.1). T also has low variability of TF content between neighbours overall but does appear to be somewhat more variable in closer to the midline and in the PS. Tbx6 however looks much more heterogenous, especially around the periphery of where Tbx6 expression first arises.

Overall, Tbx6 expression appears to be much more heterogeneous in the epiblast than Sox2 or T, including within the T/Sox2 coexpression region generally defined as the NMP niche. Other details are difficult to confidently assess by eye and a quantitative approach.

4.2.2 Epiblast normalisation method.

The epiblast of an E8.5 embryo is not a flat structure, but curves and bends in many directions. This makes visualisation difficult since a top-down view will produce artefacts where cells overlap, visualising in this way is not representative of a cell's position in the epiblast relative to each putative developmental axis. Further, separate epiblasts are likely to curve differently and are not the same size with the same cell numbers. This makes it challenging to directly compare epiblasts as they cannot be simply overlaid. Finally, the midline has not been quantitatively described in 3D, this complicates the analysis methods when it comes to assessing the overall success of ROI definition.

A method to render raw images of 3D curved epithelial tissues to a 2D plane using artificial intelligence has been developed (Haertter et al., 2022), but this normalised the raw image not the subsequent data, and has not been challenged with a simultaneously concave and convex structure, as is the case with the epiblast. Further, the subsequent data would still require normalising to allow direct comparison after using this method.

To address these issues, I developed a normalisation method to calculate a cell's relative position to the midline and then flatten the epiblast to allow for direct overlaying and comparisons between epiblasts. The methodology is outlined by the following steps:

1. The epiblast is manually oriented to be roughly perpendicular to the anterior posterior axis, such that the Y axis represents the A-P axis.
2. From the posterior end, cells centroids within +/-25μm (50μm total) along the T axis from the start point are isolated (Figure 4.3.a.i).
3. The slingshot tool (Street et al., 2018) creates a principal curve for the slice isolated in the XZ space giving a position along this curve for each cell (Figure 4.3ai).
4. The midline cells are identified as the average midline position of the top 10% T expressing cells (Figure 4.3.a.ii).
5. Cells position relative to the midline is calculated as being normalised to the average XY principal curve position of midline cells, which is set as zero. Such that cells on either side of the midline will have a positive or negative value.
6. Two metrics are stored, the distance in real μm and the relative position to the midline, and each position as a percentage from the distance to terminal edge of the epiblast.
7. Steps 2-6 are repeated for successive slice in the Y axis with each slice marginally overlapping the previous slice, resulting in each cell multiple relative position values.
8. After a full run through the Y axis, the average of all the recorded relative positions for each cell are used as the final value. An example of midline cells after this process is shown in (Figure 4.3.a.iii).

This method reveals the true shape of the epiblast, where the width of the epiblast is much greater in certain A-P positions which is not reflected in a top-down view (Figure 4.3.a.iii). and is much more representative. Calculating the relative position to the midline and the edge of the epiblast creates a near-rectangular epiblast (Figure 4.3.b).which, after normalising the Y position to the start of the notochord and PS, allows separate epiblasts can be directly overlaid. The start of the Notochord is at 1 on the Anterior-posterior scale.

To reduce the distortion after this transformation, the X axis is retransformed the better reflect the “winged” epiblast shape, producing an idealised epiblast XY graphical display containing multiple epiblasts (Figure 4.3.c). The density of cells in this display is relatively consistent and the coverage of the area does not appear to be biased between replicates (Figure 4.3.c), but there is a slight increase in density to the posterior end (Figure 4.3.d). This is likely due to not including a A-P position normalisation process and the posterior most cells overlay in the top-down view used in the XY normalisation process.

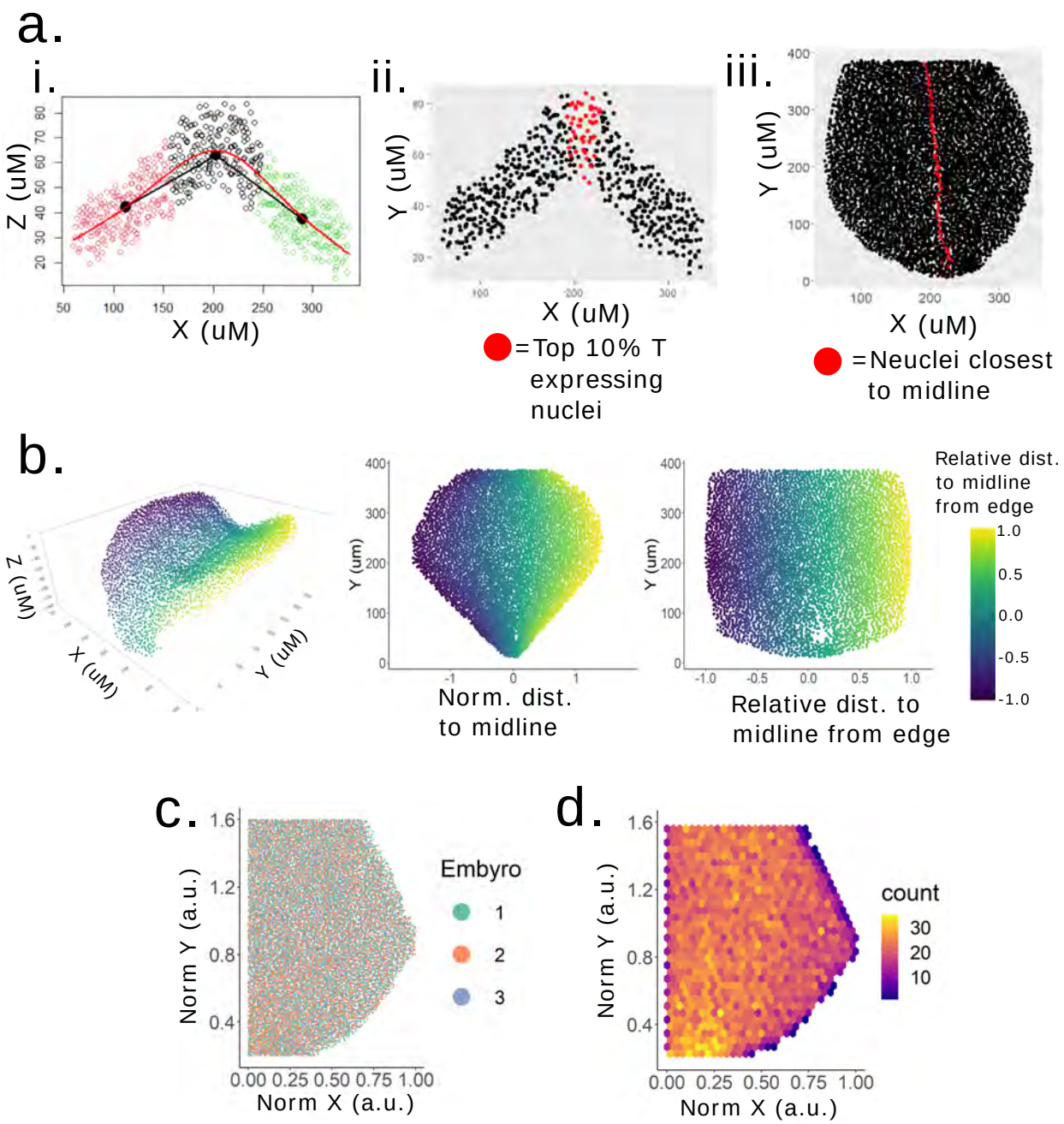

Figure 4.3 Epiblast normalisation method. .

a. Steps in the normalisation algorithm where a segment of the epiblast in the XZ axis is identified, then (i) using the pseudotime tool slingshot (Street et al., 2018) a principle curve is found (red line) between clusters of nuclei (coloured circles) to provide each nuclei a position along the epiblast from left to right. (ii) Then the top 10% T expressing cells are found (red), with the average left/right position fir these cells representing the midline. Cells left/right position are normalised to this. (iii) This is carried out along the length of the epiblast and produces a midline, as shown in a

top-down view of an epiblast with cells closest to the midline in red. b. Multiple views of the epiblast in 3D plot with a raw XYZ values, the normalised distance to the midline, and the relative distance to the midline from epiblast edge. Colour scheme for the three graphs is the relative distance to the midline from epiblast edge metric on a scale from 0 to 1. Overlaying the epiblasts using the relative distance to the midline from epiblast edge allows the epiblasts to be combined, which when retransformed present an idealised epiblast (c.) does not display a bias artefact for any replicate and (d.) is evenly distributed across the Euclidian space.

Overall, this method successfully combines the spatial data for three epiblasts without obvious artefacts and now permits the interrogation of spatial TF expression and pattering.

4.2.3 Characterising the TF gradients in the epiblast

I next sought to ensure the expected TF gradients of T/Sox2/Tbx6 are maintained and quantitively explore them further. The epiblast normalisation presents an opportunity to evaluate the gradients of TF expression more explicitly.

The expected gradients of T, Sox2 and Tbx6 are recapitulated with no obvious artefacts (Figure 4.4.a), Sox2 and T do form opposing gradients around the anterior PS forming the previously described “U-shape” where the Sox2 and T gradients overlap and NMPs reside (Figure 4.4.a). Interestingly, the focal point of the Sox2 gradient appears to emanate from the preneural tube, and as the epiblast widens Sox2 forms a curved diffusing gradient in the lateral epiblast. This does not anti-correlate with T and as such cannot explained by antagonistic activity of T.

T forms a V gradient with a focal point of the length of the PS and extends anteriorly and laterally. The gradient of the T contours is greatest in the CLE just anterior of the PS and the lateral PS region (Figure 4.4.b), with a shallower slope further away from the PS in the PS itself. But the T gradient is increased at the interface with Sox2 in the anterior primitive streak, where a small increase in the Sox2 gradient is also found (Figure 4.4.b.). Indicating Sox2/T interaction creates a sharper T and Sox2 gradient, where the Sox2/T gradients in other lateral areas are more diffuse.

Since tbx6 is downstream of T, one might expect Tbx6 to directly mirror T. However, the Tbx6 gradient focal point appears to be the mid primitive streak, region rather than the whole streak as with T and evenly extends laterally (Figure 4.4.a). The shape of the gradient it different from T as in the Tbx6 gradient decreases posteriorly and anteriorly in a hemisphere around the mid primitive streak. This indicates the gradient of Tbx6 expression does not directly correlate T in all regions.

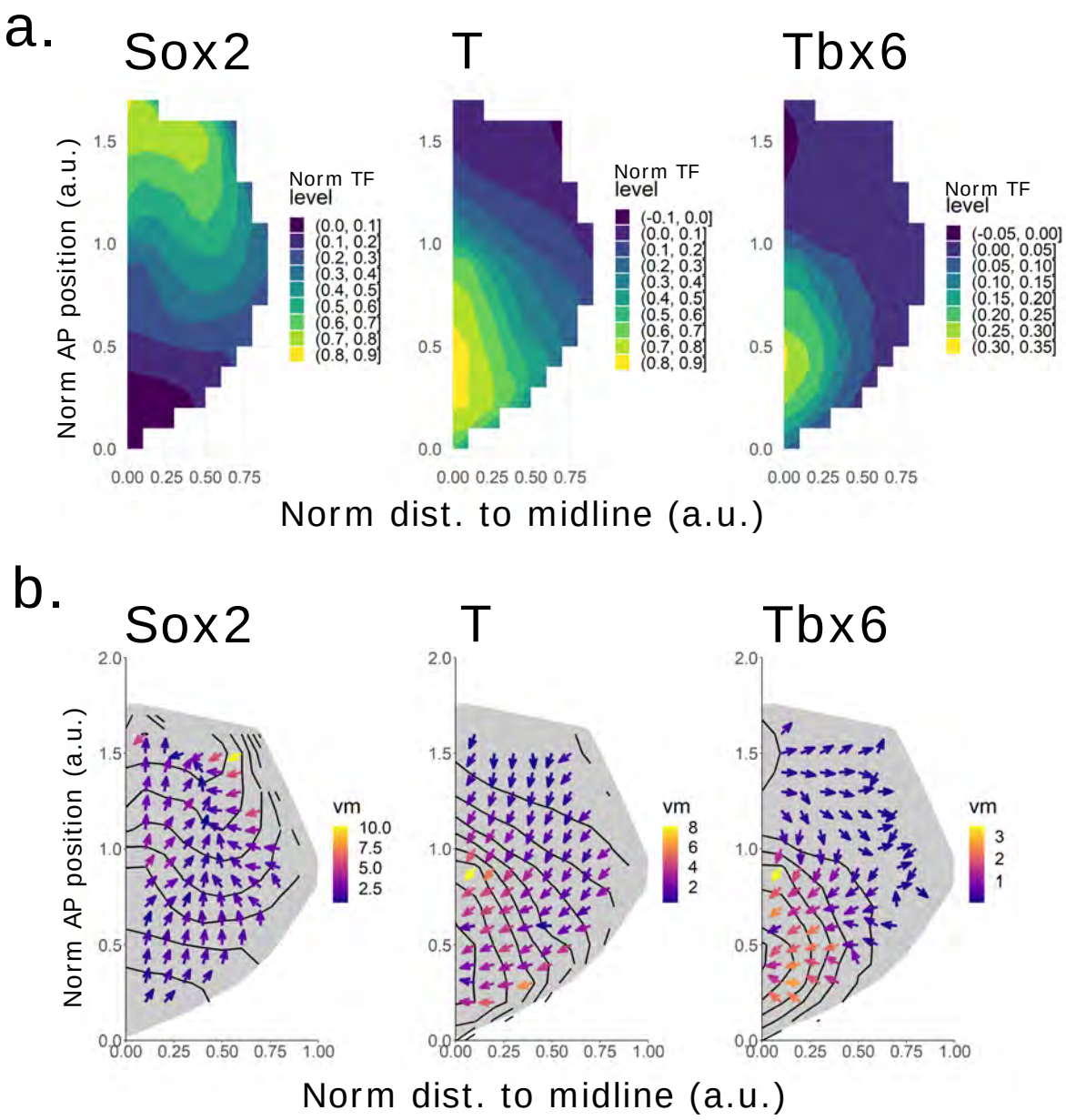

Figure 4.4 TF expression gradient analysis.

a. Contours of expression gradients for each TF in the normalised distance to midline and anterior/posterior position, showing different expression patterns and focal points for each TF b. Quantification of gradient changes and directionality, showing location of increased gradient for T and Tbx6 in the CLE. Colour scale indicates the magnitude of the vector (vm).

Overall, after evaluating the contours of TF expression indicates the epiblast normalisation retained the expected features. Also, this analysis uncovered details in the gradients of each TF to show they are distinct do not directly correlated or anticorrelated in all regions, providing material to speculate as to how the gradients are shaped by signalling morphogens and intracellular GRNs. Further, this provides a challenge to define the regions of ROIs as each TF expression changes across the anterior-posterior and Left-Right axis, mathematically describing the spatial locations of patterning cannot be easily performed.

4.2.4 TF based region of interest definition methods can identify axial progenitor niches.

I next set out to define the NMP niche region relative to other niches in the epiblast in order to examine patterning of cell fates within that region. Instead of focussing on the NMP niche alone, I wanted to use a systems approach and look at the NMP niche relative to the neighbouring niches. It has been proposed that the NMP niche can be defined solely by T+/Sox2+ coexpression at E8.5 with ~4 SPs (Wymeersch et al., 2016, Guillot et al., 2021). However, with this dataset gating as +/- creates a broad region of Sox2+/T+ coexpression (Figure 4.2.b, 4.5.a), extending far beyond the CLE identified from lineage tracing experiments (Cambray and Wilson, 2007, Wymeersch et al., 2016). Further, many cells on the periphery of the T or Sox2 gradients intermingle with non-Sox2+T+ cells and result in an ill-defined boundary. Taken together, other methods to define the NMP ROI using TF expression are required before downstream patterning analysis can be performed.

To address the issue of the ill-defined boundaries that arises from inherent spatial heterogeneity, the intensity values for each TF were spatially smoothed. This was done by multiple rounds of neighbour-based kernel smoothing, which involves iteratively taking the average expression of a cell and its neighbours to increasingly smooth the TF values. Doing so integrates spatial information into TF expression gradients, as such cells close together in smoothed TF Euclidian space are closer together in real space within the epiblast then with the raw TF expression Euclidian

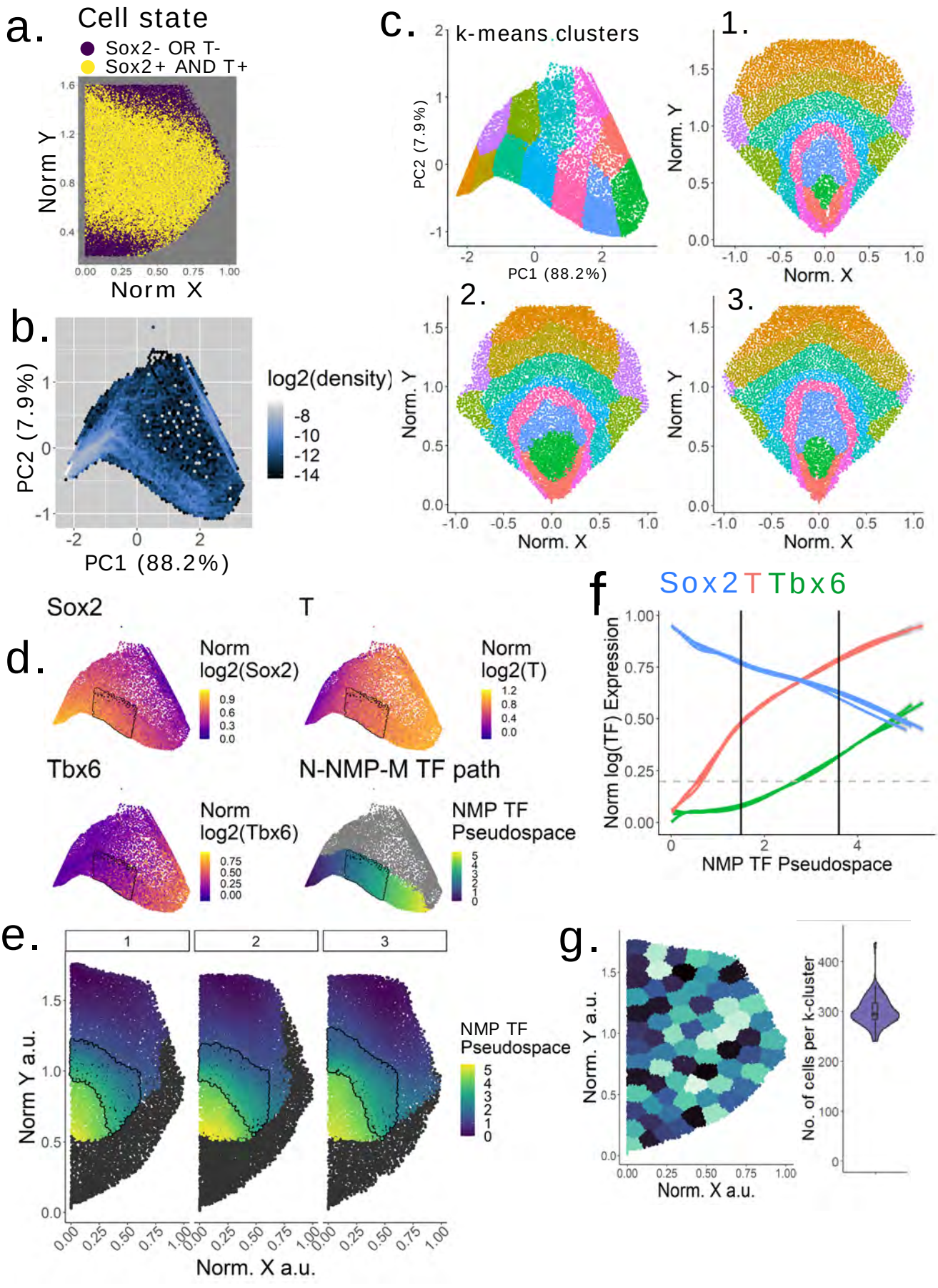
a.
Cell state
Sox2- OR T-
Sox2+ AND T+
Norm Y
Norm X
b.
log2(density)
PC2 (7.9%)
PC1 (88.2%)
c.
k-means clusters
PC2 (7.9%)
PC1 (88.2%)
1.
2.
3.
Norm. Y
Norm. X
d.
Sox2
T
Tbx6
N-NMP-M TF path
Norm log2(Sox2)
Norm log2(T)
Norm log2(Tbx6)
NMP TF Pseudospace
e.
Norm Y a.u.
Norm. X a.u.
f
Sox2 T Tbx6
Norm log(TF) Expression
NMP TF Pseudospace
g.
Norm. Y a.u.
Norm. X a.u.
No. of cells per k-cluster

Figure 4.5 Region of interest definition methods.

a. Sox2+T+ cells covers a broad region with ill-defined boundaries in the epiblast and is not suitable to identify the CLE. b. PCA of spatially smoothed TF values highlights paths in this Euclidian space. Percent explained variances for each principal component displayed. c. K-means clustering of the PCA in 3D PCA space shows regions and paths in the PCA can reproducibly identify separate regions in the epiblast with defined boundaries across each separate embryo in the dataset. d. TF values in the PCA space show the differentiation path from Sox2+ to T+Sox2+ and T+Tbx6+, which is then isolated using Slingshot (Street et al., 2018) and named TF Pseudospace. NMP niche outlined by black line. e. NMP niche as defined along the TF pseudospace recapitulates the Sox2/T bipotent portion of the CLE as described in lineage tracing (Cambray and Wilson, 2007, Wymeersch et al., 2016). NMP niche outlined in black. f. Gradients of TF expression along TF pseudospace replicate expected dynamics. A Loess linear model was used to provide a line per replicate n=3, shading indicates 95% confidence interval for cells within the replicate. Dashed line shows approximate background level. g. unbiased k-means clustering of normalised XY space creates evenly spaced small ROIs of ~300 cells from all epiblasts.

space (data not shown). To define cells along gradients of expression with the smoothed TF values, principal component analysis (PCA) dimension reduction technique (Pearson, 1901) was used to project smoothed Sox2, T, and Tbx6 gradients onto a 2D plane for analysis (Figure 4.5.b). PCA was chosen as it is a linear dimension reduction method and closely retains the structure of the original data. The principal component 1 (PC1) and PC2 of these smoothed TF values show paths overpopulated by cells and correspond to the gradients of TF expression between cell states (Figure 4.5.d). To explore how these paths of expression gradient map onto the epiblast, k-means clustering (Ghoshal et al., 1979, MacQueen, 1967) of the 3D PCA dimension reduction of these smoothed TF values show this Euclidian TF space reproducibly identifies different regions (Figure 4.5.c) in the epiblast with highly defined boundaries, where each cluster from the PCA locates a similar epiblast region between replicates and has limited mixing with other clusters.

A path from Sox2 high, to Sox2+T+, and then T+Tbx6+ can be observed in in the first two principal components (Figure 4.5.d). Using the RNA-seq pseudotime tool Slingshot, this path can be isolated and each cell's position along this Neural-NMP-Mesoderm (N-NM-M) pseudospace axis (TF-Pseudospace) can be quantified (Figure 4.5.b). This provides a unifying continuous metric that describes each TF gradient in units which closely resemble the original TF expression data structure (Figure 4.5.f.)

Rather than a continuous measurement, I next aimed to used TF-Pseudospace to discretely define the CLE for statistical spatial analysis. To find the mesodermal/PS limit, I used the normalised Y position of 1 (the start of the notochord) to define the beginning of the anterior PS. This corresponded to TF Pseudospace 1.5 (arbitrary units). Similarly, the "neural" limit was defined using a combination of the first emerging Tbx6 expression and the normalised X to exclude the more lateral regions. To summarise, the NMP niche is defined as cells between 1.5 and 3.6 TF Pseudospace and <0.6 Norm X from midline (Figure 4.5.e). This recapitulates a ROI similar to the reported bi-potent region of the CLE (Cambray and Wilson, 2007, Wymeersch et al., 2016) across all embryos (Figure 4.5.e), containing T+/Sox2+

cells at the location of Tbx6 expression emergence (Figure 4.5.d,f). Although the exact locations and boundaries of the NMP ROI do not exactly match between embryos, the gradients of normalised TF values along TF pseudospace are reproducible so the ROI contains cells of a similar TF state (Figure 4.5.e). The analysis can be performed along TF pseudospace to find trends in patterning while the discretised NMP region can provide data linked to the lineage tracing data.

For a more unbiased approach and to include other axial progenitor niches, k-means clustering of the normalised X and Y position creates evenly spaced groups of ~300 cells and ~100 cells per embryo (Figure 4.5.g). After this, each cluster can be individually evaluated for analysis and displayed on the normalised X and Y position and the NMP ROI, among other niches, will be evaluated exclusively by relative proximity to the midline and relative position from the notochord to the end of the PS.

Overall, this work produces two methodologies that can be used to identify the CLE and other axial progenitors as discrete regions of interest or along a N-NMP-M gradient. The two approaches give similar results and can be used to directly compare regions of interest across different embryos to allow for statistical analysis. Both approaches shall be carried forward for downstream analysis to explore if either proves to be superior.

4.2.5 Spatial patterning analysis suggests highly heterogenous T and Tbx6 patterning exists in NMP niche.

Work described so far indicates that the NMP niche can be identified and the epiblast can be graphically visualised. This sets the groundwork for assessing whether the emerging mesoderm is arranged into a spatial pattern within ROIs.

Lateral inhibition creates heterogeneity where cells of one identity are surrounded by cells of a different identity. To assess if any TF-defined cell states arrange into this pattern, the number of neighbouring cells that are TF+ as a percentage of all neighbours was measured for each cell. This shows that there is a broad region

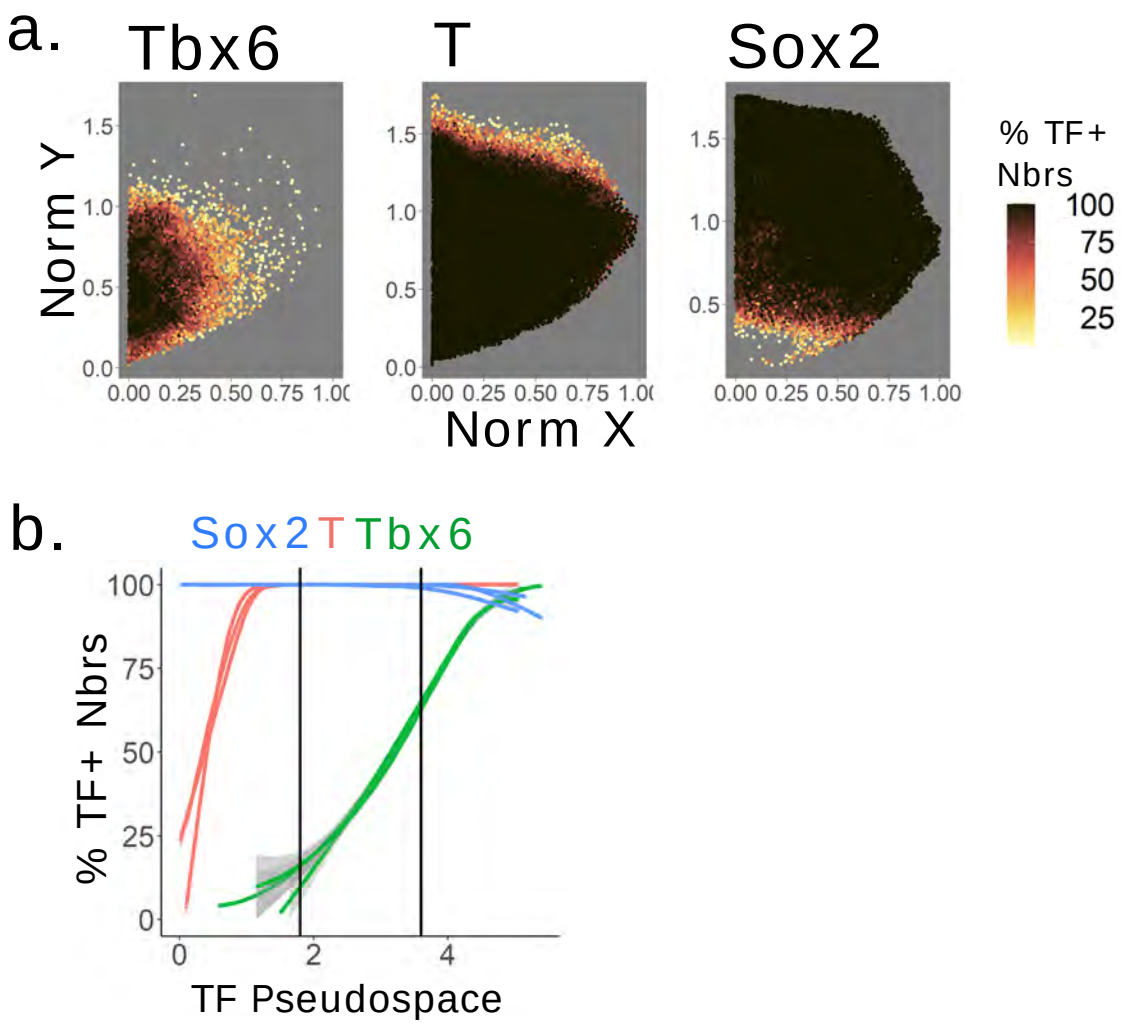

Figure 4.6 Number of TF+ neighbour analysis.

a. The number of TF+ neighbours as a percentage of total neighbours in the normalised XY view. b. A quantification of TF+ neighbour percentage along TF-pseudospace shows difference in T and Tbx6 gradients from low TF+ to high TF+ percentage. A Loess linear model was used to provide a line per replicate n=3, shading indicates 95% confidence interval for cells within the replicate.

where Tbx6+ cells have no or few Tbx6+ neighbours (Figure 4.6a.), whereas T+ or Sox2+ cells have small region as the end of their respective gradients which have few same-TF+ neighbours. Displaying this quantification along TF-pseudospace shows that the gradient of from 0 to 100% TF+ neighbours is much shallower than Sox2 or T and the Tbx6+ cells in the NMP niche have on average between 10-60% Tbx6+ neighbours (Figure 4.6.b). This analysis suggests that early mesoderm cells, defined as Tbx6+ cells, arising in the NMP niche have few or no Tbx6+ neighbours, which is consistent with a theoretical lateral inhibition model. However, the previous analysis shows there is much detail in TF expression across the full expression range that is lost during discretisation.

To statistically test if the patterning of any TF patterning metric is random or non-random, as in an enforced lateral inhibition spatial pattern, a randomised simulation of TF expression was first created for a null model comparison. In this simulation, each cell's TF expression (S) was generated using the normal random variable generator function "rnorm" (van den Boogart, 2019) in the R language (2021), where the generator provides a value from a normal distribution with the average (μ) and standard deviation (σ^2) of TF values of a cell and its neighbours. Defined as $S=N(\mu,\sigma^2)$ where N is a normal distribution generator function. I used this approach to ensure that the levels of TF expression and degree of local variability in each region of the simulated dataset matched that in the observed data. It is important to maintain spatial heterogeneity since we do not know the source of heterogeneity. The key difference is now the simulated values follow a normal distribution.

To validate the simulation accurately recapitulated the observed dataset, I compared them across the previously identified analysis methods. Pairwise comparison of TF expression compared to the synthetic TF values show a close linear correlation for Sox2 and T, whereas a looser linear correlation with Tbx6 was observed (Figure 4.7.a). However, the average expression for each simulated TF closely correlated with the gradients of raw TF along the TF-pseudospace axis (Figure 4.7.b). No consistent significant difference between the simulated or raw TF values can be found in the epiblast (Figure 4.7.c.ii) and the spatial gradients closely match that of

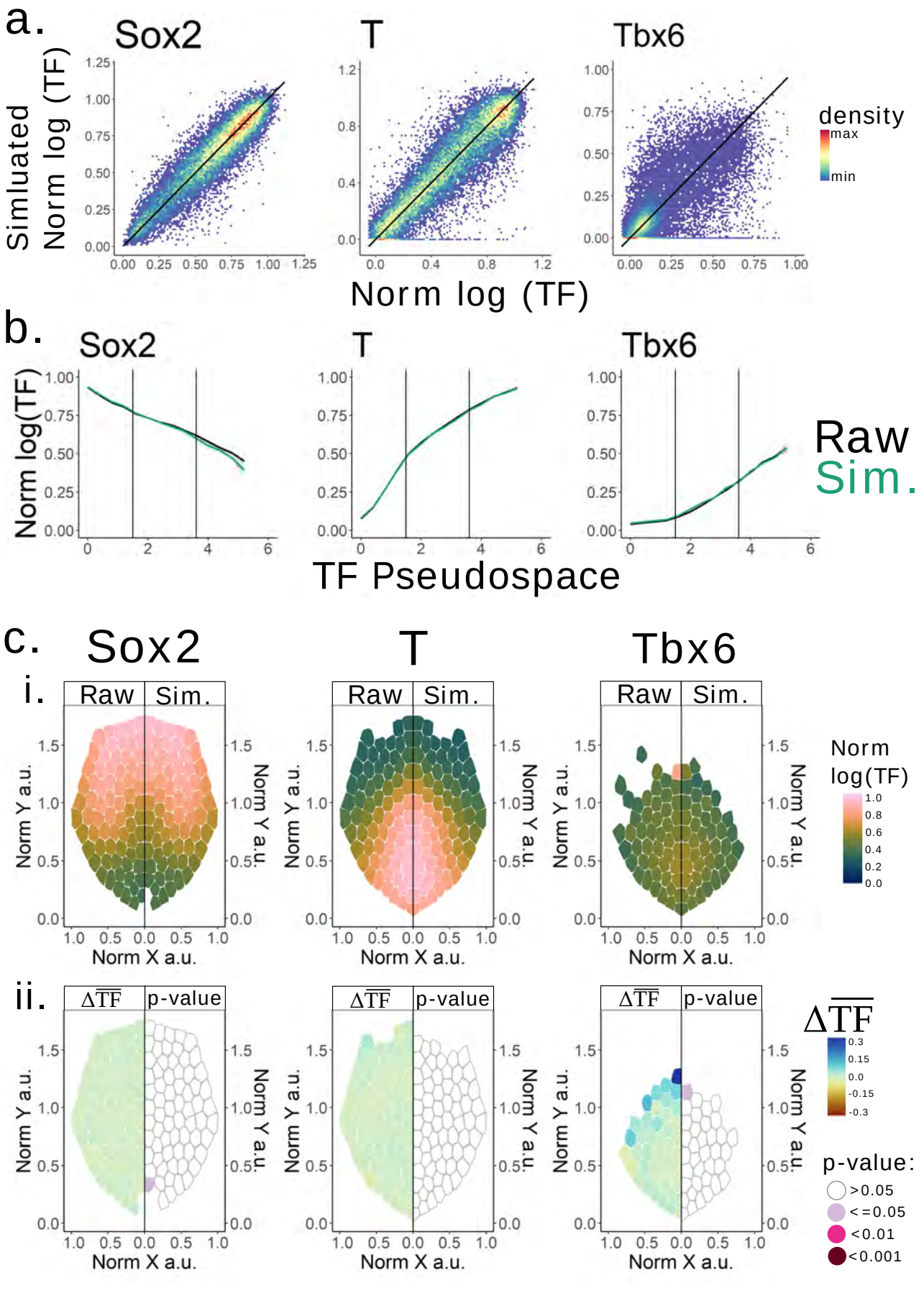
a.
Sox2
T
Tbx6
Simluated Norm log (TF)
density
max
min
Norm log (TF)
b.
Sox2
T
Tbx6
Norm log(TF)
Raw
Sim.
TF Pseudospace
c.
Sox2
T
Tbx6
i.
Raw
Sim.
Norm Y a.u.
Norm X a.u.
Norm log(TF)
ii.
ΔTF
p-value
p-value:
>0.05
<=0.05
<0.01
<0.001

Figure 4.7 Simulation of TF values recapitulates observed TF gradients.

a. Using the rnorm package in R (Team, 2021, van den Boogart, 2019) the TF for a nuclei was simulated based upon the mean and standard deviation of TF expression between a cell and its neighbours (similar to Figure 4.8a) assuming a normal distribution. See main text for equation. Pairwise density plots of simulated vs raw TF values with the x=y line in black. b. Average raw and simulated values along psuedospace, shaded area indicates 95% confidence interval. c. Using the k-clustering XY method, the average observed and simulated TF value for each cluster compared in space, with the difference in means and statistical significance between each cluster. Statistical analysis performed by one way ANOVA.

the raw values (Figure 4.7.c.i). Overall, the simulation was successful in recapitulating the observed TF gradients.

To formally quantify the level of heterogeneity between a cell and its neighbours, which would be enforced and heightened by lateral inhibition or limited by lateral induction, the coefficient of variation (CV) of TF expression for a cell and its neighbours was used as a dimensionless continuous metric of variation (Figure 4.8.a). Using a dimensionless variation metric is useful as it is a measure of variability relative to local expression, standard deviation or confidence interval measurements would be influenced by larger numbers and would also require the data to be normalised before comparison between replicates or genes. This will also capture detail lost during discretisation. For CV analysis, only TF+ve cells are included for each gene. For example, when evaluating Tbx6 CV, only Tbx6+ve nuclei are included.

Comparing the CV between TFs within the NMP niche, as defined by TF-Pseudospace, shows that Tbx6 is significantly more variable than T or Sox2, and T is significantly more variable than Sox2 (Figure 4.8.b). This recapitulates my previous visual observation that Tbx6 was more variable than Sox2 or T. This quantitatively confirms that indeed T is more variable than Sox2, which was unclear by eye.

I then asked how this patterning changes across the TF-Pseudo space axis to evaluate if this is unique to the NMP niche. T increases in CV into the NMP niche and decreases into the PS (Figure 4.8.c). Similarly, CV for Tbx6 is high when it emerges in the NMP niche and like T decreases in the PS. Interestingly, the CV for T is lower when it arises along its gradient compared to the peak in the NMP niche. Overall, this analysis shows the NMP ROI is a region of increased CV for T and Tbx6 but not Sox2.

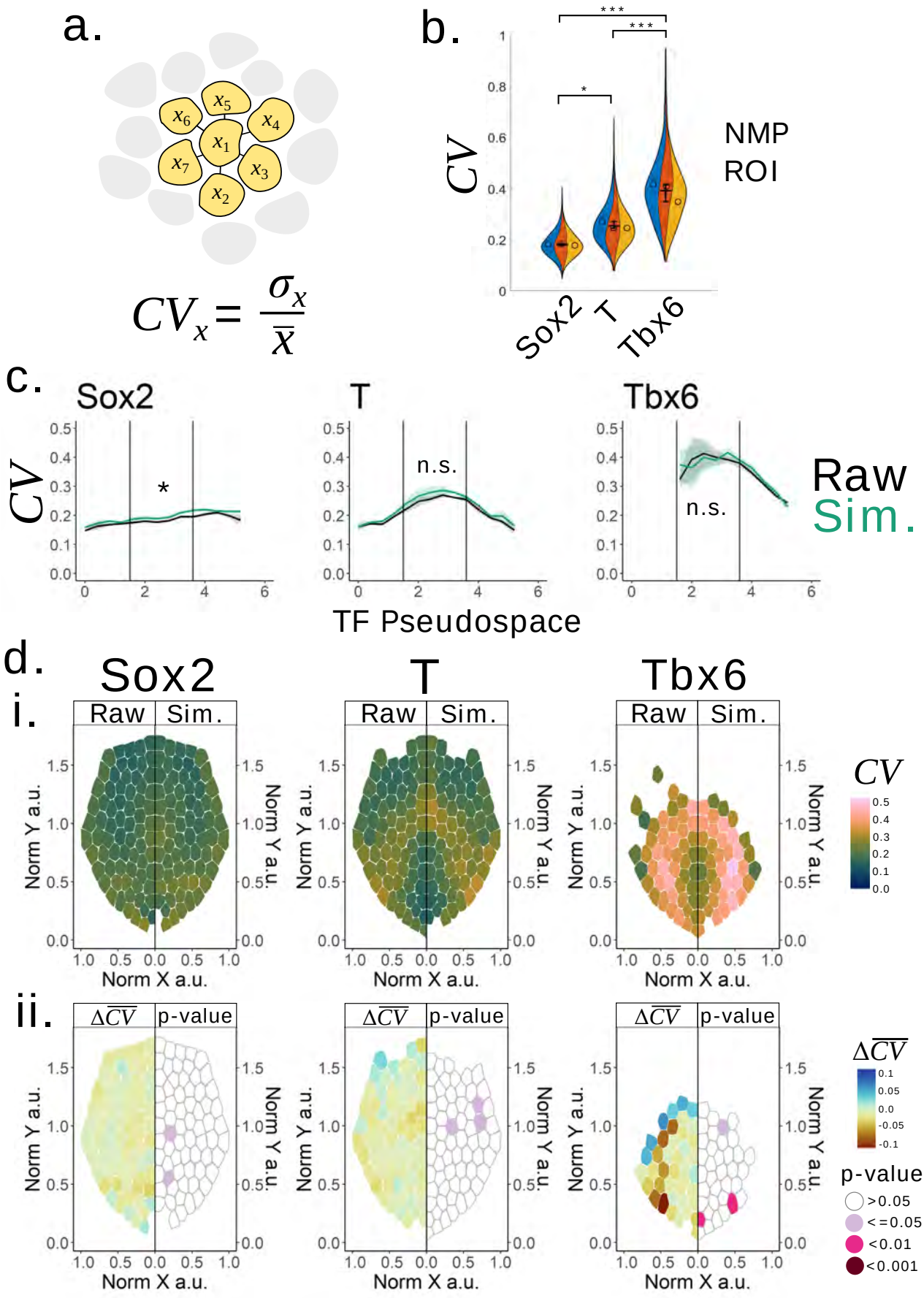
a.
x_1
x_2
x_3
x_4
x_5
x_6
x_7
$CV_x = \frac{\sigma_x}{\bar{x}}$
b.
CV
NMP ROI
Sox2
T
Tbx6
c.
Sox2
T
Tbx6
CV
*
n.s.
n.s.
Raw
Sim.
TF Pseudospace
d.
Sox2
T
Tbx6
i.
Raw
Sim.
Norm Y a.u.
Norm X a.u.
CV
ii.
$\Delta\overline{CV}$
p-value
$\Delta\overline{CV}$
p-value:
>0.05
<=0.05
<0.01
<0.001

Figure 4.8 Coefficient of variation to measure heterogeneity.

a. Coefficient of variation (CV) between a cell and its neighbours. b. Comparing T, Sox2, and Tbx6 in the NMP niche with Violin Superplots shows Tbx6 is significantly higher than T/Sox2, and T is significantly higher than Sox2. Statistical analysis carried out using Tukey's HSD test, Error bars show standard error. c. Average raw and simulated values of CV along psuedospace, shaded area indicates 95% confidence interval. Black lines indicate the NMP niche defined by pseudospace. Statistical analysis between raw and simulated CV values within the NMP niche. ***=$p<0.001$, ** = $p<0.01$, *=$p<0.05$. d. Using the k-clustering of normalised XY method, the average observed and simulated CV value for each cluster and TF is compared, with the difference in mean CV and statistical significance between each cluster. Statistical analysis for c. and d. performed by one way ANOVA.

I next asked how local variability in cell states differs between different regions across the whole epiblast. Although the pattern of CV is similar for T and Tbx6, where CV is heightened in the NMP niche and decreases into the primitive streak (Figure 4.8.c), closer inspection across the whole epiblast revealed that peak Tbx6 variability is located as a ring around the PS as it first emerges ((Figure 4.8.di). This does not directly reflect the increased variation in T, which appears to be V shaped (Figure 4.8.d). This indicates that the increase in CV for T and Tbx6 may not be directly linked as they occur along specific regions of their own expression gradients but overlap in the NMP niche.

Next, calculated the CV for a cell and it's neighbours simulated TF values. Then, I evaluated if the CVs of the simulated data were significantly different from the observed data. Along the TF pseudospace, the CV for each TF in either dataset showed similar trends with no significant difference for T or Tbx6 within the NMP ROI (Figure 4.8.c). Across the epiblast, no consistent difference in CV for any gene can be found with very few XY clusters showed a significant difference (Figure 4.8.d). Overall, as intended this analysis shows the simulated values recapitulate the raw TF expression gradients and variation.

In summary, my novel analysis methods show that Tbx6 and T have increased local heterogeneity in the NMP niche compared with other regions in the epiblast, but the heterogeneity for each TF extends along the gradient of expression and is not unique to the NMP niche.

4.2.6 Tbx6 patterning in the NMP niche is significantly different to randomised control.

Local variability in cell identities could be consistent with a lateral inhibition mechanism driving differentiation, but it could also be consistent with stochastic emergence of different cell fates. I therefore next asked if the cell id entities in variable regions were organised in a random or non-random pattern.

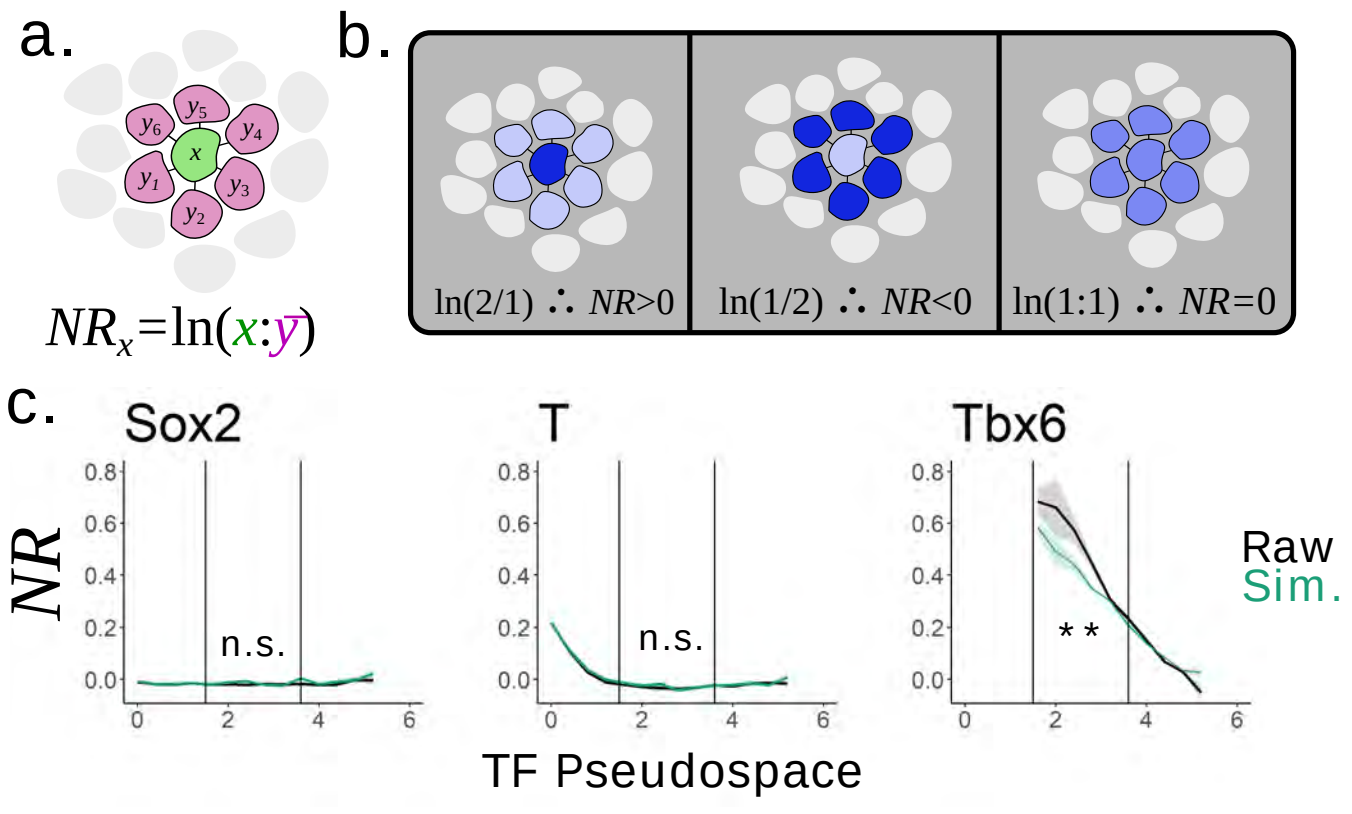
a.
y_5
y_6
y_4
x
y_1
y_3
y_2
$NR_x = \ln(x:\bar{y})$
b.
ln(2/1) ∴ NR>0
ln(1/2) ∴ NR<0
ln(1:1) ∴ NR=0
c.
Sox2
T
Tbx6
NR
n.s.
n.s.
* *
Raw
Sim.
TF Pseudospace
d.
Sox2
T
Tbx6
i.
Raw
Sim.
Norm Y a.u.
Norm X a.u.
NR
ii.
ΔNR
p-value
ΔNR
p-value:
>0.05
<=0.05
<0.01
<0.001

Figure 4.9 Cell to neighbour ratio (NR) to measure lateral inhibition type patterning.

a. Graphic showing NR calculation as the natural log of a cells TF expression divided by the average neighbouring TF expression. b. Graphic outlining scenarios which result in NR values >0, <0, or =0. Lateral inhibition could result in NR >0 or NR<0, lateral induction may result in NR=0. c. Average raw and simulated values of NR along psuedospace, shaded area indicates 95% confidence interval. Black lines indicate the NMP niche defined by pseudospace. Statistical analysis between raw and simulated NR values within the NMP niche. ***=p<0.001, ** = p<0.01, *=p<0.05. c. Using the k-clustering XY method, the average observed and simulated NR value for each cluster and TF is compared, with the difference in means and statistical significance between each cluster. All statistical analysis performed by one way ANOVA.

I sought to use a metric of heterogeneity that is indicative of lateral inhibition to allow quantitative statistical testing for random or non-random heterogeneity. In a lateral inhibition context, a cell's neighbours would have reduced fate marker TF expression compared to itself. To quantify if a cell has disproportionally higher TF expression compared to its neighbours, the ratio of TF expression to the average neighbour expression was used as unitless relative metric (Figure 4.9.a), termed neighbour ratio (NR)(as defined in the methods section 2.2.7.4). NR uses the natural log ($\ln$) of the ratio between a cells TF expression (C_{TF}) and its neighbours (N_{TF}) to achieve symmetry around 0 for changes in C_{TF} or N_{TF}, such that $\ln(C_{TF} / N_{TF}) = -\ln(N_{TF} / C_{TF})$. As outlined in Figure 4.8.b, NR=0 means the values for the source cell and neighbouring cell expression are the same [ln(1)], NR >0 indicate neighbouring cells are lower than the source cell [ln(>1)], and NR<0 means the source cell TF is lower than its neighbouring cell TF [ln(<1)].

Within the NMP niche defined by TF-Pseudospace, average NR for Sox2 and T is ~0, but Tbx6 is >0 (Figure 4.9.c). The overall trends of NR for all TFs appear to be >0 at the low end of their respective gradients, but NR for Tbx6 is three-fold higher than T or Sox2 in these regions (Figure 4.9.c). This indicates that the nature of heterogeneity in the NMPs niche for Tbx6 arises by high expressing cells surrounded by low Tbx6, which is consistent with a lateral inhibition model but is not the only possible explanation.

Interestingly, the NR for T is consistently ~0 in the NMP niche and into the PS (Figure 4.9.c) despite increased heterogeneity in the NMP niche as measured by CV (Figure 4.8.c). This suggests the increased T heterogeneity is created both equally high and lower T cells surrounded by lower and higher expressing T respectively. Overall indicating the nature of heterogeneity for T and Tbx6 in the NMP niche is different.

Finally, I calculated the NR values for a cell's simulated TF value relative to its neighbours and assessed if the Tbx6 NR in the NMP niche was significantly different from the null model simulation, which is produced randomly generated from a normal distribution. The average NR for Tbx6 in the NMP niche, defined by TF-

Pseudospace, is significantly higher than the simulated random control (Figure 4.9.c), which is not the case for T or Sox2. Using the clustering analysis method for the whole epiblast, an increase in Tbx6 NR within the NMP niche for the observed data compared to the simulated control is observed (Figure 4.9.di), but this effect did not consistently reach significance in this region (Figure 4.9.dii).

In summary, NR values for Tbx6 in the NMP were significantly increased compared to the simulated control. This indicates the increased local heterogeneity for Tbx6 arises from high Tbx6 cells neighbouring low Tbx6 expressing cells, and the difference in local heterogeneity compared to a null model of gene expression, that follows a normal distribution, is statistically significant ($p<0.01$). Such a pattern could be expected in a theoretical lateral inhibition mechanism, where Tbx6 cells down regulate Tbx6 expression in neighbouring cells.

4.3 Discussion:

From Haston (2018) and the previous chapter, there is evidence that Notch signalling controls mesoderm differentiation in NMPs, but the regulatory strategy is unknown. The general aim of this chapter was to develop quantification methods to explore whether the emerging mesoderm organises into spatial patterns consistent with lateral inhibition.

4.3.1 Epiblast normalization and ROI definition strategies as novel methods to analyse the axial progenitors in the epiblast.

Describing spatial regions in the epiblast is a challenge for novice researchers or people unfamiliar with embryology. Understanding the locations of specific tissues requires a lot of prior knowledge and, due to the curvature of the epiblast, designing easy to understand diagrammatic depictions or graphical data representations is challenging. Even for experts, it can be challenging to compare quantitative datasets between different embryos in an unbiased manner.

The epiblast normalisation method I develop here (section 4.2.2) provides a much-needed way to transform the epiblast from 3D into manageable 2D data structures, allowing consistent and accurate representations of spatial data for future studies.

Another methodology to convert curved structures to 2D planes have recently been published (Haertter et al., 2022) and may work well with this dataset. However, as mentioned this has not been tested on concave and convex epithelia. Also, a strength of my method is the normalisation process where separate curved structures can be overlaid after normalising to axes, such as the midline. Also, it could be argued that another strength of this method is the ease of use, as it does not require technical knowledge into machine learning and only uses simple tools in the widely used open-source programming language R Team (2021).

While this is a useful tool to visualise the epiblast in a comprehendible way, my experiments suggest that statistical analysis of patterning is better performed on ROIs defined by TF expression rather than position with respect to landmarks. The positional information conferred to grafted cells in lineage tracing studies (Wymeersch et al., 2016, Cambray and Wilson, 2007) is likely to be dependent on the cell state makeup of the acceptor region. I have shown there are variations in the gradients of TFs between embryos (Figure 4.5.c,e), so TF based definitions of regions are likely to be needed to accurately describe a ROI, not just the relative positions in relation to landmarks. This is accounted for in the smoothing analysis method that combined TF expression and real space, incorporating neighbouring cell information, to define ROIs. The variation between embryos for the TF-Psuedospace method was minimal across all metrics used which allowed statistical significance to be achieved when testing hypotheses, whereas the discrete clustering method did not (Fig 4.8).

Overall, more work should be done to further optimise both analysis methods and integrate other spatial patterning methodologies, but the methods described are a sufficient to accurately define regions of interest in the epiblast and provide intuitive graphical representations of their relative position in the epiblast.

4.3.2 T, Sox2, and Tbx6 have distinct spatial patterns.

The dynamics and upstream regulatory mechanisms for Sox2, T, and Tbx6 are not the same, so it is no surprise that they organise into separate distinct patterns.

However, as Tbx6 is a direct target of T (Koch et al., 2017) and both are targets of Wnt (Yamaguchi et al., 1999, Dunty Jr et al., 2008, Blassberg et al., 2022), one would expect their expression patterns to be similar. Indeed, the trends in spatial patterning of T and Tbx6 are similar, but the data presented in this chapter suggests they are distinct spatial patterns.

First, the CV for Tbx6 is significantly higher than T in the NMP niche (Figure 4.7). Second, the CV patterns of T and Tbx6 do not perfectly spatially correlate; Tbx6 forms a ring of peak CV around the PS whereas T forms a V shape that extends to the edge of the epiblast (Figure 4.4). Third, the NMP niche is the site of Tbx6 expression emergence where NR >0, whereas T NR~0 (Figure 4.9), indicating the type of increased variation measured by CV is fundamentally different. Since Tbx6 is downstream of T, it is possible that the source of variation in T feeds into Tbx6, which is then increased further by another mechanism downstream of T, such as lateral inhibition, not associated with T.

4.3.3 Potential non-signalling sources of local heterogeneity for T and Tbx6.

Both T and Tbx6, but not Sox2, showed an increase in at certain points in their expression gradients, which overlapped in the NMP niche, that decreased into the PS or towards the neural tube (Figure 4.7.c.). The key question is what is the source of this variation? CV is a dimensionless metric used to describe heterogeneity. This encompasses all sources of gene expression variation between neighbouring cells, providing an unbiased description of the overall state of TF heterogeneity in the epiblast.

Motility and neighbour exchange are obvious candidate contributors to local heterogeneity. It is known that cell motility and neighbour exchange is high in the PS and CLE NMP niche where motility is increased in T expressing cells (Romanos et al., 2021, Guillot et al., 2021, McDole et al., 2018). This would theoretically lead to higher local heterogeneity in PS and CLE, not the decrease observed in T and Tbx6 in the PS. It is possible CV would be low if a population of cells expressed very

similar TF levels even with high motility and neighbour exchange, which might explain the decrease in CV for T where cells all express near maximal levels of T in the PS (Figure 4.5.f). However, this is not the case for Tbx6 as maximal levels are not reached till mesoderm fated cells exit leave the epiblast (Figure 4.5.f), so the decrease in CV cannot be explained by this. Similarly, the directionality and synchronicity of motility would theoretically be key for variation, where if asynchronous motility is mostly parallel to the TF gradients, this would not result in increased CV even with high neighbour exchange as cells with similar TF profiles would mix. Whereas asynchronous movement perpendicular to the TF gradient would result in high CV. However, Sox2 CV is consistently low in all regions across its gradient and not heightened in the NMP niche as T and Tbx6 is. There is a small increase in CV for Sox2 into the PS (Figure 4.8.c.), perhaps representing the extent of contribution to CV from cell motility.

While it is highly likely motility is creating some variation, the difference in CV for each TF in the NMP niche suggests that motility, or another universal source of variation, is not a responsible for the CV trends, rather that heterogeneity in T and Tbx6 within the NMP niche is the result of distinct spatial patterning mechanisms not controlling Sox2 expression. Again, raising the question as to what type of patterning mechanisms these may be.

4.3.4 Potential signalling mechanisms to drive T and Tbx6 heterogeneity.

For T, the NR of 0 with a high CV indicates the presence of a source of local heterogeneity which does not create patterns statistically significant from the null model of gene expression, arising from a normal distribution (Figure 4.9). Independent oscillations of T expression could explain the NR of 0 but high CV, where there is no bias in the ratio of cell:neighbour expression but high overall local variation. Since feedback loops often overcorrect and sometimes lead to oscillations (Snoussi, 1998, Del Vecchio et al., 2016, Ananthasubramaniam and Herzel, 2014), the GRN with Wnt/FGF positive feedback and Sox2 negative feedback on T may create overcorrections in expression, where the set T value of the expression

gradient may be dictated by the balance Wnt/FGF and RA as previously posited (Gouti et al., 2017). This would require further mathematical exploration in the steady state dynamics and stability of the GRN, as this effect is limited to T and no variability in Sox2 was observed. Also, whether sustained oscillations are present again would require further mathematical exploration of the GRN and perhaps live imaging of T expression levels in time.

Notch may be involved in spatially regulating T. I showed Notch signalling promotes T and that T expression correlates with Jag1 expression in the previous chapter, Notch signalling via Jag1 may contribute to homogenise local T expression via lateral induction with Wnt/FGF. This cannot be explained by the theoretical interactions between NMP TFs and Wnt/FGF/Notch, with evidence for upstream Wnt/T/Tbx6/Msgn1 positive regulation of Dll1, Jag1, Notch1, Notch3. But now with data from Haston (2018) and Chapter 3 in this thesis, Notch appears to have a pro-mesodermal effect upstream of T/Tbx6, and therefore implicated in the Wnt/FGF positive feedback loop sustaining NMP identity and mesoderm differentiation. However, further experimental evidence is required to eliminate possibilities.

Tbx6 CV is higher than T in the NMP niche (Figure 4.8.b) and higher than Sox2 or T at the low end of their respective gradients (Figure 4.8.c), which suggests that heightened Tbx6 variation is not characteristic of the tail end of TF gradients and not only a consequence of variation from T. Further, while NR is elevated for all TFs in the low end of TF gradients, only Tbx6 NR was significantly increased when compared to the randomised simulation (Figure 4.,8.,9c). This suggests that given the variability, Tbx6 expression is disproportionally lower in cells neighbouring a cell expressing high Tbx6 when compared to a randomised scenario. This is consistent with Dll1 mediated lateral inhibition, which in this case would be Tbx6/Dll1 expression laterally repressing mesoderm fate in neighbouring cells. It is not clear how this observation can be explained by alternative mechanisms aside from artefacts in the measurement and simulation analysis. However, it is not yet certain whether Notch is directly downregulating Tbx6 in the context of NMPs, but it has been suggested Notch may only upregulate Tbx6 in the PSM and not PS (White et al., 2005). Further, while I showed that Dll1 was shown to be negatively regulated by

Notch signalling, I also showed Notch positively regulates T/Tbx6 expression, so it is not possible to confirm the presence of lateral inhibition with this data.

4.3.5 Summary.

Overall, this chapter demonstrates how the novel spatial patterning analysis methods I developed can be used to dissect the differences in patterning between closely associated TFs in the epiblast, showing that Sox2, T, and Tbx6 have distinct spatial patterning. Further, it can be concluded that heterogeneity is a feature of the NMP niche for both T and Tbx6 expression, but the source is unclear. Mathematical modelling of different patterning mechanisms, such as lateral inhibition or intrinsic gene expression oscillations, would be beneficial to suggest the sources of variation in each instance. This is essential to explore how the different spatial patterns manifest given the complex intracellular GRN. This analysis provides a platform for further investigations to manipulate signalling pathways to measure changes in patterning, which is the focus of the next chapter.

Chapter 5:

Exploring TF spatial patterning within NMP niches after Notch inhibition.

In the previous chapter, I explored methods to quantify the spatial patterning of TFs within the E8.5 epiblast, showing distinct gradients and patterning for Sox2, T and Tbx6 expression. Regions of increased heterogeneity for Tbx6 and T coincided in the NMP niche, and the local Tbx6 expression heterogeneity was statistically significantly different when compared to a null model of random gene expression. The mechanisms that explain this heterogeneity remain unknown. One possible mechanism could be lateral inhibition mediated by Notch receptors: this would be consistent with the observed Tbx6 patterning. To investigate whether Notch mediates lateral inhibition, and creates the observed heterogeneity, requires experiments in which Notch activity is manipulated.

The methods presented earlier in this thesis for quantifying patterning should be well suited to investigating the effect of Notch inhibition on TF spatial patterning. This chapter aims to implement these spatial analysis methods extending them to notch inhibition models of NMP culture to test if any measurable effect occurs. Specifically:

1. Apply epiblast normalisation and spatial analysis methods to the ex vivo culture of E8.5 embryos to explore whether patterning is altered in the presence of Notch inhibitors.
2. Similarly, extend the spatial analysis methods to gastruloids as a model of NMP self-organisation to quantify changes in pattering in the presence of Notch inhibitors and infer fundamental processes of patterning related to Notch signalling.

5.1 Results

5.1.1 Heterogeneity and patterning analysis in Notch inhibited E8.5 epiblast.

To carry out the first aim, I applied the analysis pipeline from Chapter 2 to the dataset from Chapter 1 (see section 3.2.2), where posterior portions of E8.5 embryos were cultured for 12 hours with DMSO or the Notch inhibitor LY. As in the previous chapter, Pickcells was used to manually labelled and isolate the epiblast epithelia and the neighbours of cells in the epiblast only were inferred with Delaunay triangulation.

5.1.1.1 NMP ROI definition in DMSO control and Notch inhibited epiblasts.

First, the epiblast normalisation method previously described was utilised to visualise this data. During the 12-hour culture, the epiblast in all embryos had undergone further conformational changes where the posterior section around the primitive streak began to curl and the neural folds became steeper (Figure 5.1a). As such, this dataset provided an increased challenge for the epiblast normalisation procedure due to increased curvature along multiple axis. Because of this, an additional step was included for this dataset to provide a more representative anterior-posterior position; I calculated the centroid of each cell along a principal curve in the YZ axis instead of the Y axis from the raw confocal image. While some artefacts were produced when calculating the distance of a cell to the midline, especially in the most posterior regions, this methodology was successful in flattening the epiblast to provide a 2D representation of each epiblast (Figure 5.1.b).

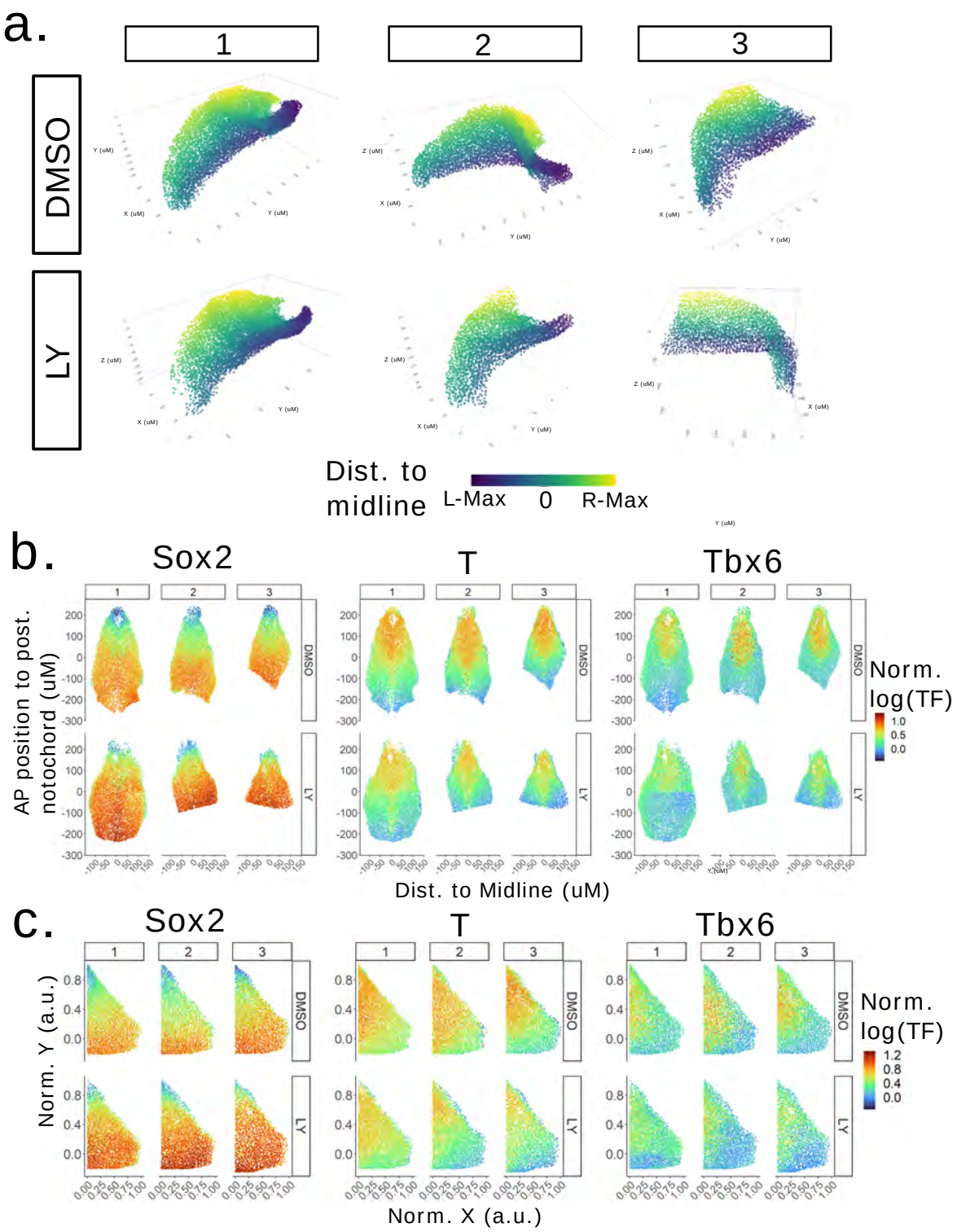

Figure 5.1 Epiblast normalisation of cultured embryos.

a. XYZ scatter plots of nuclei in isolated epiblasts in DMSO and LY condition. Colour scheme indicates the distance to midline calculated during epiblast normalisation b. Scatter plot of distance to midline against anterior-posterior position for nuclei in each epiblast showing symmetry and changes in TF gradients. c. Result of epiblast combination and renormalisation recapitulating TF gradients.

The Anterior/posterior positions were again manually aligned along the Y axis to the start of the notochord, the resulting symmetry of TF gradients and epiblast edge shows T to be an accurate prediction of the midline in both conditions (Figure 5.1.b). Flattening the epiblasts allows better visual analysis of details in patterning, such as how the TF gradients change after Notch inhibition, where Sox2 increases posteriorly while T and Tbx6 are reduced. Also, lone cells expressing high Tbx6 (>0.9 Normalised log[TF]) can be found in the Notch inhibited epiblasts (Figure 5.1.b,c).

To combine the datasets for direct comparison and further analysis, the epiblasts were overlaid and normalised to create an idealised 2D representation of the epiblasts (Figure 5.1.c) as previously described. To summarise, the epiblasts were folded at the midline, overlayed using the cellular position relative to the midline and edge of the epiblast as the X axis (on a scale of 0 to 1), and then the X position was re-transformed to produce a more uniform Euclidian density. In this case, cells >50uM posterior to the notochord were excluded (Figure 5.1.c), since some portions of the epiblast beyond this threshold are absent as they were not captured during confocal imaging (Figure 5.1.b), which was a consequence of the orientation of how the embryo was mounted and the limits of the wring range of the microscope objective.

The next step was to define the CLE ROI for analysis (Figure 5.2.a), where I used the two methods previously described (See section 4.2.2); (i) an unbiased direct comparison using k-means clustering in real space (Figure 5.2.b) and (ii) TF based by spatial smoothing and manual isolation of NMP-like profiles (Figure 5.2.c). Both methods were included since I previously showed that Sox2, T and Tbx6 expression was significantly affected by Notch inhibition, and it is likely that both the gradients and locations of specific TF profiles will be different. As such, using TF-Pseudospace for both was not possible as the change in TF expression confounded the dimension reduction aspect of the method (data not shown). However, it would be possible to project the TF-Pseudospace of nuclei from the DMSO control onto nuclei in the LY condition in normalised epiblast space.

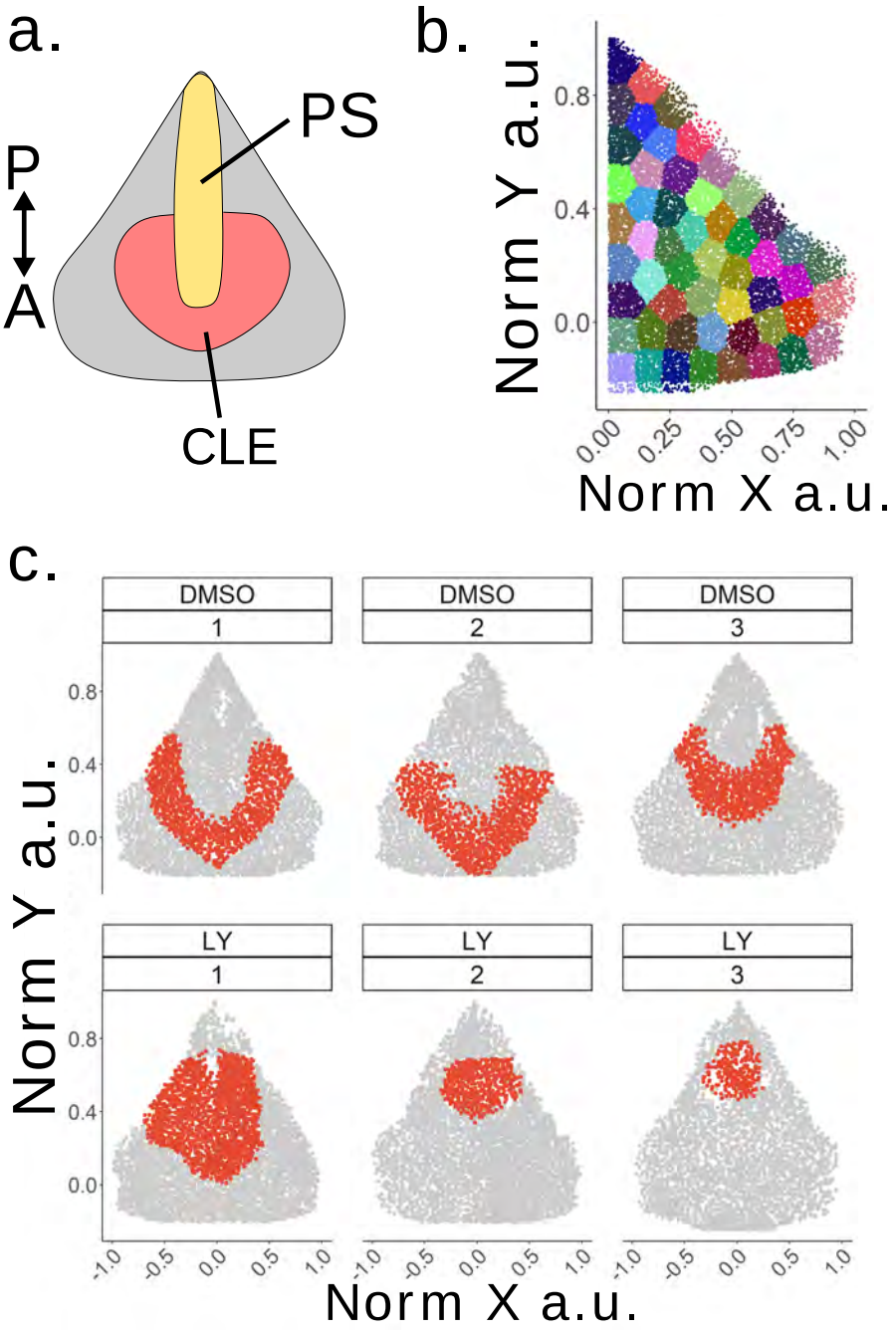

Figure 5.2 ROI definition in cultured embryos.

a. graphic showing approximate caudal lateral epiblast (CLE) and primitive streak (PS) position in normalised XY axis. b. K-means clustering of nuclei in XYZ for unbiased comparison. c. TF based definition of the CLE using similar thresholds in smoothed TF values previously identified. Resulting ROI marked by in red with non-ROI in grey.

An advantage of projecting data from different embryos onto a regular shape is that it then becomes possible to visualise averaged patterning across several embryos, regardless of size. To further explore how Notch inhibition spatially changes the expression of TFs within the entire epiblast, I used the unbiased k-means clustering of the normalised epiblast method. The average normalised TF expression for each cluster was visualised for the DMSO and LY condition (Figure 5.3.a), with the difference in means and associated p-value (Figure 5.3.b). This shows how Sox2 expression significantly increases broadly across the epiblast and the gradient advances posteriorly, whereas T and Tbx6 expression appears to significantly decrease close to the midline within the primitive streak. No obvious difference is seen between control and Notch-treated embryos at the lower ends of these TF gradients.

To define the NMP niche/CLE (Figure 5.2.a), I used thresholds in smoothed TF values, like those used in the previous chapter, which approximately isolated the CLE for the DMSO condition, but also included more lateral regions (Figure 5.2.c). However, assuming normal development the 12-hour culture this is a ~E9.0 embryo, and the CLE may be different than E8.5. Of note, the NMP niche as defined here highlights that there is variation in the exact position of TF gradients between the three control DMSO-treated embryos, in particular embryo 3 where the PS appears to be shorter even after normalising to the start of the notochord (Figure 5.2.c). Despite this minor variability between the three controls, it was still possible to observe clear differences in patterning and TF gradients between control and Notch-inhibited embryos.

Interestingly, applying the thresholds that approximately define the NMP niche in the DMSO condition to the Notch inhibited condition results in isolating a different ROI relative to the epiblast, which is closer to the midline and around the PS (Figure 5.2.c). Indicating that the niche containing NMP like TF profile is not lost but moves spatial location.

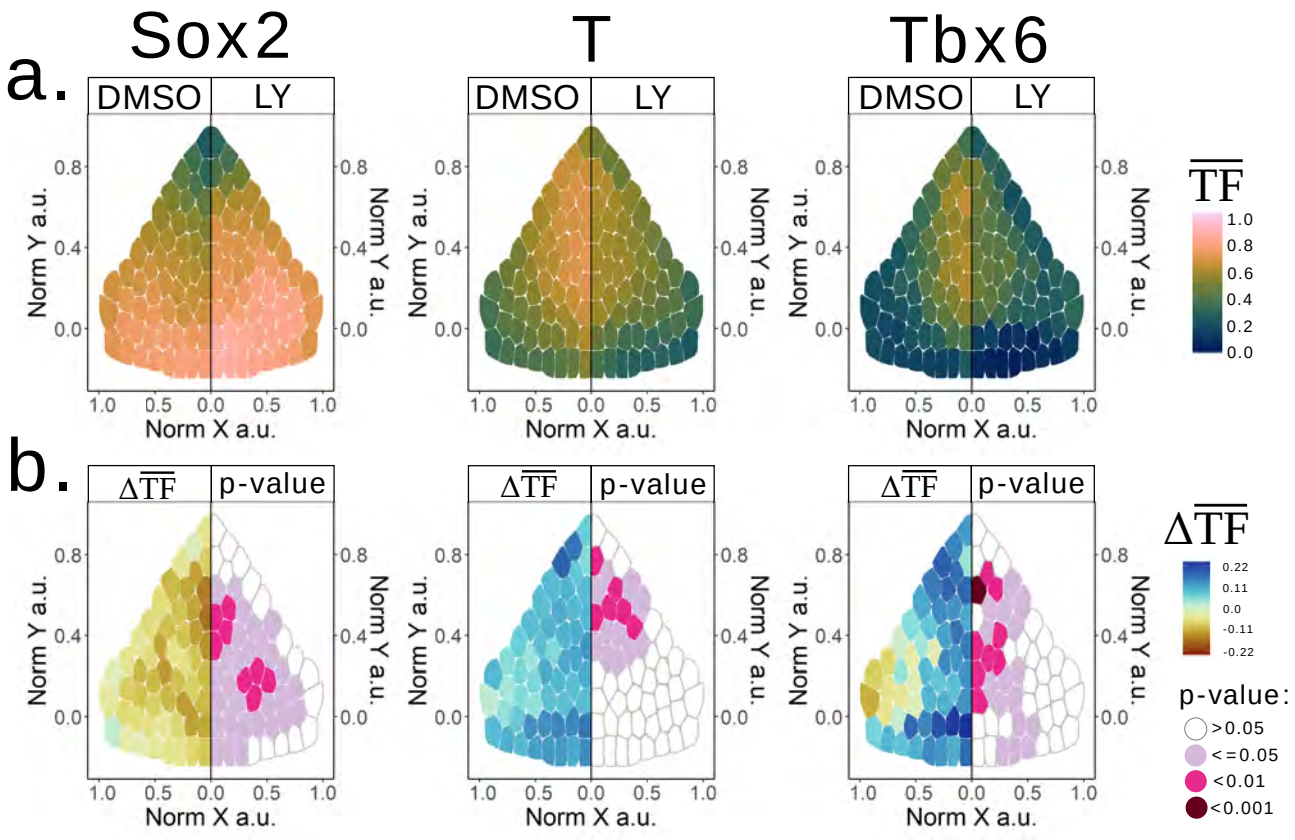

Figure 5.3 Change in spatial TF expression in the epiblast following Notch inhibition.

a. Using the k-clustering of normalised XY method, the average DMSO control and LY Notch inhibited normalised TF value for each cluster and TF is compared. b. The difference in mean normalised TF and statistical significance between each cluster shows regionalisation of statistically significant TF expression changes. Statistical analysis performed by one way ANOVA.

5.1.1.2 Heterogeneity of T and Tbx6 decreases in the epiblast NMP niche following Notch inhibition.

If Notch mediates a heterogeneity increasing lateral inhibition mechanism to control spatial TF expression in this context, then the LY-treated embryos then we would expect that LY-treated embryos should exhibit a decrease in TF heterogeneity. This was tested by comparing the *CV* metric, as a measure of how similar or different TF expression in each cell is compared to the averaged expression in its neighbours (see section 4.2.5). Again, only TF+ cells for each gene were included in the analysis.

First, the spatial k-clustering method shows peaks in T and Tbx6 CV heterogeneity at the lower end of their TF gradients in the DMSO condition that overlap in the CLE (Figure 5.5.ai), as had previously been observed in the wild type embryo E8.5 6 SP dataset (Figure 4.8). In contrast, in the LY condition the peaks in CV for T and Tbx6 were significantly reduced, with the biggest effect on Tbx6 heterogeneity equating to a ~50% reduction in average CV (Figure 5.5ai,aii). Furthermore, visual comparison of the spatial locations indicated that the peak CV may be closer to the midline in the LY condition. No consistent significant change in CV for Sox2 was observed. These results suggest that inhibiting Notch reduces local heterogeneity of Tbx6 expression and may result in a change in the location of the most heterogenous region of Tbx6 expression.

I next used the TF based method to assess CV values within each NMP-LC region (Figure 5.2.c). This approach was used to define regions containing NMP like TF profiles and then CV values for TF heterogeneity were measured within this region, as described above. This analysis confirmed the previous observation that Tbx6 and T showed a significant reduction in average CV (Figure 5.4b). No significant change in Sox2 CV was observed. Overall these findings suggest that Notch inhibition decreases heterogeneity in T and Tbx6, and disrupt the characteristic spatial patterning of these TFs that is observed in DMSO control-treated embryos and untreated wild type WtE8 embryos.

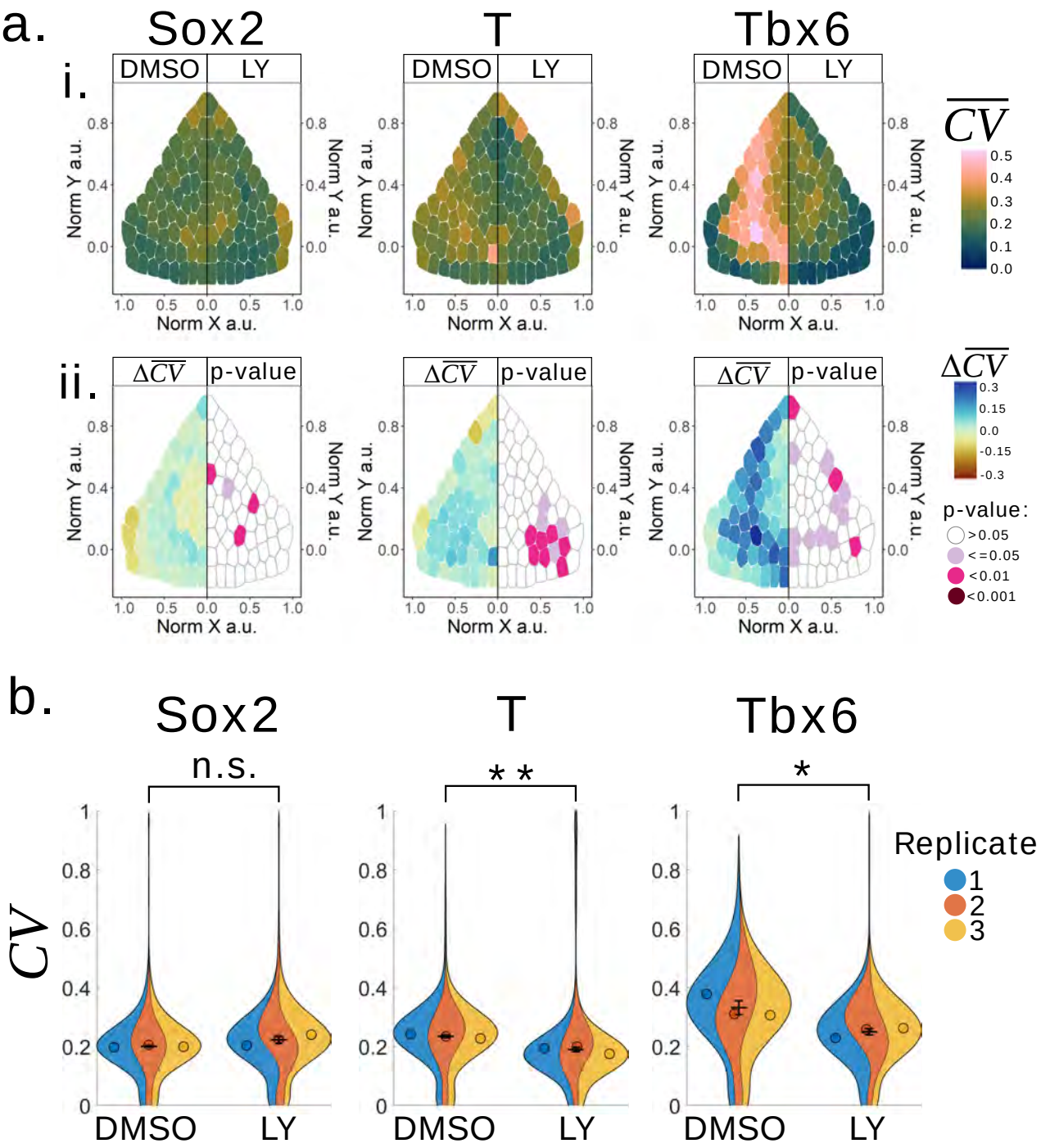

Figure 5.4 Effect of Notch inhibition on TF coefficient of variation (CV).

a. Using the k-clustering of normalised XY method, (i) the average DMSO control and LY Notch inhibited CV value for each cluster and TF is compared, (ii) with the difference in mean CV and statistical significance between each cluster. b. Comparing T, Sox2, and TBx6 CV in the TF defined NMP niche with Violin Superplots shows a significant reduction in T and Tbx6 CV after Notch inhibition . Error bars show standard error. All statistical analysis performed by one way ANOVA. ***=p<0.001, ** = p<0.01, *=p<0.05.

5.1.1.3 No significant change in cell:neighbour TF expression ratio for Tbx6 following Notch inhibition.

To indicate if the observed decrease in local heterogeneity of T and Tbx6 is consistent with an abolishment of Notch mediated lateral inhibition, the TF cell to neighbour ratio (NR) was utilised to quantify the nature of heterogeneity for each TF. As previously described (Section 4.2.5), NR is a linear metric to describe the ratio of a cell's TF expression to neighbouring cells. Positive NR values mean a cell is surrounded by cells expressing less TF than itself, negative NRs is the reverse of this, and NR ~0 means that the TF expression is even between a cell and its neighbours (Figure 4.8.b). A lateral inhibition pattern may result in positive NR values, such as Tbx6+ve cells surrounded by Tbx6-ve cells.

NR was first evaluated using the clustering method of the whole epiblast. In Figure 5.5ai, regions where cells are similar to their neighbours are shown in paler colours (NR closer to 0) while cells different from their neighbours are shown in darker colours. As before in the control WtE8 data (Figure 4.8), both T and Sox2 show a balanced NR in the NMP region, indicating low heterogeneity (Figure 5.5.ai, b) whereas Tbx6 expression shows a slightly positive average NR (Figure 5.5.ai, b). There appears to be a decrease in average Tbx6 NR around the more lateral CLE region when compared to the control, but this difference did not reach significance (Figure 5.5.aii). Unexpectedly, there was a significant increase in Tbx6 NR within the PS region in the LY condition (Figure 5.5.ai,aii). Again, indicating the region of heterogeneity for Tbx6 moves following Notch inhibition.

When comparing the NMP-LC containing domains as defined by smoothed TF thresholds, there was no significant difference between NR for Tbx6 or Sox2, but there was a significant increase in NR in the LY condition for T expression (Figure 5.5.b). However, the effect is very small relative to the variation within each replicate.

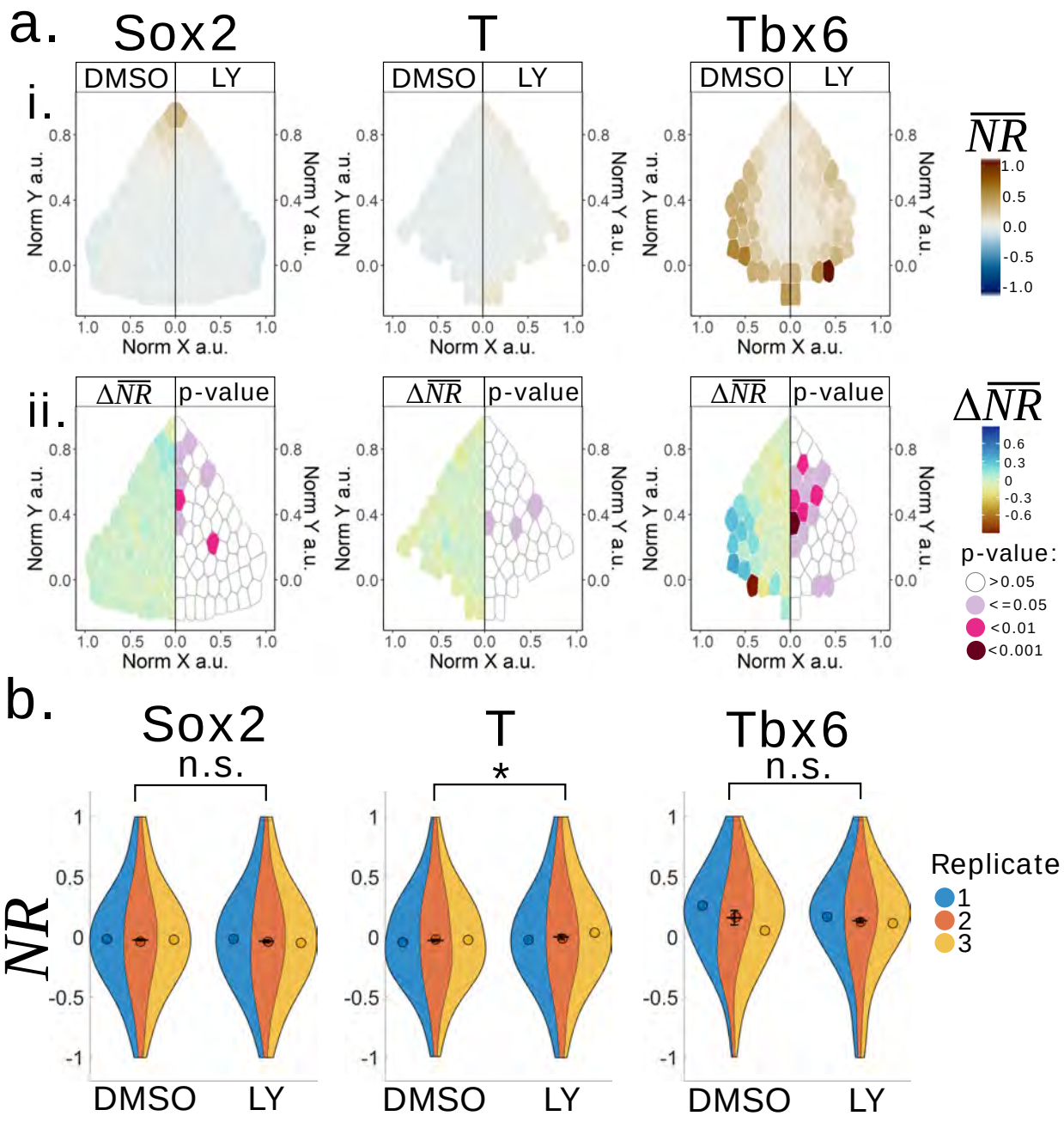

Figure 5.5 Effect of Notch inhibition on TF cell to neighbour ratio (NR).

a. Using the k-clustering of normalised XY method, (i) the average DMSO control and LY Notch inhibited NR value for each cluster and TF is compared, (ii) with the difference in mean NR and statistical significance between each cluster. b. Comparing T, Sox2, and TBx6 NR in the TF defined NMP niche with Violin Superplots shows a significant increase in NR, but no effect on Sox2 and Tbx6. Error bars show standard error. All statistical analysis performed by one way ANOVA. ***=p<0.001, ** = p<0.01, *=p<0.05.

The lack of difference in this analysis may be due to the NMP region not being isolated as accurately as in the wild type dataset. The average NR for the NMP niche in the DMSO control (Figure 5.5.b) is lower than what was calculated in the wild type E8.5 data (Figure 4.8.c), indicating the NMP ROI may not directly comparable to the WtE8 dataset. This may be due to a fundamental change in patterning resulting from the culture conditions or inaccurate ROI isolation confounding the analysis.

5.1.1.4 Summary.

Overall, the increased curvature of the epiblast and spatial change in TF expression, introduced from Notch inhibition, made the normalisation process more challenging, but it appears robust enough to serve the purpose for graphical representation and direct epiblast comparison. The patterning analysis shows a decrease in T and Tbx6 heterogeneity when comparing regions around the primitive streak and in regions with similar NMP-LC TF profiles. However, while there was a decrease in heterogeneity for T and Tbx6, no clear decrease in Tbx6 NR within the NMP niche, that would indicate a loss of lateral inhibition, was observed.

5.1.2 Notch inhibition has a limited effect on local heterogeneity in Gastruloids.

Gastruloids present an exciting opportunity to model how axial progenitors self-organise to a trunk like structure (Veenvliet et al., 2020, Van den Brink et al., 2014, Moris et al., 2020), allowing us to explore what regulatory mechanisms are utilised to robustly maintain axial progenitors during axial elongation. To date, neighbour-based TF expression patterning in gastruloids has not been quantitatively evaluated. To assess if Notch inhibition affected features of patterning identified in the epiblast, this analysis pipeline was extended to the gastruloids.

5.1.2.1 NMP ROI definition.

In this analysis, I used the same dataset of gastruloids cultured from Day4 to Day 5 in DMSO or DAPT to inhibit Notch (see section 3.2.5). Visual analysis of the Day5

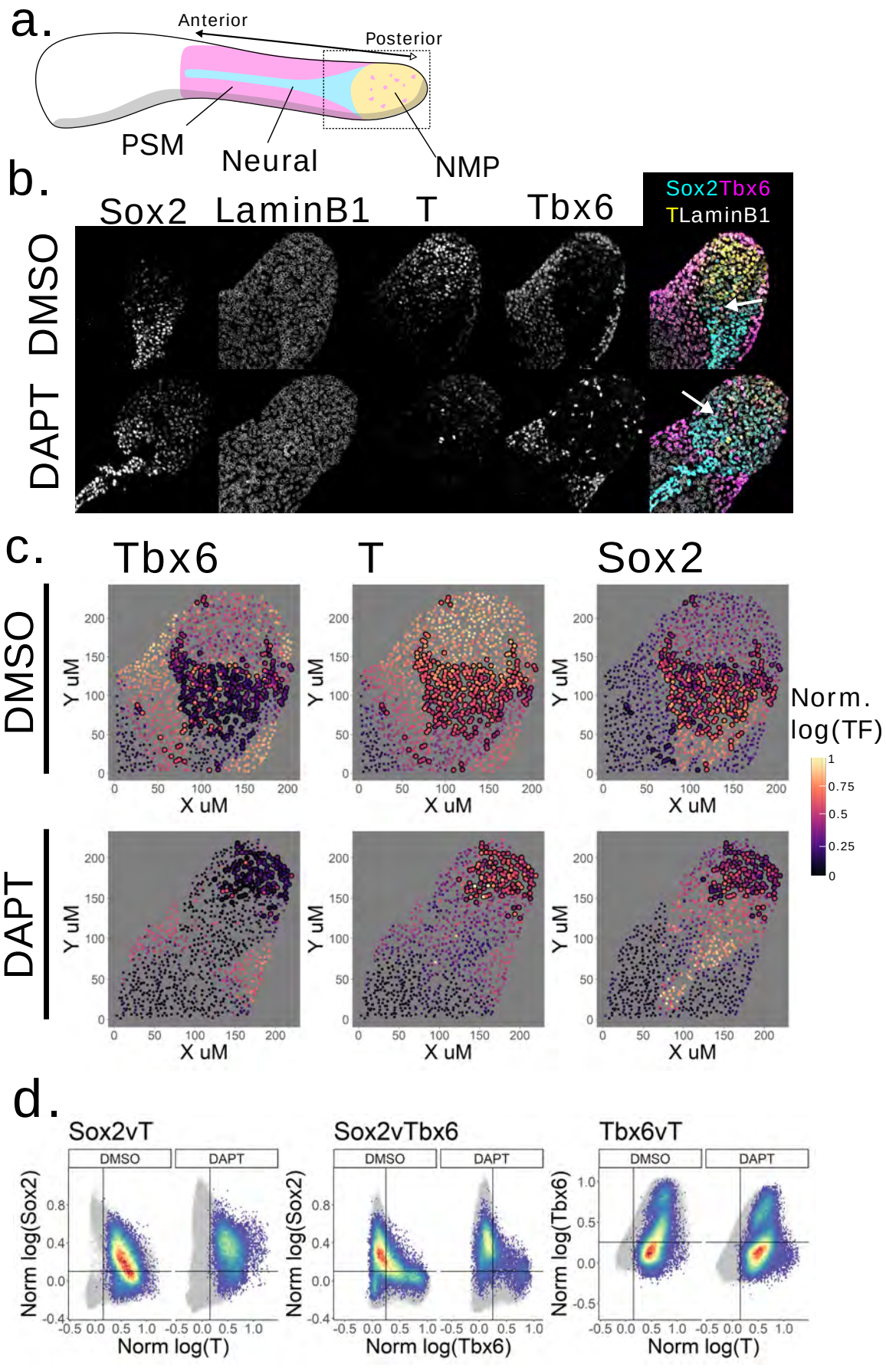
a.
Anterior
Posterior
PSM
Neural
NMP
b.
Sox2
LaminB1
T
Tbx6
Sox2Tbx6
TLaminB1
DMSO
DAPT
c.
Tbx6
T
Sox2
DMSO
DAPT
Y uM
X uM
Norm. log(TF)
1
0.75
0.5
0.25
0
d.
Sox2vT
Sox2vTbx6
Tbx6vT
DMSO
DAPT
Norm log(Sox2)
Norm log(Tbx6)
Norm log(T)

Figure 5.6 Defining NMP niche in gastruloids.

a. Graphic showing the field of view anterior/posterior axis in gastruloids with locations of the pre-somitic mesoderm lie tissues (PSM, magenta), neural tissues (blue) and neuromesodermal progenitors (NMP, yellow). b. Confocal slice from same dataset as in chapter 3 showing IF for Sox2, T, Tbx6, and LaminB1, arrows indicating high TBx6 cells in DMSO control and Notch inhibited LY condition. c. Scatterplots of nuclei in the Z slice in b. shown in XY space (um) with TF expression. NMP niche as defined by similar thresholds in average neighbour expression of T/Tbx6 as defined in the wild type E8.5 analysis. Resulting cells outlined in black. d. Density plots comparing TF values of NMP niche nuclei show a T/Sox2 profile for both conditions, but marginally more neural profile in LY condition.

gastruloid indicated that near the region at the “posterior tip” contains NMP-LCs as, defined by co-expression of T and Sox2, and the emerging Tbx6 cells (Figure 3.8.b,, 5.6.a). This has been extensively explored by SC and spatial transcriptomics where the posterior ends of gastruloids express an NMP like profile (Veenvliet et al., 2020, van den Brink et al., 2020, Moris et al., 2020). This posterior tip region shows similar TF patterning to the *in vivo* epiblast, where a gradient of T peaks at the tip, analogous to the primitive streak, in which nascent-mesodermal Tbx6+ cells are found in a “salt and pepper” pattern (Figure 4.1, 5.6.b). Also, Sox2 appears to organise into an opposing gradient to T. By eye, features of patterning identified *in vivo* can be found in gastruloids, I sought to assess if inhibiting Notch similarly affects gastruloid local heterogeneity.

To analyse TF patterning in the gastruloid NMP niche and to compare patterning across multiple gastruloids, the NMP niche must first be defined. The neighbours of cell’s were calculated in Pickcells using Delaunay triangulation with the same parameters as for the epiblast. In the same way the epiblast was manually isolated from the PSM in the embryo datasets, the clusters of Tbx6 cells and adjacent cells were mathematically detected and excluded from this analysis. It was not possible to directly use the methods that I had developed for defining ROIs in embryos as the TF expression gradients and boundaries between tissues of different identities are not as coherent as *in vivo*. I therefore adapted these methods to isolate the regions containing NMP-LCs profiles found in the epiblast. Here, similar thresholds in the average normalised TF expression of a cell and its neighbours that were used in the epiblast to define the CLE (Figure 4.5d,e,f) were applied to gastruloids. These thresholds defined a discrete NMP ROI in both DMSO control and Notch inhibited DAPT conditions (Figure 5.6.c).

Interestingly, using this method isolates a region around the periphery of the “posterior” tip along the Sox2/T gradient in the DMSO condition, not at the posterior-most tip itself (Figure 5.6.c). In contrast, this isolates the region at the posterior-most tip in the Notch inhibited condition (Figure 5.6.c). Evaluating the TF expression

profile of cells from the isolated regions shows that in both conditions contain predominantly Sox2/T copositive cells with some Tbx6 expression (Figure 5.6.d). Although, the Sox2/T copositive cells in the T/Sox2 TF expression state space have a more neural profile with higher Sox2 and lower T in the Notch inhibited condition. This indicates that the NMP profile is more neural but is maintained while the nascent mesodermal cells are lost after Notch inhibition, and the location of the NMP profile moves along the T/Sox2 expression gradient. Also, this indicates the T/Sox2 profile identified in the CLE is not found in the tip of the gastruloid, which has previously been described as the location of NMPs (Veenvliet et al., 2020, van den Brink et al., 2020, Moris et al., 2020), but more “anteriorly” along the gastruloid axis. Whether or not these cells are bipotent/bi-fated, and the limits of bipotency or fate in relation to the gastruloid axis, is unknown.

5.1.2.2 Notch inhibition does not affect overall heterogeneity but increases the cell:neighbour ratio for Tbx6.

Next, I aimed to ask if Notch inhibition reduces local TF expression patterning in T and Tbx6 within the NMP niche of gastruloids. Using CV of TF expression for a cell and its neighbours as a measure of local heterogeneity, no significant difference in Sox2, T, or Tbx6 CV was observed following Notch inhibition (Figure 5.7.a). This is contrary to the epiblast data, which resulted in a decrease in T and Tbx6 CV when comparing regions containing cells with an NMP like profile (Figure 5.4.b). Interestingly, the full distribution of CV values for Tbx6 expression in the Notch inhibited condition appears broader and bimodal across all replicates (Figure 5.7.a), indicating Notch inhibition creates two patterns in the NMP, a high and low Tbx6 local heterogeneity pattern.

Next, I used the NR metric in relevant TF+ expressing cells to assess if lateral inhibition like patterning of the nascent mesoderm is found in the NMP niche, and if this is affected by Notch inhibition. For Tbx6+ cells in the DMSO condition, average NR is marginally above 0, indicating Tbx6 expressing cells in the NMP niche tend to be surrounded by lower Tbx6 expressing cells. Sox2 and T NR in Sox2+ and T+ cells respectively appear to average ~ 0 (Figure 5.5.b). Interestingly, an increase in

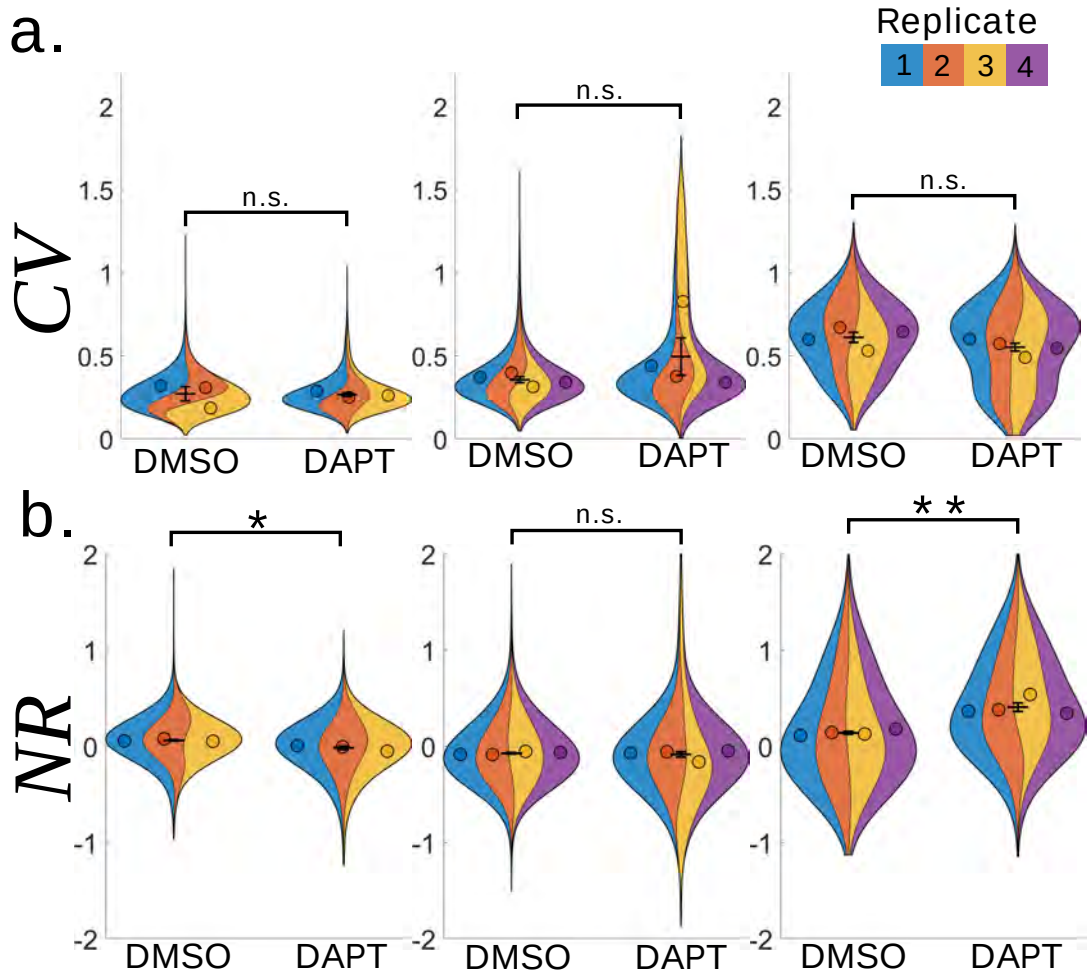

Figure 5.7 Notch inhibition has limited effect on patterning in gastruloids.

a. CV values for TF expression in the NMP niche shown by Violin super plots show no significant difference after Notch inhibition. b. Similarly, comparing NR values for each TF in the NMP niche, shown by Violin super plots, only indicates a significant increase in Tbx6 after Notch inhibition. All statistical analysis performed by one way ANOVA. ***=p<0.001, ** = p<0.01, *=p<0.05. n=3 for Sox2, n=4 for T/Tbx6.

Tbx6 NR was observed after Notch inhibition, indicating that after Notch inhibition, Tbx6 cells are surrounded by cells expressing lower levels of Tbx6 than found in the control. This does not support the Notch mediated lateral inhibition hypothesis where we would expect a reduction in both heterogeneity and NR.

Overall, defining the NMP ROI as was performed in the epiblast reveals a different location of the NMP T/Sox2 profile in the gastruloid than previously reported (van den Brink et al., 2020, Veenvliet et al., 2020). Further, Notch inhibition does not remove this profile but changes its location more posteriorly along the gastruloid axis. Notch inhibition did not significantly affect local heterogeneity in the NMP niche for any TF, but it did change the nature of the heterogeneity for Tbx6.

5.1.3 Gastruloids recapitulate many features of patterning quantified in the E8.5 embryo.

The anterior posterior patterning of gene expression in gastruloids, and similar organoids, compared to embryos has been analysed with transcriptomics and image analysis (Beccari et al., 2018, van den Brink et al., 2020, Moris et al., 2020, Yamanaka et al., 2022, Miao et al., 2022), but how these gastruloids compare to embryos in terms of local neighbour patterning has not been evaluated. Since different results were obtained after Notch inhibition for the epiblast and in gastruloids, quantitatively comparing metrics used for patterning may elucidate the reason for this difference. Further, it may indicate how similarly gastruloids and the *in vivo* epiblast organise and suggesting of how useful a model it is to study patterning. A such, I aimed to quantitatively assess if similar patterns are present in gastruloids compared to epiblasts.

First, I compared the CV values for each TF within the NMP niches, defined as containing NMP-LC TF profiles, in each of the datasets, again only including TF+ve cells for separate TFs. This revealed that the average Tbx6 CV and T CV in gastruloids are both significantly higher than in the epiblast of embryos, with an almost 2-fold increase in Tbx6 CV (Figure 5.8.a). An apparent increase in average

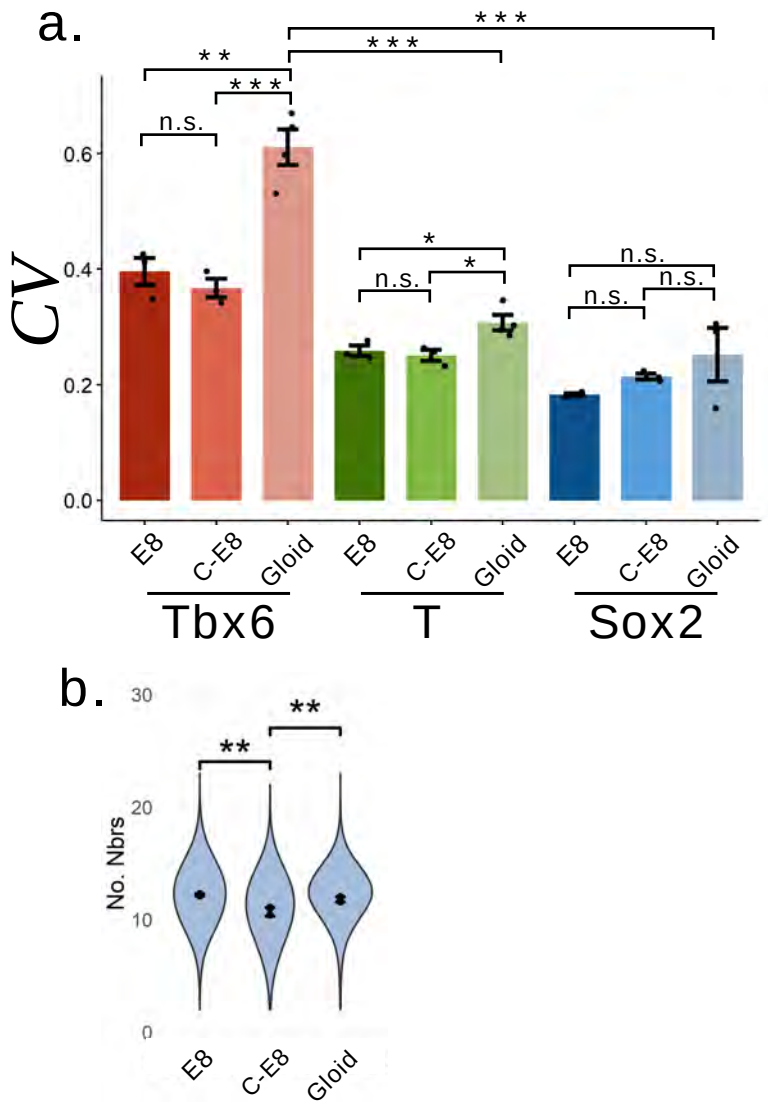

Figure 5.8 Embryo and gastruloid dataset patterning comparison.

a. Comparing the CV for each TF in the NMP niche across the wild type E8.5 embryo (E8), the DMSO control in the cultured embryo (C-E8), and gastruloids (Gloid) shows T and Tbx6 are more heterogeneous in gastruloids than epiblasts, and Tbx6 is more heterogeneous than T or Sox2 in gastruloids. Statistical analysis performed using Tukey's HSD test. b. Comparing the average number of neighbours for all nuclei in epiblasts and gastruloids show that the E8 and gastruloid showed no significant difference in the average number of neighbours, but E8 and gastruloid showed a significant increase in the number of neighbours compared to the cultured embryos. Statistical analysis performed by one way ANOVA. ***=$p<0.001$, ** = $p<0.01$, *=$p<0.05$.

Sox2 CV was observed but was not statistically significance. No significant difference between CV of any gene for the wild type or culture embryos was measured (Figure 5.8.a), suggesting that NMP-LCs in gastruloids have higher local TF expression heterogeneity than in the epiblast.

Interestingly, Tbx6 CV is significantly greater than the CV for T or Sox2 in gastruloids as is the case *in vivo* (Figure 5.8.a). Indicating that Tbx6 expression tends to have heterogenous expression in both contexts. But contrary to epiblasts, T was not significantly more heterogenous than Sox2 in the NMP-LC niche of gastruloids.

As gastruloids are 3D aggregates of cells and are much thicker than the epiblast epithelia (Figure 3.3, 3.8), one might expect the local density to be greater in gastruloids. However, comparing the average total number of neighbours in gastruloids to epiblasts reveals that they are very similar. No significant difference was observed between the average number of neighbours for gastruloids and the E8.5 embryo with ~12 neighbours on average (Figure 5.8.b). The cultured epiblasts were significantly lower than gastruloids or the E8.5 epiblasts, but the level was comparable as on average ~11 neighbours were measured. This indicates that while the tissue size is much larger in gastruloids, the cells create a similar local density to the epithelia epiblast, supporting the notion that gastruloids are a useful model to study NMP patterning. However, signalling mechanisms of Wnt/FGF/RA/Notch may be affected in ways not captured by simply counting the number of neighbours.

5.1.3.1 Using UMAP to combine TF expression and patterning data across experiments.

The wild type NMP niche, and surrounding axial progenitor niches, could be explored using PCA dimension reduction of smoothed TF values, which closely retains the features of the original global data structure, to provide a metric with relevant units of Pseudospace and so describe TF gradients (See section 4.2.2). However, the changes in gene expression that occurred during Notch inhibition confounded this analysis as the smoothed TF values were not separated well with PCA (data not

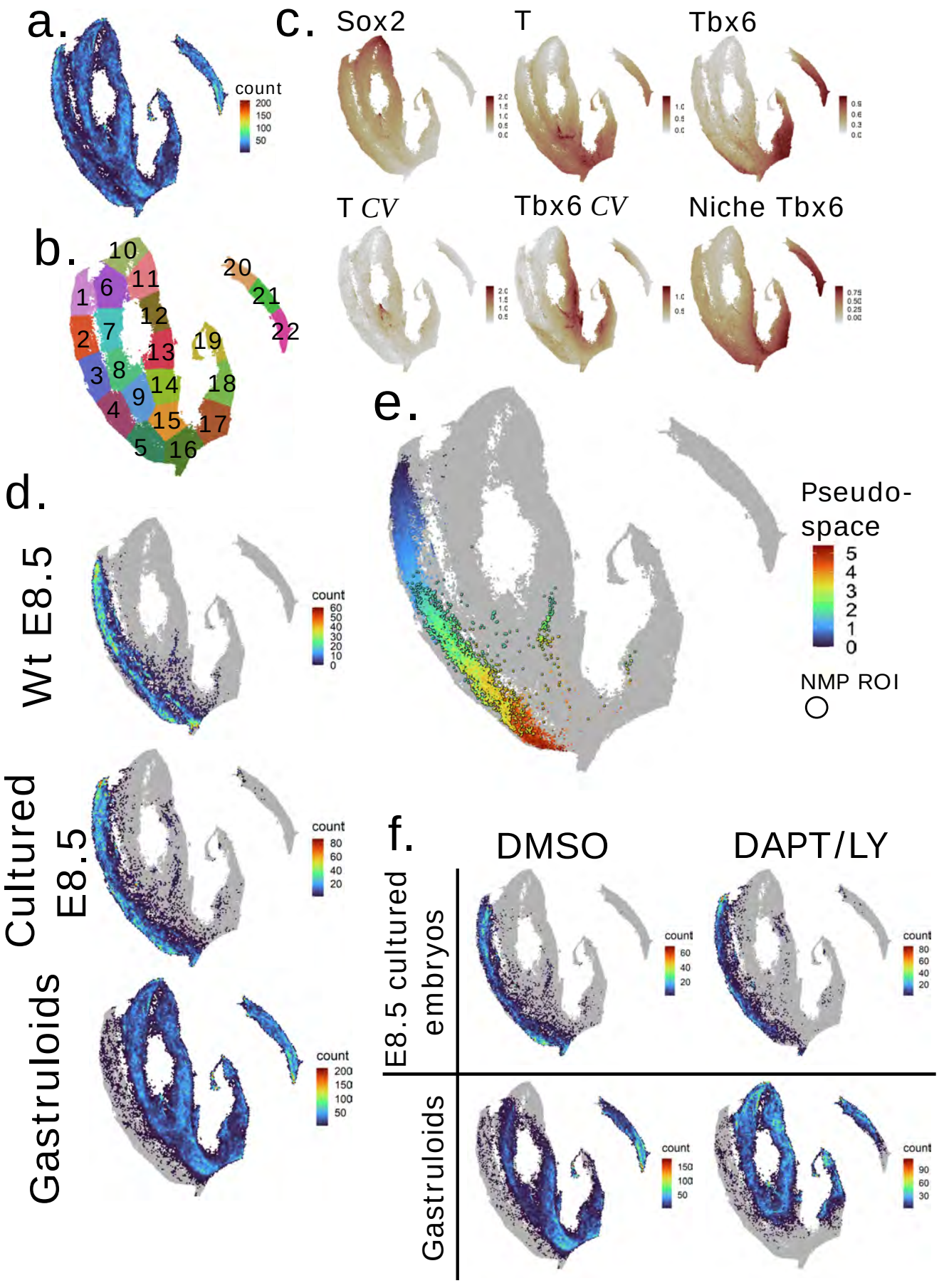
a.
count
200
150
100
50
b.
1
2
3
4
5
6
7
8
9
10
11
12
13
14
15
16
17
18
19
20
21
22
c.
Sox2
T
Tbx6
T CV
Tbx6 CV
Niche Tbx6
d.
Wt E8.5
Cultured E8.5
Gastruloids
count
e.
Pseudo-space
5
4
3
2
1
0
NMP ROI
f.
DMSO
DAPT/LY
E8.5 cultured embryos
Gastruloids
count

Figure 5.9 UMAP as a tool to combine patterning data across experimental systems.

a. CV, normalised TF expression, and mean cell + neighbouring cell (niche) normalised TF expression were used as an input for UMAP dimension reduction and trajectory inference. b. K-means clustering of UMAP c. Parameters which showed increased influence on UMAP space, such as the gradients of T, Sox2, Tbx6, niche Tbx6 and Tbx6 CV. d. Density plots of each dataset in the UMAP, showing clustering of epiblasts away from gastruloids. e. From the wild type E8.5 dataset, the pseudospace axis with the NMP niche, outlined in black, shows some cells clustering with the high tbx6 CV gastruloid cluster. f. Notch inhibition in cultured embryos and gastruloids shows a change in the distribution of nuclei away from certain clusters to more neural regions.

shown). Similarly, the heterogeneity and computational cost of smoothing TF values in gastruloids prevented a similar analysis. Another approach is required to directly integrate the full patterning data across experimental systems and allow unbiased quantitative ROI definitions and patterning analysis.

Patterning and TF expression metrics from the entire gastruloid (including Tbx6+ clusters and cells neighbouring Tbx6+ clusters) and epiblast datasets were used in the uniform manifold approximation (UMAP) dimension reduction algorithm (Becht et al., 2019). This will cluster cells according to their position along trajectories in high dimensional space, projecting this information into 2D space while retaining aspects of the original global structure. The UMAP will provide a TF based method to quantitatively define progenitor niches and changes in patterning across experimental systems, without having to manually redefine thresholds for each experiment as before. The metrics used included the normalised TF values (Sox2, T, Tbx6), average niche TF values (the average TF value of a cell and its neighbours), and TF niche CV for CE8 cultured embryos, and gastruloids). It is expected to create trajectories of TF expression and separate based on local TF expression and heterogeneity, allowing the direct comparison of gastruloids and embryos for both the wild type, DMSO control and Notch inhibition conditions.

The resulting UMAP produced several paths that correspond to TF gradients and differentiation from NMP-LC to either neural or PSM like cell states (Figure 5.9.a.c), while also clearly showing population differences between DMSO and DAPT/LY conditions (Figure 5.9.f). To navigate the UMAP, k-means clustering was used to provide numbered clusters of different regions (Figure 5.9.b). While most cells in the Wild type E8.5 epiblast dataset (WtE8 henceforth) and cultured embryo dataset (CulE8 henceforth) clustered closely (Figure 5.9.b,d, f. Clusters 1-5), the gastruloids did not and predominantly clustered separately (Figure 5.9 b,d, f. Clusters 6-22). Supporting the previous observations that Gastruloid patterning is different to the embryo.

While in Embryo datasets the neural to NMP trajectory is a single path (Figure 5.9.d.), in gastruloids the Neural-NMP trajectory is forked with two trajectories

diverging at the NMP cluster 15 and rejoining at the neural cluster 10 (Figure 5.9.b.,c.). One trajectory (clusters 11 to 14) displays increased Tbx6 CV and average Tbx6 niche values compared to the other trajectory (clusters 6 to 9) (Figure 5.9.b.,c.,d.). The fork with increased Tbx6 CV (clusters 10 to 14) is likely neural and NMP-LCs neighbouring the clusters of Tbx6 cells, which were not excluded from this to prevent bias and loss of datapoints, creating high local heterogeneity However, the gastruloids do display similarly structured paths and TF gradients compared to the WtE8 and CulE8 set with a Neural-NMP path, especially one path (clusters 6-9,15) which is only marginally separated from the embryo data (Figure 5.9.d). This suggests that much of the gastruloid tissue presents similar patterns and TF expression to the embryo but with increased heterogeneity, also highlights the prevalence of NMP and neural like cells adjacent to Tbx6+ clusters.

Interestingly, a small subset of cells from the WtE8 and CulE8 data clustered with the gastruloid data in the path with high heterogeneity (Figure 5.9.d,e. Cluster 14/15)). Using the NMP niche definition from the WtE8 dataset, this shows that the cells clustering in the high Tbx6 heterogeneity region are in the WtE8 CLE (Figure 5.9.e). This suggests that the high Tbx6 local heterogeneity aspect of patterning I quantified the epiblast CLE (Figure 4.7.c) is recapitulated in gastruloids, but instead of being a small subset of cells this is a predominant pattern.

The pro-neural effect of Notch inhibition on TF expression is captured in the UMAP, where the distribution of cells in the UMAP increases along the neural trajectory following Notch inhibition. Most notably in the gastruloid dataset where clusters 15-17 (which contain PS like high Tbx6/T TF expression) were not present in the Notch inhibited condition (Figure 5.9.f). Similarly, cluster Also, clusters 10-12 (containing high Sox2 expression) contain very few cells from the control but are high populated by the Notch inhibited condition (Figure 5.9.f). However, without quantitative analysis techniques the previous observations, such as the decrease in T/Tbx6 heterogeneity in Notch inhibited epiblast NMP niches, were not identifiable. But with such quantitative methods, this provides a route to simultaneously describe changes in TF expression in the context of local patterning through movement in UMAP space.

Overall, gastruloids recapitulated a number of patterning features of the epiblast, such as the increased local heterogeneity for Tbx6 expression compared to Sox2 or T. Also, UMAP presents another method to directly compare data across experimental systems and culture conditions, providing another route to quantitatively define cell identity, ROIs, and potentially changes in patterning with reduced human input. But this method requires further mathematical analysis techniques to elucidate finer details.

5.2 Discussion:

5.2.1 Analysis pipeline for quantifying spatial patterning in the epiblast after Notch inhibition.

The Epiblast normalisation method I developed successfully flattened the 3D epiblasts despite the increased curvature. However, some noticeable artefacts were observed in the posterior sections where a gap is created (Figure 5.1.b). The reason for this is not clear and it may be affecting the analysis, but this does not appear to be affecting the regions around the anterior primitive streak and where the NMP-LCs reside. Further, the analysis of gradients in TF expression and heterogeneity closely resembled the wild type and overall, the epiblasts appeared to be symmetrical in size when normalised to the midline. Further improvements to the algorithm to prevent the artefacts in posterior tissues may help improve downstream conclusions.

The next step in the pipeline included defining the regions of interest to statistically analyse. I developed two methods for defining ROI : 1: unbiased real space clustering and 2: manual isolation based upon local TF values, and I showcase their individual strengths in the Notch inhibition analysis. The epiblast normalisation, alignment, and unbiased clustering analysis revealed how the differences in TF expression and heterogeneity were decreased or increased in particular areas compared to the control (Figure 5.3,4). However, there was some variation in the exact location of the NMP-LC populations in the control group (Figure 5.2.c) where in the third replicate the isolated region was more posterior, potentially due to the

embryo itself more advanced and the primitive streak being shorter. Using embryos as close to a specific developmental stage as possible would benefit this analysis and allow more definitive conclusions to be drawn. The method for defining ROI based on local TF values could help compensate for the differences in TF gradients and relative locations of cell types, in doing so providing more relevant comparisons between cell types even if these change location in the epiblast and could not be compared using the unbiased real space clustering method.

Overall, this pipeline performed well with only minor adjustments needed to meet the objective requirements in normalising pharmacologically manipulated epiblasts that display differential TF gradients and patterning.

5.2.2 UMAP as method to combine datasets for quantitative analysis.

Between experiments the NMP niche required redefining, which was performed semi-manually and so injecting bias into the analysis pipeline. While the PCA of smoothed TF values presented an effective technique to describe the NMP niche along a neural-NMP-mesoderm TF profile gradient, it could not be immediately extended to Notch inhibition conditions. UMAP offers another route to combine datasets and define ROIs across experiments and culture techniques. While I used a select few patterning parameters to explore its utility, further metrics such as the number of neighbours, the average distance of neighbours to a cell, the magnitude of TF gradients (as in section 4.2.3), could all be used as an input. Synthetic data could also be used as an input to test the hypothesis that certain patterns are created by specific regulatory mechanisms, such as lateral inhibition or lateral induction. However, UMAP requires data types to be on similar scales or standardised to not bias the clustering and trajectory inference to metrics with higher unit scales. Also, as with non-linear dimension reduction techniques like t-SNE (Van der Maaten and Hinton, 2008), the parameters for UMAP may need adjusting to optimise the density of clustering in the result final 2D projection.

While metrics like CV and NR are relative and unitless, I manually normalised and aligned the fluorescence units of TF profiles across experimental systems using the control TF profiles as a guide, potentially inducing bias and increasing the level of similarity between samples. More rigorous mathematical techniques such as batch correction in RNAseq (Zhang et al., 2019, Polański et al., 2020) or absolute protein content measurement (Csibra and Stan, 2022) would benefit in the normalisation of fluorescence units. In general, fluorescence units are difficult to work with, further methods to rigorously normalise fluorescence would greatly benefit this analysis.

The UMAP projection recapitulated previous observations in TF expression changes following Notch inhibition, but further quantitative methods would be required to reveal fine details. As I have done with pseudotime tools (Street et al., 2018) and using dimension reduction (Becht et al., 2019), one can look to many tools from SC-RNAseq to quantitatively explore the UMAP space. Beyond this, to further develop this analysis there is a blooming field of GRN inference from SC-RNAseq data (Kumar et al., 2021, Spiess et al., 2022, Skok Gibbs et al., 2022, Rukhlenko et al., 2022, Kamimoto et al., 2023), it may be possible to implement inference-based techniques to spatial data to infer spatial regulatory mechanisms.

Overall, this type of data is new and analysis methods are still in their infancy, as such there is a wide opportunity to develop quantitative analysis methods for patterning.

5.2.3 Effect of Notch inhibition on TF expression and patterning in the epiblast and gastruloids.

Using the analysis pipelines previously outlined again demonstrated the pro-neural effect of Notch inhibition, but further details of this were revealed. A significant decrease in expression of both T/Tbx6 mesodermal TFs at the midline in response to Notch inhibition was demonstrated, whereas Sox2 expression increased across the epiblast after inhibiting Notch (Figure 5.3.c). There are many plausible explanations of this, such as Notch signalling influence on mesoderm differentiation being restricted to the PS, or simple inaccuracies in the normalisation procedure

preventing statistical significance. Without further data this would be undue speculation. But since the experimental timeframe is 12 hours, we can surmise that the high T and Tbx6 expression at the midline is relatively quick to downregulate after Notch inhibition. Consequently, Sox2 was upregulated broadly across the epiblast in regions, supporting the hypothesis the Sox2 gradient is shaped from negative regulation via a mesoderm related signalling (Boulet and Capecchi, 2012, Olivera-Martinez and Storey, 2007, Olivera-Martinez et al., 2012, del Corral et al., 2003, Gouti et al., 2017) and that Notch is now implicated in this role. Further work to understand how the Wnt/Fgf/Notch signalling mechanisms work in concert to control fate in the epiblast is required.

While an NMP-like identity was retained after Notch inhibition and T expression was not lost entirely, the location of these profiles moved along the T/Sox2 gradient in the epiblast and in gastruloids (Fig5.3,6). This suggests that the Wnt/Fgf positive feedback is enough to maintain T expression without Notch. But whether these cells are still bipotent and if this phenotype is maintained and given enough time, not on a trajectory to a neural like profile with a total loss in T in unclear and requires further analysis of Notch inhibition in time.

In the wild type E8.5 embryo and DMSO control condition in the cultured embryos, T and Tbx6 displayed increased local expression heterogeneity at certain points in their expression gradients that overlapped in the CLE (Figure 4.7,5.4). Further analysis revealed that the heterogeneity of T and Tbx6 was fundamentally different, in that the heterogeneity in Tbx6 was created by high Tbx6 expressing cells being surrounded by low Tbx6 expressing cells, whereas the heterogeneity in T was a mix of high and low T expressing cells. While T and Tbx6 was downregulated in the epiblast PS, the bands of increased local variability for T and Tbx6, that were also found as in the E8.5 wild type and DMSO control, were abolished in the Notch inhibited condition (Figure 5.4.a,b). This suggests Notch signalling, or a mechanism related to Notch, may contribute to heterogeneity. It curious that Notch inhibition should affect both T and Tbx6 heterogeneity, which suggests that the source of heterogeneity for these TFs is linked.

Embryos exhibited a decrease in Tbx6 heterogeneity after Notch inhibition in the NMP niche. However, no significant decrease in the ratio of Tbx6 expression compared to its neighbours (measured by NR) was measured, which was expected to occur if indeed lateral inhibition was creating heterogeneity. This suggests that the high Tbx6 local heterogeneity patterning may not arise from Notch mediated lateral inhibition mechanisms but rather from alternative mechanisms. For instance, a mesoderm lineage affirming GRN mechanism may rapidly upregulate Tbx6 creating seemingly asynchronous Tbx6 expression. During Notch inhibition, Tbx6 is downregulated most in the low expressing Tbx6 cells but not the Tbx6 high cells, the Tbx6 high cells remain thus the NR metric is less affected.

5.2.4 Committed Tbx6+ cells influence on patterning quantification.

Further support for the idea that heterogeneity in Tbx6 expression cells arises due to the GRN rather than lateral inhibition comes from the results in the gastruloids. Notch inhibition in gastruloids NMP niche did not change the local heterogeneity of Tbx6 but did increase the NR ratio (Figure 5.4,5.5). This is likely due to Tbx6 high cells that are committed to mesoderm and not as greatly affected by Notch inhibition remain in the NMP niche, while cells expressing lower levels of Tbx6 not yet committed to mesoderm cells were downregulated by Notch inhibition, thus increasing the NR ratio. This phenomenon is clearly visible by eye, where lone high Tbx6+ cells are found in previously NMP containing regions (Figure 5.6.b).

This may indicate that the source of heterogeneity and high NR in wild type and control conditions of epiblasts and gastruloids are the committed mesoderm cells, where beyond a certain TF expression threshold Tbx6 expression may be rapidly upregulated in the mesoderm lineage reaffirming Wnt/Fgf/Msgn1 positive feedback loop without the contribution of Notch signalling.

5.2.5 Summary.

To summarise, this chapter explores novel and repurposed analysis methods to directly compare spatial patterning across replicates and experimental systems, namely embryos and gastruloids. It revealed further details in the pro-neural Notch inhibition effect, in that the NMP profile was not lost but shifted location and changed the spatial gradient of T/Sox2 following Notch inhibition, implicating Notch in shaping the CLE and the boundary of mesoderm fate.

T local heterogeneity in the CLE, observed in this chapter and chapter 3, was reduced following Notch inhibition. But the patterning did not resemble a theoretical lateral inhibition pattern. As such, the mechanism that creates the increased T heterogeneity, and the contribution from Notch signalling, was not clear, whether this has a role in NMP maintenance differentiation is an open question.

These results highlight that Tbx6+ high cells not greatly affected by Notch inhibition likely contributed to the increased local heterogeneity for Tbx6 expression in epiblasts and gastruloids, suggesting the intracellular GRN may be the source of local heterogeneity. But whether the location of these Tbx6+ high cells within the NMPC contributes to NMP maintain the niche by a mesoderm related signal profile from these cells does not influence NMP differentiation.

Chapter 6:

Concluding remarks and future directions.

5.3 Overview of findings

In this thesis, I set out to answer two questions:

1. Does Notch regulate NMP TF fate marker expression in a pro-mesoderm, pro-neural, or pro-maintenance effect?
2. Does Notch operate in the NMP context by lateral inhibition or lateral induction?

5.3.1 RNAseq datamining Notch genes are expressed in NMPs and the nascent mesoderm from E8.5 to E9.5.

Datamining public RNAseq of in vivo NMPs micro-dissected from the CLE (Gouti et al., 2017, Dias et al., 2020) confirmed the extensive Notch pathway gene expression previously identified in the literature by ISH, also showing an increase in Notch genes Jag1, Hes1, Notch1 expression from E8.0 to E9.5. Correlation analysis shows Notch pathway genes Jag1, Notch3, Hes1, Hes6 correlated with genes associated with the Wnt/FGF/T NMP feedback circuit separate to a nascent mesoderm profile expected of the PSM (Hes7, Dll1, Dll3, Notch1, Tbx6, Msgn1). Indicating the necessary Notch components for lateral induction or lateral inhibition are expressed in NMPs.

For instance, lateral inhibition could operate through Dll1/Tbx6 expressing cells signalling to neighbouring NMPs via Notch3 and nascent mesoderm cells via

Notch1, upregulating Hes1/Hes7 to repress Dll1, and potentially other genes necessary for mesoderm differentiation in a novel gene interaction.

Lateral induction in NMPs could operate through Jag1 to signal to neighbouring NMPs through Notch3 and Notch1 to upregulate Myc and supporting Sox2 and Fgf expression (Mastromina et al., 2018). Hes6 expression in NMPs may also protect them from Hes1 mediated transcriptional inhibition (Bae et al., 2000). If lateral inhibition is present, inhibiting Notch would increase Dll1 expression and increase mesoderm differentiation. But since lateral induction is associated with NMPs, in theory inhibiting Notch would primarily result in a downregulation of NMP identity and therefore reduce mesodermal differentiation, countering the pro-mesodermal effect Notch inhibition would have in a lateral inhibition model.

5.3.2 Notch inhibition has a pro-neural effect on human and mouse NMP identity.

Notch inhibition, using gamma secretase inhibitors, inhibited mesoderm differentiation in human and mouse cells, resulting in a downregulation of T/Tbx6 and an upregulation of Sox2. This recapitulated the result from Haston (2018) with a restriction of NMP fates to neural in chick embryo NSB cells. However, this is distinct from the c-Myc inhibition effect, posited to be a downstream actuator of Notch signalling on the NMP identity, where inhibition of c-Myc resulted in downregulation of Sox2 and T with no pro-neural effect or premature differentiation (Mastromina et al., 2018). Like the c-Myc inhibition study, Notch inhibition appeared to slow proliferation with shorter gastruloids and smaller epiblasts in the Notch inhibited conditions.

The pro-neural effect of Notch inhibition was not as strong as Wnt inhibition via porcupine inhibitors. Also, TF expression after Notch inhibition could not be rescued to levels of the control condition with the addition of CHIR. Conversely, increasing CHIR did rescue TF expression to the DMSO control level during Wnt inhibition, suggesting the notion Notch plays a distinct role from Wnt. Critically, I presented

evidence that a NMP T/Sox2 profile is not lost entirely in the epiblast and gastruloids following Notch inhibition, but the NMP profile was more neural.

I also developed a high throughput assay technique, analogous to cytospinning, to provide unbiased and representative quantifications of changes to TF expression within a heterogeneous NMP-LC population.

Overall, these results are consistent with the lateral induction hypothesis where Notch supports NMP identity and permits mesoderm differentiation.

5.3.3 Distinct gradients and patterning of Sox2, T, and Tbx6 in the E8.5 epiblast.

I developed a novel method to normalise the 3D curvature of the E8.5 epiblast to a 2D plane, allowing graphical representation and spatial TF expression interrogation. This provided more explicit quantification of TF expression gradients and each TF factor had distinct patterns, which were previously described as “U-shaped”.

In conjunction with the epiblast normalisation, I employed two separate methods to quantitatively define ROIs within the epiblast, including the NMP niche. First, I used the TF expression gradients to identify a Neural-NMP-Mesoderm cell identity pseudospace axis to produce a unified continuous metric, representing each TF’s gradient of expression. I also used k-means clustering to produced evenly sized discrete spatial groups for analysis.

I used these methods to evaluate the changes in patterning along the TF gradients, identifying increased neighbourhood heterogeneity along certain sections of the T and Tbx6 gradient, which overlap in the NMP niche. In the NMP niche, Tbx6 was more heterogenous than T and Sox2, and T was more heterogeneous than Sox2. With randomised simulations, this revealed the increased variation for T followed a normal distribution, but the heterogeneityTbx6 heterogeny did not with Tbx6 cells surrounded by disproportionately lowly Tbx6 expressing cells. Which would be expected of lateral inhibition, but other mechanisms cannot be ruled out.

5.3.4 The effect of Notch inhibition on patterning remains unclear.

Notch inhibition did result in a reduction in T and Tbx6 heterogeneity in the epiblast NMP niche, but no change in the lateral inhibition type patterning was observed. The reason was speculated as committed mesodermal cells unaffected by Notch inhibition remained in the NMP niche creating local heterogeneity. Also, the dominant pro-neural effect of Notch inhibition may mask the lateral inhibition mechanism. As such, no clear indication for a loss of lateral inhibition-like patterning was observed after Notch inhibition. Most evidence suggests a positive feedback for Notch on NMP identity and mesoderm differentiation. As mentioned, the only line of evidence suggesting negative regulation by Notch, as required of lateral inhibition, was an increase in Dll1 expression following Notch inhibition in EpiSC derived NMP-LCs. As previously discussed, further controls to establish the efficacy of Notch inhibition and the effect on Notch components would benefit the overall interpretation of these results. However, the literature indicates that many Notch components may not be solely controlled by Notch but also by T-box proteins T/Tbx6, Sox2, and Wnt.

5.3.5 Tbx6 temporal and spatial dynamics indicates presence of committed mesodermal cells in NMP niche creating heterogeneity.

Using the high throughput image quantification technique, I created an analysis method to study gene expression in time, complementary to fluorescent reporter live imaging methods. In human NMP-LCs, this method provided preliminary evidence to the location of a threshold in mesoderm commitment along the Tbx6 expression range, suggesting that mid/low Tbx6+ cells can revert to Tbx6- when exogenous Wnt/FGF is removed or Notch/Wnt is inhibited.

Tbx6 cells remaining in the NMP niche after Notch inhibition indicate cells committed to mesoderm are present in NMP niche that are yet to organise into a coherent PSM tissues, posing the question if these have a role in NMP maintenance or mesoderm

differentiation control. Overall, this suggests that the intracellular GRN is more responsible for the Tbx6 heterogeneity than signalling mediated enforcement.

5.3.6 Summary.

Overall, these results are consistent with a role of Notch signalling in controlling NMP maintenance and mesoderm differentiation not limited to a role operating downstream c-Myc action. These findings start to address the how Notch signalling might influence spatial patterning of transcription factors associated with NMP maintenance and mesoderm differentiation. This work also provides analysis methods to quantify patterning in technically challenging 3D environments, exposing questions as to the role of the different spatial patterns in controlling NMP differentiation and maintenance. Overall contributing knowledge and methodologies to further understand the complex signalling pathways and regulatory landscape that maintains NMP identity and differentiation.

5.4 Implications of Notch signalling and heterogeneity when culturing NMPs *in vitro*.

A critical roadblock in the extended culture of NMPs to posterior identities is spontaneous differentiation and heterogeneity. The *in vivo* quantifications of TF expression heterogeneity within the NMP niche suggests heterogeneity in mesoderm differentiation is built into the NMP niche architecture. One can speculate on the source and purpose of the regulatory mechanism enforcing the heterogeneity, such as to create symmetry breaking events or to negatively regulate local positive feedback loop or “community effect” (Gurdon, 1988, Bolouri and Davidson, 2010).But regardless, local heterogeneity of T and Tbx6 expression is found in distinct regions of their expression gradients and a certain proportion of cells within the NMP niche may be committed to mesoderm. This must be accounted for when culturing the NMPs for extended periods of time, for instance it may be the case that mesodermal

cells integrated or adjacent to the NMP niche are required to maintain NMP identity and proliferation.

In the same way Wnt and Chiron is stimulated, Notch could be modulated to control differentiation. Also, if culturing NMPs *in vitro* will inevitably produce mesodermal cells that increasingly contribute to a Wnt/FGF/Notch local mesoderm affirming positive feedback signalling mechanism, to culture NMPs for extended periods a culture technique that provides route for the exit of mesoderm cells to a cell sink away from the NMP niche, analogous to the primitive streak, may be required. Instead of mesoderm signalling antagonists, such as RA in NMPs balancing Wnt/Fgf (Gouti et al., 2017), a population size reducing mechanism may be a powerful negative regulatory process to control a self-sustaining positive feedback "community effect".

Alternatively, conditional and reversable knockouts for mesodermal genes that block nascent mesoderm differentiation may provide a route to stably culture NMPs. Regardless, when culturing NMPs a heterogeneity must be expected to a certain degree and not circumventable without manipulation.

5.5 Future directions.

It remains unclear what the specific mechanism of action Notch signalling uses to control NMP identity and mesoderm differentiation. Future studies may look to further characterise the effect of Notch inhibition on NMPs and mesoderm differentiation, such as SC-RNAseq following Notch inhibition to identify differential gene expression in Notch components and the effect on other signalling pathways. Chromatin immunoprecipitation followed by sequencing (ChIP–seq) to identify Hes genes targets in NMPs would indicate what function the Hes genes have, as Hes gene targets has the least information from the literature relating to the interaction between NMP markers and Notch components. Similarly, Chip-seq of RBP-Jk in NMP would indicate what are the direct targets of Notch signalling. Together, this would build a picture of the regulatory control Notch has in the broader established NMP signalling pathways and GRNs.

The Notch and NMP gene profiles associations, namely the NMP Wnt/FGF/T/Jag1/Notch3 and PSM Tbx6/Dll1/Notch1/Lfng profiles, offer an interesting route to explore how Notch components regulate NMP vs mesoderm differentiation. Instead of total Notch inhibition as in the experiments I performed, manipulating individual components, such as Jag1 or Dll1, may be able to separate theoretical lateral induction and lateral inhibition mechanisms. For instance, selective knockdown of Dll1 may block Dll1 lateral mediate lateral inhibition and reduce overall heterogeneity, while preserving the function of the Wnt/FGF/T/Jag1/Notch3 Notch component signalling. In contrast, the Jag1 knockdown may reduce Jag1 mediated lateral induction of the T/Wnt/FGF feedback loop and recapitulate the results I presented from total Notch inhibition, namely a Notch mediated pro-NMP and mesoderm differentiation.

It is also not clear if given enough time, Notch inhibition would abolish the NMP profile. Longer culture times, of NMPs *ex vivo* or in gastruloids perhaps, would be necessary evaluate if Notch inhibition results in complete loss of T, or if the NMP like state and potency is retained and transitions to another location in the epiblast perhaps. The data I present represented short experimental timeframes and T/Tbx6 was never completely abolished. In chick embryos, axial extension continued during Notch inhibition and new PSM tissue was produced suggesting Notch inhibition did not completely abolish mesoderm commitment (Haston, 2018) or no ectopic neural tubes, as found in mouse Tbx6 mutants (Takemoto et al., 2011).

Due to the oscillatory nature of many Notch components (Chen et al., 2005, Kageyama et al., 2018), incorporating time into the experimental design may be required to fully capture the regulatory mechanisms of Notch signalling in controlling NMP differentiation. Future experiments should make use of live imaging of fluorescent reporters of Notch components and transcriptional regulators.

In accordance with this, exploring the time dimension with TF expression and patterning would yield insights into how these patterns arise and are maintained. For instance, what are the limits of correction to perturbations in maintaining a TF gradient in the epiblast? It would be interesting to combine the analysis methods I

presented with live imaging and single cell tracking of reporter lines in 3D, such as by McDole et al. (2018), to track the patterning data in time and quantify changes resulting from manipulation. This however will be technically challenging.

To understand how the different signalling molecules and GRNs maintain the NMP niche, it would be prudent to explore the mechanism by which TF gradients are established, and how T/Tbx6 heterogeneity is created and then overridden during the transition from heterogenous in the NMP niche to homogenous within the PS. It is not clear whether heterogeneity has an active role in regulating NMP maintenance or differentiation, such as negatively regulating a mechanism to promote homogeneity like lateral induction or a community effect, or if the heterogeneity is just a feature of the GRN dynamics to quickly repress the progenitor state. A mathematical model of the GRN with morphogen inputs, as in Gouti et al. (2017), could be extended to include Notch and in a spatial context. For instance, a mathematical model, similar to Boareto et al. (2016), could explore how local lateral inhibition and lateral induction type mechanisms may interact in this context to achieve the different spatial patterns of T, Sox2, and Tbx6 observed here. Exploring what GRN and cell-cell signalling motifs can produce the patterning quantified in this thesis may suggest what mechanism is theoretically plausible and guide future experiments. Due to complexity and technical limitations, exploring this *in silico* is likely to be the optimal next step to address this rather than *in vitro* or *in vivo.*

Overall, a systems level approach is essential to quantitatively investigate how the RA/Wnt/FGF/Notch pathways individually and collectively interact across different scales and integrate into the increasingly complex NMP gene regulatory network, shaping TF expression gradient and cell behaviour in the epiblast. Ultimately to understand what regulatory mechanisms confer robustness and reproducibility are so we can produce equally robust and reproducible axial progenitor/NMP culture techniques.

References:

ABU-ABED, S., DOLLÉ, P., METZGER, D., BECKETT, B., CHAMBON, P. & PETKOVICH, M. 2001. The retinoic acid-metabolizing enzyme, CYP26A1, is essential for normal hindbrain patterning, vertebral identity, and development of posterior structures. *Genes & development,* 15**,** 226-240.

ACAR, A., HIDALGO-SASTRE, A., LEVERENTZ, M. K., MILLS, C. G., WOODCOCK, S., BARON, M., COLLU, G. M. & BRENNAN, K. 2021. Inhibition of Wnt signalling by Notch via two distinct mechanisms. *Scientific Reports,* 11**,** 9096.

AKAI, J., HALLEY, P. A. & STOREY, K. G. 2005. FGF-dependent Notch signaling maintains the spinal cord stem zone. *Genes & development,* 19**,** 2877-2887.

AMIN, S., NEIJTS, R., SIMMINI, S., VAN ROOIJEN, C., TAN, S. C., KESTER, L., VAN OUDENAARDEN, A., CREYGHTON, M. P. & DESCHAMPS, J. 2016. Cdx and T brachyury co-activate growth signaling in the embryonic axial progenitor niche. *Cell reports,* 17**,** 3165-3177.

ANANTHASUBRAMANIAM, B. & HERZEL, H. 2014. Positive feedback promotes oscillations in negative feedback loops. *PLoS One,* 9**,** e104761.

ANDERSON, M. J., MAGIDSON, V., KAGEYAMA, R. & LEWANDOSKI, M. 2020. Fgf4 maintains Hes7 levels critical for normal somite segmentation clock function. *Elife,* 9**,** e55608.

ARKELL, R. M. & TAM, P. P. 2012. Initiating head development in mouse embryos: integrating signalling and transcriptional activity. *Open biology,* 2**,** 120030.

ARNOLD, S. J. & ROBERTSON, E. J. 2009. Making a commitment: cell lineage allocation and axis patterning in the early mouse embryo. *Nature reviews Molecular cell biology,* 10**,** 91-103.

BAE, S., BESSHO, Y., HOJO, M. & KAGEYAMA, R. 2000. The bHLH gene Hes6, an inhibitor of Hes1, promotes neuronal differentiation. *Development,* 127**,** 2933-2943.

BARDOT, E. S. & HADJANTONAKIS, A.-K. 2020. Mouse gastrulation: Coordination of tissue patterning, specification and diversification of cell fate. *Mechanisms of Development,* 163**,** 103617.

BARSI, J. C., RAJENDRA, R., WU, J. I. & ARTZT, K. 2005. Mind bomb1 is a ubiquitin ligase essential for mouse embryonic development and Notch signaling. *Mechanisms of development,* 122**,** 1106-1117.

BECCARI, L., MORIS, N., GIRGIN, M., TURNER, D. A., BAILLIE-JOHNSON, P., COSSY, A.-C., LUTOLF, M. P., DUBOULE, D. & ARIAS, A. M. 2018. Multi-axial self-organization properties of mouse embryonic stem cells into gastruloids. *Nature,* 562**,** 272-276.

BECHT, E., MCINNES, L., HEALY, J., DUTERTRE, C.-A., KWOK, I. W., NG, L. G., GINHOUX, F. & NEWELL, E. W. 2019. Dimensionality reduction for visualizing single-cell data using UMAP. *Nature biotechnology,* 37**,** 38-44.

BEDDINGTON, R. 1983. Histogenetic and neoplastic potential of different regions of the mouse embryonic egg cylinder.

BEDDINGTON, R. 1994. Induction of a second neural axis by the mouse node. *Development,* 120**,** 613-620.

BEDDINGTON, R. S. & ROBERTSON, E. J. 1999. Axis development and early asymmetry in mammals. *Cell,* 96**,** 195-209.

BEN-HAIM, N., LU, C., GUZMAN-AYALA, M., PESCATORE, L., MESNARD, D., BISCHOFBERGER, M., NAEF, F., ROBERTSON, E. J. & CONSTAM, D. B. 2006. The nodal precursor acting via activin receptors induces mesoderm by maintaining a source of its convertases and BMP4. *Developmental cell,* 11**,** 313-323.

BESSHO, Y., HIRATA, H., MASAMIZU, Y. & KAGEYAMA, R. 2003. Periodic repression by the bHLH factor Hes7 is an essential mechanism for the somite segmentation clock. *Genes & development,* 17**,** 1451-1456.

BESSHO, Y., MIYOSHI, G., SAKATA, R. & KAGEYAMA, R. 2001a. Hes7: a bHLH-type repressor gene regulated by Notch and expressed in the presomitic mesoderm. *Genes to Cells,* 6**,** 175-185.

BESSHO, Y., SAKATA, R., KOMATSU, S., SHIOTA, K., YAMADA, S. & KAGEYAMA, R. 2001b. Dynamic expression and essential functions of Hes7 in somite segmentation. *Genes Dev,* 15**,** 2642-7.

BETTENHAUSEN, B., HRABE DE ANGELIS, M., SIMON, D., GUENET, J. L. & GOSSLER, A. 1995. Transient and restricted expression during mouse embryogenesis of Dll1, a murine gene closely related to Drosophila Delta. *Development,* 121**,** 2407-2418.

BINAGUI-CASAS, A., DIAS, A., GUILLOT, C., METZIS, V. & SAUNDERS, D. 2021. Building consensus in neuromesodermal research: Current advances and future biomedical perspectives. *Current opinion in cell biology,* 73**,** 133-140.

BLASSBERG, R., PATEL, H., WATSON, T., GOUTI, M., METZIS, V., DELÁS, M. J. & BRISCOE, J. 2022. Sox2 levels regulate the chromatin occupancy of WNT mediators in epiblast progenitors responsible for vertebrate body formation. *Nature Cell Biology,* 24**,** 633-644.

BLIN, G. 2018. *PickCells* [Online]. Available: https://pickcellslab.frama.io/docs/ [Accessed 2023].

BLIN, G., SADURSKA, D., PORTERO MIGUELES, R., CHEN, N., WATSON, J. A. & LOWELL, S. 2019. Nessys: A new set of tools for the automated detection of nuclei within intact tissues and dense 3D cultures. *PLOS Biology,* 17**,** e3000388.

BLIN, G., WISNIEWSKI, D., PICART, C., THERY, M., PUCEAT, M. & LOWELL, S. 2018. Geometrical confinement controls the asymmetric patterning of brachyury in cultures of pluripotent cells. *Development,* 145.

BOARETO, M., JOLLY, M. K., GOLDMAN, A., PIETILÄ, M., MANI, S. A., SENGUPTA, S., BEN-JACOB, E., LEVINE, H. & ONUCHIC, J. N. 2016. Notch-Jagged signalling can give rise to clusters of cells exhibiting a hybrid epithelial/mesenchymal phenotype. *J R Soc Interface,* 13.

BOARETO, M., JOLLY, M. K., LU, M., ONUCHIC, J. N., CLEMENTI, C. & BEN-JACOB, E. 2015. Jagged–Delta asymmetry in Notch signaling can give rise to a Sender/Receiver hybrid phenotype. *Proceedings of the National Academy of Sciences,* 112**,** E402-E409.

BOLOURI, H. & DAVIDSON, E. H. 2010. The gene regulatory network basis of the "community effect," and analysis of a sea urchin embryo example. *Dev Biol,* 340**,** 170-8.

BONGSO, A., FONG, C.-Y., NG, S.-C. & RATNAM, S. 1994. Fertilization and early embryology: Isolation and culture of inner cell mass cells from human blastocysts. *Human Reproduction,* 9**,** 2110-2117.

BOULDIN, C. M., MANNING, A. J., PENG, Y.-H., FARR III, G. H., HUNG, K. L., DONG, A. & KIMELMAN, D. 2015. Wnt signaling and tbx16 form a bistable switch to commit bipotential progenitors to mesoderm. *Development,* 142**,** 2499-2507.

BOULET, A. M. & CAPECCHI, M. R. 2012. Signaling by FGF4 and FGF8 is required for axial elongation of the mouse embryo. *Dev Biol,* 371**,** 235-45.

BRENNAN, J., LU, C. C., NORRIS, D. P., RODRIGUEZ, T. A., BEDDINGTON, R. S. & ROBERTSON, E. J. 2001. Nodal signalling in the epiblast patterns the early mouse embryo. *Nature,* 411**,** 965-969.

BRONS, I. G. M., SMITHERS, L. E., TROTTER, M. W., RUGG-GUNN, P., SUN, B., CHUVA DE SOUSA LOPES, S. M., HOWLETT, S. K., CLARKSON, A., AHRLUND-RICHTER, L. & PEDERSEN, R. A. 2007. Derivation of pluripotent epiblast stem cells from mammalian embryos. *Nature,* 448**,** 191-195.

CAMBRAY, N. & WILSON, V. 2007. Two distinct sources for a population of maturing axial progenitors.

CAMERON, D. E., BASHOR, C. J. & COLLINS, J. J. 2014. A brief history of synthetic biology. *Nature Reviews Microbiology,* 12**,** 381-390.

CARRIERI, F. A. & DALE, J. K. 2017. Turn it down a Notch. *Frontiers in cell and developmental biology,* 4**,** 151.

CASTEL, D., MOURIKIS, P., BARTELS, S. J., BRINKMAN, A. B., TAJBAKHSH, S. & STUNNENBERG, H. G. 2013. Dynamic binding of RBPJ is determined by Notch signaling status. *Genes Dev,* 27**,** 1059-71.

CHALAMALASETTY, R. B., DUNTY JR, W. C., BIRIS, K. K., AJIMA, R., IACOVINO, M., BEISAW, A., FEIGENBAUM, L., CHAPMAN, D. L., YOON, J. K. & KYBA, M. 2011. The Wnt3a/β-catenin target gene Mesogenin1 controls the segmentation clock by activating a Notch signalling program. *Nature communications,* 2**,** 390.

CHALAMALASETTY, R. B., GARRIOCK, R. J., DUNTY JR, W. C., KENNEDY, M. W., JAILWALA, P., SI, H. & YAMAGUCHI, T. P. 2014. Mesogenin 1 is a master regulator of paraxial presomitic mesoderm differentiation. *Development,* 141**,** 4285-4297.

CHAMBERS, I. & TOMLINSON, S. R. 2009. The transcriptional foundation of pluripotency.

CHAPMAN, G., SPARROW, D. B., KREMMER, E. & DUNWOODIE, S. L. 2011. Notch inhibition by the ligand DELTA-LIKE 3 defines the mechanism of abnormal vertebral segmentation in spondylocostal dysostosis. *Human molecular genetics,* 20**,** 905-916.

CHAZAUD, C. & YAMANAKA, Y. 2016. Lineage specification in the mouse preimplantation embryo. *Development,* 143**,** 1063-1074.

CHAZAUD, C., YAMANAKA, Y., PAWSON, T. & ROSSANT, J. 2006. Early lineage segregation between epiblast and primitive endoderm in mouse blastocysts through the Grb2-MAPK pathway. *Developmental cell,* 10**,** 615-624.

CHEN, J., KANG, L. & ZHANG, N. 2005. Negative feedback loop formed by Lunatic fringe and Hes7 controls their oscillatory expression during somitogenesis. *Genesis,* 43**,** 196-204.

CHEN, X., STOECK, A., LEE, S. J., SHIH, I.-M., WANG, M. M. & WANG, T.-L. 2010. Jagged1 expression regulated by Notch3 and Wnt/β-catenin signaling pathways in ovarian cancer. *Oncotarget,* 1**,** 210.

CHIBA, S. 2006. Concise review: Notch signaling in stem cell systems. *Stem cells,* 24**,** 2437-2447.

CHRYSOSTOMOU, E., GALE, J. E. & DAUDET, N. 2012. Delta-like 1 and lateral inhibition during hair cell formation in the chicken inner ear: evidence against cis-inhibition. *Development,* 139**,** 3764-3774.

CHU, Y., SOLSKI, P. A., KHOSRAVI-FAR, R., DER, C. J. & KELLY, K. 1996. The Mitogen-activated Protein Kinase Phosphatases PAC1, MKP-1, and MKP-2 Have Unique Substrate Specificities and Reduced Activity in Vivo toward the ERK2 sevenmaker Mutation (∗). *Journal of Biological Chemistry,* 271**,** 6497-6501.

CIRUNA, B. & ROSSANT, J. 2001. FGF Signaling Regulates Mesoderm Cell Fate Specification and Morphogenetic Movement at the Primitive Streak. *Developmental Cell,* 1**,** 37-49.

COLLIER, J. R., MONK, N. A., MAINI, P. K. & LEWIS, J. H. 1996. Pattern formation by lateral inhibition with feedback: a mathematical model of delta-notch intercellular signalling. *J Theor Biol,* 183**,** 429-46.

CONCEPCION, D., WASHKOWITZ, A. J., DESANTIS, A., OGEA, P., YANG, J. I., DOUGLAS, N. C. & PAPAIOANNOU, V. E. 2017. Cell lineage of timed cohorts of Tbx6-expressing cells in wild-type and Tbx6 mutant embryos. *Biol Open,* 6**,** 1065-1073.

CONLON, F. L., LYONS, K. M., TAKAESU, N., BARTH, K. S., KISPERT, A., HERRMANN, B. & ROBERTSON, E. J. 1994. A primary requirement for nodal in the formation and maintenance of the primitive streak in the mouse. *Development,* 120**,** 1919-1928.

CONLON, R. A., REAUME, A. G. & ROSSANT, J. 1995. Notch1 is required for the coordinate segmentation of somites. *Development,* 121**,** 1533-1545.

CRAMERI, F. 2018. *Scientific colour maps*.

CROSSLEY, P. H. & MARTIN, G. R. 1995. The mouse Fgf8 gene encodes a family of polypeptides and is expressed in regions that direct outgrowth and patterning in the developing embryo. *Development,* 121**,** 439-451.

CSIBRA, E. & STAN, G.-B. 2022. Absolute protein quantification using fluorescence measurements with FPCountR. *Nature Communications,* 13**,** 6600.

CUNNINGHAM, T. J., COLAS, A. & DUESTER, G. 2016. Early molecular events during retinoic acid induced differentiation of neuromesodermal progenitors. *Biology open,* 5**,** 1821-1833.

DAMJANOV, I., SOLTER, D. & ŠKREB, N. 1971. Teratocarcinogenesis as related to the age of embryos grafted under the kidney capsule. *Wilhelm Roux'Archiv für Entwicklungsmechanik der Organismen,* 167**,** 288-290.

DEL BARCO BARRANTES, I., ELIA, A. J., WÜNSCH, K., DE ANGELIS, M. H., MAK, T. W., ROSSANT, J., CONLON, R. A., GOSSLER, A. & DE LA POMPA, J. L. 1999. Interaction between Notch signalling and Lunatic fringe during somite boundary formation in the mouse. *Current Biology,* 9**,** 470-480.

DEL CORRAL, R. D., OLIVERA-MARTINEZ, I., GORIELY, A., GALE, E., MADEN, M. & STOREY, K. 2003. Opposing FGF and Retinoid Pathways Control Ventral Neural Pattern, Neuronal Differentiation, and Segmentation during Body Axis Extension. *Neuron,* 40**,** 65-79.

DEL VECCHIO, D., DY, A. J. & QIAN, Y. 2016. Control theory meets synthetic biology. *Journal of The Royal Society Interface,* 13**,** 20160380.

DELFINO-MACHÍN, M., LUNN, J. S., BREITKREUZ, D. N., AKAI, J. & STOREY, K. G. 2005. Specification and maintenance of the spinal cord stem zone.

DENG, C.-X., WYNSHAW-BORIS, A., SHEN, M. M., DAUGHERTY, C., ORNITZ, D. M. & LEDER, P. 1994. Murine FGFR-1 is required for early postimplantation growth and axial organization. *Genes & development,* 8**,** 3045-3057.

DENHAM, M., HASEGAWA, K., MENHENIOTT, T., ROLLO, B., ZHANG, D., HOUGH, S., ALSHAWAF, A., FEBBRARO, F., IGHANIYAN, S., LEUNG, J., ELLIOTT, D. A., NEWGREEN, D. F., PERA, M. F. & DOTTORI, M. 2015. Multipotent Caudal Neural Progenitors Derived from Human Pluripotent Stem Cells That Give Rise to Lineages of the Central and Peripheral Nervous System. *Stem Cells,* 33**,** 1759-1770.

DESCALZO, S. M. & ARIAS, A. M. The structure of Wntch signalling and the resolution of transition states in development. Seminars in cell & developmental biology, 2012. Elsevier, 443-449.

DIAS, A., LOZOVSKA, A., WYMEERSCH, F. J., NÓVOA, A., BINAGUI-CASAS, A., SOBRAL, D., MARTINS, G. G., WILSON, V. & MALLO, M. 2020. A Tgfbr1/Snai1-dependent developmental module at the core of vertebrate axial elongation. *Elife,* 9**,** e56615.

DUNTY JR, W. C., BIRIS, K. K., CHALAMALASETTY, R. B., TAKETO, M. M., LEWANDOSKI, M. & YAMAGUCHI, T. P. 2008. Wnt3a/β-catenin signaling controls posterior body development by coordinating mesoderm formation and segmentation.

DUNWOODIE, S. L., HENRIQUE, D., HARRISON, S. M. & BEDDINGTON, R. 1997. Mouse Dll3: a novel divergent Delta gene which may complement the function of other Delta homologues during early pattern formation in the mouse embryo. *Development,* 124**,** 3065-3076.

EDRI, S., HAYWARD, P., JAWAID, W. & MARTINEZ ARIAS, A. 2019. Neuro-mesodermal progenitors (NMPs): a comparative study between pluripotent stem cells and embryo-derived populations. *Development,* 146**,** dev180190.

EHEBAUER, M., HAYWARD, P. & ARIAS, A. M. 2006. Notch, a universal arbiter of cell fate decisions. *Science,* 314**,** 1414-1415.

ESKANDARI, E. & EAVES, C. J. 2022. Paradoxical roles of caspase-3 in regulating cell survival, proliferation, and tumorigenesis. *J Cell Biol,* 221.

EVANS, A. L., FAIAL, T., GILCHRIST, M. J., DOWN, T., VALLIER, L., PEDERSEN, R. A., WARDLE, F. C. & SMITH, J. C. 2012. Genomic targets of Brachyury (T) in differentiating mouse embryonic stem cells. *PloS one,* 7**,** e33346.

EVANS, M. J. & KAUFMAN, M. H. 1981. Establishment in culture of pluripotential cells from mouse embryos. *nature,* 292**,** 154-156.

FENG, R. & WEN, J. 2015. Overview of the roles of Sox2 in stem cell and development. *Biological Chemistry,* 396**,** 883-891.

FENG, X., KREBS, L. T. & GRIDLEY, T. 2010. Patent ductus arteriosus in mice with smooth muscle-specific Jag1 deletion. *Development,* 137**,** 4191-9.

FERJENTSIK, Z., HAYASHI, S., DALE, J. K., BESSHO, Y., HERREMAN, A., DE STROOPER, B., DEL MONTE, G., DE LA POMPA, J. L. & MAROTO, M. 2009. Notch is a critical component of the mouse somitogenesis oscillator and is essential for the formation of the somites. *PLoS genetics,* 5**,** e1000662.

FERRELL, J. E. 2016. Perfect and near-perfect adaptation in cell signaling. *Cell systems,* 2**,** 62-67.

FIOR, R. & HENRIQUE, D. 2009. " Notch-Off": a perspective on the termination of Notch signalling. *International Journal of Developmental Biology,* 53**,** 1379-1384.

FORLANI, S., LAWSON, K. A. & DESCHAMPS, J. 2003. Acquisition of Hox codes during gastrulation and axial elongation in the mouse embryo. *Development,* 130**,** 3807-3819.

FRITH, T. J. R. & TSAKIRIDIS, A. 2019. Efficient Generation of Trunk Neural Crest and Sympathetic Neurons from Human Pluripotent Stem Cells Via a Neuromesodermal Axial Progenitor Intermediate. *Curr Protoc Stem Cell Biol,* 49**,** e81.

FUJIMURO, T., MATSUI, T., NITANDA, Y., MATTA, T., SAKUMURA, Y., SAITO, M., KOHNO, K., NAKAHATA, Y. & BESSHO, Y. 2014. Hes7 3'UTR is required for somite segmentation function. *Scientific Reports,* 4**,** 6462.

FULTON, T., SPIESS, K., THOMSON, L., WANG, Y., CLARK, B., HWANG, S., PAIGE, B., VERD, B. & STEVENTON, B. 2021. Cell Rearrangement Generates Pattern Emergence as a Function of Temporal Morphogen Exposure. bioRxiv.

GALCERAN, J., SUSTMANN, C., HSU, S.-C., FOLBERTH, S. & GROSSCHEDL, R. 2004. LEF1-mediated regulation of Delta-like1 links Wnt and Notch signaling in somitogenesis. *Genes & development,* 18**,** 2718-2723.

GARNIER, S., ROSS, N., RUDIS, B., FILIPOVIC-PIERUCCI, A., GALILI, T., GREENWELL, B., SIEVERT, C., HARRIS, D. & CHEN, J. 2021. Sjmgarnier/viridis: viridis 0.6. 0 (pre-CRAN release). Zenodo.

GARPINGER, O., HÄGGLUND, T. & ÅSTRÖM, K. J. 2014. Performance and robustness trade-offs in PID control. *Journal of Process Control,* 24**,** 568-577.

GARRIOCK, R. J., CHALAMALASETTY, R. B., KENNEDY, M. W., CANIZALES, L. C., LEWANDOSKI, M. & YAMAGUCHI, T. P. 2015. Lineage tracing of neuromesodermal progenitors reveals novel Wnt-dependent roles in trunk progenitor cell maintenance and differentiation. *Development,* 142**,** 1628-1638.

GEFFERS, I., SERTH, K., CHAPMAN, G., JAEKEL, R., SCHUSTER-GOSSLER, K., CORDES, R., SPARROW, D. B., KREMMER, E., DUNWOODIE, S. L. & KLEIN, T. 2007. Divergent functions and distinct localization of the Notch ligands DLL1 and DLL3 in vivo. *The Journal of cell biology,* 178**,** 465-476.

GENTSCH, G. E., OWENS, N. D., MARTIN, S. R., PICCINELLI, P., FAIAL, T., TROTTER, M. W., GILCHRIST, M. J. & SMITH, J. C. 2013. In vivo T-box transcription factor profiling reveals joint regulation of embryonic neuromesodermal bipotency. *Cell reports,* 4**,** 1185-1196.

GHOSHAL, S., NOHRIA, N. & WONG, M. 1979. A K-means clustering algorithm. Algorithm AS 136. *Applied Statistics,* 28**,** 100-08.

GONZALEZ, A., MANOSALVA, I., LIU, T. & KAGEYAMA, R. 2013. Control of Hes7 expression by Tbx6, the Wnt pathway and the chemical Gsk3 inhibitor LiCl in the mouse segmentation clock. *PloS one,* 8**,** e53323.

GOUTI, M., DELILE, J., STAMATAKI, D., WYMEERSCH, F. J., HUANG, Y., KLEINJUNG, J., WILSON, V. & BRISCOE, J. 2017. A gene regulatory network balances neural and mesoderm specification during vertebrate trunk development. *Developmental cell,* 41**,** 243-261. e7.

GOUTI, M., TSAKIRIDIS, A., WYMEERSCH, F. J., HUANG, Y., KLEINJUNG, J., WILSON, V. & BRISCOE, J. 2014. In vitro generation of neuromesodermal progenitors reveals distinct roles for wnt

signalling in the specification of spinal cord and paraxial mesoderm identity. *PLoS biology,* 12**,** e1001937.

GRAINGER, S., LAM, J., SAVORY, J. G., MEARS, A. J., RIJLI, F. M. & LOHNES, D. 2012. Cdx regulates Dll1 in multiple lineages. *Developmental biology,* 361**,** 1-11.

GUIBENTIF, C., GRIFFITHS, J. A., IMAZ-ROSSHANDLER, I., GHAZANFAR, S., NICHOLS, J., WILSON, V., GÖTTGENS, B. & MARIONI, J. C. 2021. Diverse routes toward early somites in the mouse embryo. *Developmental cell,* 56**,** 141-153. e6.

GUILLOT, C., DJEFFAL, Y., MICHAUT, A., RABE, B. & POURQUIÉ, O. 2021. Dynamics of primitive streak regression controls the fate of neuromesodermal progenitors in the chicken embryo. *Elife,* 10**,** e64819.

GUO, G., VON MEYENN, F., SANTOS, F., CHEN, Y., REIK, W., BERTONE, P., SMITH, A. & NICHOLS, J. 2016. Naive pluripotent stem cells derived directly from isolated cells of the human inner cell mass. *Stem cell reports,* 6**,** 437-446.

GURDON, J. B. 1988. A community effect in animal development. *Nature,* 336**,** 772-774.

HAERTTER, D., WANG, X., FOGERSON, S. M., RAMKUMAR, N., CRAWFORD, J. M., POSS, K. D., DI TALIA, S., KIEHART, D. P. & SCHMIDT, C. F. 2022. DeepProjection: specific and robust projection of curved 2D tissue sheets from 3D microscopy using deep learning. *Development,* 149.

HAMADA, Y., KADOKAWA, Y., OKABE, M., IKAWA, M., COLEMAN, J. R. & TSUJIMOTO, Y. 1999. Mutation in ankyrin repeats of the mouse Notch2 gene induces early embryonic lethality. *Development,* 126**,** 3415-3424.

HASTON, S. 2018. *The role of Notch signaling in early avian embryo progenitor cell fate decisions.* BSc Thesis, University of Dundee, Dundee.

HAYASHI, S., NAKAHATA, Y., KOHNO, K., MATSUI, T. & BESSHO, Y. 2018. Presomitic mesoderm-specific expression of the transcriptional repressor Hes7 is controlled by E-box, T-box, and Notch signaling pathways. *Journal of Biological Chemistry,* 293**,** 12167-12176.

HAYWARD, P., BRENNAN, K., SANDERS, P., BALAYO, T., DASGUPTA, R., PERRIMON, N. & ARIAS, A. M. 2005. Notch modulates Wnt signalling by associating with Armadillo/β-catenin and regulating its transcriptional activity.

HAYWARD, P., KALMAR, T. & MARTINEZ ARIAS, A. 2008. Wnt/Notch signalling and information processing during development.

HENRIQUE, D., ABRANCHES, E., VERRIER, L. & STOREY, K. G. 2015. Neuromesodermal progenitors and the making of the spinal cord. *Development,* 142**,** 2864-2875.

HICKS, C., JOHNSTON, S. H., DISIBIO, G., COLLAZO, A., VOGT, T. F. & WEINMASTER, G. 2000. Fringe differentially modulates Jagged1 and Delta1 signalling through Notch1 and Notch2. *Nature cell biology,* 2**,** 515-520.

HIRATA, H., BESSHO, Y., KOKUBU, H., MASAMIZU, Y., YAMADA, S., LEWIS, J. & KAGEYAMA, R. 2004. Instability of Hes7 protein is crucial for the somite segmentation clock. *Nature genetics,* 36**,** 750-754.

HOFMANN, M., SCHUSTER-GOSSLER, K., WATABE-RUDOLPH, M., AULEHLA, A., HERRMANN, B. G. & GOSSLER, A. 2004. WNT signaling, in synergy with T/TBX6, controls Notch signaling by regulating Dll1 expression in the presomitic mesoderm of mouse embryos. *Genes & development,* 18**,** 2712-2717.

HONG, C.-S. & SAINT-JEANNET, J.-P. 2018. The b-HLH transcription factor Hes3 participates in neural plate border formation by interfering with Wnt/β-catenin signaling. *Developmental biology,* 442**,** 162-172.

HU, W. S. & ZENG, A.-P. 2012. *Genomics and systems biology of mammalian cell culture*, Springer Science & Business Media.

ISHIKAWA, A., KITAJIMA, S., TAKAHASHI, Y., KOKUBO, H., KANNO, J., INOUE, T. & SAGA, Y. 2004. Mouse Nkd1, a Wnt antagonist, exhibits oscillatory gene expression in the PSM under the control of Notch signaling. *Mechanisms of development,* 121**,** 1443-1453.

ISO, T., KEDES, L. & HAMAMORI, Y. 2003. HES and HERP families: multiple effectors of the Notch signaling pathway. *Journal of cellular physiology,* 194**,** 237-255.

JAFARI MAMAGHANI, M., ANDERSSON, M. & KRIEGER, P. 2010. Spatial point pattern analysis of neurons using Ripley's K-function in 3D. *Frontiers in Neuroinformatics,* 4.

JANG, J., KU, S. Y., KIM, J. E., CHOI, K., KIM, Y. Y., KIM, H. S., OH, S. K., LEE, E. J., CHO, H.-J. & SONG, Y. H. 2008. Notch inhibition promotes human embryonic stem cell-derived cardiac mesoderm differentiation. *Stem Cells,* 26**,** 2782-2790.

JAVALI, A., MISRA, A., LEONAVICIUS, K., ACHARYYA, D., VYAS, B. & SAMBASIVAN, R. 2017. Co-expression of Tbx6 and Sox2 identifies a novel transient neuromesoderm progenitor cell state. *Development,* 144**,** 4522-4529.

KAGEYAMA, R., ISOMURA, A. & SHIMOJO, H. 2023. Biological significance of the coupling delay in synchronized oscillations. *Physiology,* 38**,** 000-000.

KAGEYAMA, R., OHTSUKA, T., SHIMOJO, H. & IMAYOSHI, I. 2008. Dynamic Notch signaling in neural progenitor cells and a revised view of lateral inhibition. *Nature neuroscience,* 11**,** 1247-1251.

KAGEYAMA, R., SHIMOJO, H. & ISOMURA, A. 2018. Oscillatory Control of Notch Signaling in Development. *Adv Exp Med Biol,* 1066**,** 265-277.

KAMIMOTO, K., STRINGA, B., HOFFMANN, C. M., JINDAL, K., SOLNICA-KREZEL, L. & MORRIS, S. A. 2023. Dissecting cell identity via network inference and in silico gene perturbation. *Nature,* 614**,** 742-751.

KATOH, M. & KATOH, M. 2006. Notch ligand, JAG1, is evolutionarily conserved target of canonical WNT signaling pathway in progenitor cells. *International journal of molecular medicine,* 17**,** 681-685.

KATOH, M. & KATOH, M. 2007. Integrative genomic analyses on HES/HEY family: Notch-independent HES1, HES3 transcription in undifferentiated ES cells, and Notch-dependent HES1, HES5, HEY1, HEY2, HEYL transcription in fetal tissues, adult tissues, or cancer. *International journal of oncology,* 31**,** 461-466.

KAUR, H., HEISER, C. N., MCKINLEY, E. T., VENTURA-ANTUNES, L., HARRIS, C. R., ROLAND, J. T., SHRUBSOLE, M. J., COFFEY, R. J., LAU, K. S. & VANDEKAR, S. 2023. Consensus tissue domain detection in spatial multi-omics data using MILWRM. *bioRxiv***,** 2023.02.02.526900.

KENNY, M. & SCHOEN, I. 2021. Violin SuperPlots: visualizing replicate heterogeneity in large data sets. *Molecular Biology of the Cell,* 32**,** 1333-1334.

KHAMMASH, M. H. 2021. Perfect adaptation in biology. *Cell Systems,* 12**,** 509-521.

KINDER, S. J., TSANG, T. E., QUINLAN, G. A., HADJANTONAKIS, A.-K., NAGY, A. & TAM, P. 1999. The orderly allocation of mesodermal cells to the extraembryonic structures and the anteroposterior axis during gastrulation of the mouse embryo. *Development,* 126**,** 4691-4701.

KITANO, H. 2002. Systems biology: a brief overview. *science,* 295**,** 1662-1664.

KOBAYASHI, T. & KAGEYAMA, R. 2010. Hes1 regulates embryonic stem cell differentiation by suppressing Notch signaling. *Genes to Cells,* 15**,** 689-698.

KOCH, F., SCHOLZE, M., WITTLER, L., SCHIFFERL, D., SUDHEER, S., GROTE, P., TIMMERMANN, B., MACURA, K. & HERRMANN, B. G. 2017. Antagonistic activities of Sox2 and brachyury control the fate choice of neuro-mesodermal progenitors. *Developmental cell,* 42**,** 514-526. e7.

KOJIMA, Y., KAUFMAN-FRANCIS, K., STUDDERT, J. B., STEINER, K. A., POWER, M. D., LOEBEL, D. A., JONES, V., HOR, A., DE ALENCASTRO, G. & LOGAN, G. J. 2014a. The transcriptional and functional properties of mouse epiblast stem cells resemble the anterior primitive streak. *Cell stem cell,* 14**,** 107-120.

KOJIMA, Y., TAM, O. H. & TAM, P. P. Timing of developmental events in the early mouse embryo. Seminars in cell & developmental biology, 2014b. Elsevier, 65-75.

KOPAN, R. & ILAGAN, M. X. G. 2009. The canonical Notch signaling pathway: unfolding the activation mechanism. *Cell,* 137**,** 216-233.

KOVALL, R. A., GEBELEIN, B., SPRINZAK, D. & KOPAN, R. 2017. The canonical Notch signaling pathway: structural and biochemical insights into shape, sugar, and force. *Developmental cell,* 41**,** 228-241.

KREBS, L. T., XUE, Y., NORTON, C. R., SUNDBERG, J. P., BEATUS, P., LENDAHL, U., JOUTEL, A. & GRIDLEY, T. 2003. Characterization of Notch3-deficient mice: Normal embryonic

development and absence of genetic interactions with a Notch1 mutation. *genesis,* 37**,** 139-143.

KUMAR, N., MISHRA, B., ATHAR, M. & MUKHTAR, S. 2021. Inference of Gene Regulatory Network from Single-Cell Transcriptomic Data Using pySCENIC. *Methods Mol Biol,* 2328**,** 171-182.

LADI, E., NICHOLS, J. T., GE, W., MIYAMOTO, A., YAO, C., YANG, L.-T., BOULTER, J., SUN, Y. E., KINTNER, C. & WEINMASTER, G. 2005. The divergent DSL ligand Dll3 does not activate Notch signaling but cell autonomously attenuates signaling induced by other DSL ligands. *The Journal of cell biology,* 170**,** 983-992.

LAFOYA, B., MUNROE, J. A., MIA, M. M., DETWEILER, M. A., CROW, J. J., WOOD, T., ROTH, S., SHARMA, B. & ALBIG, A. R. 2016. Notch: A multi-functional integrating system of microenvironmental signals. *Developmental biology,* 418**,** 227-241.

LANDER, A. D. 2011. Pattern, growth, and control. *Cell,* 144**,** 955-969.

LAWSON, K. A., MENESES, J. J. & PEDERSEN, R. A. 1991. Clonal analysis of epiblast fate during germ layer formation in the mouse embryo. *Development,* 113**,** 891-911.

LAZEBNIK, Y. 2002. Can a biologist fix a radio?—Or, what I learned while studying apoptosis. *Cancer cell,* 2**,** 179-182.

LEBON, L., LEE, T. V., SPRINZAK, D., JAFAR-NEJAD, H. & ELOWITZ, M. B. 2014. Fringe proteins modulate Notch-ligand cis and trans interactions to specify signaling states. *elife,* 3**,** e02950.

LEIMEISTER, C., DALE, K., FISCHER, A., KLAMT, B., HRABE DE ANGELIS, M., RADTKE, F., MCGREW, M. J., POURQUIÉ, O. & GESSLER, M. 2000. Oscillating Expression of c-Hey2 in the Presomitic Mesoderm Suggests That the Segmentation Clock May Use Combinatorial Signaling through Multiple Interacting bHLH Factors. *Developmental Biology,* 227**,** 91-103.

LIENERT, F., LOHMUELLER, J. J., GARG, A. & SILVER, P. A. 2014. Synthetic biology in mammalian cells: next generation research tools and therapeutics. *Nature reviews Molecular cell biology,* 15**,** 95-107.

LIPPMANN, E. S., WILLIAMS, C. E., RUHL, D. A., ESTEVEZ-SILVA, M. C., CHAPMAN, E. R., COON, J. J. & ASHTON, R. S. 2015. Deterministic HOX patterning in human pluripotent stem cell-derived neuroectoderm. *Stem cell reports,* 4**,** 632-644.

LIU, P., WAKAMIYA, M., SHEA, M. J., ALBRECHT, U., BEHRINGER, R. R. & BRADLEY, A. 1999. Requirement for Wnt3 in vertebrate axis formation. *Nature genetics,* 22**,** 361-365.

LOBE, C. G. 1997. Expression of the helix-loop-helix factor, Hes3, during embryo development suggests a role in early midbrain-hindbrain patterning. *Mech Dev,* 62**,** 227-37.

LOLAS, M., VALENZUELA, P. D., TJIAN, R. & LIU, Z. 2014. Charting Brachyury-mediated developmental pathways during early mouse embryogenesis. *Proceedings of the National Academy of Sciences,* 111**,** 4478-4483.

LOUDIG, O., BABICHUK, C., WHITE, J., ABU-ABED, S., MUELLER, C. & PETKOVICH, M. 2000. Cytochrome P450RAI (CYP26) promoter: a distinct composite retinoic acid response element underlies the complex regulation of retinoic acid metabolism. *Molecular endocrinology,* 14**,** 1483-1497.

LOUDIG, O., MACLEAN, G. A., DORE, N. L., LUU, L. & PETKOVICH, M. 2005. Transcriptional co-operativity between distant retinoic acid response elements in regulation of Cyp26A1 inducibility. *Biochemical Journal,* 392**,** 241-248.

LOWELL, S., BENCHOUA, A., HEAVEY, B. & SMITH, A. G. 2006. Notch promotes neural lineage entry by pluripotent embryonic stem cells. *PLoS biology,* 4**,** e121.

LOZACHMEUR, G., BRAMOULLE, A., AUBERT, A., STÜDER, F., MOEHLIN, J., MADRANGE, L., YATES, F., DESLYS, J.-P. & MENDOZA-PARRA, M. A. 2023. A 3-dimensional molecular cartography of human cerebral organoids revealed by double-barcoded spatial transcriptomics. *bioRxiv***,** 2023.01.18.524520.

LU, C. C., BRENNAN, J. & ROBERTSON, E. J. 2001. From fertilization to gastrulation: axis formation in the mouse embryo. *Current opinion in genetics & development,* 11**,** 384-392.

MACQUEEN, J. Classification and analysis of multivariate observations. 5th Berkeley Symp. Math. Statist. Probability, 1967. University of California Los Angeles LA USA, 281-297.

MAIER, M. M. & GESSLER, M. 2000. Comparative analysis of the human and mouse Hey1 promoter: Hey genes are new Notch target genes. *Biochemical and biophysical research communications,* 275**,** 652-660.

MALAGUTI, M., MIGUELES, R. P., BLIN, G., LIN, C.-Y. & LOWELL, S. 2019. Id1 Stabilizes Epiblast Identity by Sensing Delays in Nodal Activation and Adjusting the Timing of Differentiation. *Developmental Cell,* 50**,** 462-477.e5.

MANDERFIELD, L. J., HIGH, F. A., ENGLEKA, K. A., LIU, F., LI, L., RENTSCHLER, S. & EPSTEIN, J. A. 2012. Notch activation of Jagged1 contributes to the assembly of the arterial wall. *Circulation,* 125**,** 314-23.

MARKS, H., KALKAN, T., MENAFRA, R., DENISSOV, S., JONES, K., HOFEMEISTER, H., NICHOLS, J., KRANZ, A., STEWART, A. F. & SMITH, A. 2012. The transcriptional and epigenomic foundations of ground state pluripotency. *Cell,* 149**,** 590-604.

MARTIN, B. L. & KIMELMAN, D. 2008. Regulation of canonical Wnt signaling by Brachyury is essential for posterior mesoderm formation. *Developmental cell,* 15**,** 121-133.

MARTIN, B. L. & KIMELMAN, D. 2012. Canonical Wnt signaling dynamically controls multiple stem cell fate decisions during vertebrate body formation. *Developmental cell,* 22**,** 223-232.

MARTIN, G. R. 1981. Isolation of a pluripotent cell line from early mouse embryos cultured in medium conditioned by teratocarcinoma stem cells. *Proceedings of the National Academy of Sciences,* 78**,** 7634-7638.

MASTROMINA, I., VERRIER, L., SILVA, J. C., STOREY, K. G. & DALE, J. K. 2018. Myc activity is required for maintenance of the neuromesodermal progenitor signalling network and for segmentation clock gene oscillations in mouse. *Development,* 145**,** dev161091.

MATHIS, L. & NICOLAS, J. F. 2000. Different clonal dispersion in the rostral and caudal mouse central nervous system. *Development,* 127**,** 1277-1290.

MCCRIGHT, B., LOZIER, J. & GRIDLEY, T. 2006. Generation of new Notch2 mutant alleles. *Genesis,* 44**,** 29-33.

MCDOLE, K., GUIGNARD, L., AMAT, F., BERGER, A., MALANDAIN, G., ROYER, L. A., TURAGA, S. C., BRANSON, K. & KELLER, P. J. 2018. In Toto Imaging and Reconstruction of Post-Implantation Mouse Development at the Single-Cell Level. *Cell,* 175**,** 859-876.e33.

MIAO, Y., DJEFFAL, Y., DE SIMONE, A., ZHU, K., LEE, J. G., LU, Z., SILBERFELD, A., RAO, J., TARAZONA, O. A. & MONGERA, A. 2022. Reconstruction and deconstruction of human somitogenesis in vitro. *Nature***,** 1-3.

MILLER, I., MIN, M., YANG, C., TIAN, C., GOOKIN, S., CARTER, D. & SPENCER, S. L. 2018. Ki67 is a Graded Rather than a Binary Marker of Proliferation versus Quiescence. *Cell Rep,* 24**,** 1105-1112.e5.

MINOWADA, G., JARVIS, L. A., CHI, C. L., NEUBUSER, A., SUN, X., HACOHEN, N., KRASNOW, M. A. & MARTIN, G. R. 1999. Vertebrate Sprouty genes are induced by FGF signaling and can cause chondrodysplasia when overexpressed. *Development,* 126**,** 4465-4475.

MORGANI, S., NICHOLS, J. & HADJANTONAKIS, A.-K. 2017. The many faces of Pluripotency: in vitro adaptations of a continuum of in vivo states. *BMC developmental biology,* 17**,** 1-20.

MORIS, N., ANLAS, K., VAN DEN BRINK, S. C., ALEMANY, A., SCHRÖDER, J., GHIMIRE, S., BALAYO, T., VAN OUDENAARDEN, A. & MARTINEZ ARIAS, A. 2020. An in vitro model of early anteroposterior organization during human development. *Nature,* 582**,** 410-415.

MUGELE, D., MOULDING, D. A., SAVERY, D., MOLÈ, M. A., GREENE, N. D. E., MARTINEZ-BARBERA, J. P. & COPP, A. J. 2018. Genetic approaches in mice demonstrate that neuro-mesodermal progenitors express T/Brachyury but not Sox2. *bioRxiv***,** 503854.

NAICHE, L. A., HOLDER, N. & LEWANDOSKI, M. 2011. FGF4 and FGF8 comprise the wavefront activity that controls somitogenesis. *Proceedings of the National Academy of Sciences,* 108**,** 4018-4023.

NAKAYA, Y. & SHENG, G. 2008. Epithelial to mesenchymal transition during gastrulation: an embryological view. *Development, growth & differentiation,* 50**,** 755-766.

NANDAGOPAL, N., SANTAT, L. A. & ELOWITZ, M. B. 2019. Cis-activation in the Notch signaling pathway. *Elife,* 8.

NICHOLS, J. & SMITH, A. 2009. Naive and primed pluripotent states. *Cell stem cell,* 4**,** 487-492.

NICHOLS, J. & SMITH, A. 2012. Pluripotency in the embryo and in culture. *Cold Spring Harbor perspectives in biology,* 4**,** a008128.

NICOLAS, J., MATHIS, L., BONNEROT, C. & SAURIN, W. 1996. Evidence in the mouse for self-renewing stem cells in the formation of a segmented longitudinal structure, the myotome. *Development,* 122**,** 2933-2946.

NISHIMURA, M., ISAKA, F., ISHIBASHI, M., TOMITA, K., TSUDA, H., NAKANISHI, S. & KAGEYAMA, R. 1998. Structure, Chromosomal Locus, and Promoter of MouseHes2Gene, a Homologue ofDrosophila hairyandEnhancer of split. *Genomics,* 49**,** 69-75.

NIWA, Y., MASAMIZU, Y., LIU, T., NAKAYAMA, R., DENG, C.-X. & KAGEYAMA, R. 2007. The Initiation and Propagation of Hes7 Oscillation Are Cooperatively Regulated by Fgf and Notch Signaling in the Somite Segmentation Clock. *Developmental Cell,* 13**,** 298-304.

NOWOTSCHIN, S., FERRER-VAQUER, A., CONCEPCION, D., PAPAIOANNOU, V. E. & HADJANTONAKIS, A.-K. 2012. Interaction of Wnt3a, Msgn1 and Tbx6 in neural versus paraxial mesoderm lineage commitment and paraxial mesoderm differentiation in the mouse embryo. *Developmental biology,* 367**,** 1-14.

OKUBO, Y., SUGAWARA, T., ABE-KODUKA, N., KANNO, J., KIMURA, A. & SAGA, Y. 2012. Lfng regulates the synchronized oscillation of the mouse segmentation clock via trans-repression of Notch signalling. *Nature communications,* 3**,** 1141.

OLIVERA-MARTINEZ, I., HARADA, H., HALLEY, P. A. & STOREY, K. G. 2012. Loss of FGF-Dependent Mesoderm Identity and Rise of Endogenous Retinoid Signalling Determine Cessation of Body Axis Elongation. *PLOS Biology,* 10**,** e1001415.

OLIVERA-MARTINEZ, I. & STOREY, K. G. 2007. Wnt signals provide a timing mechanism for the FGF-retinoid differentiation switch during vertebrate body axis extension. *Development,* 134**,** 2125-2135.

OLMSTED, Z. T., STIGLIANO, C., MARZULLO, B., CIBELLI, J., HORNER, P. J. & PALUH, J. L. 2022. Fully Characterized Mature Human iPS- and NMP-Derived Motor Neurons Thrive Without Neuroprotection in the Spinal Contusion Cavity. *Frontiers in Cellular Neuroscience,* 15.

OSORNO, R., TSAKIRIDIS, A., WONG, F., CAMBRAY, N., ECONOMOU, C., WILKIE, R., BLIN, G., SCOTTING, P. J., CHAMBERS, I. & WILSON, V. 2012. The developmental dismantling of pluripotency is reversed by ectopic Oct4 expression. *Development,* 139**,** 2288-2298.

PALOMERO, T., LIM, W. K., ODOM, D. T., SULIS, M. L., REAL, P. J., MARGOLIN, A., BARNES, K. C., O'NEIL, J., NEUBERG, D. & WENG, A. P. 2006. NOTCH1 directly regulates c-MYC and activates a feed-forward-loop transcriptional network promoting leukemic cell growth. *Proceedings of the National Academy of Sciences,* 103**,** 18261-18266.

PEARSON, K. 1901. LIII. On lines and planes of closest fit to systems of points in space. *The London, Edinburgh, and Dublin philosophical magazine and journal of science,* 2**,** 559-572.

PIJUAN-SALA, B., GRIFFITHS, J. A., GUIBENTIF, C., HISCOCK, T. W., JAWAID, W., CALERO-NIETO, F. J., MULAS, C., IBARRA-SORIA, X., TYSER, R. C. V., HO, D. L. L., REIK, W., SRINIVAS, S., SIMONS, B. D., NICHOLS, J., MARIONI, J. C. & GÖTTGENS, B. 2019. A single-cell molecular map of mouse gastrulation and early organogenesis. *Nature,* 566**,** 490-495.

POLAŃSKI, K., YOUNG, M. D., MIAO, Z., MEYER, K. B., TEICHMANN, S. A. & PARK, J.-E. 2020. BBKNN: fast batch alignment of single cell transcriptomes. *Bioinformatics,* 36**,** 964-965.

POURQUIÉ, O. 2001. Vertebrate somitogenesis. *Annual review of cell and developmental biology,* 17**,** 311-350.

PRZEMECK, G. K., HEINZMANN, U., BECKERS, J. & HRABÉ DE ANGELIS, M. 2003. Node and midline defects are associated with left-right development in Delta1 mutant embryos.

QIU, X., ZHU, D. Y., YAO, J., JING, Z., ZUO, L., WANG, M., MIN, K. H., PAN, H., WANG, S., LIAO, S., LAI, Y., HAO, S., LU, Y. R., HILL, M., MARTIN-RUFINO, J. D., WENG, C., RIERA-ESCANDELL, A. M., CHEN, M., WU, L., ZHANG, Y., WEI, X., LI, M., HUANG, X., XIANG, R., YANG, Z., LIU, C., XIA, T., LIANG, Y., XU, J., HU, Q., HU, Y., ZHU, H., LI, Y., CHEN, A., ESTEBAN, M. A., GU, Y., LAUFFENBURGER, D. A., XU, X., LIU, L., WEISSMAN, J. S., LIU, S. & BAI, Y. 2022. Spateo: multidimensional spatiotemporal modeling of single-cell spatial transcriptomics. *bioRxiv***,** 2022.12.07.519417.

RAMPAL, R., LI, A. S., MOLONEY, D. J., GEORGIOU, S. A., LUTHER, K. B., NITA-LAZAR, A. & HALTIWANGER, R. S. 2005. Lunatic fringe, manic fringe, and radical fringe recognize similar specificity determinants in O-fucosylated epidermal growth factor-like repeats. *Journal of Biological Chemistry,* 280**,** 42454-42463.

RIPLEY, B. D. 1976. The second-order analysis of stationary point processes. *Journal of Applied Probability,* 13**,** 255-266.

ROMANOS, M., ALLIO, G., ROUSSIGNÉ, M., COMBRES, L., ESCALAS, N., SOULA, C., MÉDEVIELLE, F., STEVENTON, B., TRESCASES, A. & BÉNAZÉRAF, B. 2021. Cell-to-cell heterogeneity in Sox2 and Bra expression guides progenitor motility and destiny. *Elife,* 10.

ROSSANT, J. 2015. Mouse and human blastocyst-derived stem cells: vive les differences. *Development,* 142**,** 9-12.

ROSSANT, J. & TAM, P. P. 2009. Blastocyst lineage formation, early embryonic asymmetries and axis patterning in the mouse.

RUKHLENKO, O. S., HALASZ, M., RAUCH, N., ZHERNOVKOV, V., PRINCE, T., WYNNE, K., MAHER, S., KASHDAN, E., MACLEOD, K., CARRAGHER, N. O., KOLCH, W. & KHOLODENKO, B. N. 2022. Control of cell state transitions. *Nature,* 609**,** 975-985.

RUVINSKY, I., SILVER, L. M. & HO, R. K. 1998. Characterization of the zebrafish tbx16 gene and evolution of the vertebrate T-box family. *Development genes and evolution,* 208**,** 94-99.

SAMBASIVAN, R. & STEVENTON, B. 2021. Neuromesodermal progenitors: a basis for robust axial patterning in development and evolution. *Frontiers in Cell and Developmental Biology,* 8**,** 607516.

SARAVANAMUTHU, S. S., GAO, C. Y. & ZELENKA, P. S. 2009. Notch signaling is required for lateral induction of Jagged1 during FGF-induced lens fiber differentiation. *Dev Biol,* 332**,** 166-76.

SASAI, N., KUTEJOVA, E. & BRISCOE, J. 2014. Integration of signals along orthogonal axes of the vertebrate neural tube controls progenitor competence and increases cell diversity. *PLoS biology,* 12**,** e1001907.

SASAI, Y., KAGEYAMA, R., TAGAWA, Y., SHIGEMOTO, R. & NAKANISHI, S. 1992. Two mammalian helix-loop-helix factors structurally related to Drosophila hairy and Enhancer of split. *Genes & development,* 6**,** 2620-2634.

SAVORY, J. G., BOUCHARD, N., PIERRE, V., RIJLI, F. M., DE REPENTIGNY, Y., KOTHARY, R. & LOHNES, D. 2009. Cdx2 regulation of posterior development through non-Hox targets. *Development,* 136**,** 4099-4110.

SCHAPIRO, D., JACKSON, H. W., RAGHURAMAN, S., FISCHER, J. R., ZANOTELLI, V. R. T., SCHULZ, D., GIESEN, C., CATENA, R., VARGA, Z. & BODENMILLER, B. 2017. histoCAT: analysis of cell phenotypes and interactions in multiplex image cytometry data. *Nature Methods,* 14**,** 873-876.

SELLECK, M. & STERN, C. D. 1991. Fate mapping and cell lineage analysis of Hensen's node in the chick embryo. *Development,* 112**,** 615-626.

SHI, S., STAHL, M., LU, L. & STANLEY, P. 2005. Canonical Notch signaling is dispensable for early cell fate specifications in mammals. *Molecular and cellular biology,* 25**,** 9503-9508.

SHI, S. & STANLEY, P. 2003. Protein O-fucosyltransferase 1 is an essential component of Notch signaling pathways. *Proceedings of the National Academy of Sciences,* 100**,** 5234-5239.

SHIMIZU, K., CHIBA, S., SAITO, T., KUMANO, K. & HIRAI, H. 2000. Physical Interaction of Delta1, Jagged1, and Jagged2 with Notch1 and Notch3 Receptors. *Biochemical and Biophysical Research Communications,* 276**,** 385-389.

SHIMIZU, T., KAGAWA, T., INOUE, T., NONAKA, A., TAKADA, S., ABURATANI, H. & TAGA, T. 2008. Stabilized β-Catenin Functions through TCF/LEF Proteins and the Notch/RBP-Jκ Complex To Promote Proliferation and Suppress Differentiation of Neural Precursor Cells. *Molecular and Cellular Biology,* 28**,** 7427-7441.

SHIMOJO, H., ISOMURA, A., OHTSUKA, T., KORI, H., MIYACHI, H. & KAGEYAMA, R. 2016. Oscillatory control of Delta-like1 in cell interactions regulates dynamic gene expression and tissue morphogenesis. *Genes Dev,* 30**,** 102-16.

SIEBEL, C. & LENDAHL, U. 2017. Notch signaling in development, tissue homeostasis, and disease. *Physiological reviews,* 97**,** 1235-1294.

SILVA, J. & SMITH, A. 2008. Capturing pluripotency. *Cell,* 132**,** 532-536.

SKOK GIBBS, C., JACKSON, C. A., SALDI, G.-A., TJÄRNBERG, A., SHAH, A., WATTERS, A., DE VEAUX, N., TCHOURINE, K., YI, R., HAMAMSY, T., CASTRO, D. M., CARRIERO, N., GORISSEN, B. L., GRESHAM, D., MIRALDI, E. R. & BONNEAU, R. 2022. High-performance single-cell gene regulatory network inference at scale: the Inferelator 3.0. *Bioinformatics,* 38**,** 2519-2528.

SMITH, A. G., HEATH, J. K., DONALDSON, D. D., WONG, G. G., MOREAU, J., STAHL, M. & ROGERS, D. 1988. Inhibition of pluripotential embryonic stem cell differentiation by purified polypeptides. *nature,* 336**,** 688-690.

SMITH, R. & MCLAREN, A. 1977. Factors affecting the time of formation of the mouse blastocoele.

SNOUSSI, E. H. 1998. Necessary conditions for multistationarity and stable periodicity. *Journal of Biological Systems,* 6**,** 3-9.

SOUILHOL, C., PEREA-GOMEZ, A., CAMUS, A., BECK-CORMIER, S., VANDORMAEL-POURNIN, S., ESCANDE, M., COLLIGNON, J. & COHEN-TANNOUDJI, M. 2015. NOTCH activation interferes with cell fate specification in the gastrulating mouse embryo. *Development,* 142**,** 3649-3660.

SPIESS, K., FULTON, T., HWANG, S., TOH, K., SAUNDERS, D., PAIGE, B., STEVENTON, B. & VERD, B. 2022. Approximated Gene Expression Trajectories (AGETs) for Gene Regulatory Network Inference on Cell Tracks. *bioRxiv***,** 2022.01.12.476060.

SPRINZAK, D., LAKHANPAL, A., LEBON, L., SANTAT, L. A., FONTES, M. E., ANDERSON, G. A., GARCIA-OJALVO, J. & ELOWITZ, M. B. 2010. Cis-interactions between Notch and Delta generate mutually exclusive signalling states. *Nature,* 465**,** 86-90.

STOLTZFUS, C. R., FILIPEK, J., GERN, B. H., OLIN, B. E., LEAL, J. M., WU, Y., LYONS-COHEN, M. R., HUANG, J. Y., PAZ-STOLTZFUS, C. L., PLUMLEE, C. R., PÖSCHINGER, T., URDAHL, K. B., PERRO, M. & GERNER, M. Y. 2020. CytoMAP: A Spatial Analysis Toolbox Reveals Features of Myeloid Cell Organization in Lymphoid Tissues. *Cell Reports,* 31.

STOWER, M. J. & SRINIVAS, S. 2014. Heading forwards: anterior visceral endoderm migration in patterning the mouse embryo. *Philosophical Transactions of the Royal Society B: Biological Sciences,* 369**,** 20130546.

STREET, K., RISSO, D., FLETCHER, R. B., DAS, D., NGAI, J., YOSEF, N., PURDOM, E. & DUDOIT, S. 2018. Slingshot: cell lineage and pseudotime inference for single-cell transcriptomics. *BMC Genomics,* 19**,** 477.

SUBRAMANIAN, V., MEYER, B. I. & GRUSS, P. 1995. Disruption of the murine homeobox gene Cdx1 affects axial skeletal identities by altering the mesodermal expression domains of Hox genes. *Cell,* 83**,** 641-653.

SWIATEK, P. J., LINDSELL, C. E., DEL AMO, F. F., WEINMASTER, G. & GRIDLEY, T. 1994. Notch1 is essential for postimplantation development in mice. *Genes & development,* 8**,** 707-719.

TAKEBAYASHI, K., SASAI, Y., SAKAI, Y., WATANABE, T., NAKANISHI, S. & KAGEYAMA, R. 1994. Structure, chromosomal locus, and promoter analysis of the gene encoding the mouse helix-loop-helix factor HES-1. Negative autoregulation through the multiple N box elements. *Journal of Biological Chemistry,* 269**,** 5150-5156.

TAKEMOTO, T., UCHIKAWA, M., KAMACHI, Y. & KONDOH, H. 2006. Convergence of Wnt and FGF signals in the genesis of posterior neural plate through activation of the Sox2 enhancer N-1.

TAKEMOTO, T., UCHIKAWA, M., YOSHIDA, M., BELL, D. M., LOVELL-BADGE, R., PAPAIOANNOU, V. E. & KONDOH, H. 2011. Tbx6-dependent Sox2 regulation determines neural or mesodermal fate in axial stem cells. *Nature,* 470**,** 394-398.

TAM, P. P. & BEHRINGER, R. R. 1997. Mouse gastrulation: the formation of a mammalian body plan. *Mechanisms of development,* 68**,** 3-25.

TAM, P. P. L. & LOEBEL, D. A. F. 2007. Gene function in mouse embryogenesis: get set for gastrulation. *Nature Reviews Genetics,* 8**,** 368-381.

TAMASHIRO, D. A. A., ALARCON, V. B. & MARIKAWA, Y. 2012. Nkx1-2 is a transcriptional repressor and is essential for the activation of Brachyury in P19 mouse embryonal carcinoma cell. *Differentiation,* 83**,** 282-292.

TARKOWSKI, A. K. & WRÓBLEWSKA, J. 1967. Development of blastomeres of mouse eggs isolated at the 4-and 8-cell stage.

TEAM, R. C. 2021. R: A language and environment for statistical computing.: R Foundation for Statistical Computing, Vienna, Austria.

TESAR, P. J., CHENOWETH, J. G., BROOK, F. A., DAVIES, T. J., EVANS, E. P., MACK, D. L., GARDNER, R. L. & MCKAY, R. D. 2007. New cell lines from mouse epiblast share defining features with human embryonic stem cells. *Nature,* 448**,** 196-199.

THOMSON, J. A., ITSKOVITZ-ELDOR, J., SHAPIRO, S. S., WAKNITZ, M. A., SWIERGIEL, J. J., MARSHALL, V. S. & JONES, J. M. 1998. Embryonic stem cell lines derived from human blastocysts. *science,* 282**,** 1145-1147.

TOH, K., SAUNDERS, D., VERD, B. & STEVENTON, B. 2022. Zebrafish neuromesodermal progenitors undergo a critical state transition in vivo. *iScience,* 25.

TSAKIRIDIS, A., HUANG, Y., BLIN, G., SKYLAKI, S., WYMEERSCH, F., OSORNO, R., ECONOMOU, C., KARAGIANNI, E., ZHAO, S., LOWELL, S. & WILSON, V. 2014. Distinct Wnt-driven primitive streak-like populations reflect in vivo lineage precursors. *Development,* 141**,** 1209-1221.

TSAKIRIDIS, A. & WILSON, V. 2015. Assessing the bipotency of in vitro-derived neuromesodermal progenitors [version 1; peer review: 1 approved, 2 approved with reservations]. *F1000Research,* 4**,** 100.

TZOUANACOU, E., WEGENER, A., WYMEERSCH, F. J., WILSON, V. & NICOLAS, J.-F. 2009. Redefining the progression of lineage segregations during mammalian embryogenesis by clonal analysis. *Developmental cell,* 17**,** 365-376.

VAN DEN AKKER, E., FORLANI, S., CHAWENGSAKSOPHAK, K., DE GRAAFF, W., BECK, F., MEYER, B. I. & DESCHAMPS, J. 2002. Cdx1 and Cdx2 have overlapping functions in anteroposterior patterning and posterior axis elongation.

VAN DEN BOOGART, G. 2019. compositions: Compositional Data Analysis.

VAN DEN BRINK, S. C., ALEMANY, A., VAN BATENBURG, V., MORIS, N., BLOTENBURG, M., VIVIE, J., BAILLIE-JOHNSON, P., NICHOLS, J., SONNEN, K. F. & MARTINEZ ARIAS, A. 2020. Single-cell and spatial transcriptomics reveal somitogenesis in gastruloids. *Nature,* 582**,** 405-409.

VAN DEN BRINK, S. C., BAILLIE-JOHNSON, P., BALAYO, T., HADJANTONAKIS, A.-K., NOWOTSCHIN, S., TURNER, D. A. & MARTINEZ ARIAS, A. 2014. Symmetry breaking, germ layer specification and axial organisation in aggregates of mouse embryonic stem cells. *Development,* 141**,** 4231-4242.

VAN DER MAATEN, L. & HINTON, G. 2008. Visualizing data using t-SNE. *Journal of machine learning research,* 9.

VEENVLIET, J. V., BOLONDI, A., KRETZMER, H., HAUT, L., SCHOLZE-WITTLER, M., SCHIFFERL, D., KOCH, F., GUIGNARD, L., KUMAR, A. S. & PUSTET, M. 2020. Mouse embryonic stem cells self-organize into trunk-like structures with neural tube and somites. *Science,* 370**,** eaba4937.

VERMOT, J., LLAMAS, J. G., FRAULOB, V., NIEDERREITHER, K., CHAMBON, P. & DOLLÉ, P. 2005. Retinoic Acid Controls the Bilateral Symmetry of Somite Formation in the Mouse Embryo. *Science,* 308**,** 563-566.

VERRIER, L., DAVIDSON, L., GIERLIŃSKI, M., DADY, A. & STOREY, K. G. 2018. Neural differentiation, selection and transcriptomic profiling of human neuromesodermal progenitor-like cells in vitro. *Development,* 145.

VIDIGAL, J. A., MORKEL, M., WITTLER, L., BROUWER-LEHMITZ, A., GROTE, P., MACURA, K. & HERRMANN, B. G. 2010. An inducible RNA interference system for the functional dissection of mouse embryogenesis. *Nucleic acids research,* 38**,** e122-e122.

VITILLO, L., DURANCE, C., HEWITT, Z., MOORE, H., SMITH, A. & VALLIER, L. 2020. GMP-grade neural progenitor derivation and differentiation from clinical-grade human embryonic stem cells. *Stem Cell Res Ther,* 11**,** 406.

WAHL, M. B., DENG, C., LEWANDOSKI, M. & POURQUIÉ, O. 2007. FGF signaling acts upstream of the NOTCH and WNT signaling pathways to control segmentation clock oscillations in mouse somitogenesis. *Development,* 134**,** 4033-4041.

WAITES, W., CAVALIERE, M., CACHAT, E., DANOS, V. & DAVIES, J. A. 2018. An information-theoretic measure for patterning in epithelial tissues. *IEEE Access,* 6**,** 40302-40312.

WANG, H.-Y., HUANG, Y.-X., QI, Y.-F., ZHANG, Y., BAO, Y.-L., SUN, L.-G., ZHENG, L.-H., ZHANG, Y.-W., MA, Z.-Q. & LI, Y.-X. 2013. Mathematical models for the Notch and Wnt signaling pathways and the crosstalk between them during somitogenesis. *Theoretical Biology and Medical Modelling,* 10**,** 27.

WANG, M., HU, Q., LV, T., WANG, Y., LAN, Q., XIANG, R., TU, Z., WEI, Y., HAN, K., SHI, C., GUO, J., LIU, C., YANG, T., DU, W., AN, Y., CHENG, M., XU, J., LU, H., LI, W., ZHANG, S., CHEN, A., CHEN, W., LI, Y., WANG, X., XU, X., HU, Y. & LIU, L. 2022. High-resolution 3D spatiotemporal transcriptomic maps of developing Drosophila embryos and larvae. *Developmental Cell,* 57**,** 1271-1283.e4.

WANG, T., HOLT, C. M., XU, C., RIDLEY, C., JONES, R. P., BARON, M. & TRUMP, D. 2007. Notch3 activation modulates cell growth behaviour and cross-talk to Wnt/TCF signalling pathway. *Cellular signalling,* 19**,** 2458-2467.

WENNEKAMP, S., MESECKE, S., NÉDÉLEC, F. & HIIRAGI, T. 2013. A self-organization framework for symmetry breaking in the mammalian embryo. *Nature reviews Molecular cell biology,* 14**,** 452-459.

WESTON, D. J., ADAMS, N. M., RUSSELL, R. A., STEPHENS, D. A. & FREEMONT, P. S. 2012. Analysis of Spatial Point Patterns in Nuclear Biology. *PLOS ONE,* 7**,** e36841.

WHITE, P. H. & CHAPMAN, D. L. 2005. Dll1 is a downstream target of Tbx6 in the paraxial mesoderm. *genesis,* 42**,** 193-202.

WHITE, P. H., FARKAS, D. R. & CHAPMAN, D. L. 2005. Regulation of Tbx6 expression by Notch signaling. *genesis,* 42**,** 61-70.

WILKINSON, D. G., BHATT, S. & HERRMANN, B. G. 1990. Expression pattern of the mouse T gene and its role in mesoderm formation. *Nature,* 343**,** 657-659.

WILLIAMS, D. R., SHIFLEY, E. T., BRAUNREITER, K. M. & COLE, S. E. 2016. Disruption of somitogenesis by a novel dominant allele of Lfng suggests important roles for protein processing and secretion. *Development,* 143**,** 822-830.

WILLIAMS, R., LENDAHL, U. & LARDELLI, M. 1995. Complementary and combinatorial patterns of Notch gene family expression during early mouse development. *Mechanisms of development,* 53**,** 357-368.

WILSON, V. & BEDDINGTON, R. S. 1996. Cell fate and morphogenetic movement in the late mouse primitive streak. *Mechanisms of development,* 55**,** 79-89.

WILSON, V., OLIVERA-MARTINEZ, I. & STOREY, K. G. 2009. Stem cells, signals and vertebrate body axis extension.

WIND, M., GOGOLOU, A., MANIPUR, I., GRANATA, I., BUTLER, L., ANDREWS, P. W., BARBARIC, I., NING, K., GUARRACINO, M. R., PLACZEK, M. & TSAKIRIDIS, A. 2021. Defining the signalling determinants of a posterior ventral spinal cord identity in human neuromesodermal progenitor derivatives. *Development,* 148.

WINNIER, G., BLESSING, M., LABOSKY, P. A. & HOGAN, B. 1995. Bone morphogenetic protein-4 is required for mesoderm formation and patterning in the mouse. *Genes & development,* 9**,** 2105-2116.

WITTLER, L., SHIN, E. H., GROTE, P., KISPERT, A., BECKERS, A., GOSSLER, A., WERBER, M. & HERRMANN, B. G. 2007. Expression of Msgn1 in the presomitic mesoderm is controlled by synergism of WNT signalling and Tbx6. *EMBO reports,* 8**,** 784-789.

WOLPERT, L. 1969. Positional information and the spatial pattern of cellular differentiation. *Journal of theoretical biology,* 25**,** 1-47.

WOOD, T. R., KYRSTING, A., STEGMAIER, J., KUCINSKI, I., KAMINSKI, C. F., MIKUT, R. & VOICULESCU, O. 2019. Neuromesodermal progenitors separate the axial stem zones while producing few single- and dual-fated descendants. *bioRxiv***,** 622571.

WYMEERSCH, F. J., HUANG, Y., BLIN, G., CAMBRAY, N., WILKIE, R., WONG, F. C. & WILSON, V. 2016. Position-dependent plasticity of distinct progenitor types in the primitive streak. *Elife,* 5**,** e10042.

WYMEERSCH, F. J., SKYLAKI, S., HUANG, Y., WATSON, J. A., ECONOMOU, C., MAREK-JOHNSTON, C., TOMLINSON, S. R. & WILSON, V. 2019. Transcriptionally dynamic progenitor populations organised around a stable niche drive axial patterning. *Development,* 146**,** dev168161.

WYMEERSCH, F. J., WILSON, V. & TSAKIRIDIS, A. 2021. Understanding axial progenitor biology in vivo and in vitro. *Development,* 148**,** dev180612.

YAMAGUCHI, T. P., HARPAL, K., HENKEMEYER, M. & ROSSANT, J. 1994. fgfr-1 is required for embryonic growth and mesodermal patterning during mouse gastrulation. *Genes & development,* 8**,** 3032-3044.

YAMAGUCHI, T. P., TAKADA, S., YOSHIKAWA, Y., WU, N. & MCMAHON, A. P. 1999. T (Brachyury) is a direct target of Wnt3a during paraxial mesoderm specification. *Genes & development,* 13**,** 3185-3190.

YAMANAKA, Y., HAMIDI, S., YOSHIOKA-KOBAYASHI, K., MUNIRA, S., SUNADOME, K., ZHANG, Y., KUROKAWA, Y., ERICSSON, R., MIEDA, A. & THOMPSON, J. L. 2022. Reconstituting human somitogenesis in vitro. *Nature***,** 1-3.

YING, Q.-L. & SMITH, A. G. 2003. Defined conditions for neural commitment and differentiation. *Methods in enzymology,* 365**,** 327-341.

YING, Q. L., NICHOLS, J., CHAMBERS, I. & SMITH, A. 2003. BMP induction of Id proteins suppresses differentiation and sustains embryonic stem cell self-renewal in collaboration with STAT3. *Cell,* 115**,** 281-92.

YOON, J. K. & WOLD, B. 2000. The bHLH regulator pMesogenin1 is required for maturation and segmentation of paraxial mesoderm. *Genes & development,* 14**,** 3204-3214.

YOSHIKAWA, Y., FUJIMORI, T., MCMAHON, A. P. & TAKADA, S. 1997. Evidence That Absence ofWnt-3aSignaling Promotes Neuralization Instead of Paraxial Mesoderm Development in the Mouse. *Developmental Biology,* 183**,** 234-242.

ZHANG, F., WU, Y. & TIAN, W. 2019. A novel approach to remove the batch effect of single-cell data. *Cell discovery,* 5**,** 46.

ZHANG, N. & GRIDLEY, T. 1998. Defects in somite formation in lunatic fringe-deficient mice. *Nature,* 394**,** 374-377.